Molecular Reorientation and Transport in Liquid Water and Ice

Molecular Reorientation and Transport in Liquid Water and Ice

ACADEMISCH PROEFSCHRIFT

ter verkrijging van de graad van doctor
aan de Universiteit van Amsterdam
op gezag van de Rector Magnificus
prof. dr. D. C. van den Boom
ten overstaan van een door het college voor promoties
ingestelde commissie,
in het openbaar te verdedigen in de Agnietenkapel
op dinsdag 26 januari 2010, te 14:00 uur

door

Rutger Laurens Alexander Timmer

geboren te Vriezenveen

Promotiecommissie

promotor:	prof. dr. H. J. Bakker
overige leden:	prof. dr. M. Bonn
	prof. dr. A. M. Brouwer
	prof. dr. M. L. Groot
	prof. dr. S. R. Keiding
	dr. E. J. Meijer
	dr. S. Woutersen

Faculteit der Natuurwetenschappen, Wiskunde en Informatica

ISBN 978-90-77209-39-4

The work described in this thesis was performed at the FOM-*Institute for Atomic and Molecular Physics* (AMOLF), Kruislaan 407, 1098 SJ Amsterdam, The Netherlands. This work is part of the research programme of the *Stichting Fundamenteel Onderzoek der Materie* (FOM), which is financially supported by the *Nederlandse Organisatie voor Wetenschappelijk Onderzoek* (NWO).

What is time,
but a progression of
moments?

Publications covered in this thesis

R. L. A. Timmer and H. J. Bakker. Water as a molecular hinge in amidelike structures. *J. Chem. Phys. 127*, 154507 (2007).

H. J. Bakker, Y. L. A. Rezus and R. L. A. Timmer. Molecular Reorientation of Liquid Water Studied with Femtosecond Midinfrared Spectroscopy. *J. Phys. Chem. A 112*, 11523 (2008).

R. L. A. Timmer and H. J. Bakker. Hydrogen Bond Fluctuations of the Hydration Shell of the Bromide Anion. *J. Phys. Chem. A 103*, 6104 (2009).

M. J. Cox, R. L. A. Timmer, H. J. Bakker, S. Park, and N. Agmon. Distance-Dependent Proton Transfer along Water Wires Connecting Acid-Base Pairs. *J. Phys. Chem. A 113*, 6599 (2009).

R. L. A. Timmer and H. J. Bakker. Direct observation of proton transfer in ice I_H using femtosecond spectroscopy. *Submitted.*

R. L. A. Timmer, K. J. Tielrooij and H. J. Bakker. Vibrational Förster energy transfer between water and hydrated protons. *Submitted.*

R. L. A. Timmer and H. J. Bakker. Vibrational Förster transfer in ice I_H. *Submitted.*

Other publications

P. Bodis, R. L. A. Timmer, S. Yeremenko, W. J. Buma, J. S. Hannam, D. A. Leigh, and S. Woutersen. Heterovibrational Interactions, Cooperative Hydrogen Bonding, and Vibrational Energy Relaxation Pathways in a Rotaxane. *J. Phys. Chem. C 111*, 6798 (2007).

K. J. Tielrooij, R. L. A. Timmer, H. J. Bakker, and M. Bonn. Structure Dynamics of the Proton in Liquid Water Probed with Terahertz Time-Domain Spectroscopy. *Phys. Rev. Lett. 102*, 198303 (2009).

Contents

1 Introduction

1.1 Water

Water (H_2O) is a ubiquitous substance that shows surprising complexity in its behavior, especially considering its relatively simple chemical composition. It consists of two of the most commonly found reactive elements in the universe, hydrogen and oxygen. The main reason for its complexity lies in the arrangement of its three constituent atoms. The water molecule has a total of four sp^3-hybridized electron pairs, two of which are associated with the hydrogen atoms while the other two remain as lone pairs. This arrangement causes the two covalent O–H bonds close to the tetrahedral angle and gives the water molecule its polar character. This in turn leads to the possibility for water molecules to form hydrogen bonds (O–H$\cdots$O) with up to four of their closest neighbors. Hydrogen bonds are about 10–100 times weaker than covalent bonds allowing the water molecules to quickly rearrange their configurations, while still forming a cohesive three dimensional network.

Because of its polar nature, water is able to screen excess charges by adapting the configuration of its molecules. This property greatly enhances the solubility of ions and polar molecules in water. Conversely, uncharged particles are usually hydrophobic and dissolve very poorly in water. Water also greatly facilitates the transport of excess charges on protons (i. e. hydrogen atoms) through a mechanism known as Grotthuss hopping [31]. This mechanism leads to anomalously

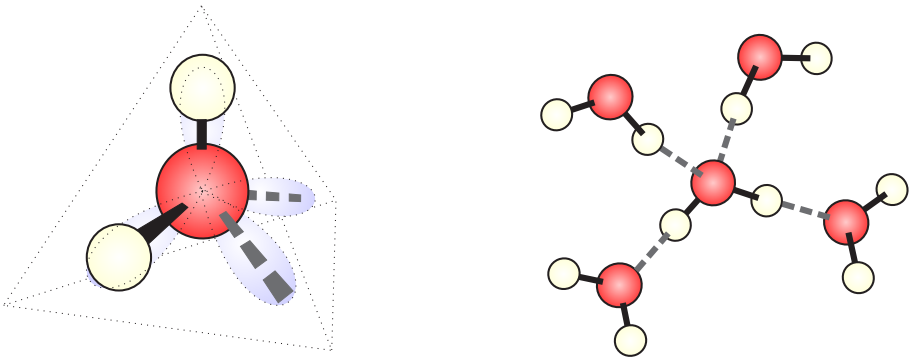

Figure 1.1. Left: tetrahedral arrangement of the hydrogen atoms and lone electron pairs in the water molecule. Right: water molecules can form hydrogen bonds with up to four neighbors.

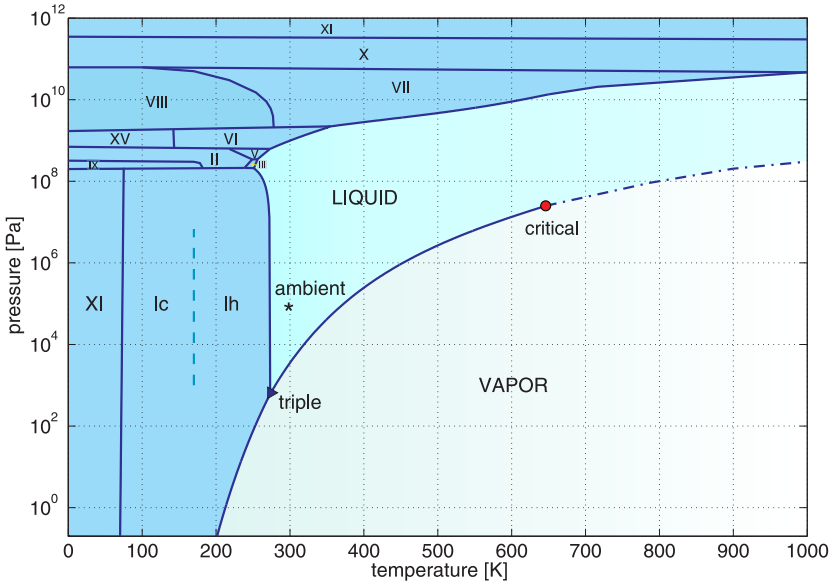

FIGURE 1.2. Phase diagram of water, which includes all known polymorphs of ice. Additionally, there exist a range of (meta-stable) amorphous ice structures with various densities. Data on phase boundaries and triple points was collected by [22].

high proton transfer rates in liquid water and ice alike.

Water thus plays an essential role as mediator and active participant in a wide variety of chemical interactions. In biology it is referred to as the 'lubricant of life' [13] due to its ability to facilitate crucial interactions ranging from the passing of ions [152] to the folding of proteins [94]. Protein structure and stability are governed in large part by hydrophobic collapse and hydrophilic interactions with water. Single embedded water molecules can form bridges between oxygen atoms of different amide groups through double hydrogen bond formation [112]. In this way they can hold together bio-molecular chains and assist in the formation of tertiary structures. Functionally, water plays an important role as a reactant at active sites or in molecular recognition through the unique directionality and adaptability of its hydrogen bonds [113].

1.2 PHASE DIAGRAM

The complexity of water and its hydrogen bond network is perhaps best illustrated by the following. Besides the well known forms of liquid water, (hexagonal) ice, and vapor there are actually more than a dozen additional crystalline ice polymorphs, as shown in Fig. 1.2. These polymorphs are stable or metastable at various temperatures and pressures not commonly found on earth, but may be created under (extreme) laboratory conditions. Structurally, they differ

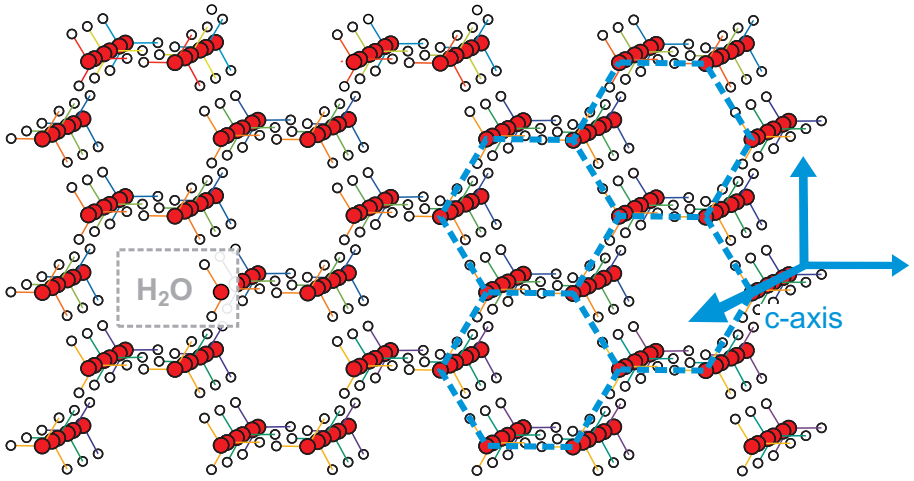

FIGURE 1.3. Frontal view of the crystal structure of hexagonal ice I_H.

in the arrangement of the oxygen atoms, the ordering of the protons, and their overall density. Furthermore, solid water at low temperatures can exist in a number of non-crystalline forms (glasses) as amorphous ice [33]. These types of ice are generally non-equilibrium states of frozen water that can be achieved through very rapid cooling ($\sim 10^5$ K/s), e. g. by spraying a fine mist of water droplets onto a very cold surface.

As can be deduced from Fig. 1.2, by far the most common form of water found on earth is in the liquid phase comprising 98.2% of the total [130]. This liquid water resides predominantly in saline environments, i. e. oceans, which cover about 70% of the earth's surface. Solid water, making up 1.76% of the total, exists almost exclusively in the form of hexagonal ice (I_H) in icecaps and glaciers [130]. Additionally, cubic ice (Ic) is a meta-stable form of ice that may naturally form in the upper atmosphere at lower pressures [105]. For the remainder, gaseous water (vapor) in the atmosphere makes up only 0.001% of the total water supply on earth [130]. In this thesis we are mostly concerned with the liquid phase of water and hexagonal ice, in the temperature range between 200–350 K at atmospheric pressures (10^5 Pa).

1.3 ICE I_H

Unlike most other substances, the density of water is lower in the solid phase than in the liquid phase (0.92 vs 1.0 g/cm^3), being most dense at 4 °C. This reduced density is due to the fact that at lower temperatures the hydrogen bonds become more dominant. Whereas in liquid water the average number of hydrogen bonds is about 3.5, in ice the water molecules become fully four-fold coordinated, leading to a more open configuration. This anomaly has many

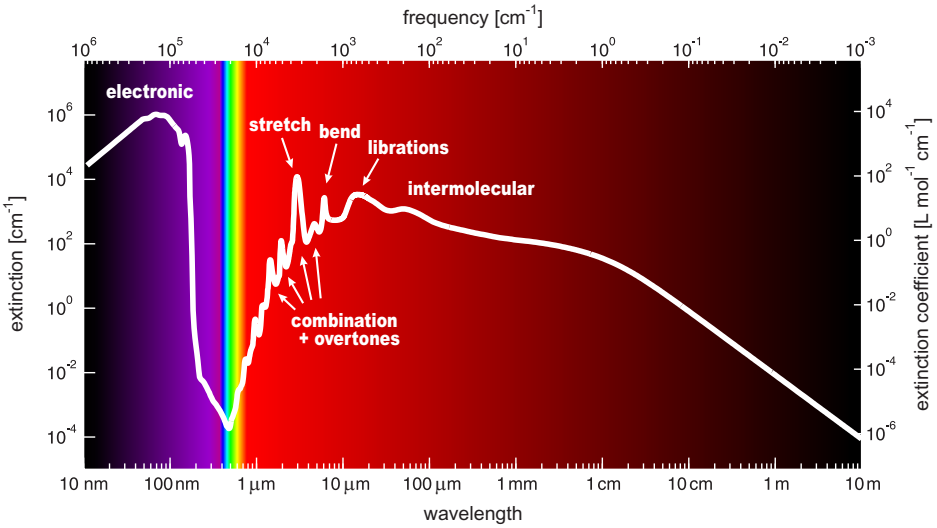

FIGURE 1.4. Absorption spectrum for liquid water (H_2O) at room temperature and nominal pressure [128]. The range around 380-780 nm is indicated with corresponding colors from the visible spectrum. The non-visible ultraviolet and infrared regions are colored purple and red, respectively.

important consequences which strongly affect the climate and life on earth. The most obvious consequence is the fact that ice floats on water and that freezing thus always starts from the top down. This insulates the underlying water from further freezing and allows aquatic life to survive under the surface. Another consequence is the enhanced convection of water. For example, surface water at a temperature of $\sim 4\,^{\circ}\mathrm{C}$ is more dense than the colder water layers underneath. This causes the surface water to sink while the lower layers will rise. This convection, combined with the high heat capacity of water has a moderating effect on our climate.

The crystal structure of ice I_H is shown in Fig. 1.3. The oxygen atoms lie on a hexagonal "wurtzite" lattice (symmetry C_{6h}, space group $P6_3/mmc$) [103]. Different polymorphs may vary in crystalline structure, ordering and density, but the water molecule is always hydrogen bonded to four neighbors in a tetrahedral arrangement. There are six different arrangements of the two hydrogen atoms of water over these four neighbors, leading to six different orientations. In ice I_H these orientations are randomly ordered, subject to the so-called Bernal-Fowler ice rules [15]. These state that each oxygen atom is connected to two nearby hydrogen atoms and that on each connection between two oxygen atoms, exactly one hydrogen resides.

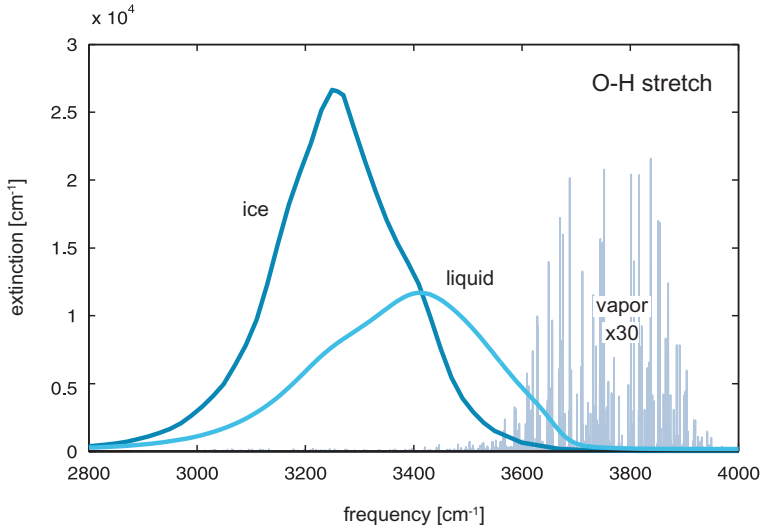

FIGURE 1.5. O–H stretching mode of pure H_2O in ice, liquid, and vapor. The vapor spectrum corresponds roughly to 30 cm of normal humidity air, the substructure is caused by rotational transitions.

1.4 ABSORPTION SPECTRUM

We study the structure and dynamics of water using its interaction with light as a measurement tool. From daily life we know water mostly as a transparent liquid, but it turns out that this is not true for all frequencies. The absorption spectrum of H_2O liquid water, shown in Fig. 1.4, reveals that water absorbs over a wide range of frequencies and is only transparent around the visible region. In fact one could state that visible light is only 'visible', because it is *not* absorbed by the water in our eyes and life on earth has adapted to use mostly visible colors (e. g. photosynthesis) because one of its fundamental building blocks is water.

On the high frequency side of the spectrum, ultraviolet light is absorbed by water through the excitation of electronic modes, which is true for almost all substances. On the other side of the visible spectrum the weak red absorptions caused by various combination and overtone bands of intramolecular vibrational modes give water a slightly blue color. The strongest vibrational absorption band of water is the O–H stretch mode at a frequency of about 3400 cm^{-1}. Further to the red side we find the H–O–H bending mode (1640 cm^{-1}) and the librational (wagging) modes of single water molecules. If we go even further to the red side, we get to low frequency intermolecular vibrations and collective motions of water molecules. Finally, if we go to very long wavelengths ($>$ 10 m) the water becomes more transparent, allowing e. g. the low frequency communication of sub-marines.

For our study of the molecular dynamics of water we mainly use the prominent absorption band of the O–H stretch mode, shown in Fig. 1.5. As noted before, the hydrogen bond network in liquid water is very dynamic. This dynamic behavior causes a large variety of different hydrogen bond strengths, which in turn influence the absorption frequencies of the stretching modes. The inhomogeneity between different water molecules thus causes a broadening of the spectrum, where O–H groups donating weak hydrogen bonds absorb on the blue side of the O–H stretch absorption band and strong hydrogen bonds on the red side. The speed with which these configurations exchange can be measured by their spectral diffusivity, as will be done in Chapter 7.

The water spectrum is not only broadened by its inhomogeneity but also due to a frequency splitting between two overlapping stretching modes. Because each water molecule has in fact two O–H groups, that can both accommodate a stretching mode, the modes couple leading to symmetric and anti-symmetric stretching normal modes. The former lies at a slightly lower frequency than the original mode, while the latter lies slightly higher. The coupling between O–H modes also occurs intermolecularly, e. g. through dipole-dipole coupling [48,162].

When we compare the spectra of the three different phases of water in Fig. 1.5, we note several important differences. First of all the absorption spectrum of ice is red-shifted with respect to that of liquid water. This observation is indicative of the stronger hydrogen bonds in ice compared to those in the liquid phase. Because the hydrogen bond pulls on the hydrogen atom in the opposite direction to that of the covalent bond, it causes a weakening of the O–H bond thus lowering its restoring force. This results in a lowering of the frequency of the stretch vibration as will be shown in the next chapter. We note also that the absorption band of ice has a much higher cross-section than that of water which indicates that the transition dipole moment between the ground state and the first excited state of the O–H stretch is higher in ice than in water. For water vapor the hydrogen bond is completely absent and consequently its absorption spectrum shifts towards higher frequencies. Its absorption spectrum consists of a large number of discrete absorption peaks. The different frequencies correspond to the various discrete rotational transitions of water. The small width of the individual peaks indicates the long life time of the vibrational excitation in gaseous water. This is due to the spatial isolation of the individual water molecules and the subsequent large reduction of intermolecular coupling mechanisms compared to water and ice.

1.5 Proton transfer

Proton (H^+) mobility in liquid water and ice is abnormally high compared to that of other cations, e. g. about seven times faster than sodium (Na^+). The mechanism responsible for this high mobility is known as the Grotthuss hopping mechanism [31]. In this mechanism not a single proton diffuses through the water, but rather the protonic charge is transferred by a relay of water molecules that each accepts a proton from their neighbor and passes their own

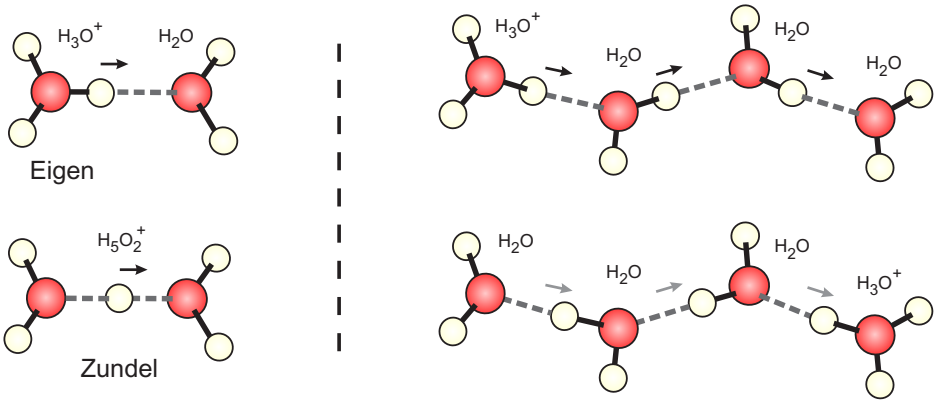

FIGURE 1.6. Left: Limiting case hydration structures of the proton in water. Right: Grotthuss hopping along a water wire changes hydrogen bonds into covalent bonds and vice versa.

proton on to the next (see Fig. 1.6). The solvation of excess protons in water is thought to occur in two limiting forms. When the proton is associated with one central water molecule, an H_3O^+ complex is formed known as the Eigen cation. In the other form, the proton is shared equally between two neighboring water molecules, forming an $H_5O_2^+$ complex, known as the Zundel cation. The molecular mechanism behind proton mobility involves a periodic series of isomerizations between Eigen and Zundel. This isomerization involves a cooperative effort of surrounding water molecules up to the second solvation shell [4].

In our experiments we study the molecular transfer of protons in water and ice. For this we use special molecules known as photo-acids. These photo-acids can be triggered with a laser pulse that causes an electronic transition in the molecule. This transition causes an intramolecular charge transfer that leads to a weakening of the covalent bond of an attached hydrogen atom. These electronic processes generally occur on sub-picosecond timescales and result in a large increase of the molecule's acidity. This photo-acid is excited with a pump pulse while the resulting proton release, transfer, and arrival at a base molecule are probed at various frequencies coinciding with spectral signatures of these processes. The proton release is probed at the absorption bands of the photo-acid and conjugate base, usually in the visible region. Proton transfer in the water is monitored using the broad absorption band of the proton [60]. As a proton acceptor we use the carboxyl class of conjugate base molecules such as formate and acetate. We probe the arrival of the proton at the base from the resulting shift of the peak of the carbonyl stretch vibration.

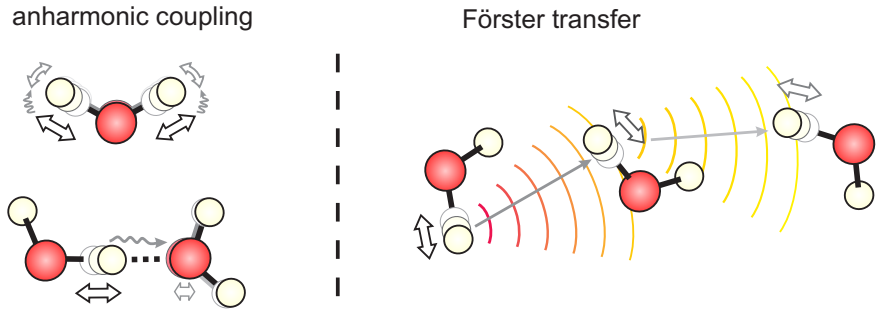

FIGURE 1.7. Energy transfer in water. Left: Intramolecular anharmonic coupling between the symmetric stretch mode and the bending mode (top) and intermolecular anharmonic coupling between the O–H stretch mode and a hydrogen bond mode (bottom). Right: Intermolecular Förster transfer through dipole-dipole coupling between O–H stretch modes. White arrows indicate the direction of the vibration, curved lines illustrate the dipole field.

1.6 ENERGY TRANSFER

An important property of water is its ability to quickly accept and distribute excess energy e. g. from chemical or biological reactions. Molecular energy transfer in water occurs through both intra- and intermolecular coupling mechanisms [84] (Fig. 1.7). In general, the dissipation rate of (vibrational) energy depends on the number density and coupling strength of accepting modes that are present in proximity to the excited oscillator. In liquids, such as water, the frequencies of these modes are continuously modulated, e. g. through variations in the hydrogen bond distance, angle, and strength. Energy distribution in water is thus greatly facilitated by the fast rearrangements of the hydrogen bond network.

The main transfer mechanism within molecules consists of anharmonic couplings between molecular modes. Anharmonic couplings occur when two anharmonic oscillators share a common set of coordinates. For example in water the O–H stretch mode is coupled intramolecularly to the H–O–H bending mode. Intermolecular anharmonic coupling is also possible, e. g. between the O–H stretch and the hydrogen bond mode. These couplings not only lead to energy transfer, but also affect the energy levels and spacings of both modes.

Energy transfer between water molecules is also possible through a direct dipole-dipole coupling mechanism, called Förster energy transfer [48, 162]. In this mechanism, an excited-state donor molecule passes its energy to a nearby acceptor molecule which has an absorption spectrum that overlaps with the emission spectrum of the donor. The transfer is mediated through dipole-dipole coupling and does not involve the exchange of a real photon, i. e. non-radiative transfer. The interaction radius is typically much smaller than the wavelength of the oscillating electric field and its coupling is highly distance dependent [47]. The Förster radius is the distance at which half the excitation energy is dis-

sipated through Förster transfer within the lifetime of the excitation. Förster transfer is sometimes used as a "molecular ruler" to determine the proximity between different molecular complexes [141].

Traditionally Förster transfer is employed in fluorescence spectroscopy, where it involves the transfer of an electronic excitation between chromophores. However, the coupling can also occur between vibrational excitations, such as the O–H stretch mode in water. In fact, in pure liquid water (and ice) it is the dominant mechanism for resonant vibrational energy transfer.

1.7 Heavy water

Both intra- and intermolecular vibrational transfer may be undesired if one wishes to follow the dynamical behavior of a specific subensemble of water molecules. Rapid energy transfer between different O–H groups scrambles the direction of the original excitation in pump-probe experiments, which we use to determine reorientational motion (see Fig. 1.7). To prevent this transfer, we use mixtures of normal water (H_2O) and so-called heavy or deuterated water (D_2O). Heavy water is water that contains deuterium atoms instead of hydrogen. The chemical properties of D_2O are similar to those of H_2O but are not quite the same. The isotopic substitution alters various properties of water such as its melting point (+3.8 °C), density (+10%), and viscosity (+25%). Because of the extra neutron, the deuterium atom is about twice as heavy as the hydrogen atom while the total mass of the molecule increases about 10%. In recent diffraction studies, it was shown [136] that D_2O is more structured (tetrahedral) than H_2O, and that the O–D bond is 3% shorter and the hydrogen bond 4% longer in D_2O. The main difference from a spectroscopic point of view is the fact that the frequency of the O–D stretch vibration (2500 cm^{-1}) is substantially red-shifted compared to that of the O–H (3400 cm^{-1}). The ratio is close to what would be expected on the basis of an ideal (harmonic) mass-spring system ($\sqrt{2}$).

Mixtures of H_2O and D_2O rapidly exchange their protons and deuterons to form a nearly statistical distribution of H_2O:HDO:D_2O with equilibrium constant $K_{eq} = 3.86$ [37]. The deviation from a completely statistical distribution ($K_{eq} = 4$) shows that there is a slight difference in the formation energies of H_2O, HDO, and D_2O. Even though these effects may seem small, heavy water can interfere with the normal operation of organisms. However, in most life forms it only becomes toxic when 25 to 50% of the organism's water has been replaced. In nature the isotope is present in about 156 ppm [1] but higher concentrations, used mainly for scientific study, can be produced using distillation, electrolysis or chemical exchange processes.

Because of its similarities and differences, heavy water is an excellent aid in the study of water dynamics. By isotopically diluting a water sample, we can shift part of the frequencies allowing us to study regions of the absorption spectrum that would otherwise be too optically dense. Another useful consequence of the difference between the O–H and O–D stretch frequency is the ability to tune the amount of vibrational Förster transfer between these modes.

This allows us to study the reorientational diffusion of water by measuring the anisotropy of isolated stretch vibrations. The effect of substituting the heavier deuterium atom in proton transfer reactions is also useful in understanding its underlying dynamics. Finally, the substitution may provide insight into the quantum effects on the dynamics of water.

1.8 OUTLINE

This thesis discusses several topics concerning molecular reorientation, charge transport and energy transfer in liquid water and ice. The first chapters (2–4) discuss the theoretical and experimental aspects of the work discussed in this thesis. The subsequent chapters deal with work pertaining to the reorientation of water molecules in bulk environment (Chapter 5), in the presence of biologically relevant (amide) groups (Chapter 6), and in the presence of high salt concentrations (Chapter 7). The subsequent chapters discuss transport of excess protons in liquid water (Chapter 8) and ice (Chapter 9). The last chapters discuss reorientation and (vibrational) energy transfer in protonated water (Chapter 10) and bulk ice (Chapter 11).

2 Spectroscopy

2.1 Light-matter interaction

Electromagnetic spectroscopy deals with the interaction between light and matter. Depending on the situation, light can behave either as an electromagnetic wave or as a quantized photon (wave-particle duality). The interaction between light and matter can only occur through the electromagnetic force as light exerts forces on charged and magnetic particles. Although photons are the fundamental carriers of the electromagnetic force, they do not carry charge themselves and are thus unaffected by static electric or magnetic fields. The frequencies at which matter can interact with light depend on the specifics of the system. In conventional (linear) spectroscopy, light-matter interaction is only efficient in the presence of oscillating charges that can match their frequency to that of the incoming electromagnetic wave. Such oscillations consists of time varying displacement of charges with a fundamental frequency that depends on the inertial mass attached to the charge and the restoring force acting upon that mass. Light is thus absorbed at any frequency that matches a specific periodic motion within the material (see Fig. 2.1).

Absorptions involving electrons are typically the highest in frequency (10^{15}–10^{16} Hz) because of the relatively low electron mass. These electronic transitions are responsible for most visible and ultra-violet frequencies of light. If the frequency is high enough, electrons can also be removed from the atom/molecule (ionization). Intramolecular vibrations involving the dis-

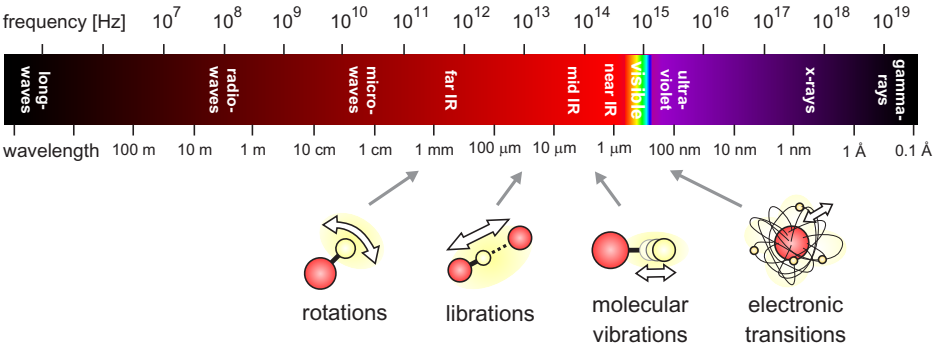

Figure 2.1. Molecular processes associated with frequencies in the electromagnetic spectrum.

placement of atoms within molecules typically absorb in the mid-infrared region (10^{13}–10^{14} Hz) with heavier atoms and weaker bonds leading to lower absorption frequencies. Librational modes are swaying or rocking motions of whole molecules and lead to absorption at frequencies around 10^{12}–10^{13} Hz. Rotational motions of molecules can also displace charges and can thus absorb light. In liquids, rotational frequencies depend on the viscosity of the system and can be typically 10^{10}–10^{12} Hz (i. e. picosecond timescale).

2.2 Equation of motion

To determine the frequency of periodic motions within a material we use the general equation of motion of a particle with mass m that is acted upon by (time-dependent) forces F_i. We start with Newton's second law of motion

$$\sum_i F_i(t) = m\,\frac{d^2x}{dt^2}\,, \tag{2.1}$$

where $x(t)$ is the particle position as a function of time.

Let us suppose the particle with electric charge q and damping constant $m\,\Gamma$ resides within a one-dimensional potential $V(x)$ and is driven by a time dependent electric field $E(t)$. The three forces working on this particle can be written as:

$$F_q(t) = q\,E(t)\,, \qquad \text{(charge)} \tag{2.2}$$

$$F_d(t) = -m\,\Gamma\,\frac{dx}{dt}\,, \qquad \text{(damping)} \tag{2.3}$$

$$F_v(t) = -\frac{dV(x)}{dx}\,. \qquad \text{(potential)} \tag{2.4}$$

Filling these three equations into Eq. (2.1), results in:

$$m\left[\frac{d^2x}{dt^2} + \Gamma\,\frac{dx}{dt} + \frac{1}{m}\,\frac{dV(x)}{dx}\right] = q\,E(t)\,. \tag{2.5}$$

We expand the potential $V(x)$ around the equilibrium position ($x = 0$) as:

$$V(x) \;=\; V_0 \;+\; k_0 x \;+\; k_1 x^2 \;+\; k_2 x^3 \;+\; \ldots\,, \tag{2.6}$$

where k_i are the proportionality constants for different orders of the displacement x. We may ignore the offset V_0, as it vanishes in the derivative of Eq. (2.3). Furthermore we are looking for equilibrium solutions, so the constant force k_0 must vanish. Finally, we will also ignore the higher order terms $k_2, k_3, \ldots$ for the moment and consider the harmonic response to a continuous electric field of the form:

$$E(t) \;=\; E_0\,e^{-i\omega t} \;+\; \text{c. c.}\;, \tag{2.7}$$

where E_0 is the amplitude of the electric field, ω is the frequency, and c.c. denotes the complex conjugate terms. Substituting Eqs. (2.6) and (2.7) into Eq. (2.5) results in a linear equation, the solution to which is:

$$x(t) \;=\; \frac{-q}{m}\,\frac{E_0\,\exp(-i\omega t)}{\omega_0^2 - i\,\Gamma\omega - \omega^2} \;+\; \text{c.c.}\;, \tag{2.8}$$

and the resonance frequency ω_0 is defined as:

$$\omega_0 = \sqrt{\frac{k_1}{m}}\,. \tag{2.9}$$

This equation is valid for harmonic oscillators, i. e. with a restoring force that is linear in the displacement.

The imaginary part in Eq. (2.8) implies that the response of the charge $x(t)$ has a certain phase relation with respect to the driving field $E(t)$. When the driving field exactly matches the resonance frequency ω_0, $x(t)$ is fully imaginary, which implies that the response of the oscillating charge is exactly 90 ° behind that of the driving field. This oscillating charge, in turn, will radiate an electric field which lags another 90 ° behind its own movement. In total the newly generated field will thus be 180 ° out of phase with the original incoming field and the two fields interfere destructively. This is a way to look at absorption of the electric field by the charge in the frequency region around the resonance.

2.3 Linear response

2.3.1 Susceptibility and refractive Index

The electric field thus induces a moving charge in the material. This moving charge results in a polarization response $P = q\,x$. If this response is linearly dependent on the electric field E, such as the case for the harmonic oscillator (Eq. (2.8)), it can be written in terms of the linear susceptibility $\chi^{(1)}$ as:

$$P \;=\; \epsilon_0\,\chi^{(1)}\,E\,, \tag{2.10}$$

where

$$\chi^{(1)}(\omega) \;=\; \frac{q^2}{\epsilon_0\,m}\cdot\frac{1}{\omega_0^2 - i\,\Gamma\omega - \omega^2}\,, \tag{2.11}$$

and ϵ_0 is the permittivity of free space. Fig. 2.2 shows the frequency dependence of the real and imaginary parts of the linear susceptibility around a resonance frequency ω_0. The width of the Lorentzian shaped imaginary peak is determined by the friction force Γ.

The induced polarization response acts as a source of new radiation into the material and affects the propagation of the original wave. The electric displacement D is the sum of the original electric field and the induced polarization:

$$D \;=\; \epsilon_0\,E \;+\; P \;=\; \epsilon_0\,(1+\chi)\,E \;\;\equiv\; \epsilon_0\,\epsilon_r\,E\,, \tag{2.12}$$

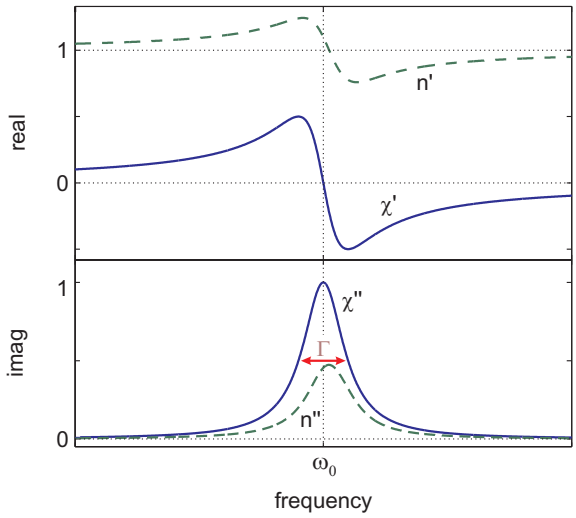

FIGURE 2.2. Frequency dependence of the real (') and imaginary (") parts of the susceptibility χ and refractive index n around a resonance frequency ω_0.

where ϵ_r is the relative permittivity.

The susceptibility χ of a material is related to its refractive index n by:

$$n = \sqrt{\epsilon_r \mu_r} \approx \sqrt{1+\chi}\,, \tag{2.13}$$

where in the last step we used Eq. (2.12) and the fact that for most materials $\mu_r \approx 1$ (non-magnetic). Using Eq. (2.13) we can relate the real (') and imaginary (") parts of the susceptibility to those of the refractive index:

$$1+\chi' = n'^2 - n''^2\,, \tag{2.14}$$

$$\chi'' = 2n'n''\,, \tag{2.15}$$

where $\chi = \chi' + i\chi''$ and $n = n' + in''$. Fig. 2.2 shows the correspondence between $\chi(\omega)$ and $n(\omega)$. We note that the imaginary part of the refractive index is slightly shifted from the resonance frequency ω_0, but mostly maintains its Lorentzian shape.

2.3.2 RESONANT VERSUS OFF-RESONANT

Depending on the spectroscopic process, we usually work either in the resonant or off-resonant regime. Resonant processes involve the absorption of light and are sensitive to the dynamical behavior of the material. In resonant processes the material absorbs part of the electric field, leading to an induced polarization

that can persist for a time after the driving electric field has passed. This persistence is determined by the population relaxation (T_1) and coherence dephasing (T_2) times and can be used as a dynamical probe of the material.

From Fig. 2.2 we note that the real part of the susceptibility extends over a much wider range than the imaginary part. This means that if we are far off-resonance (e. g. $\ll \omega_0$), the real part of the susceptibility (and refractive index) will dominate and there will be little absorption. Because there is no absorption, the induced polarization can only persist for as long as the electric field is present. The fact that the response has only real parts, also means that the polarization response instantaneously follows the oscillations of the driving electric field (no phase retardation).

Fig. 2.2 shows that in the off-resonance region the real refractive index $n'(\omega)$ has a relatively flat slope compared to the wild fluctuations seen around ω_0. Using Eqs. (2.19) and (2.20) we can conclude that the phase velocity in this off-resonance region is nearly frequency independent and equal to the group velocity, i. e. there is no dispersion. In the resonant region, on the other hand, there is appreciable dispersion.

2.3.3 WAVE PROPAGATION

We now consider what happens to an oscillating plane wave that is propagating through a piece of material with susceptibility χ. The position and time dependence of this wave is given by:

$$E(x,t) \;=\; \exp\left(i(kx-\omega t)\right)\,, \tag{2.16}$$

with wave vector k defined as

$$k(\omega) \;=\; \frac{n(\omega)\,\omega}{c}\,. \tag{2.17}$$

where c is the speed of light. Combining Eqs. (2.16) and (2.17) gives us:

$$E(x,t) \;=\; \exp\left(i\omega(\frac{n'}{c}\,x-t)\right)\,\exp\left(-\omega n''\,x/c\right)\,. \tag{2.18}$$

This equation consists of two exponentials. The first (imaginary) exponential relates the phase propagation of the wave to the real part of the refractive index n'. From this we can determine the phase velocity v_p and the group velocity v_g as:

$$v_p \;=\; \frac{c}{n'}\,, \tag{2.19}$$

$$v_g \;=\; \frac{c}{n'+\omega(dn'/d\omega)}\,. \tag{2.20}$$

The second (real) exponential of Eq. (2.18) determines the attenuation of the electric field as it travels through the material. This attenuation is thus

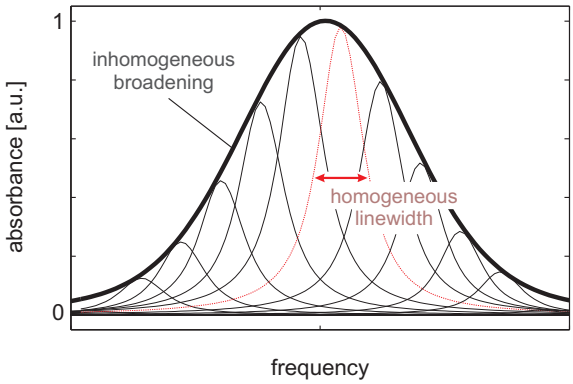

FIGURE 2.3. Inhomogeneously broadened absorption and its underlying homogeneous line shapes.

related to the imaginary part of the refractive index n''. The intensity I of a wave traversing a material is given by:

$$I \;=\; E^* E \;=\; \exp\left(-2\omega n'' \, x/c\right) . \tag{2.21}$$

Comparing this expression with **Lambert-Beer law**:

$$I(x) \;=\; I(0) \, \exp\left(-\,\alpha \, x\,\right) , \tag{2.22}$$

we can conclude that the absorption coefficient $\alpha = 2\omega n''/c$. From n'' in Fig. 2.2 we conclude that the absorption of a single resonance has a mostly Lorentzian profile.

2.3.4 INHOMOGENEOUS BROADENING

In a real material all oscillators may not have exactly the same resonance frequency. This leads to a spread of the absorption and dispersion line shapes, called inhomogeneous broadening. Let us assume that the resonance frequency ω_0 of a line shape L is modulated through an external coordinate G. The total absorption is then given by the cross-correlation of the distribution G with the original line shape L:

$$\alpha(\omega) \;=\; (G \star L)(\omega) \;=\; \int_{-\infty}^{\infty} L(\omega_0) \; G(\omega - \omega_0) d\omega_0 \tag{2.23}$$

Fig. 2.3 illustrates the resulting absorption spectrum, in the case that G has a Gaussian distribution. In this case the inhomogeneous broadening is much higher than the homogeneous broadening, and we may effectively describe the spectrum as a Gaussian line shape. Using linear spectroscopy alone it is not possible to distinguish between homogeneous and inhomogeneous broadening because we can only measure a convolution of the two. To make the distinction we need higher order techniques such as pump-probe spectroscopy.

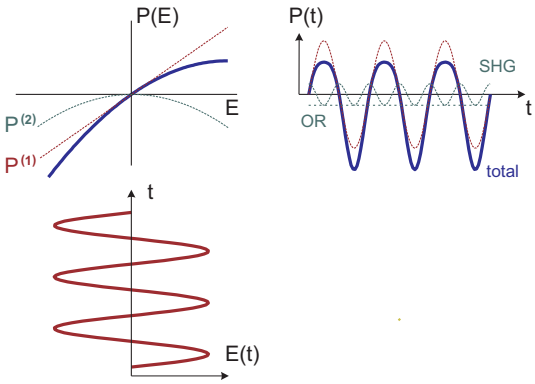

FIGURE 2.4. Decomposed non-linear polarization response $P(t)$ to an oscillating electric field $E(t)$. The second-order non-linear polarization $P^{(2)}$ consists of optical rectification (OR) and second harmonic generation (SHG).

2.4 NON-LINEAR RESPONSE

2.4.1 DIFFERENT ORDERS

In the derivation of Eq. (2.8), we have neglected the higher order anharmonic terms $k_2, k_3, ...$ in the potential energy $V(x)$. This resulted in a linear response of the polarization induced by the electric field. If we wish to include these higher order terms, the equation of motion (Eq. (2.5)), in general, has no exact analytical solutions. However, if the anharmonic terms are small compared to the harmonic term, we can approximate these solutions to any desired degree of accuracy by using perturbation theory. We can solve Eq. (2.5) to successive orders of approximation by writing x as a power series in E. The general solution for the non-linear response of the polarization can then be written as:

$$P = \epsilon_0 \left(\chi^{(1)} E + \chi^{(2)} E^2 + \chi^{(3)} E^3 + ... \right) , \tag{2.24}$$

where $\chi^{(n)}$ are different orders of the susceptibility. We shall refer to $P^{(n)} = \chi^{(n)} E^n$ as the nth-order nonlinear polarization. Fig. 2.4 shows an example of a decomposed response of the polarization, consisting of $P^{(1)}$ and $P^{(2)}$ terms.

Up until now we have only considered the polarization response of a material in the same direction as that of the driving electric field. However, for a general anisotropic medium this polarization response can be in any of three directions (x, y, z) for any combination of field directions. In general the nth order susceptibility is given by an $(n+1)$-rank tensor which has 3^{n+1} elements. To calculate the total polarization response in a direction i we need to sum over

all electric field combinations contributing to that direction:

$$\begin{aligned} P_i &= \epsilon_0 \sum_{j=1}^{3} \chi_{ij}^{(1)} E_j \\ &+ \epsilon_0 \sum_{j=1}^{3}\sum_{k=1}^{3} \chi_{ijk}^{(2)} E_j E_k \\ &+ \epsilon_0 \sum_{j=1}^{3}\sum_{k=1}^{3}\sum_{l=1}^{3} \chi_{ijkl}^{(3)} E_j E_k E_l \;+\; ... \end{aligned} \tag{2.25}$$

It can be shown that even-order nonlinear interactions, such as $P^{(2)}$, cannot occur in isotropic materials possessing inversion symmetry such as liquids, gasses, and amorphous solids. This restriction does not hold for odd-order nonlinear interactions.

Eqs. (2.24) and (2.25) have various useful applications that will be discussed in the following.

2.4.2 Frequency mixing

We start with the description of a three wave frequency mixing process, in which two oscillating electric field are overlapped in a material to generate a third. Let us consider a set of electric fields containing two frequencies of the form:

$$E = E_1 e^{-i\omega_1 t} + E_2 e^{-i\omega_2 t} + \text{c.c.}\,. \tag{2.26}$$

We write out the second-order non-linear polarization response ($P^{(2)}$) induced by this electric field:

$$\begin{aligned} P^{(2)} &= \chi^{(2)}\, E^2 \\ &= \chi^{(2)} \left(E_1 e^{-i\omega_1 t} + E_1^* e^{i\omega_1 t} + E_2 e^{-i\omega_2 t} + E_2^* e^{i\omega_2 t}\right)^2 \\ &= \chi^{(2)} \Big\{ 2(E_1^2 + E_2^2) + && \text{(OR)} \\ &\qquad E_1^2 e^{-i\,2\omega_1 t} + E_2^2 e^{-i\,2\omega_2 t} + \text{c.c.} + && \text{(SHG)} \\ &\qquad 2E_1 E_2 e^{-i(\omega_1+\omega_2)t} + \text{c.c.} + && \text{(SFG)} \\ &\qquad 2E_1 E_2^* e^{-i(\omega_1-\omega_2)t} + \text{c.c.} \Big\} && \text{(DFG)}\,. \end{aligned} \tag{2.27}$$

From this equation we see that the combination of two frequencies ω_1 and ω_2, in a material with non-zero $\chi^{(2)}$ leads to a wide variety of new frequencies. We note that $\chi^{(2)}$ is itself a frequency dependent function, which means that the response for different mixing processes is in general not the same. Due to the asymmetry of $P^{(2)}$, the polarization response is different depending on the direction of the electric field. This leads to a static response called optical rectification (OR). Second harmonic generation (SHG) leads to new frequency components at twice

the original frequencies. Finally, there are two processes that mix the original two frequencies called sum- and difference frequency generation (SFG, DFG).

When one of the two frequencies in Eq. (2.27) is a static (d.c.) electric field, this leads to cross-terms whose magnitude is proportional to this static field, but are still linear to the oscillating field. This effect is similar to changing $\chi^{(1)}$ by an amount proportional to the static field. This is known as the Pockels effect and corresponds to a change of the material's refractive index under the influence of an external electric field. In our laser setup the Pockels effect is used to change the birefringence of a crystal and alter the polarization of a transmitted laser beam. Combining this with polarization dependent optics allows for an ultra-fast switching mechanism of laser pulses.

PHASE MATCHING The second-order nonlinear response is the basis for the frequency mixing processes used to generate the infrared light for our pump-probe experiments. This process is a $\chi^{(2)}$ process and thus involves a non-centrosymmetric medium. In practical applications we wish to avoid absorptive losses in the medium and are thus working in the off-resonant regime. In general the second-order response of a material is very small, however because it scales with E^2, it becomes larger for higher electric field strengths. We are helped by the fact that the field strength during a sub-picosecond laser pulse is far higher than that of a continuous wave. To even further enhance the efficiency of the frequency mixing process we need the constructive interference of electromagnetic waves, generated in different parts of the material. To achieve this we need the phase of newly generated light to match that of the already generated propagating light. For a process

$$\omega_1 \; + \; \omega_2 \; \rightarrow \; \omega_3 \, . \tag{2.28}$$

the spatial variation of the propagating fields is given by $e^{ik_1 x}$ and $e^{ik_2 x}$, where k_i is the wave vector defined in Eq. (2.17). The generated polarization follows these fields and varies as $e^{i(k_1+k_2)x}$. This polarization has to match the propagation of the generated field $e^{ik_3 x}$ which leads to the phase matching condition $k_1 + k_2 = k_3$ or in terms of the frequencies ω_i and refractive indices n_i:

$$n_1 \, \omega_1 \; + \; n_2 \, \omega_2 \quad = \quad n_3 \, \omega_3 \, . \tag{2.29}$$

Taking also into account the required conservation of energy $\omega_1 + \omega_2 = \omega_3$ this seems to lead to a rather restrictive condition on the possible frequencies of light that can be generated in a material with any given refractive indices n_i. Luckily there are several methods to tune the refractive indices of a material, including angular and temperature phase-matching.

The easiest method involves the angular tuning of a birefringent crystal. Uniaxial birefringent crystals have two refractive indices: n_e along the optical axis and n_o in the other two directions. By rotating the crystal over an axis perpendicular to the optical axis the refractive index along that axis remains n_o while the refractive index in a direction in the plane perpendicular tot the rotation axis can be varied anywhere between n_o and n_e. By setting the direction

of the polarization of the electric fields ω_i with respect to the optical axis we can choose which of the two refractive indices is applied for that frequency. We can further select a specific frequency conversion process by tuning the angle of the crystal to fulfill its phase matching condition. Different crystals are suitable for different frequency mixing processes. Besides their non-linear response and birefringence, it is also important that they do not absorb any of the frequencies involved in the mixing process. If a crystal is dedicated for a specific mixing process, it can be cut or coated such that reflection losses are also minimized.

2.4.3 Pump-probe spectroscopy

Molecular processes in water take place on extremely fast time scales ranging from nanoseconds (proton transfer) down to picoseconds (reorientation) or even tens of femtoseconds (Förster transfer). If we wish to follow the occurrence of such events in 'real-time' we need to employ ultrafast optical techniques that are able to capture such events. Analogous to the short flashes of a camera, used to capture a moving objects frame-by-frame, we use ultra-short light pulses delivered by a femtosecond laser system. These short laser pulses generally consist of a range of frequencies that are selectively absorbed as they travel through the sample.

The technique we use is called 'pump-probe spectroscopy'. An intense pump pulse prepares the system (sample) in a non-equilibrium state at a specific instance in time. This state subsequently evolves according to the underlying physical processes that occur in the sample. This evolution is monitored using a separate probe pulse, that is scanned over any number of specific delay times between pump and probe. We monitor the pump-induced absorption differences in the sample by blocking every second pump pulse and comparing the resulting probe spectra with and without the pump. With every pair of probe pulses we thus measure a frequency resolved transient absorption difference spectrum. The time evolution of these transient spectra are subsequently analyzed (Chapter 4)) and reveal information about the underlying physical processes.

Pump-probe spectroscopy can be described as a resonant $\chi^{(3)}$ process, where an absorption in the material is saturated by the pump. Third-order non-linear interactions can occur in any material, also in isotropic samples. The response depends on the interaction of three fields and thus scales with E^3. In pump-probe spectroscopy the oscillating third-order polarization,

$$P^{(3)} = \chi^{(3)} E_{\text{pump}} E^*_{\text{pump}} E_{\text{probe}} \,, \tag{2.30}$$

with phase-matching condition,

$$\vec{k}_{\text{pump}} - \vec{k}_{\text{pump}} + \vec{k}_{\text{probe}} \,, \tag{2.31}$$

radiates an electric field in the direction of the probe. The pump field leads to a transient population in the sample that persists depending on the population relaxation time (T_1). Within this relaxation time, the process is thus also possible for a delay between pump and probe fields.

The radiated field $P^{(3)}$ interferes constructively and destructively at different frequencies of the probe field leading to induced absorption and bleach, respectively (e. g. Fig. 2.5). This interference is recorded as the pump-induced intensity difference ΔI of the probe field:

$$\Delta I_{\text{probe}} \propto P^{(3)} E^*_{\text{probe}} = I_{\text{pump}} I_{\text{probe}} . \tag{2.32}$$

Note the difference between the macroscopic description of electric field interactions and the microscopic absorption and emission of photons. In the macroscopic description, the pump-probe signal depends on the interaction of four electric fields while microscopically two photons are involved: I_{pump} to induce the absorption change and I_{probe} to probe it.

Ideally the pump-probe signal consists only of pump-induced absorption changes of the sample measured by the probe. Unfortunately there is also a contribution which involves the interaction of a pump field with the absorption changes induced by the combined pump and probe fields. In this interaction the pump scatters off a grating created by the interference between pump and probe, in the direction of the probe which has the same phase matching conditions as Eq. (2.31). From the sequence of interactions, pump-probe-pump, it can be deduced that this coherent artifact is only present when pump and probe have temporal overlap.

Another artifact arises due to a process called cross-phase modulation where the time-varying intensity of the pump causes a frequency modulation of the probe through the optical Kerr effect. The optical Kerr effect can be understood by writing out the polarization response in the direction of the probe up to third-order:

$$P = \epsilon_0 \left(\chi^{(1)} + \chi^{(3)} E^2_{\text{pump}} \right) E_{\text{probe}} . \tag{2.33}$$

Note that the $\chi^{(3)}$ in Eq. (2.33) describes an off-resonant process and is different from the one in Eq. (2.30). The result of the Kerr effect is that the refractive index and thus the phase velocity of the probe changes with the intensity $I(t) = E^2_{\text{pump}}$ of the pump envelope (the probe intensity is negligible). When the probe pulse is temporally overlapped just before the pump pulse it sees the rising edge of the pump envelope and experiences a time-dependent increasing phase velocity. This leads to a stretching of the periodic oscillations of the probe thus lowering its frequency. The opposite holds when the probe overlaps just after the pump. In that case it experiences a time-decreasing phase velocity and an increase in frequency. In a pump-probe experiment where we vary the delay between pump and probe we thus observe a frequency shifting probe spectrum during (partial) temporal overlap.

The optical Kerr-effect has also useful applications, e. g. it can be used to generate new frequencies in a process called self-phase modulation (SFM). As may be deduced from the name, the effect is very similar, except that it is the intensity dependent phase modulation of the electric field on itself, which generally broadens its original frequency range.

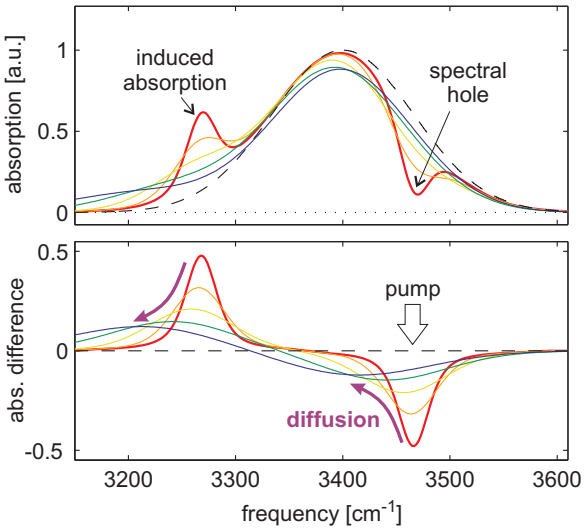

FIGURE 2.5. Simulation of hole burning and subsequent spectral diffusion on the O–H stretch mode in water. Top: temporal evolution of the absorption band. The dashed line indicates the equilibrium distribution. The induced absorption is explained in Section 2.5.4. Bottom: absorption difference spectrum, showing the effect of spectral diffusion after the excitation by a narrow band pump pulse.

2.4.4 SPECTRAL DIFFUSION

As mentioned in Section 2.3.4, pump-probe spectroscopy can be used to distinguish homogeneous and inhomogeneous broadening. In a technique called transient hole burning, a narrow-band pump is used to excite a sub-ensemble within the absorption band (see Fig. 2.5). The minimum width of this spectroscopic hole can never be narrower than twice the homogeneous line width of the individual oscillators but it can be narrower than the total inhomogeneously broadened spectrum. If the coordinate underlying the inhomogeneous broadening mechanism (G in Eq. (2.23)) for individual oscillators does not change over time, the spectroscopic hole will remain at the same frequency. If, however, this coordinate is itself fluctuating in time, covering the entire distribution, the hole will change its shape and position until the individual oscillators in the sub-ensemble have reached an equilibrium distribution. This process is called spectral diffusion, and is discussed in both Chapters 5 and 7.

In the weak modulation limit (Gauss-Markov) a diffusion process can be phenomenologically described by the following partial differential equation:

$$\frac{\partial U(t,\omega)}{\partial t} = D_S \frac{\partial}{\partial \omega}\left(\frac{\partial U(t,\omega)}{\partial \omega} + \frac{(\omega-\omega_0)}{\sigma^2} U(t,\omega)\right) - \frac{U(t,\omega)}{\mathrm{T}_1}, \qquad (2.34)$$

where $U(t,\omega)$ is the distribution at time t and frequency ω, D_S is the spectral diffusion coefficient, ω_0 and σ are the central frequency and standard deviation

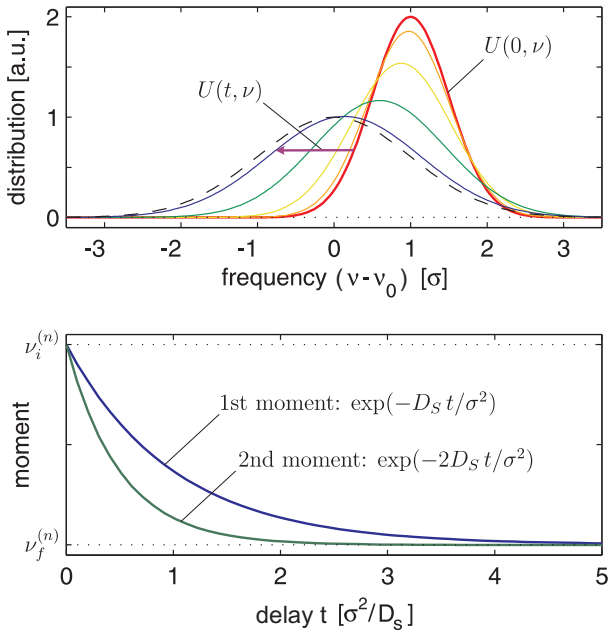

FIGURE 2.6. Spectral diffusion of an arbitrary initial distribution (top) and the temporal evolution of the first and second moment (bottom).

of the Gaussian equilibrium spectrum, and T_1 is the population relaxation time.

For the special case where the equilibrium distribution is initially excited, the solution to Eq. (2.34) is of the form

$$U(t,\omega) \;=\; U_0 \;\exp\left(-\frac{(\omega-\omega_0)^2}{2\sigma^2}\right)\; e^{-t/T_1}\,, \tag{2.35}$$

i. e. a uniformly decaying Gaussian line shape without spectral diffusion.

In general Eq. (2.34) may be evaluated through numerical integration for any initial distribution $U(0,\omega)$. Figs. 2.5 shows a simulation of transient hole burning, where the initial distribution is a spectral hole in the equilibrium distribution. To create this figure, we convoluted the solution to Eq. (2.34) with the homogeneous line width (Lorentzian), and added an equal but opposite response at the frequency of the $\nu = 1 \rightarrow 2$ induced absorption (explained in Section 2.5.4).

The nth moment of a distribution $U(t,\omega)$ around an point ω_0 is defined as:

$$\langle(\omega(t)-\omega_0)^n\rangle \;=\; \int_{-\infty}^{\infty} d\omega\,(\omega-\omega_0)^n\; U(t,\omega) \tag{2.36}$$

Fig. 2.6 illustrates the temporal evolution of the first and second moments of an arbitrary initial distribution $U(0,\omega)$. For a Gauss-Markov process, the temporal

evolution of these moments (for any initial distribution) are characterized by [20, 67]:

$$\langle \omega(t) - \omega_0 \rangle = \omega_f^{(1)} + (\omega_i^{(1)} - \omega_f^{(1)}) \exp(-t/\tau_c) , \tag{2.37}$$

$$\left\langle (\omega(t) - \omega_0)^2 \right\rangle = \omega_f^{(2)} + (\omega_i^{(2)} - \omega_f^{(2)}) \exp(-2t/\tau_c) , \tag{2.38}$$

where we defined the initial and final values of the nth moments respectively as

$$\omega_i^{(n)} \equiv \langle (\omega(0) - \omega_0)^n \rangle , \tag{2.39}$$

$$\omega_f^{(n)} \equiv \langle (\omega(\infty) - \omega_0)^n \rangle , \tag{2.40}$$

and the correlation time τ_c is related to the diffusion coefficient and the width of the distribution as:

$$\tau_c = \sigma^2 / D_S . \tag{2.41}$$

This correlation time is furthermore related to the decay of the frequency-frequency correlation function (FFCF) [67]:

$$\langle \delta\omega(t) \delta\omega(0) \rangle \propto \exp(-t/\tau_c) . \tag{2.42}$$

2.5 Quantum mechanical systems

2.5.1 Transition rate

Until now our description of the light-matter interaction has been classical. Although this classical description works well to describe most light-matter interactions, there are some cases where its description breaks down. In quantum mechanics, the state of a system is not characterized by a set of dynamic variables (position, momentum) but by a state function Ψ. In the position representation, the state of a particle is specified by the functional dependence of the state function $\Psi(r)$ on the position variable r. This position is not specified but instead has a probability density determined by $|\Psi(r)|^2$.

The time evolution of the state function $\Psi(r, t)$ (also known as wave function) is described by the Schrödinger equation:

$$i\hbar \frac{\partial}{\partial t} | \Psi(r,t) \rangle = \hat{H} | \Psi(r,t) \rangle , \tag{2.43}$$

where $\hbar$ is Planck's reduced constant and $\hat{H}$ is the Hamiltonian which describes the total energy of the system (kinetic plus potential). Instead of forces acting on a system we have the Hamiltonian acting on a state. The interaction between light and matter is described not by the electromagnetic force but by a perturbation of the Hamiltonian:

$$\hat{H}(t) = \hat{H}_0 + \hat{V}(t) , \tag{2.44}$$

where $\hat{V}(t)$ takes the form

$$\hat{V}(t) = \vec{\hat{\mu}} \cdot \vec{E}_0 (e^{i\omega t} + e^{-i\omega t}) \,, \tag{2.45}$$

where E_0 is the electric field amplitude, ω the frequency of the oscillation, and $\vec{\hat{\mu}}$ is the dipole operator.

The transition rate $\Gamma_{a\to b}$ of a system between different states $|\,\phi_a\,\rangle$ and $|\,\phi_b\,\rangle$ under the influence of perturbation $\hat{V}$ is calculated using Fermi's golden rule:

$$\Gamma_{a\to b} = \frac{2\pi}{\hbar^2} \, |\langle\, \phi_b |\, \hat{V} |\, \phi_a \,\rangle|^2 \;\; \delta(\omega \pm \omega_{ab}) \tag{2.46}$$

$$= \frac{2\pi}{\hbar^2} \, E_0^2 \cos^2\theta \, |\langle\, \phi_b |\, \hat{\mu} |\, \phi_a \,\rangle|^2 \;\; \delta(\omega \pm \omega_{ab}) \tag{2.47}$$

where in the last step we substituted Eq. (2.45) and defined θ as the angle between the transition dipole moment $\langle\, \phi_b |\, \vec{\hat{\mu}} |\, \phi_a \,\rangle$ and the polarization of the electric field $\vec{E}_0$.

We note that the transition rate is proportional to $\cos^2\theta$ which is the basic principle behind polarization resolved spectroscopy. The quantized interaction between light and matter is described with the absorption and emission of photons. The delta function δ containing the resonance frequency $\omega_{ab} = (E_a - E_b)/\hbar$ ensures that only those transitions occur whose energy difference match the energy (frequency) of the photon. When the energy difference is positive a photon is absorbed, when it is negative a photon is emitted. This stimulated emission is the basic principle behind laser operation.

In general, the dipole operator depends on the full electronic wave function and Eq. (2.47) can refer to any type of dipolar transition. In the present case we are mostly interested in vibrational transitions and we expand the dipole operator in terms of the vibrational coordinate x:

$$\vec{\hat{\mu}} \approx \vec{\mu_0} + \hat{x} \frac{\partial \vec{\mu}}{\partial x} \tag{2.48}$$

Filling in Eq. (2.48) into Eq. (2.47) yields

$$\Gamma_{a\to b} = \frac{2\pi}{\hbar^2} \, E_0^2 \cos^2\theta \left(\frac{\partial \vec{\mu}}{\partial x} \right)^2 |\langle\, \phi_b |\, \hat{x} |\, \phi_a \,\rangle|^2 \;\; \delta(\omega \pm \omega_{ab}) \tag{2.49}$$

The term $\left(\frac{\partial \vec{\mu}}{\partial x}\right)^2$ means that only those vibrational transitions occur whose vibrational motion lead to a change in dipole moment. The matrix element $\langle\, \phi_b |\, \hat{x} |\, \phi_a \,\rangle$ means that for harmonic oscillators only transitions occur that change the energy of the system by one quantum of energy.

2.5.2 OSCILLATION

We now briefly consider the nature of oscillating systems in the context of quantum mechanics. Unlike in classical systems the position is not parametrically

described by a time-evolving position, but rather by the probability density of its state. When a quantum-mechanical system has a definite energy its state is given by the corresponding eigenstate of the Hamiltonian, i. e.

$$\hat{H}|\,\phi_a(r,t)\,\rangle \;=\; E_a|\,\phi_a(r,t)\,\rangle\,, \tag{2.50}$$

where the eigenvalue E_a equals the energy of state $\phi_a(r,t)$. Using Eq. (2.43) we find that the time evolution of this state is given by

$$|\,\phi_a(r,t)\,\rangle \;=\; e^{-iE_a\,t/\hbar}\,|\,\phi_a(r,0)\,\rangle\,. \tag{2.51}$$

Note that the expectation value of the position for this state,

$$\langle x\rangle \;=\; \langle\,\phi_a(r,t)|\,\hat{x}\,|\,\phi_a(r,t)\,\rangle \;=\; \langle\,\phi_a(r,0)|\,\hat{x}\,|\,\phi_a(r,0)\,\rangle\,, \tag{2.52}$$

is time-independent because the phase in the exponential cancels out. This means that a definite energy state corresponds to a time-independent expectation value for the position, i. e. no oscillation. The only way a quantum system can have a time dependent position is, if it is in a superposition of eigenstates. For example:

$$\begin{aligned}\langle\,\phi_a+\phi_b|\,\hat{x}\,|\,\phi_a+\phi_b\,\rangle \;&=\; \langle\,\phi_a|\,\hat{x}\,|\,\phi_a\,\rangle + \langle\,\phi_b|\,\hat{x}\,|\,\phi_b\,\rangle \\ &+\; 2\,\langle\,\phi_a|\,\hat{x}\,|\,\phi_b\,\rangle\,\cos\left(\frac{E_a-E_b}{\hbar}\,t\right)\end{aligned} \tag{2.53}$$

In this case the expectation value of the position oscillates with frequency $\omega_{ab} = (E_a - E_b)/\hbar$. This frequency corresponds to the energy difference between the two eigenstates ϕ_a and ϕ_b and is also exactly the frequency of the light that can couple to this transition $\phi_a \leftrightarrow \phi_b$ (Eq. (2.49)).

2.5.3 LINE WIDTH

The chance that a photon is absorbed while traversing a piece of material depends on the number of possible transitions within the material and their corresponding transition probabilities. In Section 2.2 we have seen that for classical systems the width of the absorption peak depends on the damping force working on the oscillator. In quantum systems we argued that only those transitions occur whose energy matches exactly the energy difference between states. So it would then seem that the width of the absorption in a quantum system is infinitely small. However, this strict energy requirement for quantum systems is relaxed for small time-scales where the Heisenberg uncertainty relation states that

$$\Delta E \Delta t \gtrapprox \frac{\hbar}{2}\,. \tag{2.54}$$

This means that it is not possible to accurately determine the energy of a state that only exists for a very short time. For quantum systems the width of the absorption thus depends on the length of time that the excitation can

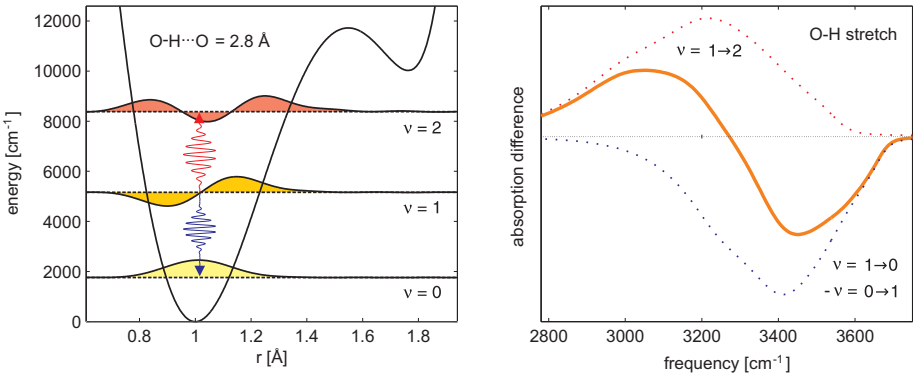

FIGURE 2.7. Left: quantum mechanical Lippincott-Schroeder potential [86, 107] for a typical O–H$\cdots$O distance of 2.8 Å. The shallow second dip on the right corresponds to the potential well of the neighboring water molecule. Right: resulting absorption difference spectrum for a population promoted from $\nu = 0$ to $\nu = 1$.

be determined. This time depends on various energy 'damping' mechanism like radiative and collision losses (lifetime broadening), but also on dephasing mechanisms. Equivalent to the classical oscillator, the more losses a system has, the broader will be its absorption (and emission) spectrum.

2.5.4 QUANTUM ANHARMONIC OSCILLATOR

We will now treat an example that is relevant in our understanding of the behavior of quantum anharmonic oscillators and their interaction with light in pump-probe experiments. Fig. 2.7 shows the Lippincott-Schroeder potential [86, 107] which is a model for the one-dimensional potential energy of a hydrogen atom in liquid water (O–H$\cdots$O). The energy levels and wave functions were calculated using Numerov's method [109]. We note that in an anharmonic potential the energy difference between energy levels goes down with increasing quantum number. This means that the $\nu = 1 \rightarrow 2$ transition lies at a lower frequency than the $\nu = 0 \rightarrow 1$ transition. This is an important aspect in pump-probe measurements because it allows us to distinguish between the two transitions. In fact, a completely harmonic oscillator has no pump-probe response at all. Classically we have shown (Eq. (2.8)) that the harmonic oscillator has no non-linear responses, required for pump-probe. Quantum-mechanically it can be shown (e. g. second quantization, Fig. 2.8) that if the energy levels all have the same spacing, the excitation leads to an induced absorption whose cross-section exactly cancels the sum of the bleach and induced stimulated emission. In fact the total absorption in a harmonic oscillator is independent of the distribution of quanta over the different levels.

In vibrational pump-probe experiments on water, the pump beam excites a population of O–H stretch modes from the vibrational ground state $\nu = 0$

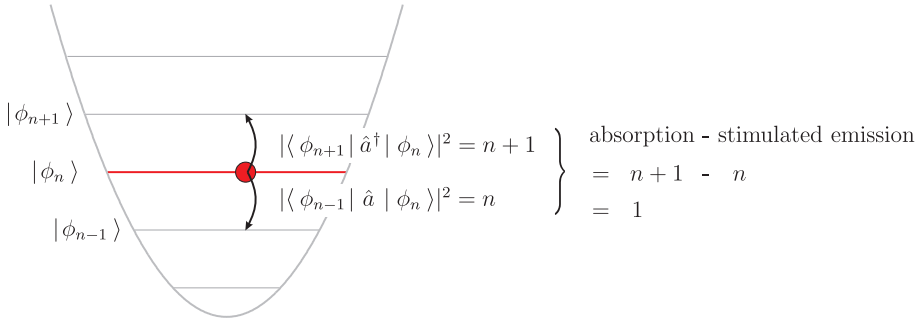

FIGURE 2.8. Second quantization of the harmonic oscillator. The ladder operators $\hat{a}$ and $\hat{a}^\dagger$ correspond to the emission and absorption of a single photon, respectively. The total absorption cross-section is independent of the distribution of the quantized states of the system $|\phi_n\rangle$.

to the first excited state $\nu = 1$. Depopulation of the ground state leads to a reduced absorption or 'bleach' at frequencies corresponding to the $\nu = 0 \rightarrow 1$ transition. This reduced absorption is enhanced by $\nu = 1 \rightarrow 0$ stimulated emission of the excited population back to the ground state. At the same time the newly created population in the first excited state $\nu = 1$ starts to absorbs light at frequencies that correspond to the $\nu = 1 \rightarrow 2$ transition. For a nearly harmonic oscillator, the total integrated cross-section of the $\nu = 1 \rightarrow 2$ induced absorption is about the same as the sum of the bleach and stimulated emission at $\nu = 0 \rightarrow 1$. The width of the inhomogeneous $\nu = 1 \rightarrow 2$ absorption in water is larger than the $\nu = 0 \rightarrow 1$ bleach, because the hydrogen bond fluctuations affect the width of the potential and thus the height of the energy level more at $\nu = 2$ than at $\nu = 0$ or $\nu = 1$. Also, the absorption bands are slightly asymmetric, mainly because the spacing between the energy levels depends non-linearly on the hydrogen bond coordinate. Another factor contributing to the asymmetry is that water molecules with stronger hydrogen bonds (lower frequencies) have a higher absorption cross-section.

3 Experimental

3.1 Pulse generation

In our experiments we use ultrashort laser pulses of <150 fs in the visible region (400-800 nm) and in the mid-infrared region between 3 and 7 μm (1500-3000 cm^{-1}). To create these pulses we use a series of non-linear techniques to convert light from a commercial Ti:sapphire regenerative amplifier system (Quantronix Titan) into the desired wavelengths. The amplifier itself is seeded by an oscillator (Spectra Physics Tsunami) that delivers 800 nm pulses with FWHM $\sim$ 17 nm at a repetition rate of 80 MHz. These seed pulses are stretched using a set of gratings and amplified at a 1 kHz rate in Ti:sapphire crystals that are pumped with the output from an intra-cavity doubled, Nd:YLF laser system (Quantronix Falcon). The amplification consists of a regenerative amplification cavity that is controlled with a Pockels cell. This amplification is followed by a multi-pass amplification stage with a second pumped Ti:sapphire crystal. The final result after compression are $\sim$100 fs 800 nm pulses with pulse energies of 3 mJ at a 1 kHz repetition rate.

To create 400 nm pump pulses, we use second-harmonic generation of part of the 800 nm light in a β barium borate (BBO) crystal. To create visible probe light, we broaden the spectrum of 800 nm pulses with self-phase modulation by focussing them into a sapphire crystal. The infrared pump and probe pulses are created according to the schematic shown in Fig. 3.1. We use parts of the 800 nm light to pump two separate BBO based Optical Parametric Amplifiers (OPA). The OPAs split the 800 nm pulses into lower frequency signal and idler pulses through a series of white light or super-fluorescence seeded parametric amplification stages. We create pump pulses in the frequency regions around 3 and 4 μm by frequency doubling the idler pulses in a BBO crystal and parametrically amplifying these doubled idler pulses with 800 nm pump pulses in either Potassium Titanyl Phosphate (KTP) or Potassium Niobate crystals (KN). Infrared probe pulses in the frequency regions between 3 and 7 μm are created using difference frequency generation between signal and idler pulses in a silver gallium disulfide (AGS) crystal. The pump and probe pulses had typical pulse energies of 5 μJ and 20 nJ, respectively.

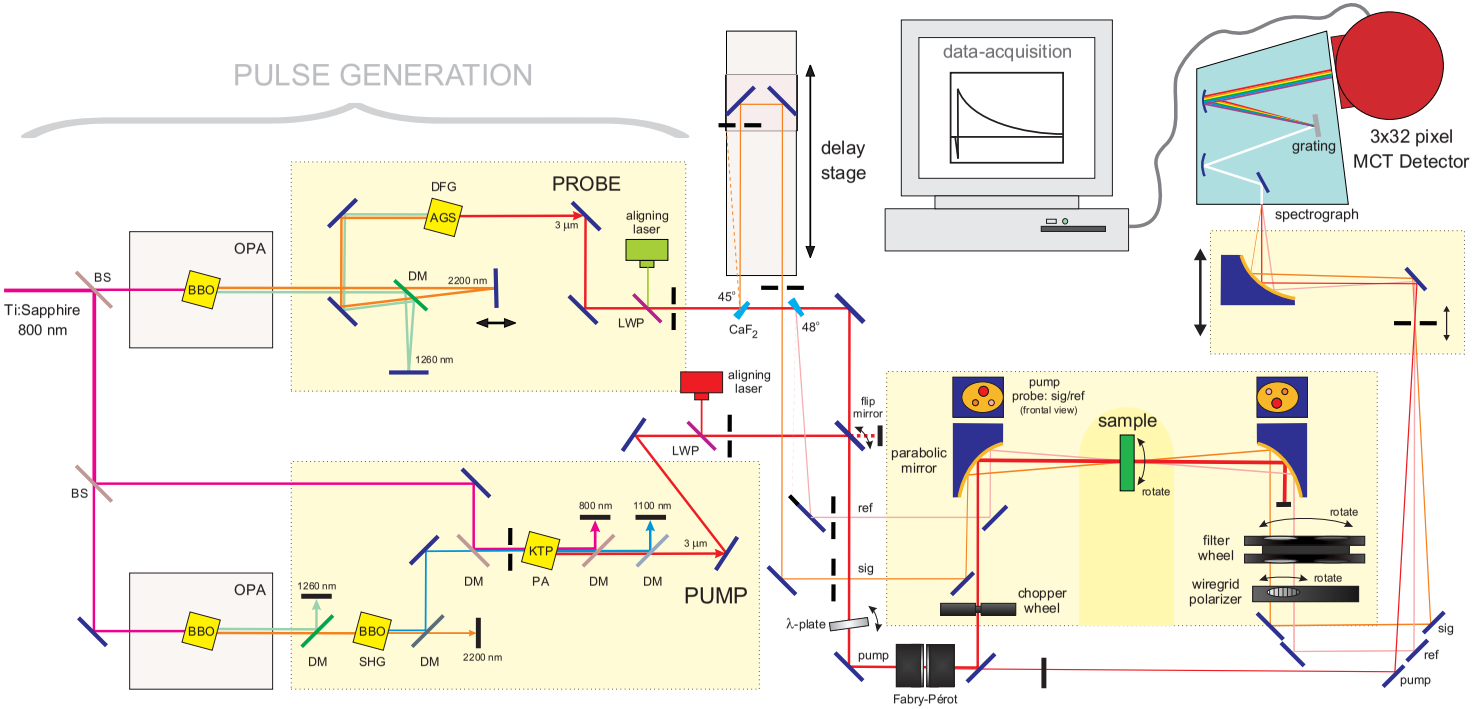

FIGURE 3.1. Infrared two-color pump-probe setup. 800 nm light from a Ti:Sapphire laser system is split in three parts using Beam Splitters (BS). Two parts are used to pump two separate Optical Parametric Amplifiers (OPA). These split the 800 nm light in signal and idler pulses using Parametric Amplification (PA) of either white-light or a super-fluorescence seed. Pump light is generated by Second Harmonic Generation of the idler followed by Parametric Amplification with 800 nm. Probe light is generated by Difference Frequency Generation (DFG) of signal and idler. Dichroic Mirrors (DM) and Long Wave Pass (LWP) filter out unwanted frequencies. The probe light is split into a probe and a reference beam using CaF_2 wedged windows. The probe beam is time-delayed with respect to the pump; the reference always precedes the pump. Half of the pump pulses are blocked by a 500 Hz chopper wheel. The pump polarization is rotated with a $\lambda/2$-plate. The pump frequency can be tuned by a Fabry-Pérot interferometer. The pump, probe, and reference are spatially overlapped and focussed by a parabolic mirror in the sample cell. The intensity of the probe and the reference are tuned with a filter wheel, and different polarization components are selected with a rotating polarizer. Probe, reference, and optionally pump are dispersed by a spectrograph and measured with a 3×32 pixel Mercury Cadmium Telluride (MCT) detector by data acquisition software. The data acquisition controls the delay-stage, Fabry-Pérot, spectrograph, and rotating polarizer.

3.2 PUMP-PROBE SETUP

The infrared two-color pump-probe setup that was used in most of the experiments is shown in Fig. 3.1 including pulse generation, pump-probe overlap and signal detection. The pulse generation part of the setup was varied slightly depending on the frequencies needed for the experiments. The basic pump-probe scheme involves the spatial overlap of two beams, pump and probe, inside the sample under study. The beams are focussed inside the sample to maximize the pump-probe signal. The relative polarization between pump and probe is either at magic angle (54.7 °), for rotation-free measurements, or 45 °, for polarization-resolved measurements. In the latter case a rotating polarizer selects parallel and perpendicular components of the probe after the sample. We split part of the probe before the sample which acts as a reference beam to correct for pulse-to-pulse fluctuations as explained in Section 4.1. The temporal overlap of pump and probe pulses is controlled with a delay stage.

3.3 SAMPLE CELL

The basic sample cell consists of a static construction which holds two calcium-fluoride windows together, separated by a teflon spacer to provide an optical path length between 10–500 μm. The sample cell holder and one of the windows provides a pair of small openings to allow for the easy exchange of different liquid samples. The standard procedure for sample replacement consists of an extensive flush by the sample solvent, followed by a flush with the new sample. This method is preferred when performing a comparative series of measurements where a particular aspect of the sample, such as the concentration, is varied. It ensures that the measured samples have the same optical path length.

For experiments that are influenced by steady state heating of the sample we use a rotating sample-cell. The main disadvantage of a rotating sample cell is the introduction of noise through either the scattering off the windows or the wobbling around the pump-probe focus overlap. Also, great care has to be taken that the thickness of the sample cell is uniform along the rotation path. This and the slightly more cumbersome procedure needed to replace samples, is why the static cell is usually preferred.

Temperature-dependence measurements in the region ∼5–70 °C are performed using a sample cell with a (thermoelectric) Peltier element. The more advanced version of this cell also allows for circular rotation. For cryogenic experiments we use a closed-cycle liquid-helium cooled cryostat. The cryostat weighs about 25 kg and is connected to a liquid helium reservoir and a vacuum pump system. The vacuum jacket of the cryostat is equipped with two calcium fluoride windows which allows optical access to the sample. For experiments that require rotation of the cryogenic sample we designed a 'cryostat rotator' as shown in Fig. 3.2.

This cryostat-rotator is mounted on a frame independent of the laser table to prevent it from influencing the vibration sensitive laser setup. This suspended

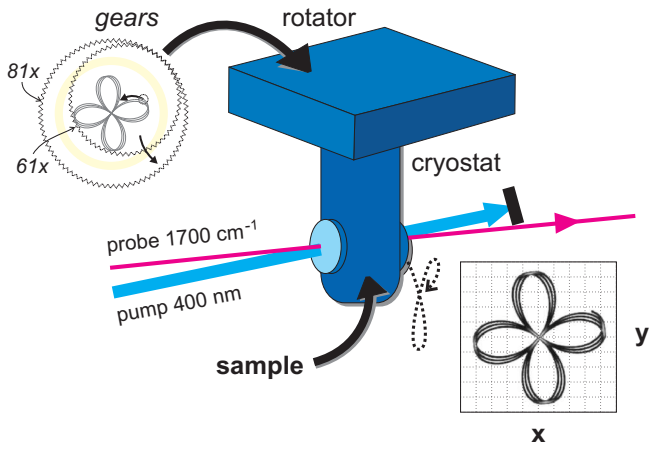

FIGURE 3.2. The middle part shows a schematic depiction of the cryostat rotator hanging in the pump-probe setup. The top left shows the outer and inner gears that together create the hypotrochoid trajectory, resulting in a period of almost five thousand rotations. The bottom right picture shows a simulation of the pump intensity distribution across the sample after a few rotations.

device is capable of moving around the entire cryostat including the attached hoses while keeping the sample within the focal length of the probe (∼1 mm). To achieve maximum spread of the pump beam across the sample and minimize photo-damage we use a pair of inner and outer gears and rotated the sample along a hypotrochoid trajectory. The x and y positions of this trajectory at time t at an angular speed ω can be described by the following set of parametric equations:

$$x(t) = (R-r)\cos(\omega t) + \delta\cos\left(-\frac{R-r}{r}\omega t\right), \tag{3.1}$$

$$y(t) = (R-r)\sin(\omega t) + \delta\sin\left(-\frac{R-r}{r}\omega t\right). \tag{3.2}$$

Here R and r are the radii of the outer and inner gears, respectively, and δ is the offset from the center of the inner wheel to which the rotating cryostat is attached. The number of teeth on the two gears were chosen to be relative prime (61 and 81) in order to achieve the maximum possible period before the trajectory turns back on itself, i. e. after $61 \times 81 = 4941$ rotations. Part of the trajectory is shown in Fig. 3.2. This device provides us the necessary time of sometimes up to six hours per measurement to achieve satisfactory signal to noise ratios for experiments on ice.

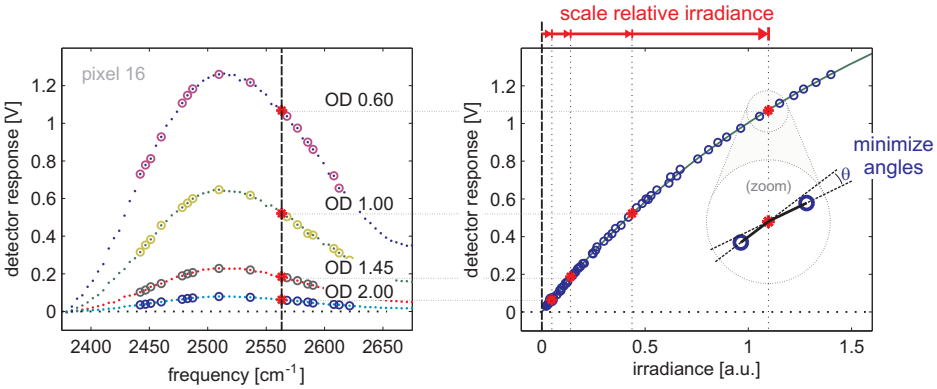

FIGURE 3.3. Detector response and calibration curves for a single pixel. Left: The detector voltages measured for different frequencies of the probe pulse and for different optical density filters. Right: Voltage response as a function of pulse intensity and the fitted calibration curve. Zoom inset shows angles between subsequent line pieces that are minimized by scaling the relative irradiances.

3.4 DETECTOR

The Mercury Cadmium Telluride (MCT) infrared pixel-detector, amplification, and data-processing result in a frequency-resolved voltage measurements that should reflect the intensity of the probe pulses through the sample. Ideally this voltage V linearly depends on the incident pulse energy I, however this was not found to be the case. First of all, we correct for zero-point drift of the detector voltages by periodic dark voltage measurements with a closed detector shutter. Because the pump-probe signal is always a relative intensity (T/T_0), the linear sensitivity of the detector has no influence on it. However, a non-linearity of the detector response causes noticeable deviations, e. g. when there is a large variation in intensities over the probe spectrum.

To correct for this non-linearity we need to find a calibration function $I(V)$ that returns the intensity of the incident laser pulse for a measured detector voltage V (see Fig. 3.3). In principle, this function can be retrieved by shining a selection of known intensities onto the detector and measuring the resulting voltages. In practice, this would be cumbersome as each point on the curve $V_i(I_i)$ needs to be measured separately, e. g. by using a discrete set of filters with known relative optical densities. Instead we proceed as follows.

Infrared probe light with the desired frequency-dependent intensity spectrum $I(\nu)$[a] is generated and coupled into the spectrograph. The spectrum should contain intensities that result in the desired range of voltages for which the detector needs to be calibrated. By rotating the spectrograph grating we scan the probe spectrum and record the frequency dependent resulting voltages

[a] in the remainder of this thesis we express the frequency in [cm^{-1}] with the symbol $\nu = \omega/200\pi c$

$V(\nu)$ separately for all pixels of the detector. This spectrograph scan is repeated for d different relative intensities by changing the optical density (OD) of filters placed in the probe path (filter wheel Fig. 3.1). We thus record for each pixel a set of voltage spectra $V_d(\nu)$ whose intensities scale as

$$I(V_d(\nu)) = I_0(\nu) \times 10^{-OD_d}\,, \tag{3.3}$$

At this point we do not know the values of $I_0(\nu)$, only the resulting spectra $V_d(\nu)$ for different filters d. Because we are only interested in relative values of I_0 we start by setting $I_0(\nu_i) = 1$ for any particular frequency ν_i. We thus find as the starting points for the calibration curve $V = V_d(\nu_i)$ as a function of $I = 10^{-OD_d}$. The algorithm proceeds by choosing a different frequency ν_j with different voltages $V_d(\nu_j)$ and scales $I_0(\nu_j)$ such that the resulting values of $V_d(\nu_j)$ together with the previously obtained values $V_d(\nu_i)$ form a bijective function of I, i. e. the calibration curve is a one-to-one correspondence between I and V. This scaling involves a chi-squared minimization of the angles between subsequent lines pieces as shown in Fig. 3.3. Additional frequencies are chosen and the procedure is iterated until a satisfactory range of voltages is covered. The advantage of this method is, that no assumptions have thus far been made about the functional form of the calibration curve. After the calibration was complete we found that its form was well described with the function

$$I = \frac{p\,V}{1 - V/V_{\max}}\,, \tag{3.4}$$

where p is an arbitrary scaling constant that reflects the absolute sensitivity of the detector pixels and $V_{\max}$ is the saturation voltage of the pixel. The procedure is repeated for all pixels of the detector and the scaling constants p are chosen such that differences in pixel-to-pixel sensitivity are compensated and their average value $\sum_{n=1}^{N} p_n/N = 1$. In the case of small transmission changes, these pixel-to-pixel sensitivities p have no influence on the dynamics of pump-probe measurements but are useful e. g. for the determination of spectral shapes.

4 Analysis and Modeling

4.1 Transient Absorption and Anisotropy

Short laser pulses, used in pump-probe experiments, generally consist of a range of frequencies that are selectively absorbed as they travel through the sample. In pump-probe spectroscopy we measure the frequency-resolved transmission spectra of probe pulses through the sample. To compensate for pulse to pulse fluctuations of the laser system the probe is split before the sample into probe and reference pulses. The reference pulses are sent through the sample before the pump pulses. The probe is spatially overlapped with the pump and focussed in the sample. The relative delay time between pump and probe probe pulses is controlled with a delay stage. To determine the pump-induced changes of the probe transmission, the signals are alternatingly measured with and without the pump pulse present using a chopper in the pump beam before the sample. The pump-induced relative transmissions are calculated from two subsequent probe measurements using

$$\frac{T(t,\nu)}{T_0(\nu)} = \frac{I_{\mathrm{probe}}(t,\nu)/I_{\mathrm{ref}}(\nu)}{I_{0,\mathrm{probe}}(\nu)/I_{0,\mathrm{ref}}(\nu)}\,, \tag{4.1}$$

where I_{probe} and I_{ref} are the probe and reference intensities measured by the detector and the subscript 0 indicates that the pump was blocked for those probe shots. From these relative transmissions we calculate the pump-induced absorption changes using Lambert-Beer law (Eq. (2.22)):

$$\Delta\alpha(t,\nu) = -\ln\left(T(t,\nu)/T_0(\nu)\right)\,. \tag{4.2}$$

We have seen in Eq. (2.49) that the absorption cross-section of infrared active modes, such as the O–H stretch vibration, is dependent on the directional overlap ($\cos^2(\theta)$) between the transition dipole moment of the absorbing oscillator and the polarization of the light. A linearly polarized pump beam thus excites an anisotropic distribution of transitions in an isotropic sample. We probe the anisotropic absorption differences ($\Delta\alpha$) caused by this distribution using a pair of probe beams with parallel ($\parallel$) and perpendicular ($\perp$) polarizations with respect to the pump. In our experiments this is achieved by rotating the polarization of the pump with a $\lambda/2$-plate to 45 ° with respect to the probe polarization and selecting parallel and perpendicular probe components with a polarizer after the sample.

It can be shown [85] that if we take the following linear combinations of these absorptions we can retrieve separately the isotropic signal $\Delta\alpha$ and the

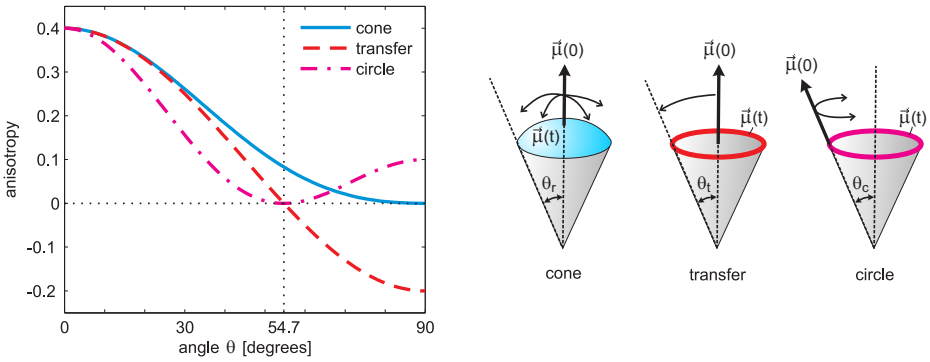

FIGURE 4.1. Dependence of the anisotropy on the reorientation angle θ of the transition dipole moment $\vec{\mu}$. The initial and final directions are indicated by $\vec{\mu}(0)$ and $\vec{\mu}(t)$, respectively.

anisotropy R:

$$\Delta\alpha(t,\nu) = \frac{\Delta\alpha_{\parallel}(t,\nu) + 2\cdot\Delta\alpha_{\perp}(t,\nu)}{3}\,, \tag{4.3}$$

$$R(t,\nu) = \frac{\Delta\alpha_{\parallel}(t,\nu) - \Delta\alpha_{\perp}(t,\nu)}{\Delta\alpha_{\parallel}(t,\nu) + 2\cdot\Delta\alpha_{\perp}(t,\nu)}\,. \tag{4.4}$$

The isotropic signal depends only on the density of the pump-induced absorption differences and is independent of rotational diffusion. Conversely, the anisotropy is proportional to the second-order orientational correlation function of the direction of the excitation and equals [85]:

$$R(t) = {}^{2}\!/_{5}\,\langle P_2(\hat{\mu}(0)\cdot\hat{\mu}(t))\rangle \tag{4.5}$$

where $\hat{\mu}(0)\cdot\hat{\mu}(t)$ is the inner product between unit vectors along the direction of transition dipole moments at times 0 and t. $P_2(x) = {}^{1}\!/_{2}\,\left(3x^2-1\right)$ is the second Legendre polynomial and $\langle ...\rangle$ denotes the ensemble average. From the isotropic signal we obtain information about the vibrational relaxation rate k which depends on the density and cross-section of nearby accepting modes. The anisotropic signal reveals information about reorientational motion (or lack thereof) as well as vibrational Förster energy transfer.

From Eqs. (4.3) and (4.4) it can be shown that when the pump-probe signal consists of multiple components that have different anisotropies, the total observed anisotropy will be the average of the individual anisotropies R_i, weighted with the isotropic intensities $\Delta\alpha_i$:

$$R_{\text{total}} = \frac{\sum_i \Delta\alpha_i \cdot R_i}{\sum_i \Delta\alpha_i} \tag{4.6}$$

In polarization resolved pump-probe spectroscopy, the observed anisotropy R depends on the average angular displacement of the transition dipole moment

as a result of reorientation or energy transfer. Using Eq. (4.5), we calculate this dependence for some of the most common scenarios, shown in Fig. 4.1:

$$R_{\text{cone}} = \tfrac{2}{5}\left(\tfrac{1}{2}\cos(\theta_r)\cdot[1+\cos(\theta_r)]\right)^2, \tag{4.7}$$

$$R_{\text{transfer}} = \tfrac{1}{5}\left(3\cos^2(\theta_t)-1\right), \tag{4.8}$$

$$R_{\text{circle}} = \tfrac{1}{10}\left(3\cos^2(\theta_c)-1\right)^2. \tag{4.9}$$

From Eq. (4.7) it follows that when the excitation is uniformly distributed over all angles ($\theta_c = 90°$) the anisotropy is zero, i. e. isotropic. From Eq. (4.8) and Fig. 4.1, we note that when the excitation is at the 'magic angle' ($\arccos(\sqrt{\tfrac{1}{3}}) = 54.7°$) with respect to the pump polarization, the observed anisotropy will be zero. This is true both if the polarization jumped as a result of energy transfer, or if pump and probe were at this magic angle from the start. The observed anisotropy is then always zero and the probed absorption changes will be independent of reorientational diffusion. Note also that when the excitation jumps over an angle larger than 54.7°, the observed anisotropy can become negative, i. e. $\Delta\alpha_{\parallel} < \Delta\alpha_{\perp}$. From Fig. 4.1 we note that the anisotropy in Eq. (4.9) is not a bijective function of the angle θ_r for $R < 0.1$, i. e. there are multiple angles corresponding to the same anisotropy. More specific distributions of $\vec{\mu}$ can always be calculated using Eq. (4.5).

4.2 Multi-component Analysis

In Section 4.1 we introduced the time and frequency dependent absorption difference spectra $\Delta\alpha(t,\nu)$ measured in our pump-probe experiments. These transient spectra result from time-dependent spectral signatures reflecting non-equilibrium physical processes caused by the pump beam, such as the excitation of a vibrational mode. The shape of these spectral signatures may themselves also be time dependent, such as in the case of spectral diffusion or coherent artifacts. In most other cases we can treat these shapes as time-independent.

The amplitude and spectral shape of the transient spectrum reflects the frequency-dependent absorption cross-section of individual excited modes and the time-dependence of their excitations. In a macroscopic sample the time-dependence of individual excitations that have the same characteristics are averaged out and can be described as a single component. Such a component consist of a time-dependent population (i. e. concentration), proportional to the number of contributing excitations and a frequency dependent spectral signature, proportional to the absorption change resulting from this excitation. The response of each component i is thus the product of its population dynamics $N_i(t)$ and spectral signatures $\sigma_i(\nu)$, while the total absorption change is the sum of these responses:

$$\Delta\alpha(t,\nu) = \sum_i N_i(t)\cdot\sigma_i(\nu). \tag{4.10}$$

This equation can be written in the form of a matrix equation as shown in Fig. 4.2

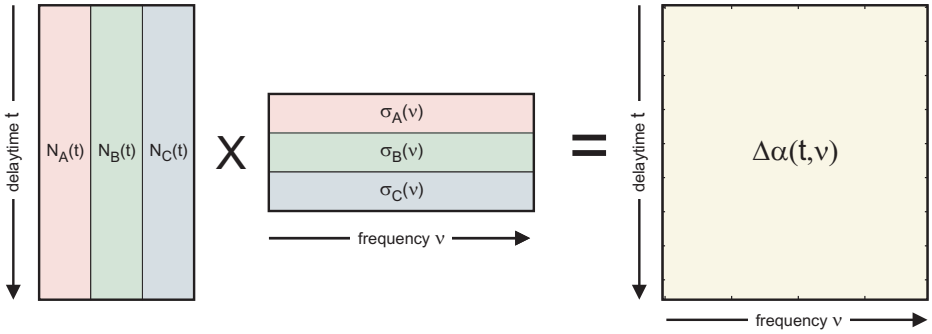

FIGURE 4.2. Decomposition of a three state model.

In general, a model that describes a data set is based on 'physical intuition', i. e. an understanding of the system under study and the general qualitative trends observed in the data. However, if a data set is congested with multiple overlapping spectral and temporal components we need a more rigorous set of tools to disentangle the observations. Thus, in order to analyze a multi-component data set, it is often necessary to isolate the dynamics and spectral signatures of its individual components.

4.2.1 SINGULAR VALUE DECOMPOSITION

Before we can isolate the constituent components, we first need to estimate the number of components that are present in the data. A useful mathematical tool for this is called 'singular value decomposition' (SVD). It can be shown [106] that for any $m \times n$ matrix M there exists a factorization of the form:

$$M \;=\; T\,S\,V \tag{4.11}$$

where T is an $m \times m$ unitary matrix, the matrix S is a nonnegative $m \times n$ diagonal matrix, and V is an $n \times n$ unitary matrix. The columns of T and the rows of V can be viewed as orthonormal basis vectors with which to construct the constituent components in M. The weight of each component is given by the diagonal entries in matrix S which are called the singular values. To clarify this point we write Eq. (4.11) as:

$$M_{mn} \;=\; \sum_i T_{mi} \times S_{ii} \times V_{in}\,, \tag{4.12}$$

where the subscripts denote the coordinates of the matrix.

The singular values can be used to determine the total number of significant components in a data set. Substituting the data matrix $\Delta\alpha(t,\nu)$ for M in Eq. (4.12), results in a decomposition of the data into orthonormal time-dynamics and spectral components, as column vectors in T and row vectors in

V, respectively. It should be clear, however, that these vectors are in general not the 'real', temporal and spectral components that we wish to find, rather they are an orthonormal basis of said components. Nevertheless the singular values indicate how many components are needed to describe in principle a data set with any degree of accuracy.

The fractional contribution of each component is obtained by normalizing the vector of singular values:

$$\hat{S}_i = S_{ii}/(\Sigma_i S_{ii})\,. \tag{4.13}$$

In a completely noise-free data set the number of non-zero singular values directly reflect the number of constituent components. However, in a real data set it may not always be possible to unambiguously distinguish the lowest amplitude signal components from the noise (background) components. As a rule of thumb we look for those components that are significantly higher than the rest. As a simple example, we suppose a noisy data set that consists of the following (normalized) singular values:

$$\hat{S}_i = [\ 0.78,\ \ 0.14,\ \ 0.05,\ \ 0.013,\ \ 0.011,\ \ 0.006\ ]\,.$$

Inspection of the first three singular values reveals that $0.78+0.14+0.05 = 97\%$ of the signals in this data set can be described as a sum of three components. The third component is still significantly above the rest ($0.05 > 3\times 0.013$), while any additional components can not be sufficiently distinguished from the noise background.

4.2.2 LEAST-SQUARES FITTING

After having established the number of components in the system, we remain with the task of finding a suitable model for the decomposition of our data set. There are several strategies that can be used. In general, we measure a data set $\Delta\alpha(t,\nu)$ with standard deviations $\epsilon(t,\nu)$ and wish to decompose and fit it using a multi component model. Each component i consist of a product of time dynamics $N_i(t)$ and spectral shapes $\sigma_i(\nu)$, which depending on the model can depend on a set of parameters $\boldsymbol{p}$. To estimate how well a given model is fitted to a data set we use the chi-squared (χ^2) function, defined as the squared average number of standard deviations between data and model:

$$\chi^2(\boldsymbol{p}) \;=\; \int\!\!\int\, dt\; d\nu\; \left(\frac{\Delta\alpha(t,\nu) - \sum_i N_i(t;\,\boldsymbol{p})\;\sigma_i(\nu;\,\boldsymbol{p})}{\epsilon(t,\nu)}\right)^2 \tag{4.14}$$

Because the time-dynamics and spectral shapes are dependant on the model parameters, so is the χ^2 function. Obviously, the best estimation for the values of these model parameters are those that minimize the χ^2 function. Following the definition of standard deviation, the minimum value that a χ^2 can reach for a perfect model is 1. In practice these values are higher because a model is usually a simplified description of reality. If the value is lower than 1, this indicates that either the standard deviations were overestimated or the model contained

too many parameters. There are several methods to find the minimum of a χ^2 function that can be broken down into numerical and analytical categories.

Concerning numerical methods, there exist computer algorithms that iteratively try to minimize the χ^2 by varying the parameter values. Such algorithms work analogous to a ball on an N-dimensional landscape (where N is the number of parameters) trying to find the lowest point by rolling down the hill. Just like a ball can get stuck in a hole, so the algorithm can get trapped in a local minimum. This is especially true if the model is complicated with many parameters or if the parameters display a large degree of covariance, i. e. changing one parameter value affects the χ^2 minimum as a function of another parameter. To remedy this, it is necessary to provide the fit algorithm with a suitable set of initial values and boundary conditions.

In the following we describe a number of analytical least-squares decomposition methods with which we directly calculate the best fitting model (spectra, time-dynamics, anisotropy) to a given set of data. The obvious advantage is that these methods do not require an iterative procedure and that they provide a unique solution (independent of starting values). Obviously it is not possible to unambiguously distinguish (deconvolve) two processes that behave in exactly the same way. Therefore least-squares decomposition is only possible if either the population dynamics or spectral signatures are linearly independent from one component to the other. In other cases, we need to impose or constrain either the spectral signatures or time dynamics.

4.2.3 Spectral decomposition

We start with the spectral decomposition, i. e. a set of spectra $\sigma_i(\nu)$ that best fit a given set of population dynamics $N_i(t)$ to data points $\Delta\alpha(t,\nu)$ with standard deviations $\epsilon(t,\nu)$. To this end we define a function χ^2 that we need to minimize:

$$\chi^2(\tilde{\sigma}_i) = \int dt \left(\frac{\Delta\alpha(t,\nu) - \sum_i N_i(t) \cdot \tilde{\sigma}_i}{\epsilon(t,\nu)} \right)^2 \tag{4.15}$$

where $\tilde{\sigma}_i$ are now i separate variables that are proportional to the relative spectral amplitudes at frequency ν. The least squares fitting linear combination can be calculated by equating the derivatives with respect to these amplitudes to zero:

$$\frac{d}{d\tilde{\sigma}_i} \int dt \left(\frac{\Delta\alpha(t,\nu) - \sum_i N_i(t) \cdot \tilde{\sigma}_i}{\epsilon(t,\nu)} \right)^2 = 0 \tag{4.16}$$

This gives us i equations with i unknowns that may be readily solved. Repeating this procedure for all frequencies results in i separate spectral signatures $\tilde{\sigma}_i(\nu)$. An example of this procedure is shown in Fig. 4.3.

4.2.4 Temporal decomposition

Equivalently, this procedure will also work the other way around. If we know (or fit) the spectral signatures $\sigma_i(\nu)$, we can calculate the unknown population

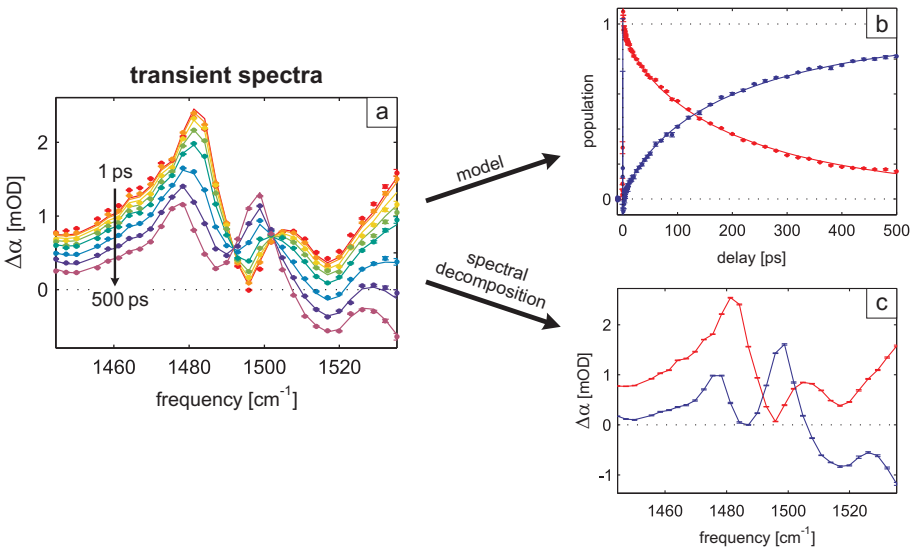

FIGURE 4.3. Decomposition of arbitrary data set into population dynamics and spectra. The population dynamics $N(t)$ were modeled (lines **b**) and the least squares corresponding spectra $\sigma(\nu)$ were extracted using spectral decomposition (**c**). The difference between the model $N(t) \times \sigma(\nu)$ and data (lines and points **a**, respectively) were minimized. As a final check we reverse the process by calculating the temporal decomposition that correspond to the extracted spectra (points **b**).

dynamics $\tilde{N}_i(t)$:

$$\frac{d}{d\tilde{N}_i} \int d\nu \left(\frac{\Delta\alpha(t,\nu) - \sum_i \tilde{N}_i \cdot \sigma_i(\nu)}{\epsilon(t,\nu)} \right)^2 = 0 \tag{4.17}$$

This will yield i time traces $\tilde{N}_i(t)$ that describe how a given set of spectra $\sigma_i(\nu)$ are individually evolving in data set $\Delta\alpha(t,\nu)$, without the need for any kinetic modeling or knowledge of initial conditions.

4.2.5 ANISOTROPIC DECOMPOSITION

Let us now assume two data sets $\Delta\alpha_\parallel(t,\nu)$ and $\Delta\alpha_\perp(t,\nu)$ that differ only in the amplitude of their spectral response as a result of a component-specific time-dependent (frequency-independent) anisotropy $R_i(t)$:

$$\Delta\alpha_\parallel(t,\nu) = \sum_i (1 + 2R_i(t)) N_i(t) \cdot \sigma_i(\nu) \equiv \sum_i N_{i,\parallel}(t) \cdot \sigma_i(\nu) \tag{4.18}$$

$$\Delta\alpha_\perp(t,\nu) = \sum_i (1 - R_i(t)) N_i(t) \cdot \sigma_i(\nu) \equiv \sum_i N_{i,\perp}(t) \cdot \sigma_i(\nu) \tag{4.19}$$

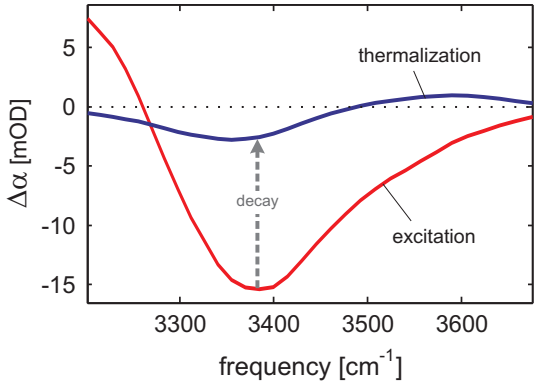

FIGURE 4.4. . Two spectral signatures typically found in pump-probe experiments on water. The excitation of the O–H stretch vibration leads to direct absorption changes associated with the transition $\nu = 0 \rightarrow 1$. The subsequent thermalization leads to indirect absorption changes resulting from the anharmonic coupling of low frequency modes to the ground state $\nu = 0$ of the O–H stretch mode.

It can be easily shown that the isotropic signal defined by Eq. (4.3) is independent of $R_i(t)$. It can be also shown, using Eq. (4.4), that if the anisotropy dynamics are the same for all components (i. e. $R_i(t) = R(t)$), we retrieve a frequency independent anisotropy.

In any case, if we know the spectra $\sigma_i(\nu)$, e. g. through spectral decomposition of the *isotropic* data, we can use temporal decomposition on both $\parallel$ and $\perp$ data sets to calculate the values of $N_{i,\parallel}(t)$ and $N_{i,\perp}(t)$ for all i and t. Having retrieved these anisotropic populations, we can use the following familiar linear combination (cf. Eq. (4.4)) to isolate the component-specific anisotropy $R_i(t)$:

$$R_i(t) = \frac{N_{i,\parallel}(t) - N_{i,\perp}(t)}{N_{i,\parallel}(t) + 2N_{i,\perp}(t)} \tag{4.20}$$

4.3 SPECTRAL SIGNATURES

In Chapter 2 we have seen how the interaction between light and matter can lead to absorption peaks at certain frequencies that are resonant with the transition between different energy levels in a system. The equilibrium occupation of these energy levels is given by the Boltzmann distribution. At room temperature ($k_B T \approx 200$ cm^{-1}), this means that for modes with vibrational transition frequencies > 1400 cm^{-1} practically only the ground-state energy level is occupied ($> 99.9\%$). The linear absorption spectra of vibrational modes in this frequency region thus mostly reflects their $\nu = 0 \rightarrow 1$ transitions.

On the other hand, in our pump-probe experiments we observe the pump induced absorption *changes* in a sample. This means that the spectral signatures we observe are not the absorption peaks themselves, but the effect of the

pump on these absorption peaks. The observed vibrational transient spectra fall into two categories. First there the direct effects resulting from the absorption changes associated with excitation of the mode itself. As we have seen in Section 2.5.4 the excitation of an anharmonic oscillator leads to a bleach at frequencies around the original ($\nu = 0 \rightarrow 1$) linear absorption and an induced absorption at lower frequencies ($\nu = 1 \rightarrow 2$). Secondly, there are the indirect effects of changes to the environment that may affect the frequency and absorption cross-section of the mode.

For example, after an excitation decays, the energy is released and goes into other modes that can be in proximity to the original excitation. If these other modes are (anharmonically) coupled to the original mode they can be observed in the transient spectra as a shift of the original (linear absorption) frequency or a change in the total absorption cross-section. For example, the thermalization of the O–H stretch mode in water leads to the occupation of low frequency modes that manifests as a decreased and blue-shifted absorption spectrum (see Fig. 4.4). Another example is the shift in frequency of the carbonyl stretch mode of acetate upon the arrival of a proton (see Chapter 8)

Absorption peaks generally consist of an inhomogeneously broadened collection of homogenous absorption line shapes (i. e. Lorentzian see Section 2.3.3). Depending on the mechanism behind the inhomogeneous broadening, the cross-section of the underlying peaks may vary. For example, the inhomogeneous broadening of the O–H stretch mode in liquid water is primarily caused by (Gaussian) fluctuations in the associated hydrogen bond strength. The transition frequencies are non-linearly dependent on the hydrogen bond fluctuations leading to an asymmetric distribution of the absorption peaks, more stretched towards the red side (see Fig. 1.5). In general, a linear absorption peak is well described using the convolution of an asymmetric distribution with a Lorentzian line shape. The absorption difference spectra can generally be described as the sum of a negative peak at the frequency of the original absorption and a positive peak at the new position of the absorption. A change in the total cross-section can be accounted for by different amplitudes of the two peaks.

In most cases, described in this thesis, we are primarily interested in a model that describes the evolution of states in the time-domain. In such cases we fit the temporal dynamics while simply calculating (not fitting) the associated spectra using spectral decomposition. A notable exception is the case of spectral diffusion in Chapter 7, where we excite a non-equilibrium sub-ensemble within an inhomogeneously broadened absorption band. The minimum width of such a sub-ensemble is determined by the homogeneous line width of the underlying spectra. Fluctuations that underly the inhomogeneous broadening lead to redistribution of the frequencies in the excited sub-ensemble until the equilibrium distribution is obtained. During the course of spectral diffusion, the spectral signatures of a mode are no longer constant, which means that we can not use the spectral decomposition methods to model the data and instead have to fit both the spectra and the time dynamics.

4.4 UNIMOLECULAR REACTIONS

4.4.1 RATE MATRIX

The time dynamics in a data set depend on the reaction[a] pathways of the constituent populations. In a first-order (unimolecular) reaction, the rates depend linearly on the concentrations of the reactants:

$$\frac{dN_i(t)}{dt} = \sum_j -k_{i\to j}N_i(t) + k_{j\to i}N_j(t)\,, \tag{4.21}$$

where $k_{i\to j}(t)$ are the rate constants for the reaction $N_i \to N_j$ and vice versa for $k_{j\to i}(t)$. Negative terms in the rate equations lead to decay of the population and positive terms lead to ingrowth. In this case the rate constants k are all time-independent and it is convenient to write the rate equations (4.21) in the form of a matrix as:

$$\frac{d}{dt}\,N_i(t) = \sum_j K_{ij}\,N_j(t)\,, \tag{4.22}$$

where the rate matrix K_{ij} contains all the transition rates $k_{i\to j}$ and $k_{j\to i}$. It can be shown that if the sum of each column of the rate matrix equals zero, we are dealing with a closed system, i. e. no population enters or leaves the system and the total population remains constant.

Eq. (4.22), constitutes a set of linear ordinary differential equations (ODE). These linear ODEs can be solved in general by diagonalizing the rate matrix K as follows. First we construct from the *eigenvalues* of K a diagonal matrix D and from the *eigenvectors* of K a matrix V, such that the following equation holds:

$$K\,V = V\,D \tag{4.23}$$

We use matrix V to construct a new vector $\vec{M}\,(t)$ such that

$$\vec{N}\,(t) = V\,\vec{M}\,(t) \tag{4.24}$$

We can now diagonalize the original problem:

$$\frac{d}{dt}\,\vec{N}\,(t) \;=\; \frac{d}{dt}\,(V\vec{M}\,(t)) = K\,(V\vec{M}\,(t)) = V\,D\,\vec{M}\,(t) \tag{4.25}$$

$$\Rightarrow \frac{d}{dt}\,\vec{M}\,(t) \;=\; D\,\vec{M}\,(t) \tag{4.26}$$

The set of equations, $\vec{M}\,(t)$, can be solved straightforwardly because D is diagonal:

$$\vec{M}(t) \;=\; \exp(D\,t)\;\vec{M}\,(0) \;=\; \exp(D\,t)\,V^{-1}\,N\,(0) \tag{4.27}$$

Finally we can transform the obtained solution for $\vec{M}\,(t)$ back to $\vec{N}\,(t)$ with Eq. (4.24):

$$\vec{N}\,(t) = V\exp(D\,t)\,V^{-1}\,\vec{N}\,(0) \tag{4.28}$$

[a] In the current context 'reaction' may refer to any change in state of the system.

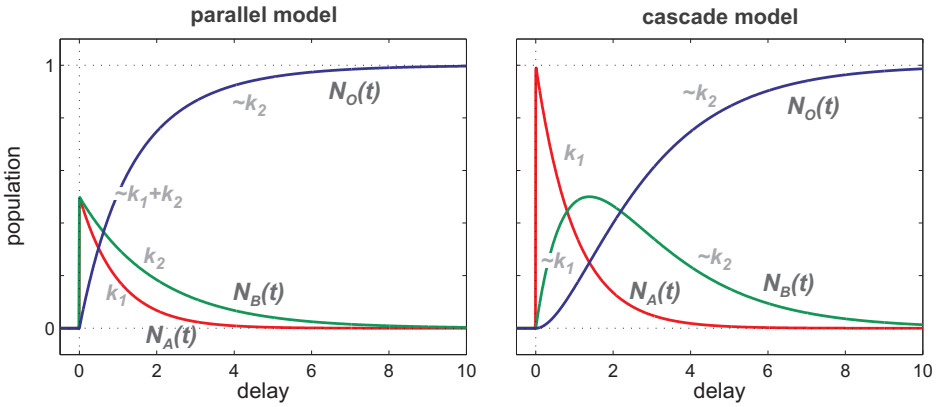

FIGURE 4.5. Typical population dynamics of three-state parallel and cascade models.

From these equations we can conclude that the time-dependent population of a unimolecular reaction scheme is always described as a linear combination of exponentials where the rates are the eigenvalues of the rate matrix. As a consequence, it can be shown that if no information is available on the spectral signatures of a multi-component data set, any model whose rate equation matrix has the same eigenvalues will fit equally well to this data set. In such cases the quality of the fit (χ^2) can not be used to determine which model is best and the distinction between models relies on the physical meaning of the least-squares associated spectra and/or anisotropy.

We will next discuss two basic examples of models that are commonly encountered when analyzing the time-dependent dynamics of a data set: the 'parallel model' and the 'cascade model'.

4.4.2 PARALLEL MODEL

First, we consider a reaction scheme where a set of populations in state $A, B, ...$ transfer independently (parallel) with respective rates $k_1, k_2, ...$ to a common end state O:

$$A \xrightarrow{k_1} O$$
$$B \xrightarrow{k_2} O \tag{4.29}$$
$$... \xrightarrow{...} ... \tag{4.30}$$

For this example, we limit the number of parallel channels to two. Together with the end state this gives us three states. The time-dependent population dynamics N_i of this three-state parallel model are described by

$$\frac{d}{dt}\begin{pmatrix} N_A(t) \\ N_B(t) \\ N_O(t) \end{pmatrix} = \begin{bmatrix} -k_1 & 0 & 0 \\ 0 & -k_2 & 0 \\ +k_1 & +k_2 & 0 \end{bmatrix} \begin{pmatrix} N_A(t) \\ N_B(t) \\ N_O(t) \end{pmatrix}. \tag{4.31}$$

Although the solutions to these rate equations are straightforward we proceed to use the methods of Section 4.4.1 as an illustrative example. Using linear algebra, we extract from the rate matrix K in Eq. (4.31) the eigenvalue matrix D and corresponding eigenvector matrix V:

$$D = \begin{bmatrix} -k_1 & 0 & 0 \\ 0 & -k_2 & 0 \\ 0 & 0 & 0 \end{bmatrix}, \quad V = \begin{bmatrix} -1 & 0 & 0 \\ 0 & -1 & 0 \\ 1 & 1 & 1 \end{bmatrix}. \tag{4.32}$$

Coincidentally, in this particular case $V^{-1} = V$. We thus fill in the values for D and V into Eq. (4.28)

$$\begin{pmatrix} N_A(t) \\ N_B(t) \\ N_O(t) \end{pmatrix} = \begin{bmatrix} -1 & 0 & 0 \\ 0 & -1 & 0 \\ 1 & 1 & 1 \end{bmatrix} \begin{bmatrix} e^{-k_1 t} & 0 & 0 \\ 0 & e^{-k_2 t} & 0 \\ 0 & 0 & 1 \end{bmatrix} \begin{bmatrix} -1 & 0 & 0 \\ 0 & -1 & 0 \\ 1 & 1 & 1 \end{bmatrix} \begin{pmatrix} N_A(0) \\ N_B(0) \\ N_O(0) \end{pmatrix} \tag{4.33}$$

yielding solutions:

$$\begin{aligned} N_A(t) &= N_A(0)\, e^{-k_1 t} \\ N_B(t) &= N_B(0)\, e^{-k_2 t} \\ N_O(t) &= 1 - N_A(0)\, e^{-k_1 t} - N_B(0)\, e^{-k_2 t} \end{aligned} \tag{4.34}$$

This reaction scheme is commonly encountered when multiple independent components are present in a data set, e. g. the overlapping spectral responses of bulk and anion-bound water molecules in Chapter 10.

4.4.3 CASCADE MODEL

Next, let us consider a slightly more complicated reaction scheme where the population starts in state A and is transferred consecutively with rates $k_1, k_2, ...$ through a number of states $B, C, ...$:

$$A \xrightarrow{k_1} B \xrightarrow{k_2} C \xrightarrow{\cdots} ... \tag{4.35}$$

In the reactions, the population is usually cascading down an energy level diagram. In principle this reaction scheme could be extended to include an arbitrary amount of states, but for most cases three suffice. The time-dependent population dynamics N_i of this three-state cascade model are described by

$$\frac{d}{dt} \begin{pmatrix} N_A(t) \\ N_B(t) \\ N_C(t) \end{pmatrix} = \begin{bmatrix} -k_1 & 0 & 0 \\ +k_1 & -k_2 & 0 \\ 0 & +k_2 & 0 \end{bmatrix} \begin{pmatrix} N_A(t) \\ N_B(t) \\ N_C(t) \end{pmatrix}. \tag{4.36}$$

Using again the methods described in Section 4.4.1 we find solutions:

$$\begin{aligned} N_A(t) &= N_A(0)\, e^{-k_1 t} \\ N_B(t) &= N_A(0)\, \frac{k_1}{k_2 - k_1} \left(e^{-k_1 t} - e^{-k_2 t}\right) \\ N_C(t) &= N_A(0)\, \left(1 + \frac{k_1 e^{-k_2 t} - k_2 e^{-k_1 t}}{k_2 - k_1}\right) . \end{aligned} \tag{4.37}$$

This three-state consecutive model is used for example to describe the vibrational energy relaxation of the O–H stretch mode in water, see Chapter 5. Note that the solutions in Eqs. (4.34) and (4.37) both consist of a linear combination of exponentials with rate constants k_1 and k_2. These two models can thus only be distinguished on the basis of their associated spectra.

4.5 Pseudo-unimolecular reactions

4.5.1 Survival probability

Until now we have considered unimolecular reactions $A \rightarrow B$ that depend only on the presence (concentration) of the reactant A itself. However there also exist reactions that depend on the proximity of two or more reactant. In the case of a bimolecular reaction, $A+B \rightarrow C$, two reactants A and B are combined and lead to a new product state C. A typical example of such a reaction are the proton transfer reactions described in Chapters 8 and 9, where the reaction rate is dependent on the proximity of acid and base molecules. Also the rate of Förster transfer, described in Chapters 10 and 11, is dependent on the proximity of two reactants, in this case the donor and acceptor vibrational modes.

The description of these reactions is simplified substantially if we work in the pseudo-unimolecular limit, where one of the reactants is in large excess and the reaction is irreversible. We describe the reaction

$$A \; + \; B_i \; \xrightarrow{\mathrm{k_i}} \; C_i \, , \tag{4.38}$$

where A reacts competitively to any B_i with unimolecular rate k_i, resulting in reaction product C_i. To solve this reaction scheme, we define the 'probability density' of the unreacted complexes:

$$\varphi_i(t) = \langle A + B_i \rangle (t) \, . \tag{4.39}$$

If we assume that A is dilute enough that we may describe each reaction complex independently, $\varphi_i(t)$ decays with the unimolecular rate k_i independent of the concentration of A. The reaction rate of A depends both on k_i and φ_i. These

assertions leads us to the following set of rate equations:

$$\frac{d\varphi_i(t)}{dt} = -k_i\,\varphi_i(t)\,, \tag{4.40}$$

$$\frac{dA(t)}{dt} = -\sum_i k_i\,\varphi_i(t)\,A(t)\,, \tag{4.41}$$

$$\frac{dC_i(t)}{dt} = +k_i\,\varphi_i(t)\,A(t)\,. \tag{4.42}$$

The solution to Eq. (4.40) is straightforward and can be written as

$$\varphi_i(t) = \lambda_i\,\exp(-k_i\,t)\,, \tag{4.43}$$

where we have defined $\lambda_i = \varphi_i(0)$, i. e. the average the number of B with which A can react through channel i.

The solutions to Eqs. (4.41) and (4.42) can be written implicitly as:

$$A(t) = A(0)\,\exp\left(-\int_0^t dt' \sum_i k_i\,\varphi_i(t)\right)\,, \tag{4.44}$$

$$C_i(t) = C_i(0) + \int_0^t dt'\;k_i\,\varphi_i(t')\,A(t')\,. \tag{4.45}$$

The term $\sum_i k_i\,\varphi_i(t)$ in Eq. (4.44) is dubbed the 'reactive flux' and is equivalent to a time-dependent reaction rate $k_{A+B\to C}(t)$. We note that Eq. (4.45) can be used to keep track of the number of reactions through channel i. By explicitly performing the integration of Eq. (4.44) by filling in Eq. (4.43) we find:

$$A(t) = A(0)\,\exp\left[-\sum_i \lambda_i\,(1-e^{-k_i\,t})\right] \tag{4.46}$$

The validity of Eq. (4.46) can be easily checked by differentiation. To better grasp its implications, we examine the 'survival probability' $S(t) = A(t)/A(0)$:

$$S(t) = \exp\left[-\sum_i \lambda_i\,(1-e^{-k_i\,t})\right] \tag{4.47}$$

$$= \prod_i \exp\left[-\lambda_i\,(1-e^{-k_i\,t})\right] \tag{4.48}$$

$$= \prod_i e^{-\lambda_i}\,\exp\left[\lambda_i\,e^{-k_i\,t}\right] \tag{4.49}$$

$$= \prod_i e^{-\lambda_i} \sum_{n_i=0}^{\infty} \frac{\left(\lambda_i e^{-k_i\,t}\right)^{n_i}}{n_i!} \tag{4.50}$$

$$= \prod_i \sum_{n_i=0}^{\infty} \frac{e^{-\lambda_i}\lambda_i^{n_i}}{n_i!}\,e^{-n_i\,k_i\,t}\,, \tag{4.51}$$

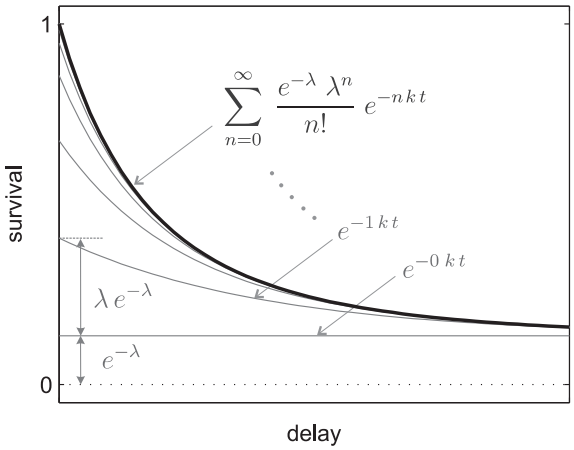

FIGURE 4.6. Decomposed survival probability as in Eq. (4.51). Thin lines show the individual rates with n reactants. Thick line shows the total sum which equals Eq. (4.47) for one component i.

where we used in step Eq. (4.50) the Taylor expansion for the exponential function. Eq. (4.51) shows that the survival probability S is the product of the individual survivals S_i:

$$S(t) \;=\; \prod_i \; S_i\,(t) \tag{4.52}$$

with

$$S_i(t) \;=\; \sum_{n_i=0}^{\infty} \; P_{n_i}(\lambda_i)\; e^{-n_i\,k_i\,t}\,, \tag{4.53}$$

where $P_n(\lambda)$ is the probability in Poisson statistics to find n occurrences for an event which has an average chance λ. We thus recognize the individual survival probability S_i equals a sum over all possible configurations $n_i = 0 \cdots \infty$, each weighted by the Poisson statistical chance of occurrence (see also Fig. 4.6). The survival probability for that particular configuration equals $\exp(n_i\,k_i\,t)$, i. e. the unimolecular rate is multiplied by the number of reaction pathways. Note that if λ is small enough, there is a substantial chance $P_0(\lambda) = e^{-\lambda}$ that no reaction will take place ($n_i = 0$). In terms of the reactants A and B this means that only if $B(0) \gg A(0)$ all A will react.

4.5.2 CONCENTRATION DEPENDENCE

To see how the survival probability of reactant A depends on the concentration of B, we define

$$\lambda_i = \rho\; V_i \tag{4.54}$$

where ρ is the concentration of B (units $1/L^3$, where L is a length scale) and V_i is the 'reactive volume' (units L^3). Filling Eq. (4.54) into Eq. (4.47) we find

$$S(t) = \exp\left[-\rho \sum_i V_i \, (1 - e^{-k_i t})\right] . \tag{4.55}$$

For $t \to \infty$ we see that Eq. (4.55) tends to $\exp[-\rho \sum_i V_i]$. The end level of the survival thus reflects the total reactive volume

$$\sum_i V_i = \frac{-\ln[\, S(\infty)\,]}{\rho}. \tag{4.56}$$

Eq. (4.55) is a specific case for the survival probability of the generalized Smoluchowski form [153]:

$$S(t) = \exp[\, -\rho \, P(t)\,] \, . \tag{4.57}$$

where $P(t)$ is the pair reaction probability. This equation holds true for any pseudo-unimolecular reaction. Vice versa, we can check if a data set can be described with pseudo-unimolecular kinetics by varying the concentration. Let us consider two data sets with concentrations of reactant $B = \rho_1$ and $B = \rho_2$ for which we measure survival probabilities $S_1(t)$ and $S_2(t)$, respectively. Then according to Eq. (4.57) we should find:

$$S_1(t) = \exp\left(-\frac{\rho_1}{\rho_2} \, \ln[\, S_2(t)\,]\right) , \tag{4.58}$$

i. e. independent of the functional form of $P(t)$. This procedure, dubbed 'concentration scaling', is used to check the applicability of Eq. (4.57) in Chapter 9 (see e. g. Fig. 9.6). Its validity is only guaranteed if the conditions for pseudo-unimolecular reactions are fulfilled, i. e. one of the reactants is in large excess and the reaction is irreversible.

4.5.3 CONTINUUM LIMIT

We now extend Eqs. (4.40)–(4.42) to the continuum limit. As before, we set $k_{ij} = 0$, i. e. we neglect diffusion. We consider a spherically symmetric system with A at the center and a uniform concentration ρ of reactants B for distances $r > r_{\min}$ (excluded volume). The reaction rate $k(r)$ depends only on the distance r between A and B. In the continuum limit we substitute:

$$\begin{aligned} k_i &\to k(r)\,, \\ \varphi_i(t) &\to \varphi(r,t)\,, \\ \lambda_i &\to \rho \, 4\pi r^2 dr\,, \end{aligned}$$

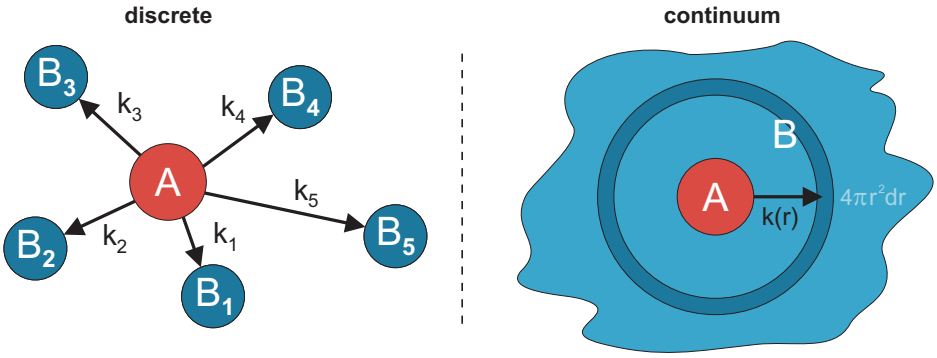

FIGURE 4.7. Discrete versus continuum: pseudo-unimolecular reaction of A with excess B. Survival of individual reactant A depends on the combined chance to react with any B. Left: Different reactive volumes B_i have different unimolecular reaction rates k_i. Right: unimolecular rate k is a continuous function of distance r for a shell with reactive volume $4\pi r^2 \mathrm{d}r$.

and replace the summation with an integral over r:

$$\frac{\partial \varphi(r,t)}{\partial t} = -k(r)\,\varphi(r,t)\,, \tag{4.59}$$

$$\frac{dA(t)}{dt} = -\int_r \varphi(r,t)\;A(t)\,, \tag{4.60}$$

$$\frac{\partial C(r,t)}{\partial t} = +k(r)\,\varphi(r,t)\;A(t)\,, \tag{4.61}$$

with solutions

$$\varphi(r,t) = \rho\;4\pi r^2 dr\;\exp\left(-k(r)\,t\right)\,, \tag{4.62}$$

$$A(t) = A(0)\;\exp\left(\rho\int_0^t dt'\int_{r_{\min}}^{\infty} dr\,4\pi r^2\;k(r)\,\varphi(r,t)\right)\,, \tag{4.63}$$

$$C(r,t) = C(r,0) + \int_0^t dt'\,k(r)\,\varphi(r,t')\;A(t')\,, \tag{4.64}$$

where $C(r,t)$ is the distance distribution of reactions $A+B\to C$ up to time t.

Analogous to Eq. (4.47), the survival probability of A can be calculated explicitly by integrating Eq. (4.63) over t:

$$S(t) = \exp\left(-\rho\int_{r_{\min}}^{\infty} dr\,4\pi r^2\;\left(1-e^{-k(r)\,t}\right)\right)\,. \tag{4.65}$$

This equation can be used to describe any type of distance dependent pseudo-unimolecular reaction $k(r)$. It is used in Chapters 8 and 10 where diffusion is neglected, with different functional forms for $k(r)$.

The distance distribution of transfer events $C(r,t)$ in Eq. (4.64) can be worked out further as

$$C(r,t) \;=\; \rho\, 4\pi r^2 dr\; k(r)\; A(0) \int_0^t dt'\, e^{-k(r)\,t'}\; S(t')\,, \tag{4.66}$$

where we set $C(r,0) = 0$ and $S(t)$ is given by Eq. (4.65). To get the total distance distribution $C(r)$ we evaluate Eq. (4.67) at $t = \infty$:

$$C(r) \;=\; \rho\, 4\pi r^2 dr\; k(r)\; A(0) \int_0^\infty dt\, e^{-k(r)\,t}\; S(t)\,. \tag{4.67}$$

4.5.4 DIFFUSION

For a distance dependent reaction rate $k(r)$, pairs that are in close proximity to each other generally react faster than those further away. As these close reaction pairs get depleted, a non-uniform distribution of pair reaction distances is created. In general, diffusion will act to counteract this non-uniformity by the exchange of pair reaction distances. In the continuum limit, this process can be described by diffusion equations which can take various forms depending on the geometry and dimensionality of the system.

In the present case we consider a spherically symmetric system and replace Eq. (4.59) by adding a diffusion term:

$$\frac{\partial\varphi(r,t)}{\partial t} \;=\; -k(r)\,\varphi(r,t) \;+\; \frac{D}{r^2}\frac{\partial}{\partial r} r^2 \frac{\partial}{\partial r}\varphi(r,t)\,. \tag{4.68}$$

The first part on the right hand side of Eq. (4.68) represents the distance dependent sink term and the second part represents the diffusion of the probability density, where D is the diffusion coefficient between reactants A and B. The relative importance of diffusion obviously depends on the coefficient D in relation to $k(r)$. In the limiting case where diffusion is negligible we can simply revert to the previously derived Eq. (4.65). In the other limit, e. g. where the only reactions that can take place are at 'contact distance', $k(r)$ is reduced to a delta function and the reaction is fully dictated by the diffusion rate.

In any case, it can be shown that also for diffusion influenced reactions, the survival probability of A still adheres to the Smoluchowski survival of Eq. (4.57). There are some analytical approximations to $S(t)$ for specific forms of $k(r)$ [36, 169], but not for a more general distance-dependence. In Chapter 8 we therefore use numerical integration to solve the diffusion and rate equations.

4.6 FÖRSTER TRANSFER

DIPOLE-DIPOLE COUPLING Förster energy transfer results from a near-field (non-radiative) dipole-dipole coupling between an excited-state donor molecule whose emission spectrum overlaps with that of a nearby acceptor molecule. In

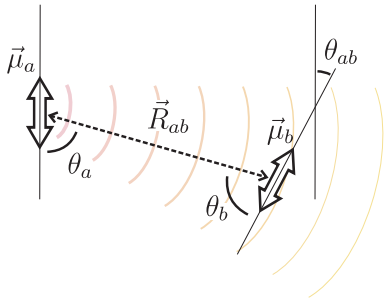

FIGURE 4.8. Spatial geometry of a dipole-dipole interaction.

general, the rate of Förster energy transfer k_F between two dipole oscillators a and b is proportional to the expression [47, 102, 165]:

$$k_{F,ab} \propto \frac{|\vec{\mu}_a|^2 |\vec{\mu}_b|^2 \kappa_{ab}^2}{|\vec{R}_{ab}|^6} \int d\nu \; \sigma_a(\nu)\, \sigma_b(\nu)\,, \tag{4.69}$$

where $\vec{\mu}_a$ and $\vec{\mu}_b$ are the transition dipole moments of the transmitting and receiving dipole modes, $\vec{R}_{ab}$ is the distance vector between the dipoles, σ_a and σ_b are the normalized vibrational line shapes of the two modes, and κ_{ab} is a geometrical factor expressing the relative orientations of the dipole moments (see Fig. 4.8):

$$\kappa_{ab} = \hat{\mu}_a \cdot \hat{\mu}_b - 3(\hat{\mu}_a \cdot \hat{R}_{ab})(\hat{\mu}_b \cdot \hat{R}_{ab}) \approx \cos\theta_{ab} + 3\cos\theta_a \cos\theta_b\,, \tag{4.70}$$

where the hats denote normalized unit vectors. The latter equality only holds if all vectors $\hat{\mu}_a$, $\hat{\mu}_b$, and $\hat{R}_{ab}$ lie in a plane as drawn in Fig. 4.8.

FÖRSTER RADIUS If we assume that the relative orientation of dipole oscillators a and b is unrelated to their distance r, we can write the rate of Förster transfer k_F phenomenologically as:

$$k_F(r) \;=\; \frac{\hat{k}_F}{r^6} \;\equiv\; \frac{1}{T_1}\left(\frac{R_0}{r}\right)^6\,, \tag{4.71}$$

where $\hat{k}_F$ is the rate of Förster transfer at $R = 1$, T_1 is the default donor lifetime in the absence of Förster transfer, and R_0 is the Förster radius. This Förster radius is defined as the distance where $k_F = 1/T_1$, meaning that half the vibrational energy is dissipated through Förster transfer.

SURVIVAL There are many systems, in which the Förster transfer process can be described by pseudo-unimolecular reaction dynamics. Examples include the loss of vibrational energy as a result of Förster energy transfer in Chapter 10 and the decay of anisotropy in Chapter 11. In the continuum description of such systems, we can use Eq. (4.65) to describe the survival probability of the

original direction or excitation. Filling in the distance dependence of Eq. (4.71) into Eq. (4.65), we get:

$$S(t) \quad = \quad \exp\left\{-\rho \int_{r_{\min}}^{\infty} dr\, 4\pi r^2 \, \left(1 - \exp\left[-\frac{1}{T_1}\left(\frac{R_0}{r}\right)^6 t\right]\right)\right\} . \quad (4.72)$$

where ρ is the concentration of Förster receivers. If we take a minimum transfer radius $r_{\min} = 0$ and explicitly perform the integration over all distances we find

$$S(t) = \exp\left(-\rho \; {}^4\!/_3 \, \pi^{3/2} \sqrt{\frac{R_0^6 t}{T_1}}\right) \quad (4.73)$$

which is equivalent to the formula developed by Förster [47]. Note that the survival dynamics are highly non-exponential as they depend on $\sqrt{t}$.

5 Molecular Reorientation of Liquid Water

We have studied the mechanism of molecular reorientation of liquid water with multi-color femtosecond mid-infrared spectroscopy. We probe the anisotropy of the O–D stretch vibration of HDO molecules dissolved in H_2O and find that the spectral dynamics of this anisotropy strongly depend on the frequency of the excitation. The observations can be well explained with a model in which a subensemble of the molecules shows a fast reorientation that is accompanied by a large change of the vibrational frequency. This description of the reorientation agrees with the molecular jumping model for the reorientation of liquid water that was recently proposed by D. Laage and J.T. Hynes [70, 71]. However, in contrast to this latter model, we find the probability for reorientation and frequency jumping to be strongly frequency dependent, being much higher in the blue wing of the absorption band than in the center and the red wing. The molecules that undergo the reorientation and frequency jump are constantly regenerated as a result of the collective slow hydrogen-bond dynamics of liquid water that has a characteristic time constant of ∼700 fs. The combination of the two processes leads to the average molecular reorientation time of liquid water of ∼2.5 ps.

5.1 Introduction

Liquid water is extremely fast in rearranging its molecules to enable the solvation of reactants and to take up dissipated energy [28, 32, 87, 162]. An important aspect of this rearrangement is the molecular reorientation of the water molecules. The molecular reorientation of liquid water has been studied with several experimental techniques like NMR [134], dielectric relaxation [61], THz absorption [127], and femtosecond mid-infrared spectroscopy [108]. These techniques have yielded consistent results concerning the average rate of molecular reorientation in liquid water. With all these techniques it was found that the second Legendre polynomial of the orientational correlation function of the water molecules shows a main component that decays with a time constant of approximately 2.5 ps [61, 108, 127, 134].

In liquid water there exists a large variation in hydrogen-bond configurations

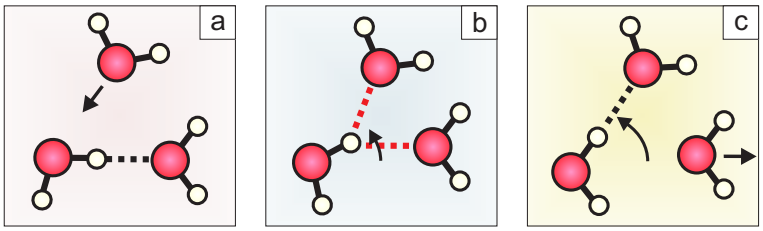

FIGURE 5.1. Reorientation of water through an intermediate bifurcated state. **(a)** A third water molecule approaches the original hydrogen bonded pair. **(b)** A bifurcated hydrogen bond is formed, the O–H/O–D frequency of hydrogen bond donor shifts to blue. **(c)** The water molecule rotates to the new hydrogen bond acceptor, the original O–H/O–D frequency is randomized.

and associated hydrogen-bond lengths and angles [8, 76, 121]. As a result, the absorption bands of the O–H/O–D stretch vibrations are strongly inhomogeneously broadened [7, 44, 45, 50, 74, 88, 139, 140, 161, 168]. Water molecules with long and bent hydrogen bonds absorb at higher frequencies than water molecules with short and linear hydrogen bonds. With femtosecond mid-infrared spectroscopy it is possible to spectrally select a sub-ensemble of water molecules and to measure the frequency dependence of the orientational dynamics. Interestingly, the study of this frequency dependence have led to contradictory results, seemingly dependent on the water isotope that was studied. In studies of the orientational dynamics of the O–H stretch vibration of HDO dissolved in D_2O, the reorientation was observed to be initially faster at the blue side of the absorption band than at the center and the red side [12, 51, 164]. However, in studies of the orientational dynamics of the O–D vibration of HDO dissolved in H_2O no frequency dependence of the reorientation was observed [122, 138].

In a recent theoretical study by Laage and Hynes [71], it was proposed that the reorientation of the water molecule in liquid water requires the temporary formation of a bifurcated hydrogen bond (see Fig. 5.1). Due to this formation, the barrier for rotation of the water molecule is much lower than the average binding energy of the hydrogen bond, which explains the high rate of molecular reorientation. In another study by the same authors the anisotropy decay was shown to depend on frequency only in a very short time range (<100 fs), as a result of the frequency dependence of the librational cone angle in which the O–H/O–D group can rotate [70]. On longer time scales (>100 fs) no frequency dependence was found, which implies that water molecules with short and long hydrogen bonds would have equal probability to reach the bifurcated transition state for reorientation.

In view of the contradictory observations and results described above, it is still not clear whether the reorientation of water shows a frequency dependence. To solve this issue, we perform a detailed femtosecond mid-infrared spectroscopic study of the anisotropy dynamics of the O–D vibration of HDO dissolved in H_2O. This system is as close as one can get to the study of the molecular

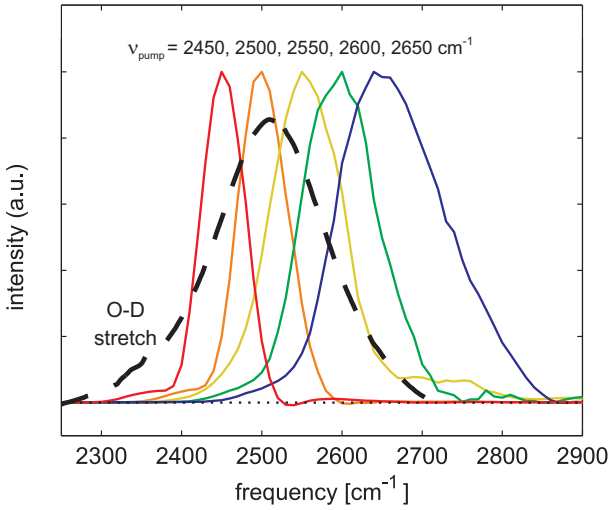

FIGURE 5.2. Typical excitation spectra that are resonant with the O–D stretch vibration of a solution of 1% HDO dissolved in H_2O. For comparison also the linear absorption spectrum of the O–D stretch vibration is shown (dashed curve).

reorientation of pure liquid H_2O. The O–H stretch vibrations of liquid H_2O are not suited for this study as these vibration show very rapid resonant intra- and intermolecular intermolecular energy transfer. An essential difference with previous work on HDO dissolved in H_2O is that here we vary both the excitation and the probing frequency. In the previous studies the O–D band was excited at its center frequency only and the anisotropy dynamics were studied as a function of the probe frequency only [122, 138]. We find that the variation of both the excitation and the probing frequency provides new insight in the mechanism of molecular reorientation of liquid water.

5.2 EXPERIMENTAL

The orientational dynamics of the O–D stretch vibration of HDO dissolved in H_2O are studied with multi-color polarization-resolved pump-probe spectroscopy. The pump and probe pulses are generated via a sequence of nonlinear frequency-conversion processes as described in Section 3.1. The central frequency of the pump was tuned between different frequencies using the methods described in Section 3.1. In Fig. 5.2 we show various pump spectra that are resonant with different parts of the O–D stretch absorption band of HDO:H_2O. The pump had a typical pulse energy of $\sim$10 μJ. The narrowing of the spectrum at lower frequencies is caused by the absorption of the asymmetric stretch vibration of CO_2 in the air. The frequency of the probe was tuned independently from the probe to about 2500 cm^{-1} with a bandwidth of $\sim$200 cm^{-1}.

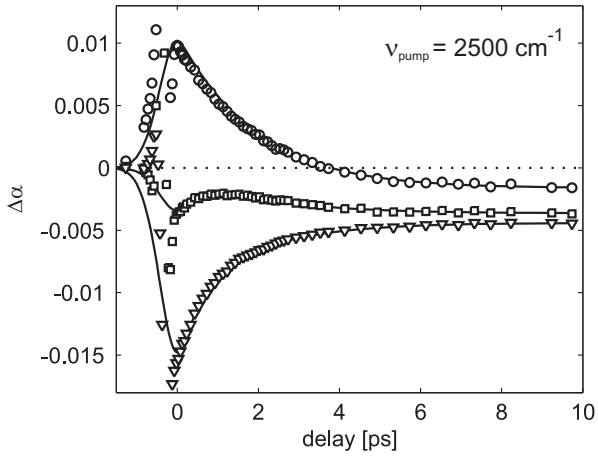

FIGURE 5.3. Absorption change as a function of delay between pump and probe for a pump frequency of 2500 cm^{-1}, and probe frequencies of 2380 cm^{-1} (circles), 2430 cm^{-1} (squares) and 2480 cm^{-1} (triangles).

The samples used in the experiment consisted of a 6% solution of HDO dissolved in H_2O. The sample was contained in a cell with CaF_2 windows and an optical path length of 50 μm. This concentration is sufficiently low to avoid the measurements to be affected by resonant energy transfer between O–D vibrations located on different HDO molecules. The pump excites a few percent of the O–D vibration of a solution of HDO:H_2O from the $\nu = 0$ ground state to the $\nu = 1$ excited state. This excitation leads to a bleaching effect at the fundamental transition frequencies, due to a decrease of the $\nu = 0 \rightarrow 1$ absorption and $\nu = 1 \rightarrow 0$ stimulated emission. The excitation also leads to induced absorption at frequencies corresponding to the $\nu = 1 \rightarrow 2$ transition. The latter absorption is red shifted with respect to the fundamental transition by 200 cm^{-1} due to the anharmonicity of the O–D stretch vibration. The rate of molecular reorientation of the water molecules is studied by measuring the time dependence of the anisotropy of the excitation of the O–D stretch vibration. In the experiment, the pump pulse is tuned through the absorption band. The frequency-resolved response of the probe is measured as a function of pump frequency and delay between pump and probe.

5.3 RESULTS

In Fig. 5.3 isotropic absorption changes are shown as a function of delay between pump and probe for a pump frequency of 2500 cm^{-1} and three different probe frequencies. At frequencies corresponding to the fundamental $\nu = 0 \rightarrow 1$ transition of the O–D stretch vibration, the excitation is observed to result in a

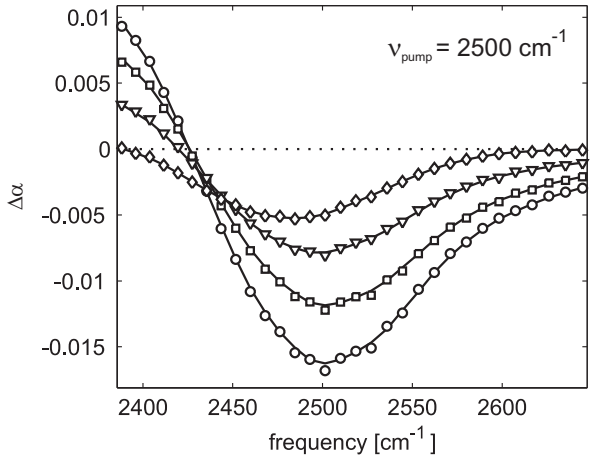

FIGURE 5.4. Absorption change as a function of frequency induced by a pump pulse at 2500 cm^{-1} exciting the O–D stretch vibration of HDO dissolved in H_2O. Shown are spectra at delays of 0.5 ps (circles), 1 ps (squares), 2 ps (triangles) and 4 ps (diamonds) between pump and probe. The solid lines represent the results of a fit of the data to a three-level cascade model (see Section 4.4).

direct absorption decrease when pump and probe pulses overlap. The absorption decrease decays due to the relaxation of the excited $\nu = 1$ vibrational state. At probe frequencies resonant with the $\nu = 1 \rightarrow 2$ excited state absorption of the O–D stretch vibration, an induced absorption is observed that also decays because of the vibrational relaxation. The signal at probe frequencies in the red wing of the fundamental absorption shows that the vibrational relaxation is not a simple single exponential decay, but involves two time constants. For large delays, persistent transmission changes are observed at all probe frequencies that do not decay on the maximum time scale of the pump-probe experiment ($\sim$1 ns). These transmission changes reflect the heating of the sample due to the complete thermalization of the energy of the pump pulse. The estimated increase in temperature in the focal volume is 1 K.

In Fig. 5.4, transient absorption spectra are shown at different delays after exciting the O–D stretch vibration with a pump pulse centered at 2500 cm^{-1}. At early delays, the transient spectra show the pump-induced bleaching of the fundamental $\nu = 0 \rightarrow 1$ transition in the frequency interval between 2425 and 2650 cm^{-1}, and the induced $\nu = 1 \rightarrow 2$ absorption at probe frequencies $<$2425 cm^{-1}. With increasing delay, the transient spectrum evolves to a response that reflects the change of the absorption of the O–D vibration that results from the thermalization of the pump-pulse energy. The spectral response of the thermalization signal consists of a bleaching in the center and in the red wing of the absorption band and an induced absorption in the blue wing of the absorption band. The thermalization signal is isotropic, meaning that

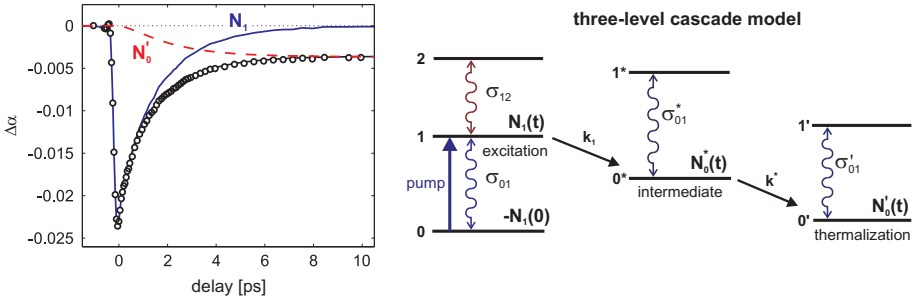

FIGURE 5.5. Decomposition of the observed transient pump-probe signal into two components. The first component $(-2\sigma_{01}+\sigma_{12})\times N_1(t)$ represents the sum of the $0 \rightarrow 1$ bleaching and the $1 \rightarrow 2$ induced absorption, the other component $(\sigma'_{01}-\sigma_{01})\times N'_0(t)$ represents the signal contribution that results from the thermalization of the energy over the focus. This latter component is subtracted to construct the data that are presented in Figs. 5.6–5.8. The intermediate state absorption difference spectrum $\sigma^*_{01}-\sigma_{01}$ is neglected.

the magnitude of this signal is the same for $\Delta\alpha_\parallel$ and $\Delta\alpha_\perp$. Hence, to obtain the anisotropy of the excited O–D vibration, the thermalization signal has to be subtracted from $\Delta\alpha_\parallel$ and $\Delta\alpha_\perp$. As the thermalization signal grows in with increasing delay, this subtraction can only be performed if the delay dependence of the thermalization is well known. To determine the delay dependence of the thermalization signal, we decomposed the spectral response measured with an excitation pulse at 2500 cm^{-1} into spectral components, following the procedure described in Section 4.2.3. At this frequency the signals show very little effects of spectral diffusion, which is a prerequisite for this decomposition. The decomposition of the measured signal is illustrated in Fig. 5.5. We find that the vibrational relaxation proceeds via a non-thermal intermediate state [122, 138, 147]. The intermediate state rises with the time constant of 1.5±0.1 ps of the relaxation of the $\nu = 1$ state of the O–D stretch vibration and decays with a time constant of 0.8±0.1 ps to the thermalized state. We use the dynamics of the thermalization signal to correct the measured data sets at all pump frequencies for the thermal contribution to the signal. The signals $\Delta\alpha_\parallel(\nu)$ and $\Delta\alpha_\perp(\nu)$ that result after this subtraction are used to construct the anisotropy parameter R as defined in Eq. (4.4).

In Fig. 5.6a the measured spectral dependence of the isotropic signals is shown for three different pump frequencies and five different delays. The transient spectra clearly show the effects of spectral diffusion. When the O–D stretch vibration is pumped in the red wing of the absorption band (top panel), the transient spectrum shows a blue shift. When the band is excited in the blue wing, the spectrum shows a red shift.

In Fig. 5.7a the anisotropy signals corresponding to the isotropic spectra of Fig. 5.6a are presented. When the O–D stretch vibration is pumped in the red wing of the absorption band or close to its central frequency (upper panel), the

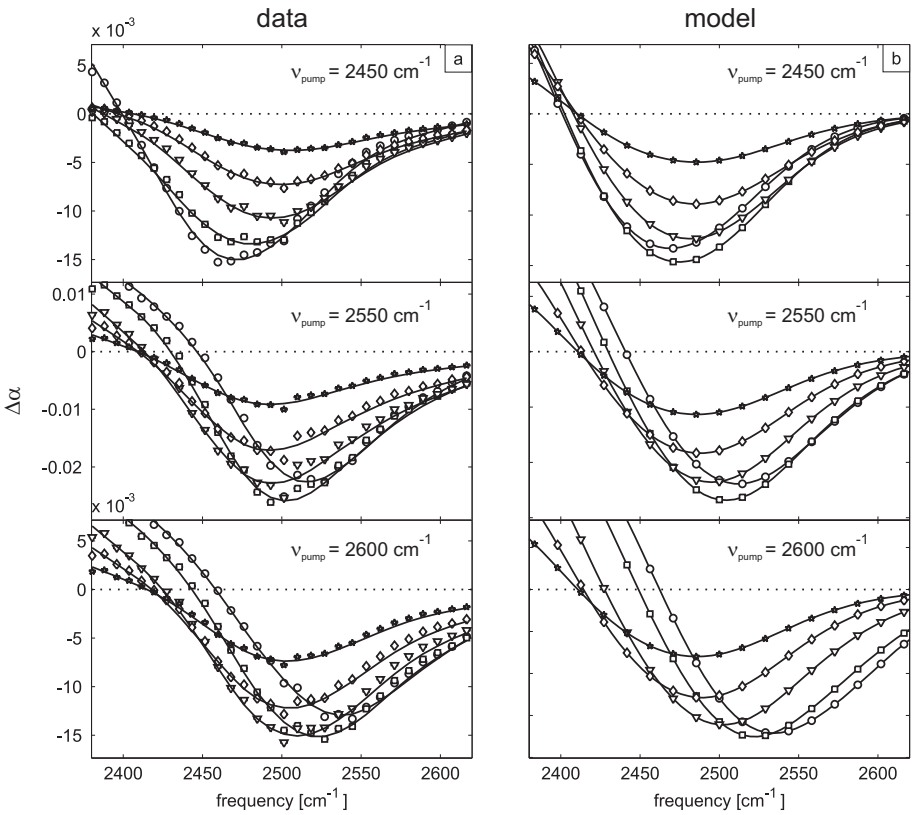

FIGURE 5.6. Isotropic transient spectra at delays of 0.2 ps (circles), 0.5 ps (squares), 1 ps (triangles), and 2 ps (diamonds). Shown are results obtained with a pump frequency of 2450 cm^{-1} (upper panel), 2550 cm^{-1} (middle panel), and 2600 cm^{-1} (lower panel). **(a)** shows the experimental results (solid lines are guides to the eye). **(b)** shows the results obtained with the model described in Appendix 5.8.

anisotropy is nearly the same at all probe frequencies, except in the frequency region where the bleaching changes into an induced absorption. As a result, the denominator of Eq. (4.4) becomes small and changes sign which leads to erratic behavior and large error bars of the anisotropy values. With increasing delay, the anisotropy decays. When the pump frequency is tuned to the blue wing of the absorption spectrum (middle and lower panel of Fig. 5.6), the anisotropy is strongly frequency dependent in the first 2 picoseconds. In this time interval, the anisotropy is higher in the blue wing of the spectrum than in the center and in the red wing of the absorption band. The divergence of the anisotropy due to the transition from the bleaching to the induced absorption region also occurs at higher frequencies than in the case where the O–D band was pumped in the center. At later delays (>2 ps), the anisotropy becomes the same at

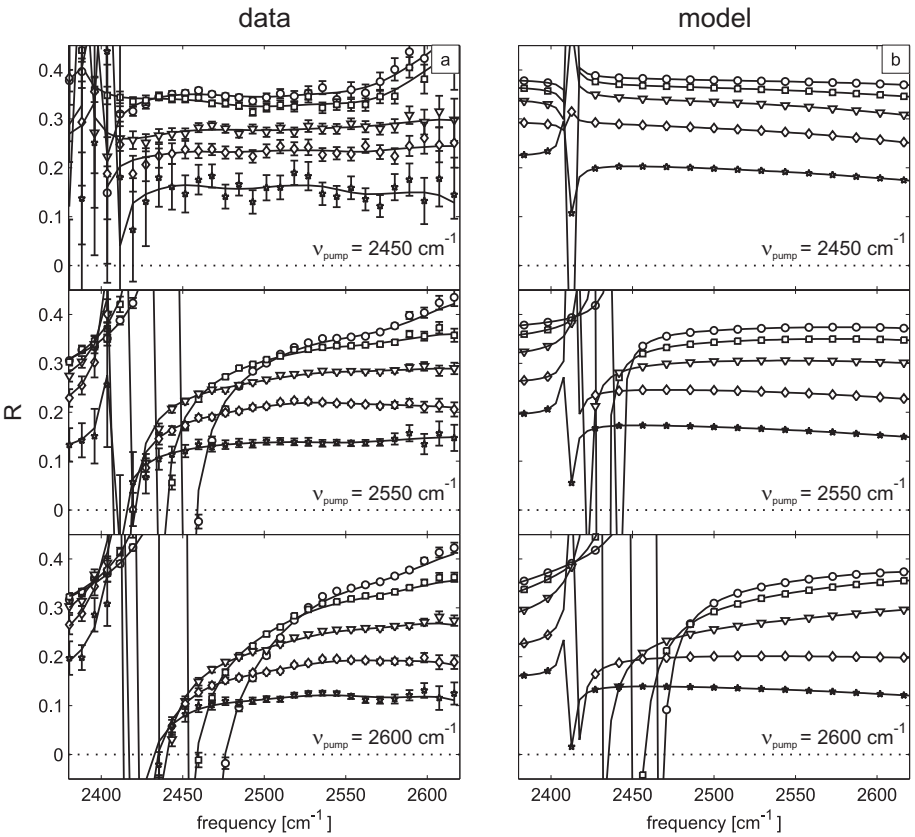

FIGURE 5.7. Experimental **(a)** and calculated **(b)** frequency dependence of the anisotropy corresponding to the isotropic transient spectra shown in Fig. 5.6.

all frequencies, which indicates the presence of a spectral diffusion process that leads to a spectral equilibration of the anisotropy.

In Fig. 5.8a the measured anisotropy is shown as a function of delay for a pump frequency of 2500 cm^{-1} and three different probe frequencies. Clearly, at all three probe frequencies the same dynamics are observed. In Fig. 5.8b, the measured anisotropy is shown as a function of delay for three cases where the pump and probe frequency are equal. Fig. 5.8b shows that the anisotropy shows an accelerated decay in the first 2 ps when *both* the pump and probe frequency are in the blue wing of the absorption band.

5.4 INTERPRETATION

The results in Fig. 5.7 show that excitation in the blue wing of the absorption bands leads to a strong frequency dependence of the anisotropy in the first 2 ps

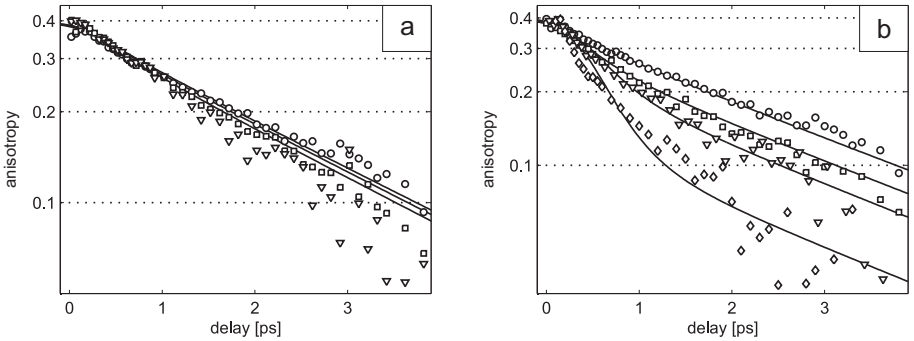

FIGURE 5.8. **(a)** Anisotropy of the O–D stretch vibration of HDO dissolved in H_2O as a function of delay between pump and probe for a pump frequency of 2500 cm^{-1}, and probe frequencies of 2500 cm^{-1} (circles), 2550 cm^{-1} (squares) and 2600 cm^{-1} (triangles). **(b)** Anisotropy of the O–D stretch vibration of HDO dissolved in H_2O as a function of delay for the same pump and probe frequency of 2500 cm^{-1} (circles), 2550 cm^{-1} (squares), 2600 cm^{-1} (triangles), and 2650 cm^{-1} (diamonds). Both panels: The points denote the experimental data and the solid lines represent the results of calculations performed with the model described in Appendix 5.8.

after excitation (middle and lower panel). This frequency dependence cannot be due to the fast inertial motion of the O–D dipoles in which the hydrogen bond remains intact. These inertial motions lead to an ultrafast partial anisotropy decay [45, 70, 100] from 0.4 to a value of ∼0.32. Recently it was shown that the anisotropy that remains after this partial anisotropy decay increases with decreasing frequency [100], which is opposite to the observations in Fig. 5.7.

In Fig. 5.9 the spectral dependence of $\Delta\alpha_{\parallel}(\nu)$ and $\Delta\alpha_{\perp}(\nu)$ are presented obtained at a delay of 0.2 ps after excitation with a pump pulse with a central frequency of 2600 cm^{-1}. It is seen that the bleaching of $\Delta\alpha_{\perp}(\nu)$ extends to significantly lower frequencies than the bleaching of $\Delta\alpha_{\parallel}(\nu)$. This difference in spectral shape is surprising because the excitation process and ordinary spectral diffusion do not lead to a difference in shape of $\Delta\alpha_{\parallel}(\nu)$ and $\Delta\alpha_{\perp}(\nu)$ the same. The difference in spectral shape of $\Delta\alpha_{\parallel}(\nu)$ and $\Delta\alpha_{\perp}(\nu)$ reveals the rapid addition of a low-anisotropy bleaching signal to the high-anisotropy initial signal. The perpendicular component of this additional signal is relatively strong and dominates the relatively weak perpendicular component of the initial $1 \rightarrow 2$ absorption over a large frequency range. The parallel component of the additional bleaching signal is relatively weak and can dominate the relatively strong parallel component of the $1 \rightarrow 2$ absorption over only a limited frequency range. As a result, the bleaching of $\Delta\alpha_{\perp}(\nu)$ extends to lower frequencies than the bleaching of $\Delta\alpha_{\parallel}(\nu)$.

The presence of a rapid broadband bleaching signal with low anisotropy indicates that part of molecules that were excited in the blue wing undergo a fast reorientation process that is accompanied by a large change in frequency. The

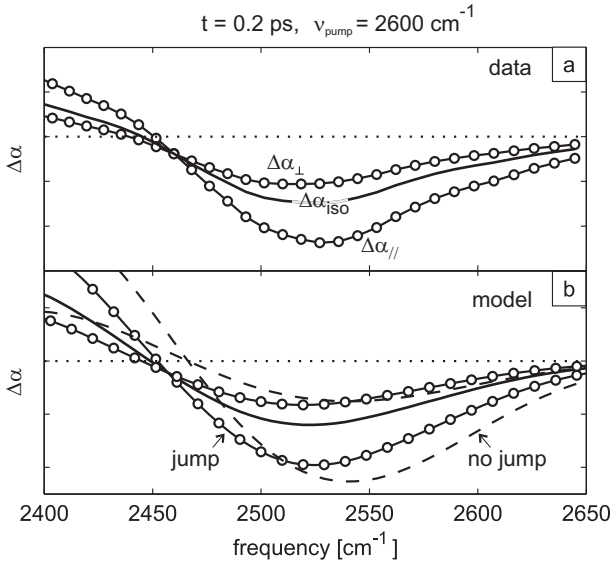

FIGURE 5.9. Transient spectra measured with probe pulses with polarizations parallel and perpendicular to that of the pump pulse for an excitation pulse with a central frequency of 2600 cm^{-1} at a delay of 0.2 ps. Also shown is the isotropic signal (thick solid curve). **(a)** Experimental data. **(b)** The results calculated with the jumping model in the text. Also also shown are the calculated transient spectra (dashed curves) in absence of the frequency jumping and reorientation process.

center and the red wing of the absorption band thus receive a significant amount of reoriented molecules shortly after excitation in the blue wing of the spectrum. In the center and the red wing of the absorption band, these reoriented molecules constitute a relatively large contribution to the total signal, because at these frequencies there are little molecules directly excited. In the blue wing, the number of directly excited molecules is large and at early delays the *relative* contribution of molecules that have reoriented will be small. Therefore, in the blue wing the anisotropy remains relatively high.

5.5 MODEL

We compared the observed excitation and probing frequency dependencies of the isotropic spectra and the anisotropy dynamics with model calculations that include the effect of rapid reorientation and frequency jumping of the molecules excited in the blue wing of the spectrum. This model also includes the vibrational relaxation and spectral diffusion of liquid water. The spectral diffusion of water has been shown to contain both fast and slow components [7, 8, 44, 45, 50, 76, 88, 121, 139, 140, 161, 168]. The slow spectral diffusion has been modeled with a single time constant with a value of

$\sim$1 ps [44, 45, 50, 76, 88, 121, 139, 140, 161, 168] or with two time constants of $\sim$0.4 ps and $\sim$1.8 ps [7]. Here we describe the slow spectral diffusion as a Gaussian spectral diffusion process (weak modulation limit) with an exponentially decaying frequency correlation function $\langle\delta\nu(t)\delta\nu(0)\rangle = e^{-t/\tau_c}$ with a time constant τ_c of 700 fs.

There are two distinct fast components to the spectral diffusion of liquid water. The first is of Gaussian nature, and leads to a broadening that is close to the motional narrowing limit. This component is included in the model via the homogeneous line width, which is a correct approach as the time resolution of our experiment is $\sim$200 fs. We use a value of 80 cm^{-1} [139]. The other fast component is a non-Gaussian process in which the frequency jumps throughout the absorption band [88,137]. This component has been observed in recent two-dimensional spectroscopic measurements of the spectral diffusion in liquid water [88, 137]. This component shows a strong frequency dependence, showing a much higher rate in the blue wing than in the center and the red wing of the absorption band [88, 137]. We assume now that this fast spectral diffusion component forms the origin of the frequency dependence of the anisotropy observed in the middle and lower panel of Fig. 5.7. Hence, we assume that the frequency jumps are accompanied by a (partial) reorientation of the water molecules. This assumption agrees with the explanation given in Ref. [88] for the frequency jumping.

In Ref. [88] the rapid change in frequency has been attributed to the evolution of the hydrogen-bond configuration of the water molecule through a short-lived bifurcated hydrogen-bonded state. The rapid contraction of one of the bonds and breaking of the other bond leads to a rapid rotation of the O–D group and a large change (decrease) of the frequency of the O–D oscillator. The return from the bifurcated state to a single strong hydrogen bond can thus be both due to the reformation of the original hydrogen bond, or due to the formation of a hydrogen bond to the new partner, i. e. a switching event [71,88]. Therefore, we assume that 50% of the frequency jumps (i. e. returns to a singly hydrogen-bonded state) results in reorientation.

Following the results of Ref. [88] and our observations we take the rate constant of the frequency jumping and reorientation to be frequency dependent. We describe this frequency dependence with a phenomenological expression that is fitted to the experimental results of Figs. 5.6–5.9. This expression is illustrated in Fig. 5.10 and explained in the Appendix. The rate constant is zero for water molecules with strong hydrogen bonds absorbing in the red wing of the spectrum, and attains a maximum value of 0.5×10^{13} s^{-1} for molecules with very weak hydrogen bonds. In view of the 50% probability that the jump results in reorientation, this rate constant corresponds to a time constant of 100 fs for the frequency jumping in the isotropic data, which is in excellent agreement with the results observed for the frequency jumping of Ref. [88]. It should be noted that the zero jumping rate of molecules absorbing in the red wing does not mean that the hydrogen bond of these molecules do not break. These molecules break their hydrogen bonds on a time scale of $\sim$1 ps, because these molecules spectrally diffuse to the blue wing of the absorption band via the slow Gaussian

spectral diffusion process with a time constant of 700 fs.

The calculated results are shown in Figs. 5.6, 5.7, and 5.9 and represented by the solid curves in Figs. 5.7 and 5.8. The model reproduces the spectral diffusion dynamics shown in Fig. 5.6, and the frequency and delay time dependence of the anisotropy at different excitation frequencies shown in Figs. 5.7 and 5.8. The reorientation and frequency jumping also accounts for the different spectral shapes of $\Delta\alpha_{\parallel}(\nu)$ and $\Delta\alpha_{\perp}(\nu)$ shown in Fig. 5.9. Without this process, $\Delta\alpha_{\parallel}(\nu)$ and $\Delta\alpha_{\perp}(\nu)$ would have exactly the same spectral shape, as illustrated by the dashed curves in Fig. 5.9b.

5.6 DISCUSSION

In Fig. 5.8b it is seen that the anisotropy shows an accelerated decay in the first 2 picoseconds after the excitation in case the water molecules are pumped and probed in the blue wing of the absorption band. This accelerated decay has been observed before in single-color studies of the anisotropy dynamics of the O–H stretch vibration of HDO dissolved in D_2O [12, 51, 108, 164]. In these studies the accelerated decay was assigned to a faster intrinsic reorientation of water molecules that remain in the blue wing. However, we now find that this interpretation is not correct because in that case the anisotropy observed at early delay times after excitation in the blue wing (lower panel of Fig. 5.7) should have shown an *increase* with decreasing frequency instead of the observed decrease. The results of Fig. 5.7 clearly show that the reoriented molecules do not remain in the blue wing but instead re-appear at all frequencies in the absorption band. The anisotropy thus decreases with decreasing frequency, because the relative contribution of reoriented, jumped molecules to the signal increases with increasing detuning from the pump frequency (middle and lower panels of Fig. 5.7). At later delay times, the spectral diffusion with a time constant of ∼700 fs leads to an equilibration of the low anisotropy of the center and the red wing with the high anisotropy in the blue wing. Hence, the accelerated decay that is observed when the absorption band is both pumped and probed in the blue wing is not due to a faster reorientation, but follows from the spectral equilibration after the frequency jumping. This notion also explains why the time constant of this accelerated decay is the same as that of the slow component of the spectral diffusion, i. e. ∼700 fs.

In case the absorption band is excited in its center, the anisotropy dynamics is practically the same at all probe frequencies. This independence on probe frequency following excitation in the center has been observed before in previous work on the O–D stretch vibration of HDO:H_2O [122, 138]. This absence of frequency dependence was interpreted as an indication that the reorientation is a collective process that shows no correlation with the strength of the local hydrogen bond [138]. However, the present observation that the anisotropy decay depends on the excitation frequency shows that this picture should be refined. In case the absorption band is pumped in the center (Fig. 5.7 upper panel, Fig. 5.8a), there will be little direct excitation of rapidly reorienting/spectrally

jumping molecules. As a result, the initially observed anisotropy will only be lower than 0.4 because of the inertial component ([45, 100]. The slow spectral diffusion will lead to an ongoing production of blue-shifted molecules that will reorient and jump in frequency. Because the frequency jumps through the whole absorption band, the jumping of reoriented molecules leads to the same decay of the anisotropy at all frequencies, with an effective time constant of 2.5 ps. The observed independence of the anisotropy dynamics on probe frequency (following excitation in the center of the absorption band) is thus not due to a frequency independence of the probability for reorientation, but caused by the fact that after the reorientation the reoriented hydroxyl group can reappear at all frequency positions in the absorption band.

The present findings are largely consistent with the molecular jumping mechanism for reorientation in liquid water that was recently proposed by Laage and Hynes [70, 71]. However, there are also differences. In Ref. [70] it was stated that the probability to evolve to the bifurcated transition state for reorientation would not depend on frequency, which is not in agreement with the present experimental findings (Figs. 5.7 and 5.9). According to the present experimental results, the molecular dynamics simulations of Laage and Hynes underestimate the correlation between frequency of the O–H/O–D oscillator and the rate for jumping and reorientation. It should also be noted here that the bifurcated transition state is likely not directly excited in the experiment, as this state has been shown to be extremely short-lived [70, 71, 88]. Therefore, the transition state configuration itself will contribute negligibly to the absorption, even in the blue wing of the absorption band. The frequency dependence of the jumping probability likely follows from the fact that the probability that the hydrogen-bond configuration evolves to the transition state increases with increasing hydrogen-bond length. In spite of this frequency dependence, the reorientation is likely a concerted process. Even for water molecules with relatively long hydrogen bonds (absorbing in the blue), the approach of a second hydrogen-bonded partner is required to further weaken and bend the hydrogen bond, and to let the system evolve to the bifurcated transition state for reorientation. Without such an approach, the long hydrogen bond will rather become shorter and stronger, thereby gradually shifting the frequency of the hydroxyl group to lower values.

5.7 Conclusions

We study the mechanism of reorientation of liquid water by measuring the anisotropy dynamics of the O–D stretch vibration of HDO dissolved in H_2O with multi-color polarization-resolved femtosecond mid-infrared pump-probe spectroscopy. We observe that the anisotropy dynamics strongly depend on the central frequency of the excitation. This frequency dependence can be well explained if part of the water molecules absorbing in the blue wing show a fast reorientation that is accompanied by a rapid frequency jump through the whole absorption band. This finding is consistent with recent measurements of the spectral dynamics of isotopically diluted water [88], and agrees with the

recently proposed jumping mechanism of molecular reorientation in liquid water [71]. We obtain a very good description of the experimental results with a model that includes the fast and slow spectral diffusion dynamics of liquid water and the jumping and reorientation process. The frequency dependence of the latter process is fitted to the data and the result is illustrated in Fig. 5.10.

The large change in frequency that accompanies the reorientation explains why in earlier studies, in which the absorption band was only excited in its center, no frequency dependence of the anisotropy dynamics was observed [122,138]. In the case of excitation in the blue wing, the reorientation and frequency jumping leads to a low value of the anisotropy in the center and red wing of the absorption already at early delay times. The subsequent exchange of the anisotropy at different frequencies due to spectral diffusion, causes the anisotropy to decay faster in the blue wing than in the center and the red wing. After the spectral equilibration is complete, the anisotropy shows the same dynamics at all frequencies. The slow spectral diffusion process (modeled as a single exponential process with τ_c = 700 fs) and the reorientation and frequency jump process together lead to the observed average molecular reorientation time of ∼2.5 ps of liquid water.

We observe the rate for frequency jumping and reorientation to be frequency dependent, whereas in the theoretical work of Laage and Hynes such a frequency dependence has not been reported [70]. We hope that the present work will stimulate further theoretical investigations of the relation between the momentary hydrogen-bond configuration and the probability to evolve to the transition state for reorientation.

5.8 APPENDIX: JUMPING MODEL

We describe the jumping mechanism for the reorientation of the O–H/O–D groups with a simple kinetic model (see Fig. 5.10). In this model the $\nu = 0 \rightarrow 1$ and $\nu = 1 \rightarrow 2$ absorption bands are described with Gaussian spectral profiles. These profiles are given by:

$$S_{mn}(\nu) = \exp\left(-4\ln 2(\nu - \nu_{c,mn})^2/\Delta_{mn}^2\right) , \tag{5.1}$$

with $\nu_{c,mn}$ the central frequency of the transition $\nu = m \rightarrow n$ and Δ_{mn} the full-width-at-half-maximum of this transition. For the $\nu = 0 \rightarrow 1$ transition $\nu_{c,01}$ = 2500 cm^{-1} and Δ_{01} = 156 cm^{-1}. For the $\nu = 1 \rightarrow 2$ transition we use the same spectral shape but shifted by the anharmonic shift of 150 cm^{-1}. Hence, $\nu_{c,12}$ = 2350 cm^{-1} and Δ_{12} = 156 cm^{-1}.

The spectra are divided into bins that each have a width of ∼5 cm^{-1}. The Gaussian spectral diffusion is described by letting the bins exchange population with their next-nearest neighbors with time constants that are given by:

$$k_{d,i\rightarrow i+1} = \begin{cases} k_g S_{mn}(\nu)_{i+1}/S_{mn}(\nu)_i & S_{mn}(\nu)_{i+1} < S_{mn}(\nu)_i \\ k_g & S_{mn}(\nu)_{i+1} > S_{mn}(\nu)_i \end{cases} . \tag{5.2}$$

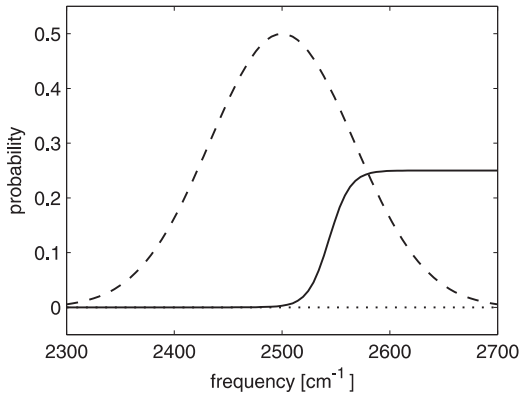

FIGURE 5.10. Illustration of the model used to describe the spectral dynamics of the anisotropy of the O–D stretch vibration of HDO:H_2O. The line shape is described as a Gaussian in which spectral diffusion takes place with a time constant τ_c of 700 fs. The figures shows the frequency dependence of the probability for reorientation. The reorientation is followed by a rapid frequency change (100 fs), as a result of which the oscillator can jump to any frequency position in the absorption band.

For each initial population distribution of the bins, the final spectral distribution of the bins will acquire the shape of the spectral function S_{mn}. The rate constant k_g is related to the time constant τ_c of the frequency correlation function via $1/k_g = \tau_c(1-\gamma)$ [20]. The parameter γ depends on the width of the Gaussian equilibrium distribution: $\gamma^2 = 1 - 4/w^2$, with w the half width at 1/e of the maximum of the equilibrium distribution. In our calculation we use $\tau_c = 700$ fs, w was equal to 19.5 bins, and thus γ=0.9947 and $1/k_g$=3.7 fs.

The fast frequency jumping is described by including an additional process in which every bin transfers population to all other bins. The rate of this transfer strongly depends on the frequency of the water molecule. We describe this frequency dependence with the following expression:

$$k_{j,mn}(r) = \frac{A}{1 + \exp\left[-b(\nu - \nu_{j,mn})\right]} \,. \tag{5.3}$$

A fit to the experimental data of Figs. 5.6–5.8 yields A=0.5×10^{13} s^{-1}, $b = 0.1$, and $\nu_{j,01} = 2543$ cm^{-1}. It should be noted that these parameters are the only fit parameters, the other parameters like τ_c and the homogenous line width are obtained from other experimental work. For the $1 \rightarrow 2$ transition we use the same frequency dependence shifted by the anharmonic shift of 150 cm^{-1}: $\nu_{j,12}$ = 2393 cm^{-1}.

The anisotropy decay is calculated by defining anisotropic and isotropic spectral changes $\Delta\alpha_{mn,\mathrm{ani}}(t,\nu)$ and $\Delta\alpha_{mn,\mathrm{iso}}(t,\nu)$ for both the $\nu = 0 \rightarrow 1$ and $\nu = 1 \rightarrow 2$ transitions. The anisotropic population change is defined as the population change probed by a probe pulse with a polarization parallel to that of

the pump, minus the population probed with a probe pulse with perpendicular polarization. The excitation by the pump pulse, which is assumed to be a Gaussian with a pulse duration of 0.2 ps, results in spectral holes $\Delta\alpha_{01,\mathrm{ani}}(t,\nu)$ and $\Delta\alpha_{01,\mathrm{iso}}(t,\nu)$ and to induced absorption bands $\Delta\alpha_{12,\mathrm{ani}}(t,\nu)$ and $\Delta\alpha_{12,\mathrm{iso}}(r,t)$. The frequency dependence of $\Delta\alpha_{mn,\mathrm{ani}}(t,\nu)$ and $\Delta\alpha_{mn,\mathrm{iso}}(t,\nu)$ follow from the central frequency and the spectral width of the pump pulse, the spectral profiles of the $\nu = 0 \rightarrow 1$ and $\nu = 1 \rightarrow 2$ transitions, and the homogeneous line width. The frequency dependence of the bands $\Delta\alpha_{12,\mathrm{ani}}(t,\nu)$ and $\Delta\alpha_{12,\mathrm{iso}}(t,\nu)$ are assumed to be the same as that of the holes $\Delta\alpha_{01,\mathrm{ani}}(t,\nu)$ and $\Delta\alpha_{01,\mathrm{iso}}(t,\nu)$, but shifted by the anharmonic shift of 150 cm^{-1}. The amplitudes are also taken to be the same.

Both the isotropic and anisotropic population distributions decay as a result of the vibrational relaxation while the frequency fluctuation processes lead to an exchange of population between the bins. In the slow Gaussian spectral diffusion process both the frequency-integrated isotropic and the anisotropic populations are conserved. In the fast frequency jumping process, only the frequency-integrated isotropic population is conserved, the anisotropic population decays. The jumping rates are taken two times larger for the isotropic population than for the anisotropic population, because the jumping can result both in the formation of a new hydrogen bond (reorientation) and in the reformation of the original hydrogen bond (no reorientation). The population changes at all times are calculated using a fourth-order Runge-Kutta scheme. The isotropic and anisotropic spectral changes are used to construct the frequency- and time-dependent anisotropy $R(t,\nu)$:

$$R(t,\nu) = \frac{\Delta\alpha_{01,\mathrm{ani}}(t,\nu) - \Delta\alpha_{12,\mathrm{ani}}(t,\nu)}{\Delta\alpha_{01,\mathrm{iso}}(t,\nu) - \Delta\alpha_{12,\mathrm{iso}}(t,\nu)} \tag{5.4}$$

The model includes the effects of the interference of the bleaching of the $0 \rightarrow 1$ transition with the induced $1 \rightarrow 2$ excited state absorption. This interference influences the anisotropy in the red wing of the absorption where the $0 \rightarrow 1$ bleaching overlaps with the $1 \rightarrow 2$ induced absorption. We find that the interference especially affects the observed anisotropy if the absorption band is excited in the blue wing. In that case, the bare early time $0 \rightarrow 1$ bleaching shows a strong decrease of the anisotropy with decreasing frequency due to the jumping. The $1 \rightarrow 2$ absorption shows the same frequency dependence as the $0 \rightarrow 1$ bleaching, but shifted to lower frequencies by the anharmonic shift of $\sim$150 cm^{-1}. Hence, in the red wing of the bleaching, the blue wing of the $1 \rightarrow 2$ absorption with a relatively high anisotropy is added to the red wing of the $0 \rightarrow 1$ bleaching that has a relatively low anisotropy. The resulting anisotropy is not the average of these anisotropy values, because the two signals have opposite signs. The addition will lead to a net bleaching signal with an even lower anisotropy than the bare $0 \rightarrow 1$ bleaching. Hence, the addition of the $1 \rightarrow 2$ absorption will further enhance the decrease in anisotropy going down from 2600 cm^{-1}. This behavior is very well reproduced by the model.

6 Water as a Molecular Hinge

We have studied the reorientational dynamics of isolated water molecules in a solution of N,N-dimethylacetamide (DMA). From the linear spectra, we find that the water in this solution forms double hydrogen bond connections to the DMA molecules resulting in the formation of DMA-water-DMA complexes. We use polarization-resolved mid-infrared pump-probe spectroscopy on the water molecule in these complexes to measure the depolarization of three distinct transition dipole moments, each with a different directionality relative to the molecular frame (O–H stretch in HDO, symmetric and asymmetric stretch normal modes in H_2O). By combining these measurements, we find that the system exhibits bimodal rotational dynamics with two distinct timescales: a slow (7±1 ps) reorientation of the entire DMA-water complex and a fast (0.5±0.2 ps) 'hinging' motion of the water molecule around the axis defined by the two connecting hydrogen bonds. Additionally, we observe an exchange of energy between the two normal modes of H_2O at a timescale of 0.8±0.1 ps and find that the vibrational excitation decays through the symmetric stretch normal mode with a time constant of 0.8±0.2 ps.

6.1 Introduction

Protein structure and stability are governed in large part by hydrophobic collapse and hydrophilic interactions with water. Single embedded water molecules can form bridges between oxygen atoms of different amide groups through double hydrogen bond formation [112]. In this way they can hold together biomolecular chains and assist in the formation of tertiary structures. Functionally, water plays an important role as a reactant at active sites or in molecular recognition through the unique directionality and adaptability of its hydrogen bonds [113]. It is clear that these bridging water molecules play an essential biological role and their properties must be carefully considered when studying the functional implications of protein structures.

The goal of this study is to model the molecular motions and energy dynamics that are exhibited by single water molecules bridged between two amide

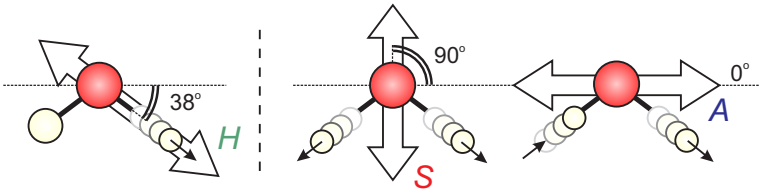

FIGURE 6.1. O–H stretching mode in HDO (left) and symmetric and asymmetric stretching modes in H_2O (middle and right). The big white arrows indicate the directions of the transition dipole moments and the small black arrows indicate the shifting of the hydrogen atoms.

groups. As a model system we use a dilute solution of water dissolved in N,N-dimethylacetamide (DMA). DMA possesses the same characteristic O=C–N group that is present in amides. The N–H groups have been replaced by aminomethyl groups (N–CH_3) to avoid spectral interference of the NH-stretching frequency on our measurements of the O–H stretching frequency of water. This replacement is expected to have negligible effects on the hydrogen bonding to the oxygen atom. By combining measurements of normal and partially deuterated water, we are able to deduce the three-dimensional rotational behavior of these water molecules as well as their energy transfer dynamics.

6.2 EXPERIMENT

The experiments were performed using two different samples. The first sample consisted of a mixture of HDO in D_2O, dissolved in N,N-dimethylacetamide (DMA). It was produced by mixing DMA, D_2O and H_2O with molar ratios DMA:D_2O:H_2O = 100:20:3. This sample is subsequently referred to as DMA-HDO. The second sample consisted of a solution of pure H_2O in DMA, with molar ratios DMA:H_2O = 100:3. This sample is subsequently referred to as DMA-H_2O. Both samples were contained in a static sample cell with an optical path length of 100 μm. A recent study on the structure of aqueous mixtures in DMA by Nishi *et al.* [145] showed that for molar fractions of DMA > 0.6, DMA clusters are dominant and very few (if any) water clusters remain. We use samples with DMA molar fractions > 0.8 so that we can safely assume that we were dealing with isolated water molecules.

As discussed in Section 4.1 polarization-resolved pump-probe spectroscopy can be used to determine the autocorrelation function of the transition dipole moment of pumped oscillators, i. e. the anisotropy decay. From a single correlation function we can determine the rate of reorientation, but not its direction. To obtain this directional information we combine the anisotropy decays of three distinct transition dipole moments of the water molecule, namely the symmetric and asymmetric stretch in H_2O and the O–H stretch in HDO. As is shown in Fig. 6.1, these three modes have different directions of their transition dipole

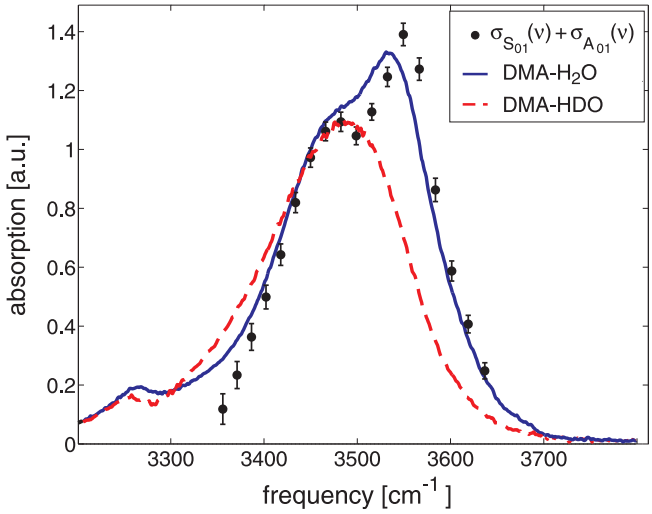

FIGURE 6.2. Linear absorption spectra of DMA-HDO and DMA-H_2O (mentioned in text), with their reference solvents subtracted. Also shown are the added $\nu = 0 \rightarrow 1$ spectra of symmetric ($\sigma_S(\nu)$) and asymmetric ($\sigma_A(\nu)$) stretch modes resulting from the global fit.

moments with respect to the molecular axis. The symmetric and asymmetric vibrational stretch modes of H_2O are orthogonal with respect to each other and have angles of 52 ° and 38 ° with respect to the O–H vibration of HDO, which is directed parallel to the stretching motion of the O–H oscillator. By combining the anisotropy decay data from these three modes we can identify the rotational motions of the embedded water molecules. The differences in anisotropy decay of the three modes will reveal the preferred direction(s) of reorientation. Furthermore, when the anisotropy of one or more modes does not decay back to zero, this implies that the orientation of the water molecule retains some long lasting, correlated direction with respect to its initial 'pumped' direction.

6.3 RESULTS

6.3.1 LINEAR SPECTRA

To isolate the absorption cross section of O–H oscillators in DMA-HDO and DMA-H_2O, we subtract reference samples consisting of the same constituents but without H_2O. For DMA-HDO, this is a mixture of DMA:D_2O with molar a ratio of 100:20 and for DMA-H_2O, this is a pure DMA sample. Fig. 6.2 shows the linear absorption spectra of DMA-HDO and DMA-H_2O, with the absorption of the reference samples subtracted. This means that the absorptions, shown here,

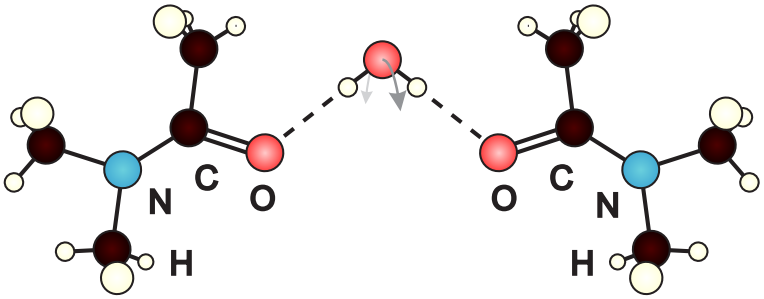

FIGURE 6.3. DMA-water complex: each water molecule is hydrogen bonded on either side to the oxygen atom of a DMA molecule. The arrows indicate the hinging motion.

are only due to the O–H oscillators in the sample. The subtracted background consists mainly of the absorption bands of DMA and overtone bands of D_2O. These bands have a much lower absorption cross-section than that of the O–H oscillator but are present due to their large excess in the sample. We can safely neglect this background in our pump-probe measurements because the pump-probe signal depends quadratically on the absorption cross-section.

The dashed line spectrum in Fig. 6.2 is that of HDO in DMA. It consists of a main absorption band, with a central frequency around 3460 cm^{-1}. The shape is slightly asymmetric, absorbing more strongly at lower frequencies. In addition to the O–H stretching mode, shown here, HDO also has an O–D stretching mode at a much lower frequency ($\sim$2550 cm^{-1}). Because the two frequencies are far apart, the mixing of these modes is minimal. Consequently in HDO it is possible to excite either the local O–D or the local O–H oscillator. The latter will subsequently be referred to as mode H (see Fig. 6.1).

When we compare the solid line spectrum of H_2O in DMA with that of HDO we find that there are *two* main absorption bands as opposed to one. Doubly hydrogen bonded H_2O has two equivalent O–H oscillators, that have the same reduced mass and experience similar potentials. These oscillators are strongly coupled and form two normal modes: symmetric and asymmetric, subsequently referred to as modes S and A (see Fig. 6.1). The S mode corresponds to the lower frequency peak in the spectrum and the A mode to the higher frequency peak. As we will see in the pump-probe experimental data, S and A are not pure normal modes but are anharmonically coupled by higher order terms in the vibrational potential, resulting in the exchange of vibrational energy.

A final important thing to note is the *absence* of a free O–H oscillator peak in these spectra which would normally be around 3670 cm^{-1}. This peak *does* show up if an apolar solvent, like carbon-tetra-chloride is added to the mixture (not shown here). The absence of this 'free' peak and the large excess of DMA over water leads us to conclude that all water molecules are doubly hydrogen bonded and form structures such as depicted in Fig. 6.3.

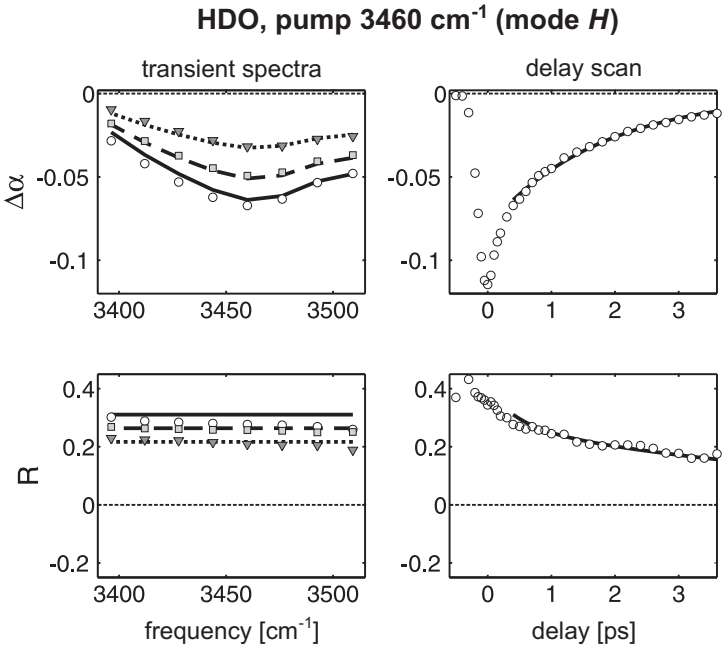

FIGURE 6.4. Left: isotropic (top) and anisotropic (bottom) transient spectra for HDO. The circles, squares and triangles are data points at pump-probe delays of 0.4, 0.8 and 1.6 ps, respectively. The solid, dashed and dotted lines are respective evaluations of the fitted model, described in the text, at these same times. Right: Delay-scan of the isotropic (top) and anisotropic (bottom) signal at 3460 cm^{-1}, circles are the data points and the line results from the fitted model.

6.3.2 NONLINEAR SPECTRA

Three different pump-probe data sets were recorded. The first is on a sample of DMA-HDO pumped at the frequency of mode H (3460 cm^{-1}). The second and third are both on DMA-H_2O, with the pump set to the frequencies of modes S (3450 cm^{-1}) and A (3550 cm^{-1}), respectively. For all samples we observe bleaching of the O–H stretch absorption bands and induced absorption at lower frequencies corresponding to $\nu = 1 \rightarrow 2$ transitions. In figures 6.4, 6.5 and 6.6 we show the bleaching parts of these spectra.

Upon inspection of the DMA-HDO data set, shown in Fig. 6.4, we note that its isotropic part can be described by an exponentially decaying, single spectrum, corresponding to the decay of $\nu = 1_H$ (first excited state of mode H). We observe no significant contribution of spectral diffusion (i. e. changes in spectral shape) for delays > 0.4 ps. The anisotropy is independent of frequency over the presented range and can be described by a single exponential, decaying towards a non-zero end-level. This end-level is an indication that the water molecule is not able to reorient freely but retains 'memory' of its initial pumped

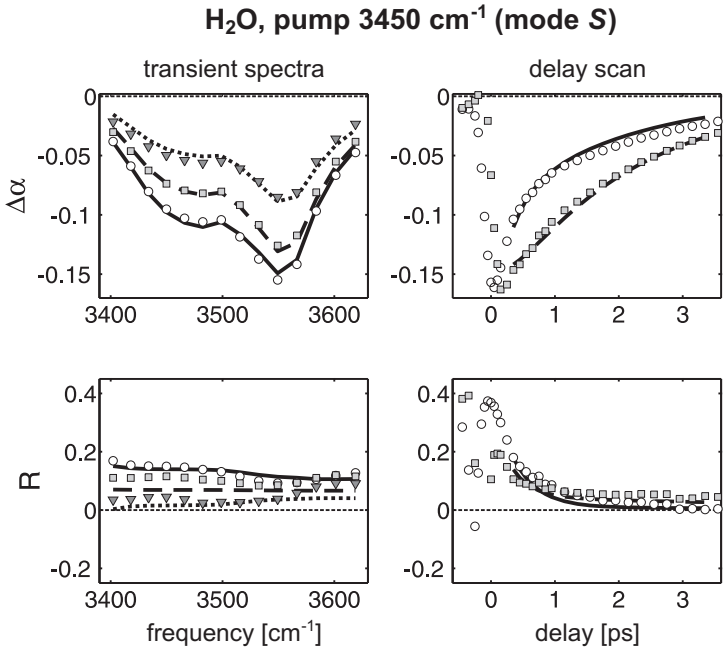

FIGURE 6.5. Left: isotropic (top) and anisotropic (bottom) transient spectra for H_2O where the pump frequency was set to 3450 cm^{-1} (resonant with the *symmetric* O–H stretch frequency). The circles, squares and triangles are data points of the absorption changes at pump-probe delays of 0.4, 0.8 and 1.6 ps, respectively. The solid, dashed and dotted lines are respective evaluations of the fitted model, described in the text, at these same times. Right: delay-scans of the isotropic (top) and anisotropic (bottom) signal at two frequencies. The circles and squares correspond to data points at 3450 and 3550 cm^{-1}, respectively. The solid and dashed lines are respective evaluations of the fitted model at these same frequencies.

direction for times > 10 ps.

Next, we compare the two data sets of DMA-H_2O shown in figures 6.5 and 6.6. The isotropic parts (top) display dynamics which indicate the presence of two underlying spectra, the amplitudes of which relate to the occupation of $\nu = 1_S$ and $\nu = 1_A$ (first excited states of modes S and A). These two experiments differ in the frequency (and power) of the pump beam and thus in the relative initial degree of excitation of the levels. In Fig. 6.5, $\nu = 1_S$ was initially predominantly excited and in Fig. 6.6, $\nu = 1_A$. Both experiments show a rapid exchange of energy between the normal modes, towards an equilibrium distribution, which looks similar to the linear spectrum. The equilibration is followed by a decay to zero.

In both Figs. 6.5 and 6.6 the anisotropy at the pump-frequency starts at a value of about 0.4, which is expected for $\hat{\mu}(0)\cdot\hat{\mu}(t) = 1$ (see Eq. (4.5)). However, at the frequency corresponding to the mode that was not initially pumped we

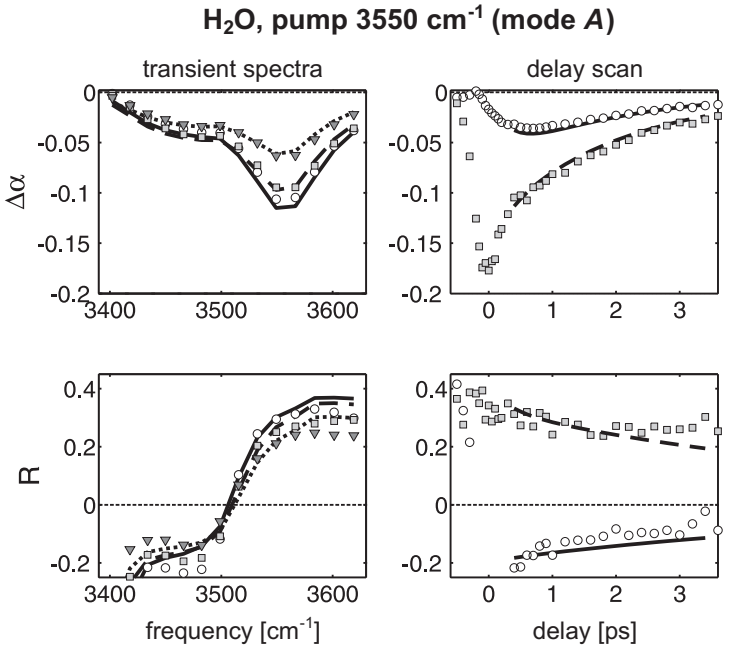

FIGURE 6.6. Same as Fig. 6.5 but with the pump frequency set at 3550 cm^{-1} (resonant with the *asymmetric* O–H stretch frequency)

find a significantly lower initial anisotropy. In the case of pumping the A mode (Fig. 6.6), we even see a negative anisotropy at frequencies corresponding to the S mode. This negative anisotropy shows that the two normal modes exchange vibrational energy. Because the modes have *perpendicular* transition dipole moments (shown in Fig. 6.1), every time a pumped mode S is converted to A and vice versa, the transition dipole moment is rotated over an angle of 90 °. If we substitute $\hat{\mu}(0) \cdot \hat{\mu}(t)$=0 in Eq. (4.5), we obtain a value of -0.2 for the anisotropy resulting from such a transfer. In the other data set, where the pump was set to mode S (Fig. 6.5), the initial anisotropy at mode A is higher than -0.2 because this anisotropy also contains a contribution of oscillators that are directly pumped in the A mode (which have an initial anisotropy of 0.4). Apparently, the pump pulse spectrum centered at the S mode overlaps with the low frequency wing of the spectrum of the A mode.

A final important observation is, that the anisotropy shows a much slower decay for the directly pumped A mode than for the directly pumped S mode. This suggests that the water molecules reorient in a way that maintains the direction of the transition dipole moment of A and not that of S. A compelling explanation for these observations is an anisotropic reorientation that prefers rotations around an axis, parallel to the transition dipole moment of A. This leads to a picture in which the water molecule hinges around its two hydrogen

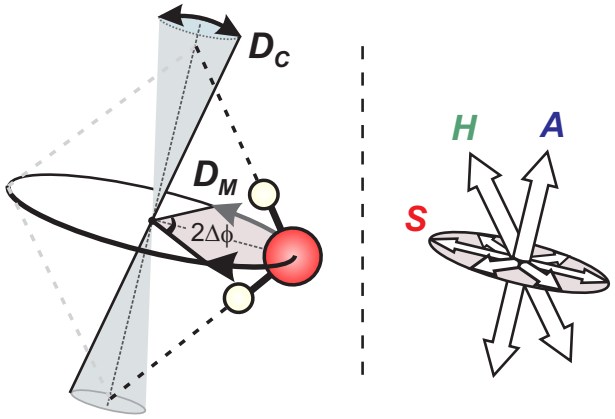

FIGURE 6.7. Left: Motion of the water molecule is split into two rotational diffusions: molecular rotations on a (partial) circle perpendicular to the transition dipole moment of A and rotations of the whole complex that spread out in a cone around it. Right: Transfer from mode S to A and vice versa is over 90° and so always into a plane perpendicular to the excitation. Subsequent rotations in this plane do not change the anisotropy further. The initial direction of mode H is shown for comparison.

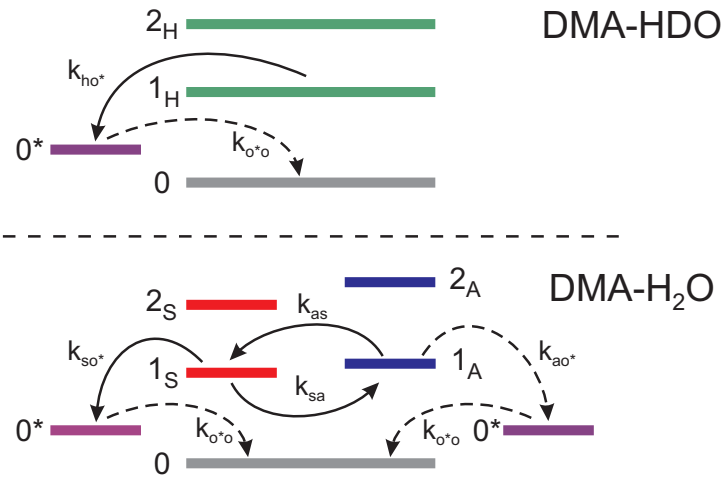

FIGURE 6.8. Energy level diagrams showing the transfer rates between levels. The top diagram shows DMA-HDO and the bottom one DMA-H_2O. Dashed arrows indicate relatively slow processes for the experiments discussed in this chapter.

bonds with DMA molecules, while the complex as a whole displays a much slower reorientation (see Fig. 6.7, left). This interpretation is also consistent with the slow anisotropy decay of the indirectly pumped population of both S and A. After transfer has occurred (from A to S or from S to A), any rotation in the plane perpendicular to the direction of A will maintain the angle of 90° between the pumped and probed transition dipole directions (see Fig. 6.7, right). As will be shown in the following section, our experimentally observed results can be reproduced quantitatively using a model based on this mechanism.

6.3.3 KINETIC MODEL

For a quantitative interpretation of the observations we first introduce the energy level diagrams of the two systems, DMA-HDO and DMA-H_2O in Fig. 6.8. The diagram also displays the relaxation channels of the first excited states.

For the HDO case, population is pumped into the first excited state of mode H, which can then decay to a thermalized ground state 0^* with rate k_{ho*}, and back to the original ground state 0 with rate k_{o^*o}. The occupation of levels 1_H and 0^* as a function of time, denoted $N_H(t)$ and $N_{0^*}(t)$, are described by the rate equations:

$$\frac{d}{dt}\begin{pmatrix} N_H(t) \\ N_{0^*}(t) \end{pmatrix} = \begin{bmatrix} -k_{ho^*} & 0 \\ k_{ho^*} & -k_{o^*o} \end{bmatrix} \begin{pmatrix} N_H(t) \\ N_{0^*}(t) \end{pmatrix} \tag{6.1}$$

In the case of H_2O, population is pumped into the first excited state of either S or A (denoted 1_S and 1_A respectively). Energy transfer between these two normal modes is governed by rate constants k_{sa} and k_{as} and the decay from levels 1_S and 1_A to thermal level 0^* by rate constants k_{so^*} and k_{ao^*}, respectively. The occupation of levels 1_S, 1_A and 0^*, denoted as $N_S(t)$, $N_A(t)$ and $N_{0^*}(t)$, is described by the rate equations:

$$\frac{d}{dt}\begin{pmatrix} N_S(t) \\ N_A(t) \\ N_{0^*}(t) \end{pmatrix} = \begin{bmatrix} (-k_{sa} - k_{so^*}) & k_{as} & 0 \\ k_{sa} & (-k_{as} - k_{ao^*}) & 0 \\ k_{so^*} & k_{ao^*} & -k_{o^*o} \end{bmatrix} \begin{pmatrix} N_S(t) \\ N_A(t) \\ N_{0^*}(t) \end{pmatrix} \tag{6.2}$$

These rate equations are solved using the matrix diagonalization method described in Section 4.4.1.

It is assumed that each occupied level has a characteristic associated transient spectrum. The spectra of levels 1_H, 1_S, and 1_A, denoted $\sigma_H(\nu)$, $\sigma_S(\nu)$, and $\sigma_A(\nu)$, consist of decreased absorption bands ($\Delta\alpha(\nu) < 0$), due to $\nu = 0 \rightarrow 1$ ground-state bleaching and $\nu = 1 \rightarrow 0$ stimulated emission, and increased absorption bands ($\Delta\alpha(\nu) > 0$), due to $\nu = 1 \rightarrow 2$ induced absorption. The spectra $\sigma_S(\nu)$ and $\sigma_A(\nu)$ may also include the effects of mode-to-mode coupling, i. e. the influence of excitation of the S mode on the frequency of the A mode and vice versa. The spectrum σ_{0^*} of level 0^* corresponds to a change in the linear absorption spectrum that results from heating of the sample. Rate constant k_{o^*o} corresponds to the rate at which heat dissipates away from the focus and is negligibly small, because this process happens on much longer timescales than

under investigation here. Because of this, $\sigma_{0^*}(\nu)$ may be equated to the absorption difference observed on long timescales (100 ps). Hence, the population $N_{0^*}(t)$ is 0 for $t = 0$ and 1 for $t \to \infty$. From the fit, which is described later, we furthermore find that $k_{ao^*} = 0$. This implies that the predominant relaxation channel of mode A is transfer of vibrational energy to mode S, from which relaxation to 0^* occurs.

With the aforementioned assumption that each occupied level corresponds with a single spectrum, the isotropic data can be described by the summed products of the time evolution of these levels and their respective spectra (see also Section 4.2):

$$\Delta\alpha_{HDO,iso}(t,\nu) = N_H(t)\sigma_H(\nu) + N_{0^*}(t)\sigma_{0^*}(\nu) \quad (6.3)$$

$$\Delta\alpha_{H_2O,iso}(t,\nu) = N_S(t)\sigma_S(\nu) + N_A(t)\sigma_A(\nu) + N_{0^*}(t)\sigma_{0^*}(\nu) \quad (6.4)$$

The difference between the two data sets of DMA-H_2O is assumed to arise purely from differences in the initial occupation: $N_S(0)$ and $N_A(0)$.

6.3.4 ANISOTROPY MODELING

A description of the anisotropy dynamics requires the inclusion of the effects of transfer and (limited) anisotropic rotations. First, we split the populations of S and A that were either excited directly by the pump or excited indirectly as a result of intramolecular transfer. Second, we break up the rotation of the water molecule into two motions (see Fig. 6.7): reorientational diffusion D_M of the water molecule within the complex and reorientational diffusion D_C of the DMA-water complex itself. Finally, we assign end-levels to the anisotropy of the water molecule in the complex, reflecting its limited range of reorientation. We thus define the following set equations describing the temporal evolution of the anisotropies:

$$R_H(t) = [R_{f,H} + (R_{i,H} - R_{f,H})\exp(-D_M t)] \cdot \exp(-D_C t) \quad (6.5)$$

$$R_{SS}(t) = [R_{f,SS} + (R_{i,SS} - R_{f,SS})\exp(-D_M t)] \cdot \exp(-D_C t) \quad (6.6)$$

$$R_{SA}(t) = [R_{f,SA} + (R_{i,SA} - R_{f,SA})\exp(-D_M t)] \cdot \exp(-D_C t) \quad (6.7)$$

$$R_{AS}(t) = [R_{f,AS} + (R_{i,AS} - R_{f,AS})\exp(-D_M t)] \cdot \exp(-D_C t) \quad (6.8)$$

$$R_{AA}(t) = [R_{f,AA} + (R_{i,AA} - R_{f,AA})\exp(-D_M t)] \cdot \exp(-D_C t) \quad (6.9)$$

Where the anisotropy of level H, in DMA-HDO, is given by $R_H(t)$. The initial and final anisotropy levels of the water molecule, in the reference frame of the complex, are given by $R_{i,H}$ and $R_{f,H}$. For the part between square brackets, these values are obtained at $t = 0$ and $t \to \infty$, respectively. This 'molecular' anisotropy, diffusing with rate D_M, is then multiplied with the anisotropy decay of the whole complex, diffusing with rate D_C. The anisotropy of levels S and A, in DMA-H_2O, is given by $R_{XY}(t)$, where X is the currently excited mode and Y is the initially excited mode (either S or A). In this way we take into account the possibility of transfer between modes. Values for $R_{i,XY}$ are 0.4 if

$X = Y$ and -0.2 if $X \neq Y$. The same rotational diffusion rates, D_M and D_C, must hold for all three experiments.

Before we can determine the values of the final anisotropy levels, $R_{f,XY}$, we must make an assumption about the range of motions of the water molecules inside the complex. Because of considerations given earlier, we assume a (partially) circular motion around the axis parallel with the asymmetric stretch mode (see Fig. 6.7). Using Eq. (4.5) with $t \rightarrow \infty$, we can evaluate some end-levels for this motion and find: $R_{f,SA} = -0.2$, $R_{f,AS} = -0.2$ and $R_{f,AA} = 0.4$. The values for $R_{f,H}$ and $R_{f,SS}$ are dependent on the angle $\Delta\phi$ over which the molecule diffuses within the circle, as explained in Appendix 6.6. This angle will be left as a free parameter in the model, but will have to give consistent values for $R_{f,H}$ and $R_{f,SS}$.

6.3.5 SPECTRAL SHAPES

By expanding Eq. (6.3) we can relate the measured values for $\Delta\alpha_{HDO,iso}(t,\nu)$, $\Delta\alpha_{HDO,\parallel}(t,\nu)$ and $\Delta\alpha_{HDO,\perp}(t,\nu)$ to the population of mode H and its corresponding anisotropy:

$$\begin{pmatrix} N_H(t) \\ N_{H,\parallel}(t) \\ N_{H,\perp}(t) \end{pmatrix} \begin{pmatrix} \sigma_H(\nu) \end{pmatrix} = \begin{pmatrix} \Delta\alpha_{HDO,iso}(t,\nu) \\ \Delta\alpha_{HDO,\parallel}(t,\nu) \\ \Delta\alpha_{HDO,\perp}(t,\nu) \end{pmatrix} \tag{6.10}$$

where $\sigma_H(\nu)$ is the absorption cross-section of mode H and we have defined the parallel and perpendicular populations for mode H as

$$N_{H,\parallel}(t) \equiv [1 + 2R_H(t)] \cdot N_H(t) \tag{6.11}$$

$$N_{H,\perp}(t) \equiv [1 - R_H(t)] \cdot N_H(t) \tag{6.12}$$

respectively.

We use the kinetic model of Eq. (6.1) and the anisotropy decay from Eq. (6.5) to find values for $N_H(t)$, $N_{H,\parallel}(t)$ and $N_{H,\perp}(t)$ as a function of the parameters for energy relaxation and rotational diffusion. We thus obtain three equations that all depend on $\sigma_H(\nu)$. This matrix equation can be solved using linear regression techniques to yield the best fitting spectral shape $\sigma_H(\nu)$. The advantage of this technique is that the spectrum σ_H follows directly from the data and model parameters.

The same expansion can be done for DMA-H_2O (Eq. (6.4)) yielding

$$\begin{pmatrix} N_S(t) & N_A(t) \\ N_{S,\parallel}(t) & N_{A,\parallel}(t) \\ N_{S,\perp}(t) & N_{A,\perp}(t) \end{pmatrix} \begin{pmatrix} \sigma_S(\nu) \\ \sigma_A(\nu) \end{pmatrix} = \begin{pmatrix} \Delta\alpha_{H2O,iso}(t,\nu) \\ \Delta\alpha_{H2O,\parallel}(t,\nu) \\ \Delta\alpha_{H2O,\perp}(t,\nu) \end{pmatrix} \tag{6.13}$$

with

$$N_{S,\parallel}(t) \equiv [1 + 2R_{SS}(t)] \cdot N_{SS}(t) + [1 + 2R_{SA}(t)] \cdot N_{SA}(t) \tag{6.14}$$

$$N_{A,\parallel}(t) \equiv [1 + 2R_{AS}(t)] \cdot N_{AS}(t) + [1 + 2R_{AA}(t)] \cdot N_{AA}(t) \tag{6.15}$$

$$N_{S,\perp}(t) \equiv [1 - R_{SS}(t)] \cdot N_{SS}(t) + [1 - R_{SA}(t)] \cdot N_{SA}(t) \tag{6.16}$$

$$N_{A,\perp}(t) \equiv [1 - R_{AS}(t)] \cdot N_{AS}(t) + [1 - R_{AA}(t)] \cdot N_{AA}(t) \tag{6.17}$$

where $N_{XY}(t)$ is population in state X that was initially pumped in state Y.

In this case we want to find the best *two* fitting spectra $\sigma_S(\nu)$ and $\sigma_A(\nu)$. We are helped by the fact that there are two separate and distinct DMA-H_2O data sets. We expand matrix Eq. (6.13) vertically to include in one equation both models and data sets. The models differ only in their initial conditions for the directly pumped populations, $N_{SS}(0)$ and $N_{AA}(0)$. Initial indirect populations $N_{SA}(0)$ and $N_{AS}(0)$ are zero by definition. From Eq. (6.13) it may be deduced that the normalization of either the initial populations or the total cross-section of the spectra is arbitrary to choose (only their product matters). This means that only the relative values of these initial populations are important and we may describe them by two fraction parameters (plus a scaling parameter between experiments):

$$N_{SS,\,\mathrm{pump@}S}(0) = f_S \tag{6.18}$$
$$N_{AA,\,\mathrm{pump@}S}(0) = 1 - f_S \tag{6.19}$$
$$N_{SS,\,\mathrm{pump@}A}(0) = r\,(1 - f_A) \tag{6.20}$$
$$N_{AA,\,\mathrm{pump@}A}(0) = r\,(f_A) \tag{6.21}$$

The values for f_S and f_A are the fractions for the directly pumped populations in levels 1_S and 1_A compared to the total excited population, for corresponding pump frequencies at modes S and A, respectively. The value for r is just a scaling parameter reflecting the ratio of total excited population between the two experiments, which will depend on relative pump intensity and cross-section.

We are then left with a total of 6 equations (isotropic, parallel and perpendicular for both experiments) to find the two spectra that best conform to data and model as a function of energy transfer and rotational diffusion rates.

6.3.6 FIT RESULTS

To avoid any influence of coherent artifacts on the modeling, we start the data analysis at 0.4 ps. For this time interval, all data is well described by the evolution of time-independent spectra, which indicates that the effects of spectral diffusion are negligible. Heating effects, caused by the shifting of absorption bands after decay and thermalization, were subtracted by an ingrowing end-spectrum (σ_{0^*}) which has the shape observed at 100 ps and time dynamics corresponding to the presented model.

The parameters entering the model are obtained by a global fitting routine that minimizes the χ^2 function (see also Section 4.2.2)

$$\chi^2(\vec{p}) = \sum_{\xi=1}^{3} \left(\frac{\Delta\alpha_{\mathrm{model}}(t,\nu,\vec{p}) - \Delta\alpha_{\mathrm{data}}(t,\nu)}{\epsilon_{\mathrm{data}}(t,\nu)} \right)^2 \tag{6.22}$$

as a function of parameters $\vec{p}$. $\Delta\alpha_{\mathrm{data}}(t,\nu)$ represents one of the three data sets of HDO and H_2O, with pump frequencies set at modes S and A, and $\epsilon(\Delta\alpha_{\mathrm{data}}(t,\nu))$ are the respective standard deviation errors on this data set. $\Delta\alpha_{\mathrm{model}}(t,\nu,\vec{p})$ represent the corresponding model defined by Eqs. (6.5)–(6.21).

TABLE I. **Fit parameters**

parameter	value	parameter	value
$k_{ho^*}^{-1}$	1.8 ± 0.2 ps	D_M^{-1}	0.5 ± 0.2 ps
k_{sa}^{-1}	0.8 ± 0.1 ps	D_C^{-1}	7 ± 1 ps
k_{as}^{-1}	0.7 ± 0.1 ps	$\Delta\phi$	52 ± 8 °
$k_{so^*}^{-1}$	0.8 ± 0.2 ps	f_S	0.69 ± 0.08
$k_{ao^*}^{-1}$	>15 ps	f_A	1.01 ± 0.06
$k_{o^*o}^{-1}$	>100 ps		

The results of the fit are shown Table I and Figs. 6.4–6.6. We find good simultaneous agreement between the data points and the fitted model (lines) for both the isotropic and anisotropic spectra. The spectra for the S and A modes, shown in Fig. 6.9, have the expected shapes with a bleaching/stimulated emission and a red-shifted induced absorption. Furthermore the added $\nu = 0 \rightarrow 1$ transitions for modes S and A agree nicely with the linear spectrum, shown in Fig. 6.2.

The fitted anisotropies of the directly and indirectly pumped populations S and A, and that of population H, are shown in Fig. 6.10. These anisotropies, defined in Eqs. (6.5)–(6.9), are used in Eqs. (6.10)–((6.17) to construct the anisotropy dynamics shown in Figs. 6.4, 6.5, and 6.6. The directly pumped population in mode S (R_{SS}) shows a much faster anisotropy decay than the directly pumped population in mode A (R_{AA}). The anisotropies of the indirectly pumped population S and A (R_{SA} and R_{AS}) show an initial value of -0.2, corresponding to transfer over a 90 ° angle, and both decay with the same time constant as the whole complex (i. e. R_{AA}). This behavior is illustrated on the right hand side of Fig. 6.7 and follows from the fact that after transfer, the rotational diffusion D_M does not change the anisotropy for either case R_{SA} or R_{AS}: only D_C contributes. All curves are consistent with the proposed model of a fast rotation of the water molecule around the axis parallel to A (see Fig. 6.1) and a slow reorientation of the DMA-water complex. As expected, the anisotropy decay curve of R_H is in between that of R_{SS} and R_{AA}.

From Table I we note that the O–H stretch mode in DMA-HDO decays with a time constant of $k_{ho^*}^{-1} = 1.8 \pm 0.2$ ps, which is about twice as long as that of the S mode in DMA-H_2O ($k_{so^*}^{-1}$) at 0.8 ± 0.1 ps. Direct decay of the A mode ($k_{ao^*}^{-1}$) is much slower and happens on timescales >15 ps. Transfer between the two normal modes (k_{sa}^{-1} and k_{as}^{-1}) happens at 0.8 ± 0.1 ps for S to A and slightly shorter, 0.7 ± 0.1 ps, for A to S. Dissipation of heat (k_{o^*o}) is found to be negligible in this experiment at timescales >100 ps.

With respect to the rotational diffusion, we find two very different timescales for the rotation of the water molecule within the complex and for the complex as a whole: $D_M^{-1} = 0.5 \pm 0.2$ ps and $D_C^{-1} = 7 \pm 1$ ps respectively. From the anisotropy end-levels, $R_{f,H}$ and $R_{f,SS}$, the standard deviation angle over which the water rotates within the complex ($\Delta\phi$) is determined to be 52 ± 8 °. This

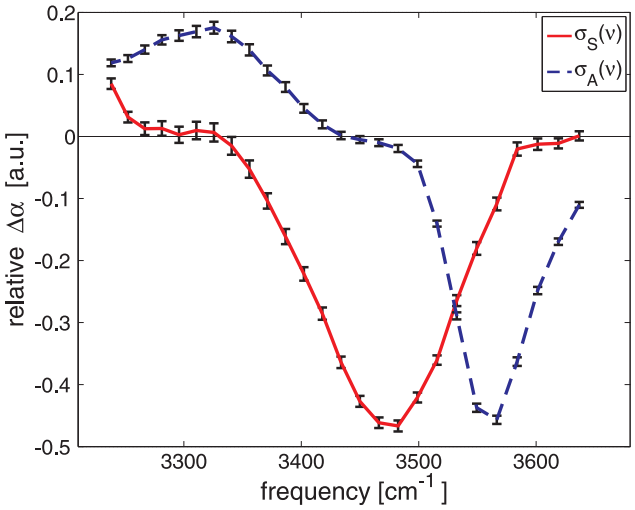

FIGURE 6.9. Decomposed spectra of the relative absorption changes corresponding to the symmetric and asymmetric O–H stretch vibrations at measured frequencies. Solid and dashed lines are used, as a guide to the eye, to connect these points for S and A, respectively.

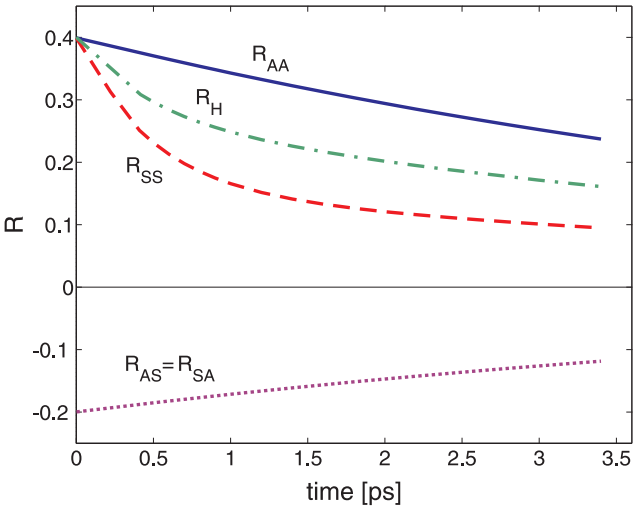

FIGURE 6.10. Fitted anisotropy curves of mode H in DMA-HDO and of the directly and indirectly pumped populations S and A in DMA-H_2O, described in the text and used in the anisotropic parts of figures 6.4, 6.5, 6.6.

angle gives consistent end values for the anisotropies of these two modes.

For f_S and f_A we find values of 0.7 and 1, respectively, which implies that the A mode was exclusively excited when the pump was at A and that 70% was excited in mode S when the pump was at S (and 30% in mode A).

6.4 DISCUSSION

6.4.1 RELAXATION

For the vibrational lifetime of DMA-HDO we measure a time constant of 1.8 ± 0.2 ps. In the case of DMA-H_2O, we find that the vibrational excitation decays almost exclusively through the symmetric stretch normal mode ($k_{so^*} \gg k_{ao^*}$) with a time constant of 0.8 ± 0.2 ps. To compare the vibrational lifetime of DMA-H_2O to that of DMA-HDO, we calculate the decay time of the (equilibrated) population $S+A$. In this way we find a time constant of 2.0 ± 0.2 ps for the vibrational relaxation of the O–H oscillators in DMA-H_2O.

These findings can be explained if we consider the overtone of the bending mode as the principal accepting mode for these vibrations. We expect a favorable coupling between the overtone of the HOH bending mode and the S mode because they both possess the same symmetry. This is in contrast with the A mode, which possesses different symmetry and is also more separated in frequency from the bending mode overtone than the S mode. For the case of DMA-HDO we can think of the vibration as being composed of equal symmetric and asymmetric parts that only constructively interfere on the O–H vibration (and destructively on the O–D). Only the symmetric part of this vibration couples to the bending mode which is why the O–H in HDO relaxes about two times slower than the pure S mode in DMA-H_2O.

We do not explicitly observe effects associated with mode-to-mode coupling between the bending mode and the symmetric stretching mode. The influence of this coupling in neat water has been studied by Lindner *et al.* [84] where it was found that excitation of the bending mode leads to a blue shift of the associated O–H stretch frequency. However, this shift is small and in fact quite similar in nature to the effects associated with heating. In the current experiment it may therefore not be possible to distinguish between these two effects. In addition, the accumulation of population in the bending mode may be low because it rapidly relaxes to librations and other low-frequency modes.

The vibrational lifetimes we find for HDO (1.8 ± 0.2 ps) and H_2O (2.0 ± 0.2 ps) in DMA are both shorter than the value of 6.3 ± 0.3 ps that was found in a previous study [11] on comparable systems of HDO-acetone and H_2O-acetone clusters in CCl_4. This difference in vibrational lifetime agrees with the notion that the frequency red-shift of the O–H stretch vibration of water-DMA (3450 cm^{-1}) is larger than that of water-acetone dissolved in CCl_4 (3520 cm^{-1}). For many hydrogen-bonded systems the vibrational lifetime T_1 can be related to the red-shift $\delta\nu_{OH}$ of the O–H stretch frequency relative to the gas phase

frequency by [96, 166]:

$$T_1 \propto (\delta\nu_{OH})^{-1.8} \tag{6.23}$$

There are several mechanisms that can account for the decrease of T_1 with increasing red-shift. In one mechanism, the decrease of T_1 is explained from the strengthening of the hydrogen-bond interaction. When the hydrogen bond gets stronger, the anharmonic coupling between this bond and the O–H stretch vibration also increases, which leads to a faster relaxation, provided the hydrogen bond forms one of the accepting modes. The decrease of T_1 with increasing red-shift can also be caused by the decrease of the energy mismatch between the O–H stretch vibration and the overtone of the bending mode. For instance, in a theoretical study on the vibrational relaxation of HDO dissolved in D_2O it was shown that this effect causes the relaxation to become slower with increasing temperature [77].

Using expression (Eq. (6.23)), the lifetime of the O–H stretch vibration is expected to decrease by a factor of 2 going from water-acetone in CCl_4 to water-DMA, which is somewhat less than the observed factor of 3.3. This latter difference may find its origin in the fact that the water-acetone system is surrounded by an apolar solvent (CCl_4). The weak interaction with this solvent will frustrate an effective compensation of the energy mismatch between the O–H stretch vibration and its main accepting mode(s), thus decelerating the relaxation.

6.4.2 Intramolecular energy transfer

Transfer between the two normal modes happens on timescales of 0.7±0.1 and 0.8±0.2 ps for $\nu = 1_S \rightarrow 1_A$ and $\nu = 1_A \rightarrow 1_S$, respectively. These transfer times are comparable to those found in the previously mentioned acetone-water study [11], where intramolecular transfer times were about 1 ps. The timescales in the water-acetone system were associated with the breaking and reforming of hydrogen bonds, converting between single and double hydrogen bound complexes. In this study, however, we do not observe a complete breaking of hydrogen bonds as reported in acetone, presumably because DMA forms more strongly bound hydrogen bond complexes than acetone. From the fact that we observe separate normal modes in the linear spectrum, which also fit with our pump-probe spectra (see Fig. 6.2), we conclude that the two hydrogen bonds must be nearly equivalent for most molecules.

6.4.3 Rotational diffusion

The timescale we associate with reorientation of the complex, ($D_C^{-1} = 7 \pm 1$ ps), is similar to those reported in previous studies on water-acetone in CCl_4 [53] (6.3±0.3 ps) and water-DMSO [167] (5 ps), although these reorientations were interpreted as being due to the water molecule alone. The rotational correlation time τ_r of a spherical particle in a solvent with viscosity μ_s may be approximated

using the Stokes-Einstein-Debye equation:

$$\tau_r = \frac{\mu_s V}{k_B T} \tag{6.24}$$

where V is the solvated volume, k_B is the Boltzman constant and T the absolute temperature. From this equation, we expect the reorientation time of these complexes to be roughly proportional to the solvated volume times the viscosity of the surrounding solvent. DMA and DMSO have very similar viscosities (both $\mu_s \approx 2 \times 10^{-3}$ Pa·s @ 25 °C and from their respective molecular structures, we expect the solvated volume V of the DMSO complex to be slightly smaller than that of DMA. These values are consistent with the slightly faster rotational diffusion of the DMSO-water complex compared to the DMA-water complex. The water-acetone-CCl_4 system, unfortunately, can not be compared in this way because it is not clear what the size of the rotating water-acetone clusters is.

Besides the slow reorientation of the complex, we observe a much faster additional reorientation with a timescale $D_M^{-1} = 0.5 \pm 0.2$ ps. The fact that $D_C^{-1} \gg D_M^{-1}$ shows that the system exhibits two very distinct rotations. As further confirmation, we find an angle of $\Delta\phi = 52 \pm 8\,^\circ$ that is consistent for the end-levels measured in *both* the O–H stretch in HDO and the symmetric stretch in H_2O. The magnitude of this angle implies that the water molecule in the DMA complex rotates approximately within a quarter circle around its hydrogen bonded equilibrium position. From this magnitude we may calculate with Eq. (6.27) that the angular restoring force constant κ_M, exhibited by the hydrogen bonds, is approximately $5 \cdot 10^{-21}$ J rad^{-2}.

6.4.4 IMPLICATIONS

Several interesting properties of water in interaction with amide-like structures were measured that may help in the modeling of configurations involving water and amide groups (such as proteins). We see from our linear spectrum and indirectly from the measured anisotropic rotational diffusion rates that the water molecules in this experiment form hydrogen bond connections on both sides to DMA molecules. Furthermore, the red-shifted O–H frequency of water in DMA indicates that these hydrogen bonds are relatively strong compared to for example water in acetone. This suggests that water can act as a sort of extension cord, creating hydrogen bond connections between different amide groups that could otherwise be sterically hindered. This study quantifies experimentally the limited range of motion (in a quarter circle) that the water molecule exhibits in such connections. It is clear that this water connection is not cylindrically symmetric but has a certain directional preference, likely such that the oxygen and hydrogen atoms partaking in either of the hydrogen bonds (O–H$\cdots$O) lie on a single line in the direction of a lone pair on the oxygen of DMA. This means that the rearrangement of amide groups connected by a water molecule has to involve also the appropriate directional reorientation of the connecting

C=O groups. An important consequence is that the protein-water chain will exhibit very specific structural rigidity.

6.5 CONCLUSION

We have studied the energy transfer and reorientational dynamics of water, hydrogen bonded in a complex of two DMA molecules, using polarization-resolved mid-infrared spectroscopy. We found that the vibrational energy relaxation for H_2O occurs mainly via the symmetric stretch normal mode with a time constant of 0.8 ± 0.2 ps. The relaxation of the equilibrated symmetric and asymmetric normal modes in DMA-H_2O was found to occur with a time constant of 2.0 ± 0.2 ps which is comparable to the relaxation time found for the O–H vibration in HDO (1.8 ± 0.2 ps). We attributed these findings to a favorable coupling between the symmetric stretch normal mode and the overtone of the bending mode in H_2O. For the energy transfer *between* the symmetric and asymmetric normal modes in H_2O we found time constants of 0.8 ± 0.1 and 0.7 ± 0.1 ps, which we associated with fluctuations in the hydrogen bond strength between the water and DMA complex. Rotational diffusion of water in DMA was found to be mainly limited to hinging motions over an angle of $52 \pm 8\,^\circ$ around the connecting hydrogen bonds on a timescale of 0.5 ± 0.2 ps. Additionally, an overall reorientation time of 7 ± 1 ps was found and associated with rotational diffusion of the water-DMA complex as a whole. The measured properties of water in interaction with amide-like structures can help in the understanding of its role in processes such as the folding of proteins.

6.6 APPENDIX: ANISOTROPY OF A HINGE

We determine the anisotropy end-levels $R_{f,H}$ and $R_{f,SS}$ as a function of the angular distribution over the partial circle shown in Fig. 6.7. We assume that the water molecule experiences a restoring force proportional to the displacement angle ϕ from its equilibrium position:

$$F_M = -\kappa_M \phi \tag{6.25}$$

with F_M the molecular restoring force and κ_M the associated force constant. This force may be equivalently described by the potential

$$V_M = -\int F_M d\phi = \frac{1}{2}\kappa_M \phi^2 \tag{6.26}$$

which, using Boltzman statistics, leads to a Gaussian distribution:

$$\rho_M = \exp(-V_M/k_B T) \equiv \exp(-\phi^2/2(\Delta\phi)^2) \tag{6.27}$$

where we implicitly define $\Delta\phi = \sqrt{k_B T/\kappa_M}$ as the standard deviation angle of the distribution. The Boltzman constant, k_B, is valued $1.38 \cdot 10^{-23}$ J K^{-1} and T is the absolute temperature.

We now evaluate Eq. (4.5) for $t \to \infty$ by integrating over all possible end states that are weighted with probability distribution ρ_M:

$$R(t \to \infty) = \frac{2}{5}\langle P_2(\hat{\mu}(0) \cdot \hat{\mu}(\infty)\rangle \tag{6.28}$$

$$= \frac{\int_{-\pi}^{\pi} \rho_M \left[3/5(\hat{\mu}(0) \cdot \hat{\mu}(\phi))^2 - 1/5\right] d\phi}{\int_{-\pi}^{\pi} \rho_M \, d\phi} \tag{6.29}$$

The last line contains the inner product between the transition dipole moments as a function of angle ϕ. This angle ϕ is defined as the angle over which the water molecule is rotated within the complex (around the axis parallel to mode A). As the water molecule rotates, so do the transition dipole moments for modes H and S (but not of A). Both these rotations can be parameterized as a function of angle ϕ using a cone with half angle α. This angle α is equal to the angle between the direction of the transition dipole moments $\hat{\mu}(\phi)$ and the axis around which it rotates (i. e. the direction of mode A). From the geometric properties of the water molecule we find that for mode H this angle is $38\,^\circ$ and for mode S it is $90\,^\circ$. Finally, we project the unit vectors $\hat{\mu}(\phi)$) and $\hat{\mu}(0)$ (which both lie on the surface of the cone) onto each other, and derive the following expression for the inner product:

$$\hat{\mu}(0) \cdot \hat{\mu}(\phi) = \cos^2(\alpha) + [1 - \cos^2(\alpha)] \cos(\phi) \tag{6.30}$$

This expression is substituted into Eq. (6.29) using $\alpha = 38\,^\circ$ and $\alpha = 90\,^\circ$ to find values for $R_{f,H}$ and $R_{f,SS}$, respectively. The integration was performed numerically as a function of parameter $\Delta\phi$ to yield the corresponding values for $R_{f,H}$ and $R_{f,SS}$ that best fit the data.

7 Spectral Diffusion of Water near Bromide Ions

We have studied the hydrogen-bond dynamics of solutions of LiBr and NaBr in isotopically diluted water (2% HDO:D_2O) with femtosecond spectral hole-burning spectroscopy. We study the frequency fluctuations of the O–H stretch vibrations of the HDO molecules and observe spectral dynamics with time constants of 0.8±0.1 ps and 4.3±0.3 ps. The slow process we assign to the hydrogen-bond fluctuations of the O–H$\cdots$$Br^-$ hydrogen bonds of the hydration shell of the Br^- anion. We find that the time scale of the hydrogen-bond fluctuations of the hydration shell of Br^- is independent of the nature of the cation and the concentration.

7.1 Introduction

The fluctuations of the hydrogen-bond network of liquid water play an essential role in many chemical processes occurring in this liquid [42, 56]. Hence, there exists a strong interest in the rate and nature of these fluctuations in the hydration shells of ions and molecules. Nonlinear vibrational spectroscopic studies of the hydrogen-bond dynamics of water make use of the fact that the frequency and absorption cross-section of the high-frequency intramolecular O–H stretch vibrations of the water molecules are sensitive probes of the strength of the intermolecular hydrogen-bond interactions. A strengthening of the hydrogen bond that is donated by the O–H group to another molecule or ion, leads to a decrease of the frequency of the O–H stretch vibration [95]. Hence, fluctuations in the strengths of the local donated hydrogen bonds are directly observable as time-dependent frequency shifts of the O–H stretch vibrations. These spectral fluctuations can be characterized by a frequency-frequency correlation function (FFCF) $\langle \delta\omega(t)\delta\omega(0)\rangle$ (Section 2.4.4).

Ions have a strong effect on the hydrogen-bond structure of liquid water. The strong electric fields exerted by the ions disrupt the local hydrogen-bond structure and orient nearby water molecules depending on their charges, leading to the formation of so-called hydration shells. For solutions containing halide anions, new types of hydrogen bonds between water and the ions are formed. These O–H$\cdots$$X^-$ (X^-= F^-, Cl^-, Br^-) hydrogen bonds are directional in character [14,154], which means that the O–H bond and the O$\cdots$$X^-$ hydrogen-bond

coordinates are collinear.

In earlier work of our group, using two-color pump-probe spectroscopy on the hydrogen-bond fluctuations of the hydration shells of ions, it was found that the time constants of the decay of the FFCF of the hydration shells were quite long (10–25 ps [63, 64]. In a recent study by Park *et al.* [114] the frequency fluctuation dynamics of NaBr solutions were measured with two-dimensional vibrational echo spectroscopy. The FFCF measured for solutions of different concentration were fitted with three time constants that represent various contribution to the structural evolution of the water-ion systems. The slowest component was observed to show the strongest slowing down with concentration, reaching a maximum value of 4.8 ps for a solution of 6 M NaBr. The slowing down of this component was assigned to a decrease of the rate of the global structural rearrangement of the liquid that follows from the increasing number of hydrogen bonds to Br^- ions. Here we present a study of the hydrogen-bond fluctuations of solutions containing bromide ions using femtosecond infrared spectral hole-burning spectroscopy. In comparison to the earlier femtosecond infrared studies [63, 64, 114, 115] we measure the spectral dynamics at higher concentrations and over a longer time scale. As a result, we obtain detailed and highly specific information on the hydrogen-bond dynamics of the hydration shells of the Br^- ions. We study the dependence of these dynamics on the concentration and the nature of the cation. We discuss the results in relation to earlier experimental and theoretical work on this system.

7.2 EXPERIMENTAL

The dynamics of the O–H stretch vibrations of HDO in the hydration shells of bromide ions were studied with femtosecond spectral hole-burning spectroscopy. The pump and probe pulses were generated via a sequence of nonlinear frequency-conversion processes as described in Section 3.1. The central frequency of the pump was tuned between 3310 and 3550 cm^{-1}. In Fig. 7.1 we show two pump spectra that are resonant with the red and blue wings of the O–H stretch absorption band of HDO:D_2O. The pump had a typical pulse energy of $\sim$10 μJ. The frequency of the probe was tuned independently from the probe to about 3400 cm^{-1} with a bandwidth of $\sim$200 cm^{-1}.

The pump and probe pulses are used in spectral hole burning experiments on aqueous solutions of LiBr and NaBr. LiBr can be dissolved up to 177 g per 100 ml water, NaBr up to 73 g per 100 ml water. The concentrations studied are 5, 10 and 15 molal for the LiBr solutions and 6 molal for the NaBr solution. For all solutions the solvent was a solution of 2% HDO in D_2O. This concentration is sufficiently low to avoid the measurements to be affected by resonant energy transfer between O–H vibrations located on different HDO molecules [162]. In principle, the hydrogen-bond dynamics of solutions of the Br^- anion can also be studied by probing the response of the O–D stretch vibration of HDO molecules dissolved in H_2O. However, in that case relatively high concentrations of HDO have to be used because the H_2O solvent gives a strong background signal in

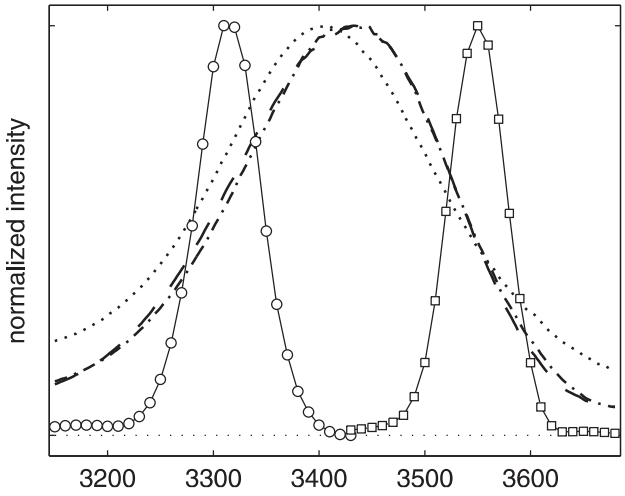

Figure 7.1. Linear absorption spectra of the O–H stretch vibration of HDO for different solutions. The dotted curve represents the absorption spectrum of a solution of 2% HDO in D_2O. The dash-dotted curve represents the absorption spectrum of a solution of 5 molal LiBr in 2% HDO:D_2O, and the dashed curve the absorption spectrum of a solution of 15 molal LiBr in 2% HDO:D_2O. Also shown are the pump spectra used in the measurement of the spectral dynamics shown in Figs. 7.2–7.6.

the absorption region of the O–D stretch vibration. As a result, the vibrational relaxation results in a relatively strong thermal signal. For the O–H stretch vibration of HDO in D_2O, the corresponding background signal is much smaller, so that lower concentrations can be used which results in a much smaller thermal signal after the relaxation is complete.

The sample is contained in a cell with CaF_2 windows and an optical path length of 200 μm. The pump pulse excites a few percent of the O–H vibration from the $v = 0$ ground state to the $\nu = 1$ excited state. This excitation leads to a bleaching effect at the fundamental transition frequency, due to a decrease of the $\nu = 0 \rightarrow 1$ absorption and an introduction of $\nu = 1 \rightarrow 0$ stimulated emission. As the absorption spectrum of the O–H stretch vibration is inhomogeneously broadened, the bleaching has the form of a spectral hole in the absorption band. The shape of the spectral hole evolves in time due to spectral fluctuations. The dynamics of the shape of the spectral hole are monitored with the broadband probe pulse that is detected by a 2×32 MCT detector array.

7.3 Results

Fig. 7.1 shows the linear absorption spectrum of the O–H stretch vibration of HDO molecules for pure HDO:D_2O and for solutions of 5 molal and 15 molal LiBr dissolved in HDO:D_2O. The absorption spectrum of the salt solution is

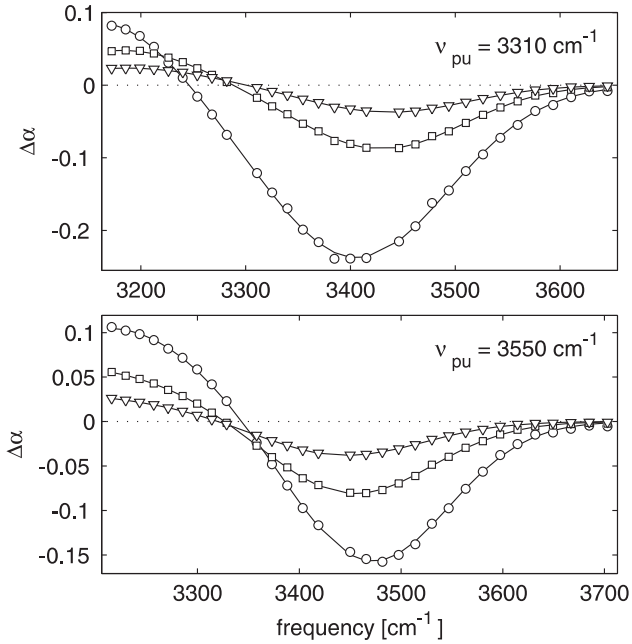

FIGURE 7.2. Transient spectra measured at different delay times for the a solution of 5 molal LiBr in 2% HDO:D_2O. Transient spectra are shown at delay times of 0.5 (circles), 1 (squares) and 2 (triangles) ps. The lines are obtained by fitting the spectra to a sum of two Gaussians with opposite sign.

blue-shifted with respect to the absorption spectrum of pure HDO:D_2O. This blue-shift has been observed before for solutions containing Cl^-, Br^- and I^- ions, and shows that the average hydrogen bond strength decreases upon the addition of these ions. The absorption spectrum of aqueous solutions containing these halide anions can be decomposed in two distinct sub-bands [14]. The first of these sub-bands corresponds to O–H groups of HDO molecules that are hydrogen bonded to the oxygen atom of nearby D_2O molecules, thus forming O–H$\cdots$O hydrogen-bonded systems. This sub-band is very similar to the absorption spectrum of pure HDO:D_2O. The second sub-band is associated with HDO molecules of which the O–H group is hydrogen bonded to X^- (X^-= Cl^-, Br^-) [14, 64], thus forming O–H $\cdots X^-$ hydrogen-bonded systems. The latter sub-band is narrower and is blue-shifted in comparison to the O–H$\cdots$O sub-band.

In Fig. 7.2 transient spectra are shown, measured at different delay times between pump and probe, for a solution of 5 molal lithium bromide in HDO:D_2O. For frequencies above $\sim$3300 cm^{-1} the spectra show the bleaching of the fundamental $\nu = 0 \rightarrow 1$ absorption and $\nu = 1 \rightarrow 0$ stimulated emission. At frequencies below $\sim$3300 cm^{-1}, the spectra show the presence of excited state $\nu = 1 \rightarrow 2$ ab-

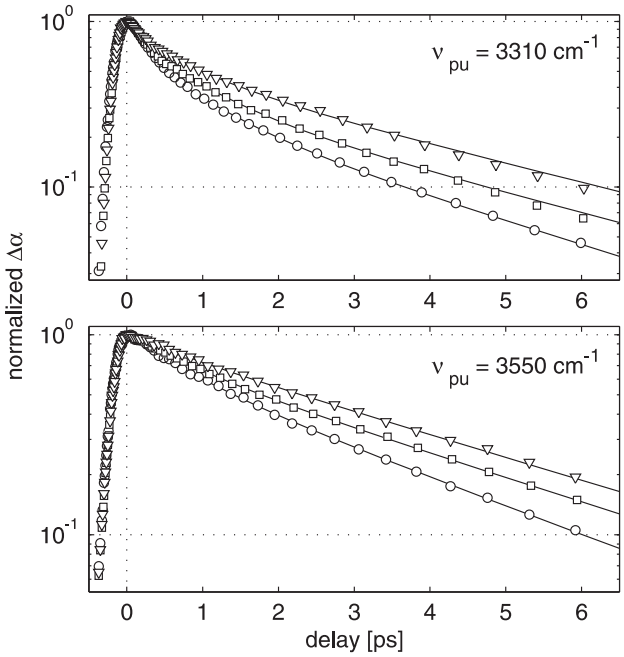

FIGURE 7.3. Bleaching signal as a function of delay measured at the maximum of the bleaching for solutions of 5 (circles), 10 (squares), and 15 (triangles) molal LiBr in 2% HDO:D_2O. The transients in the upper and lower panel are fitted with a bi-exponential decay with the same two time constants for each concentration. The two time constants represent the vibrational lifetimes T_1 of the O–H$\cdots$O and the O–H$\cdots Br^-$ oscillators.

sorption. The relaxation of the $\nu = 1$ state leads to a decay of both the bleaching and the excited-state absorption signal. The relaxation also results in a small temperature increase of the sample in the focus of the pump laser. Due to this increase in temperature, the transient spectral changes do not decay to zero, but evolve to a characteristic small-amplitude transient spectrum that does not decay on the picosecond time scale of the experiment. For the transient spectra shown in Fig. 7.2, the ingrowing heating spectrum has been subtracted, so that these spectra only represent the transient absorption changes associated with the excitation of the $\nu = 1$ state [147]. The rate at which this heating signal grows in, is the same as the vibrational relaxation rate, i. e. bi-exponential with time constants equal to the T_1 values of bulk and bromide bound water. The bleaching part of the spectrum is narrower than the linear absorption spectrum, which shows that the pump has excited a spectral hole in the inhomogeneously broadened absorption band.

In Fig. 7.3 the maximum of the bleaching signal is presented as a function of delay time for the three different LiBr solutions. For all solutions of

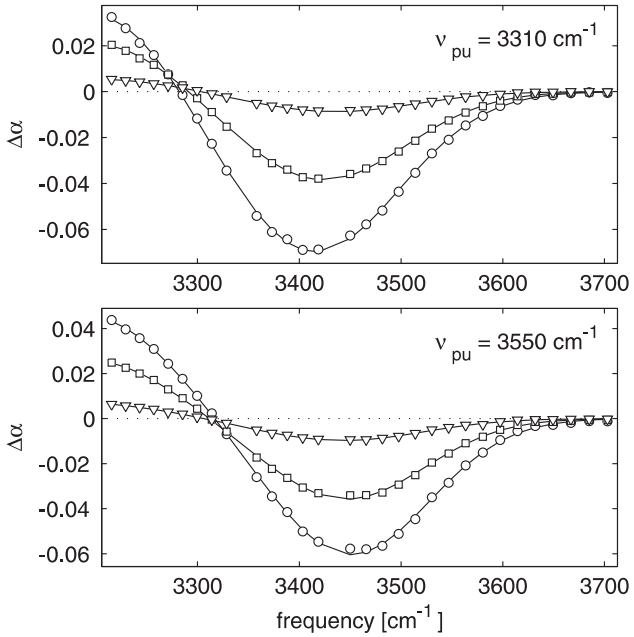

FIGURE 7.4. Transient spectra measured at different delay times for the a solution of 15 molal LiBr in 2% HDO:D_2O. Transient spectra are shown at delay times of 4 (circles), 6 (squares) and 12 (triangles) ps. The lines are obtained by fitting the spectra to a sum of two Gaussians with opposite sign.

LiBr, the signal shows a clear bi-exponential decay. The amplitude of the slow component increases with the concentration of dissolved salt, showing that this component results from water molecules interacting with the salt ions. The fast component of the relaxation has a time constant of 0.8±0.1 ps for all three solutions. We assign this component to the relaxation of the O–H groups forming an O–H$\cdots$O hydrogen bond to D_2O. The observed time constant agrees with the value of T_1 that has been observed before for the O–H stretch vibration of pure HDO:D_2O [166]. The slow component is assigned to the vibrational relaxation of O–H groups forming O–H$\cdots Br^-$ hydrogen bonds to Br^- ions. Its time constant depends slightly on the concentration of dissolved salt. For the solutions studied of 5, 10 and 15 molal LiBr, the value of T_1 is 3.1±0.2 ps, 3.6±0.2 ps, and 3.8±0.2 ps, respectively.

The signals shown in Fig. 7.2 reflect the vibrational relaxation and frequency fluctuations of both the O–H$\cdots$O and O–H$\cdots Br^-$ sub-bands. However, thanks to the difference in vibrational lifetime, the transient spectrum will become completely dominated by the O–H$\cdots Br^-$ sub-bands for delays >4 ps. Hence, we can obtain highly specific information on the spectral dynamics of the O–H$\cdots Br^-$ oscillators by monitoring the spectral dynamics at these longer delay times. In

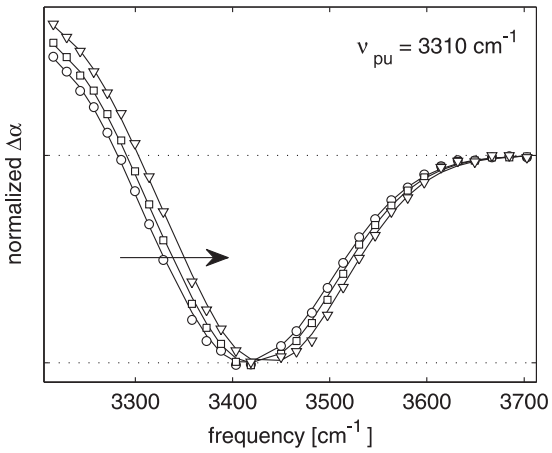

Figure 7.5. Same as the top panel of Fig. 7.4, but normalized to the maximum bleaching signal to exemplify the spectral diffusion.

Fig. 7.4 transient spectra are shown at three different long delay times for a solution of 15 molal LiBr in HDO:H_2O. In the top panel the pump pulse is tuned to 3310 cm^{-1}, in the red wing of the absorption band. The lower panel represents the case where the pump pulse was centered at 3550 cm^{-1}, in the blue wing of the absorption band. The transient spectra observed at a delay of 4 ps in the upper and lower panel are shifted with respect to each other, which shows that the O–H$\cdots$$Br^-$ sub-band is inhomogeneously broadened. With increasing delay, the transient spectra broaden and the central frequency of the spectra shifts to a value of 3450 cm^{-1}. In Fig. 7.5 the spectra of the top panel of Fig. 7.4 are shown normalized to illustrate more clearly the effect of the spectral diffusion within the O–H$\cdots$$Br^-$ sub-band. At a delay of 12 ps, the shapes of the spectral holes obtained with blue and red pumping have become indistinguishable (Fig. 7.4), showing that the spectral diffusion is complete.

To obtain more detailed information on the spectral diffusion dynamics, we determine the first moment of the bleaching of the transient spectra as a function of delay time. To determine the first moment we first determine the frequency of the zero crossing between the bleaching and the excited state absorption with great accuracy. We fit the transient spectra to two Gaussians representing the bleaching and the excited state absorption. From the fit we obtain the frequency $\nu_{\rm zc}$ at which the transient absorption change equals zero for a given delay and central pump frequency. To determine the first moment, we integrate the fitted bleaching starting from the frequency $\nu_{\rm zc}$ of the zero crossing to the highest frequency $\nu_{\rm up}$ of 3700 cm^{-1} of the measured frequency interval:

$$S_1(\tau) = \frac{\int_{\nu_{\rm zc}}^{\nu_{\rm up}} \nu \Delta\alpha(\nu,\tau) d\nu}{\int_{\nu_{\rm zc}}^{\nu_{\rm up}} \Delta\alpha(\nu,\tau) d\nu} \tag{7.1}$$

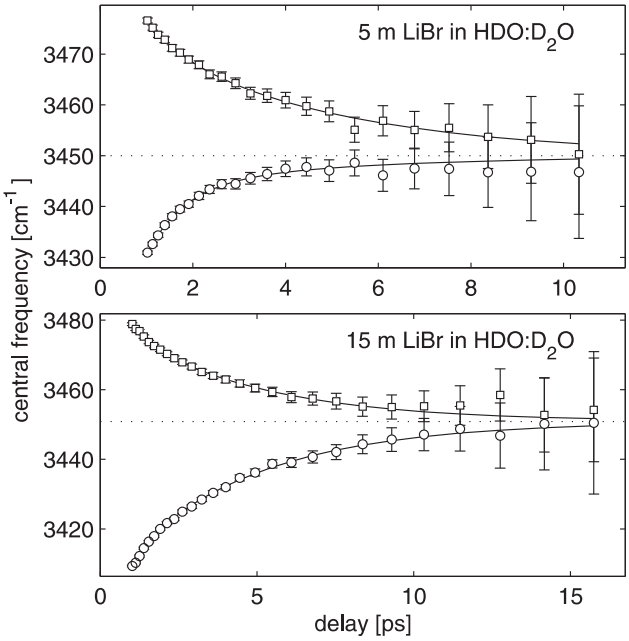

FIGURE 7.6. Spectral diffusion shown by the position of the central frequency (first moment) of the bleach signal ($\Delta\alpha < 0$) for solutions of 5 molal LiBr (upper panel) and 15 molal LiBr (lower panel) in 2% HDO:D_2O. Circles and squares denote red and blue pump frequencies. The lines represent bi-exponential fits of which the parameters are shown in Table I.

In Fig. 7.6 the resulting first moments are shown for solutions of 5 and 15 molal LiBr in HDO:D_2O. It is seen that for both solutions the first moments converge to the same central frequency $\nu_{\mathrm{c,OH-Br}}$. The dynamics can be fitted well with the following bi-exponential function:

$$S_{1,\mathrm{fit}}(\tau) = \nu_{\mathrm{c,OH-Br}} + A_1 e^{-\tau/\tau_1} + A_2 e^{-\tau/\tau_2} \tag{7.2}$$

with the same time constants τ_1 and τ_2 for red pumping (ν_{pu}=3310 cm^{-1}) and blue pumping (ν_{pu}=3550 cm^{-1}).

We also determined the dynamics of the first moment of the bleaching of the transient absorption spectra measured for a solution of 6 molal NaBr in HDO:D_2O. The first moments obtained with red and blue pumping again show the same bi-exponential dynamics and converge to the same central frequency. The time constants obtained from a simultaneous fit to the first moments obtained with red and blue pumping are shown in Table I.

	$\nu_{c,OH-Br}$	A_1 (red) A_2 (red)	A_1 (blue) A_2 (blue)	τ_1 τ_2
5 m LiBr	3450 cm^{-1}	-47±4 cm^{-1} -7.5±1 cm^{-1}	19±2 cm^{-1} 27±3 cm^{-1}	0.8±0.1 ps 4.2±0.4 ps
10 m LiBr	3449 cm^{-1}	-45±4 cm^{-1} -11±1 cm^{-1}	20±4 cm^{-1} 26±2 cm^{-1}	0.9±0.1 ps 4.3±0.3 ps
15 m LiBr	3451 cm^{-1}	-25±2 cm^{-1} -46±4 cm^{-1}	20±2 cm^{-1} 30±3 cm^{-1}	0.6±0.2 ps 4.3±0.2 ps
6 m NaBr	3460 cm^{-1}	-28±2 cm^{-1} -2±0.5 cm^{-1}	2.7±1 cm^{-1} 7±2 cm^{-1}	0.9±0.1 ps 4.7±0.4 ps

TABLE I. Time constants of the bi-exponential fits to the first moments observed for different solutions containing Br^- ions. The amplitudes A_1(red) and A_2(red) refer to the case where the absorption band is pumped in the red wing at 3310 cm^{-1}, and the amplitudes A_1(blue) and A_2(blue) correspond to the case where absorption band was pumped in the blue wing at 3550 cm^{-1}.

7.4 INTERPRETATION

The fast component of the dynamics of the first spectral moment with a time constant of 0.8±0.1 ps is important in the first few picoseconds after the excitation. This fast component contains several contributions. It contains the vibrational population decay of the excited O–H$\cdots$O oscillators. The spectral response of these oscillators differs from that of the longer-living excited O–H$\cdots Br^-$ oscillators. Hence, the decay of the O–H$\cdots$O sub-band leads to spectral dynamics with a time constant corresponding to the vibrational lifetime of the O–H$\cdots$O vibrations. The fast spectral dynamics can also contain a contribution of spectral diffusion within the O–H$\cdots$O sub-band. For bulk HDO:D_2O it was found that the FFCF contains a fast part with a time constant of ∼100 fs and a slow part with a time constant of ∼1 ps. [7, 8, 44, 45, 50, 76, 88, 121, 139, 140, 161, 168]. The slow component of the FFCF has been described with a single time constant with a value of ∼1 ps [44, 45, 50, 76, 88, 121, 139, 140, 161, 168] or with two time constants of ∼0.4 ps and ∼1.8 ps [7]. The slow part of the spectral diffusion of the O–H$\cdots$O oscillators may well contribute to the fast component with a time constant of ∼0.8 ps observed for the LiBr and NaBr solutions. Finally, the fast component of the observed spectral dynamics can contain a fast component of the spectral dynamics of the O–H$\cdots Br^-$ oscillators. For an HDO molecule for which the O–H group is hydrogen bonded to Br^-, the O–D group will likely be bonded to the oxygen atom of a D_2O molecule. The FFCF of this O–D$\cdots$O system will show a component with a time constant of ∼1 ps and the corresponding hydrogen-bond fluctuations may well affect the O–H$\cdots Br^-$ hydrogen-bond and

thus the O–H frequency at the other side of the HDO molecule. In that case the spectral dynamics of the O–H$\cdots$Br$^-$ oscillators will also show a contribution of the O–D$\cdots$O hydrogen-bond fluctuations. The fast component will likely not contain a contribution of the exchange between O–H$\cdots$Br$^-$ and O–H$\cdots$O oscillators, i. e. a switching of hydrogen bonds between the hydration shell and the surrounding liquid. In a recent study of the spectral dynamics of $NaBF_4$ solutions it was shown that this exchange takes place on a substantially longer time scale of $\sim$7 ps [101].

From the values shown in Table I it follows that the relative amplitude of the fast component strongly decreases with increasing salt concentration, especially in the case of pumping in the red wing of the absorption band. Because the contribution of O–H$\cdots$O to the signal decreases with increasing concentration, this result indicates that the fast component in the dynamics of the first spectral moment is dominated by the O–H$\cdots$O component. Moreover, in the case of pumping in the red wing, the ratio A_1/A_2 is larger than in the case of pumping in the blue wing. As the O–H$\cdots$O sub-band is redshifted with respect to the O–H$\cdots$Br$^-$ sub-band, this result also indicates that the fast component in the dynamics of the first spectral moment is associated with dynamics of the O–H$\cdots$O sub-band. The fast component is likely dominated by the vibrational relaxation of the O–H$\cdots$O sub-band, because the time constant of this component of 0.8$\pm$0.1 agrees very well with the value of T_1 of the excited O–H$\cdots$O and because the transient spectra at early delay times clearly show the decay of the O–H$\cdots$O sub-band (Fig. 7.2).

For the solution of 15 molal LiBr the ratio A_1/A_2 is smaller for red pumping than for blue pumping. This indicates that at this very high concentration the absorption spectrum of the hydration shell of Br$^-$ possesses a strong red wing. In the linear absorption spectrum of Fig. 7.1 it is seen that for a solution of 15 molal LiBr the absorption spectrum has a slightly stronger red absorption wing than for a solution of 5 molal LiBr (Fig. 7.1). Here it should also be realized that the amplitude of the O–H$\cdots$O sub-band will be significantly lower for a 15 molal LiBr solution than for a 5 molal LiBr solution. The fact that nevertheless the absorption spectrum shows a slight redshift going from a 5 molal to a 15 molal solution shows that for the latter solution the O–H$\cdots$Br$^-$ sub-band must indeed possess a stronger red wing. This red wing is likely due to the fact that at this high concentration the Li^+ ions will be close to the hydration shell of the Br$^-$ ions, thus forming Li^+O–H$\cdots$Br$^-$ hydrogen-bonded systems. The high charge density of the Li^+ ion polarizes the O–H$\cdots$Br$^-$ hydrogen bond, leading to a strengthening of this bond and a redshift of the corresponding O–H stretch frequency.

We find that the time constant of the fluctuations of the O–H$\cdots$Br$^-$ hydrogen bonds is not very much dependent on the concentration of dissolved salt and also not very much dependent on the nature of the cation. This indicates that the dynamics of the hydration shell are relatively uncoupled from the dynamics of the rest of the water network. For bulk water the FFCF shows time constants of $\sim$100 fs and $\sim$1 ps, significantly faster than the fluctuations of the hydration shell of Br$^-$. This large difference in time scales probably explains

why the dynamics of the hydration shell are not strongly coupled to the rest of the liquid. The comparison of solutions of LiBr and NaBr shows that the nature of the cation has very little effect on the time constant of the O–H$\cdots$Br$^-$ fluctuations.

7.5 Discussion

In previous two-color femtosecond pump-probe studies [63, 64], the dynamics were measured of the hydration shells of the halide anions Cl^-, Br^- and I^-. In these studies the time constants for the spectral diffusion of the hydration shells were derived from the dependence of the decays of the signals on the pump and probe frequencies. It was observed that the decay became slower when the probe frequency was increasingly detuned from the pump, showing the presence of a slow spectral diffusion process. The determination of the time constants of the spectral diffusion relied on the modeling of these spectral dynamics. Using a Brownian oscillator model this study arrived at time constants ranging between 10–25 ps [63,64]. In the present study we directly monitor the dynamics of the spectral holes burned by the excitation pulse using a broadband probe pulse. This method does not require any modeling of the spectral dynamics, and we obtain a much more accurate determination of the spectral diffusion dynamics. We now find that the time constant obtained previously were a factor 2–5 too long.

The method used in this this study is similar to two-dimensional (2D) vibrational correlation spectroscopy. There are two variations of this type of spectroscopy: double-resonance or dynamic hole burning spectroscopy and pulsed Fourier transform or heterodyne detected vibrational echo correlation spectroscopy. The method used here is the same as double resonance dynamic hole burning spectroscopy. In comparison to heterodyne detected vibrational echo correlation spectroscopy using $<$ 50 fs mid-infrared pulses [88, 114, 115], the present method has as a disadvantage that the spectral dynamics cannot be measured at times $<$150 fs after the excitation. An important advantage of the present method is that the pre-selection of particular pump frequencies allows for a high signal-to-noise ratio with the result that we can measure spectral shifts on the order of 1 cm^{-1} up to delay times of 15 ps.

The hydrogen-bond fluctuation dynamics of solutions of NaBr have recently been studied with femtosecond vibrational echo correlation spectroscopy. At the highest concentration studied (6 M) the observed FFCF showed a slow component with a time constant of 4.8$\pm$0.6 ps, in good agreement with the 4.3$\pm$0.3 ps we observe for the slow component of the FFCF of a solution of 6 molal NaBr. An important difference with the present work is that in the previous work the observed FFCF was assumed to represent the dynamics of all water molecules at all time scales [114,115]. The slow component was thus assigned to a global restructuring of the solution and was expected to slow down with increasing concentration because of the increasing number of hydrogen bonds to Br^-. However, the assumption that that the slow component would represent the

dynamics of all water molecules is not valid, because the water hydroxyl groups that form a hydrogen bond to Br^- show a much longer vibrational lifetime than the water hydroxyl groups that form hydrogen bonds to an oxygen atom of another water molecule [63,64,66,114,115]. Hence, with increasing delay time, the measured signal will show an increasing bias to the dynamics of the hydroxyl groups that form a hydrogen bond to Br^-. The slowest time scale of the FFCF will thus represent the spectral fluctuations of the O–H$\cdots$Br$^-$ systems only, i. e. the hydration shells of the Br^- ions. The dynamics of water *outside* the first hydration shell were observed and calculated not to be very different from bulk liquid water [55, 110, 111].

Recently, the O–H $\cdots$ X$^-$ hydrogen bond correlation functions of water in the hydration shell of the halide anions were calculated with molecular dynamics simulations. In these studies a distinction was made between the so-called continuous hydrogen-bond correlation function and the intermittent hydrogen-bond correlation function. The continuous correlation function represents the case where there are no bond breakups in the time interval between 0 and t. For the intermittent case temporary bond breakups are allowed, and the correlation function only decays when the hydrogen bond is broken at time t. The calculated decay time constant for the continuous hydrogen-bond correlation function ranges from 0.5 to 2 ps, depending on the definition of the hydrogen bond [24]. The intermittent time constant is $\sim$4 ps [55], which is very similar to the observed time constant of 4.3$\pm$0.3 ps we observe. This indicates that the O–H$\cdots$Br$^-$ hydrogen bond may experience rapid fluctuations including transient breaking and reformation, but the reformation tends to produce the same O–H$\cdots$Br$^-$ hydrogen bond with the same O–H stretch frequency as before the breaking. Hence, these rapid fluctuations do not lead to full spectral equilibration. The full spectral equilibration involves a much slower process, and probably involves a reorganization of the complete hydration shell. Such a complete reorganization can result in two effects. In the first place a new O–H$\cdots$Br$^-$ hydrogen bond can be formed and the corresponding O–H stretch vibrational frequency can be found at a different position in the O–H$\cdots$Br$^-$ absorption sub-band. Hence, such a complete reorganization will indeed lead to a complete spectral equilibration of the O–H$\cdots$Br$^-$ absorption sub-band. Second, the reorganization can lead to a rotation of the hydroxyl group out of the hydration shell leading to the formation of a hydrogen bond to another water molecule, i. e. an O–H$\cdots$O hydrogen bond. In this case, the O–H group will show a relatively fast vibrational relaxation with the result that the O–H oscillator vanishes from the signal [72].

The rotation out of the hydration shell will contribute to the observed vibrational relaxation of the O–H$\cdots$Br$^-$ oscillators as this rotation turns the slowly relaxing O–H$\cdots$Br$^-$ system into a rapidly relaxing O–H$\cdots$O system. Hence, the observed vibrational relaxation rate will be the sum of two channels, one being the intrinsic relaxation of the intact O–H$\cdots$Br$^-$ system, the other formed by out-of-shell rotation followed by fast relaxation. The fraction of hydroxyl groups that rotate out of the hydration shell upon reorganization will depend on the concentration dissolved salt, as this concentration determines the number

density of available water molecules to which a new O–H$\cdots$O hydrogen bond can be formed. Hence, at high concentrations rotation out of the shell becomes a less likely process, leading to an increase of T_1, as is indeed observed experimentally [65]. The concentration dependence of T_1 can be used to estimate the time constant of the out-off-shell rotation at low concentrations [10]. The value of T_1 increases from 2.5 ps for a solution of 1 M LiBr [65] to 3.8 ps for a solution of 15 m LiBr. If we assume that the out-off-shell rotation is completely switched off at high concentrations, it follows that $\tau_{oos}(Br^-) = 1/[(1/2.5 - (1/3.8)] \approx 7$ ps. This value agrees quite well with the results of a recent two-dimensional vibrational echo study of a solution of $NaBF_4$. In this study the time constant at which a hydroxyl groups switches from the $BF_4{}^-$ion to the oxygen atom of a nearby water molecule was observed to be 7±1 ps.

7.6 Conclusions

We studied the hydrogen-bond dynamics of the hydration shell of the bromide anion using femtosecond spectral hole-burning spectroscopy. We find that at short delay times the spectral dynamics are governed by the vibrational relaxation with a time constant T_1 of 0.8±0.1 ps of the O–H groups of water molecules that are hydrogen bonded to other water molecules. The O–H groups that are hydrogen bonded to Br^- anions show a much slower vibrational relaxation with a time constant T_1 of 3.1 ps for a solution of 5 m LiBr. This latter vibrational relaxation time constant increases slightly with the concentration of dissolved salt to a value of 3.8±0.2 ps for a solution of 15 m LiBr. Due to the large difference in vibrational lifetime, the spectral dynamics observed at delays >4 ps are solely due to the spectral dynamics of the water molecules forming O–H$\cdots Br^-$ hydrogen bonds in the hydration shell of Br^-.

From the measurement of the first spectral moment of the spectral holes, we deduce that the spectral dynamics of the O–H$\cdots Br^-$ oscillators are governed by a component with a time constant of 4.3±0.3 ps. This time constant shows a negligible dependence on the concentration of dissolved salt and on the nature of the cation. The process with a time constant of 4.3±0.3 ps leads to a complete spectral equilibration of the absorption band of the O–H$\cdots Br^-$ oscillators. This process likely represents a complete reorganization of the hydration shell. The value of the time constant of the reorganization agrees very well with the calculated time constant of the O–H$\cdots Br^-$ hydrogen-bond correlation function obtained with molecular dynamics simulations [24, 55]. For a fraction of the hydroxyl groups, the reorganization results in a switch of the O–H$\cdots Br^-$ hydrogen bond to an O–H$\cdots$O hydrogen bond. This switch represents an effective relaxation channel for the O–H stretch vibration, and in most cases will lead to the departure of the water molecule from the hydration shell. The increase of T_1 of the O–H$\cdots Br^-$ oscillators with increasing LiBr concentration can thus be explained from the fact that the fraction of water molecules for which the hydrogen bond switches to O–H$\cdots$O decreases with increasing salt concentration.

8 Proton Transfer in Liquid Water

We have studied time-resolved mid-infrared kinetics for the ultrafast acid-base reaction between photo-excited 8-hydroxypyrene 1,3,6-trisulfonate (HPTS) and acetate at three concentrations (0.5, 1.0, and 2.0 M) and three temperatures (5, 30, and 65 °C) in liquid D_2O. The observed proton-transfer kinetics agree quantitatively, over all times (200 fs – 500 ps), with an extended Smoluchowski model which includes distance-dependent reactivity in the form of a Gaussian rate function, *k(r)*. This distance dependence contrasts with the exponential *k(r)* that is typically observed for electron-transfer reactions. The width of *k(r)* is essentially the only parameter varied in fitting the proton transfer kinetics at each concentration and temperature. We find that *k(r)* likely represents the rate of concerted (multi-)proton hopping across 'water wires' of different length r that connect acid-base pairs in solution. The concerted nature of the proton transfer is supported by the fact that *k(r)* shows a steeper dependence on r at higher temperatures.

8.1 Introduction

Acid-base reactions are fundamental to chemical and biological reactions. In the conventional picture of solution phase proton-transfer, an acid, AH, and a base, B^-, need to diffuse toward one another before the reaction can take place. Thus Eigen and coworkers [40, 41] have suggested a two step mechanism in which an encounter complex, $AH \cdots B^-$, is formed by diffusion after which proton transfer within this complex can occur:

$$AH + B^- \underset{k_{-D}}{\overset{k_D}{\rightleftarrows}} AH \cdots B^- \xrightarrow{k_0} A^- + HB\,. \tag{8.1}$$

Here k_D and k_{-D} denote the diffusion-controlled encounter complex formation and dissociation rate coefficients, respectively, and k_0 is the intrinsic proton transfer rate coefficient. The encounter complex (sometimes called the 'contact pair') is thought to involve the acid and base molecules separated by one or two water molecules [157], leading to a typical 'contact distance', a, in the range of 6–7 Å.

In order to follow a proton transfer reaction in the time-domain one needs to trigger the reaction at a well-specified time. The temperature-jump methods developed by Eigen and coworkers allowed the study of proton transfer reactions in the μs time-regime, but faster proton transfer reactions require an optical trigger. A specific class of molecules, called photo-acids, change their pK_a upon photo-excitation, and as such are very suitable for this purpose. Early investigations into photo-acids [157], such as naphthols, have established the field of excited-state proton transfer. When a photo-acid, ROH, absorbs a photon, a cascade of events is initiated [6], including intramolecular charge transfer, relaxation to the ground vibrational state of S_1, enhancement of the $ROH \cdots OH_2$ hydrogen-bond, and reversible proton transfer to the solvent with the proton diffusing away from the RO^- via the Grotthuss mechanism [4]. When a base is added to the solution, direct proton transfer by the mechanism of Eq. (8.1) is expected to compete with proton transfer to the solvent [78, 148, 155, 156]. To obtain a good estimate of k_0, independent of proton transfer to the solvent and diffusion, the reaction was investigated at very high base concentrations (8 M) [120].

When the acid-base reaction is sufficiently downhill to be irreversible, and the base is in large excess (pseudo-unimolecular conditions, see Section 4.5), the mechanism in Eq. (8.1) leads to Smoluchowski kinetics [36, 116, 142–144, 153, 169]. This description is valid for pseudo-unimolecular irreversible reactions, in which the initially randomly distributed base molecules react independently with the acid. The survival probability, $S(t)$, of the acid is then obtained as a product of the survival probabilities due to all base molecules [142–144]. The AH/B^- pair kinetics are described by a diffusion equation. When the irreversible proton transfer reaction occurs at a fixed distance, as implicitly assumed in Eq. (8.1), an appropriate boundary condition is imposed at this distance. Smoluchowski has utilized an absorbing boundary [153], which can be generalized to a 'radiation boundary condition' (with a rate parameter k_0) [21], as suggested by Collins and Kimball [27]. The resulting model, which is equivalent to having a delta-function sink at the 'contact distance' $r = a$, is referred to as the Smoluchowski-Collins-Kimball (SCK) model. When k_0 is sufficiently large, $S(t)$ decays initially with the rate coefficient k_0, then slows down to an ultimate exponential decay characterized by a slower steady-state rate coefficient.

The SCK model was previously applied to fluorescence quenching [131]. For quenching driven by electron-transfer, difficulties with the SCK model were encountered, which could be overcome by replacing the delta-function sink by a distance-dependent rate-function, $k(r)$ [104, 129, 135]. Such an approach was suggested theoretically by Wilemski and Fixman [158], and elaborated for photoinduced charge separation elsewhere [19]. More recently the SCK model was applied successfully to excited-state proton transfer between 2-naphthol-6-sulfonate and acetate in glycerol-water solutions [25, 26]. The high solvent viscosity slowed down the reaction to the regime conveniently probed by the time correlated single photon counting (TCSPC) technique. A similar analysis has been applied to the ground-state protonation of a photochemically gener-

ated $ONOO^-$ base [59]. For proton concentrations in the range of 100 mM, the SCK model gave good agreement with the measured kinetics.

With TCSPC the time dependent fluorescence signals of a photo-acid are recorded after electronic photo-excitation. The fluorescence spectrum is dependent on the protonation state of the photo-acid and thus reveals whether the proton has been transferred to the solvent or base and/or whether it has recombined. The biggest advantages of TCSPC are its excellent signal to noise ratio and the ability to measure over a long time range (up to 50 ns). Unfortunately, the time resolution of TCSPC is limited to about 35-50 ps. A new era in the investigation of acid-base reactions began with the introduction of time-resolved infrared spectroscopy as a probe of the transient proton transfer kinetics [29, 98, 125, 132]. This method has much improved time resolution (essential for a highly reactive system) and it can follow the transient infrared signal from *both* reactants and products.

The system of choice here was the photo-acid 8-hydroxy-1,3,6-pyrenetrisulfonic acid (HPTS), with acetate derivatives as the base. At high base concentrations, biphasic proton transfer kinetics were observed [125], where the fast phase (sub 150 fs) was attributed to proton transfer within $ROH \cdots B^-$ pairs formed already in the ground state, and the slower phase was fit with the SCK model [126]. More recent work showed that the SCK model is inadequate even for the slow phase [29, 132, 133]. Chains of hydrogen-bonded water molecules ('water-wires') of different lengths supposedly connect the acid with the base resulting in proton transfer over distances bridged by several water molecules. The rate-limiting step in these reactions is the formation of a hydrogen-bonded configuration of the intervening water molecules that allows the transfer of the proton. Once an appropriate configuration for conduction is established, the transfer itself is ultrafast, in the fs time-regime. As a consequence, the product (acetic acid) infrared signal rises instantaneously with the decay of the excited HPTS reactant [125,132]. This picture contrasts with suggestions that the proton can be temporarily trapped on an intervening water molecule [80, 97, 98], and agrees with quantum calculations showing proton transfer along short water-wires occurring on the 100 fs time-scale [17, 34, 152]. The motion of protons along short wires can be concerted and synchronous [30, 152], rather than stepwise. Likewise, it was shown that intramolecular proton transfer through water molecule bridges mainly occurs via concerted double- and triple-proton transfer [69].

In electron-transfer reactions the distance dependence of $k(r)$ depends on the free energy difference between reactants and products. For highly exoergic electron-transfer reactions, $k(r)$ goes through a maximum at large distances due to the r-dependence of the reorganization energy in the Marcus-Hush theory [18]. For proton transfer in water, the distance dependence is connected to the molecular structure of the medium (water). Water wires were detected computationally in pure liquid water only when water molecules were confined into a single file within a pore [17]. The formation of interconnecting water-wires for acid-base solutions can be stimulated by either the difference in acidity of the reacting partners, or their ionic character [5]. The good agreement with

the conventional SCK model previously observed for proton transfer between 2-naphthol-6-sulfonate and acetate in glycerol-water mixtures [25, 26] may be partly due to disruption of such wires by the glycerol co-solvent.

The present work investigates the temperature dependence of an exoergic excited-state proton transfer between a photo-acid (HPTS) and an anionic base (acetate) [125, 132], which is suggested to occur via water-wires [29, 132, 133]. Assuming that proton transfer through such wires is concerted [30, 152], the transfer across the whole wire can be described with a single distance-dependent rate constant, $k(r)$, in analogy to models of photo-excited electron transfer [129, 135]. The ultrafast kinetic phase is expected to be sensitive to the functional form of $k(r)$, whereas the long-time phase will reflect the mutual acid-base diffusion.

8.2 THEORY

We aim to describe the time dependence of proton transfer by a single distance-dependent rate coefficient $k(r)$. Extending the analogous treatment for electron-transfer reactions [129, 135], we consider a family of 'sink terms' with the functional form

$$k(r) = k_0 \exp\left[-(r-a)^n / \Gamma\right] . \tag{8.2}$$

Here a is the distance of closest approach between acid and base ($r \geq a$), and k_0 is the maximal value of the rate coefficient attained at this distance. The power n is a parameter which we hope to determine by comparison with the experiment, and Γ is a parameter that determines the width of $k(r)$. Practically, it will be the only adjustable parameter in our model.

In the theoretical treatment below several approximations are invoked:

- The reaction is irreversible, which is valid since $\mathrm{pK_a}(\text{base}) \gg \mathrm{pK_a}(\text{acid})$ [2].

- The reaction is pseudo-unimolecular due to the high concentration, ρ, of the acetate base.

- The system is assumed to be spherically symmetric, even though the acidic hydroxyl occupies a small fraction of the HPTS surface. For excited-state proton transfer to solvent such an approximation is routinely applied, and with good results [6]. However, the justification given there, that the reaction is slow as compared with rotational diffusion, no longer holds in the present case. To our knowledge, an extension of the Smoluchowki theory to angular dependence has not been applied to experimental data, so it is presently hard to assess its merits.

- There is no interaction potential between HPTS and acetate. Although both are negatively charged, neglect of their Coulombic repulsion is justified in the high concentration regime where the electrostatic interaction is almost totally screened (by the sodium counter-ions).

We thus employ the methods developed for pseudo-unimolecular reactions in Section 4.5, in particular those pertaining to spherically symmetric systems in the continuum limit (4.5.3). In the first few picoseconds after photo-excitation, the molecules do not yet move. In this static limit the survival probability of the protonated acid, $S(t)$, decays as:

$$S(t) = \exp\left\{-\rho \int_a^\infty dr 4\pi r^2 [1 - e^{-k(r)t}]\right\} . \tag{8.3}$$

Thus, in the $t \to 0$ limit the decay is exponential,

$$S(t) \sim \exp(-\rho \langle k \rangle t) , \tag{8.4}$$

where the average rate constant is $\langle k \rangle \equiv \int_a^\infty dr 4\pi r^2 k(r)$.

Assuming that $S(t)$ is the product of the acid survival probability due to the randomly distributed base molecules, and going to the continuum limit [142–144], one obtains the survival probability of the generalized Smoluchowski form:

$$S(t) = \exp\left(-\rho\, P(t)\right) . \tag{8.5}$$

The pair reaction probability, $P(t)$, is calculated from its probability density, $\varphi(r,t)$, by integrating the reactive flux:

$$P(t) \equiv \int_0^t dt' \int_a^\infty dr 4\pi r^2 k(r) \varphi(r,t') . \tag{8.6}$$

Hence Eq. (8.3) is a special case of Eq. (8.5) with $\varphi(r,t) = \exp[-k(r)t]$ namely, a pair at separation r reacts unimolecularly with a rate coefficient $k(r)$.

At longer times, diffusion starts to play a role and $\varphi(r,t)$ is obtained as the solution of a spherically symmetric diffusion equation with a sink term [158],

$$\frac{\partial \varphi(r,t)}{\partial t} = -k(r)\varphi(r,t) + \frac{D}{r^2}\frac{\partial}{\partial r} r^2 \frac{\partial}{\partial r}\varphi(r,t) , \tag{8.7}$$

where D is the mutual diffusion coefficient of the acid-base partners which is the sum of their individual diffusion coefficients. Because the reaction is described by $k(r)$, we impose a reflecting boundary condition at the contact distance, a, namely $(\partial\varphi(r,t)/\partial r)|_{r=a} = 0$. This equation is solved numerically.

The SCK model is the special case of the above, where

$$k(r) = k_0 \delta(r-a)/(4\pi a^2) . \tag{8.8}$$

There are rather good analytical approximations to $S(t)$ for delta-function (Eq. (8.8)) or exponential sinks [36, 169], but not for a more general distance-dependence of $k(r)$. Because the short time behavior in Eq. (8.3) depends only on $k(r)$ (and not on D), the data up to approximately 5 ps will be utilized to search for the optimal functional dependence in Eq. (8.2). With this $k(r)$ and the experimentally determined diffusion constants, Eqs. (8.5)–(8.7) are expected to fit the data over the whole time range.

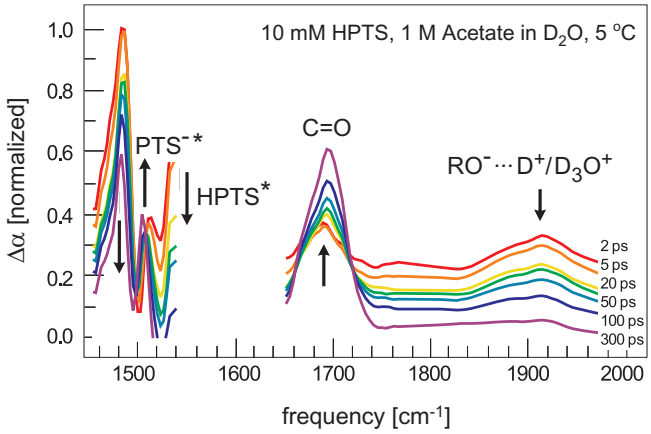

FIGURE 8.1. Transient mid-infrared absorption spectra of 10 mM HPTS in liquid D_2O solution containing 1 M of sodium acetate at 5 °C and different delay times following the exciting 400 nm pulse.

8.3 EXPERIMENTAL

We have studied the effects of temperature on the proton transfer reactions between the photo-acid 8-hydroxy-1,3,6-pyrenetrisulfonic acid (HPTS) and a base (sodium acetate) in D_2O using ultrafast visible pump-infrared probe spectroscopy. HPTS is a commonly used photo-acid in the study of reversible excited state proton transfer reactions [98,118,132] with an absorption band around 400 nm. Light at this wavelength can be conveniently generated using the second harmonic of a Ti:sapphire laser. Upon excitation, the HPTS molecule changes its electronic structure [6] leading to a massive increase of its acidity, its pK_a reduces from 7.3 to 1.4 [75]. This increase in acidity causes the release of a proton to the surrounding water/ice, from where it can travel towards the base molecule. After a few nanoseconds the excited state of the HPTS molecule decays and geminate recombination with the proton occurs.

HPTS was promoted to an electronically excited state with a 100-fs laser pulse centered at 400 nm, and probed using transient absorption of a broadband infrared pulse. The infrared pulses were tuned to the transient resonances of the excited (*) photo-acid seen in Fig. 8.1: HPTS* (1480 cm^{-1}), the conjugate photo-base, PTS^{*-} (1503 cm^{-1}), the carbonyl vibration of the acetic acid band (1710 cm^{-1}), and the hydrated proton/deuteron (> 1800 cm^{-1}). In the present work, we monitor the proton transfer reactions primarily through the dynamics of the HPTS* band.

The pump-probe setup used in the experiments is described in Section 3.1. The pump was generated through second-harmonic generation of fraction of the 800 nm laser system. The infrared probe pulses were generated using difference

frequency generation in a $AgGaS_2$ crystal, resulting in wavelengths between 2.7 and 8 μm (3700 – 1250 cm^{-1}) and a pulse duration of $\sim$150 fs. The pump and probe polarizations were set to magic angle, so that only isotropic absorption changes were detected. The excitation of HPTS molecules by the 400 nm pump causes a time and frequency dependent absorption change $\Delta\alpha(t,\nu)$ in the sample. This absorption change is comprised of both increases in absorption signals, arising from the excited HPTS* molecules and/or their reaction products, and decreases in absorption signals, due to the depletion of HPTS in the ground state.

The signals were averaged over 5000 shots at each delay time. The sample was contained in a rotating temperature controlled cell between two CaF_2 windows separated by a 50–100 μm spacer. The sample was rotated to avoid photo-product formation and long-term heating effects. The pump pulses were focussed in the sample to a relatively large spot size and attenuated to prevent any multi-photon effects. These effects include ionization of water which creates a spectral response from dissolved electrons. To check the absence of this electron response, we also measured a sample where the photo-acid was omitted. The focus of the pump was tuned, using a telescope, well below the point where no more electron signal was detected. The sample was then replaced with one containing the photo-acid. The samples each contained 10 mM of HPTS (8-hydroxy-1,3,6-pyrenetrisulfonic acid trisodium salt) dissolved in D_2O. The concentration, ρ, of the acetate base was varied (0.5, 1, and 2 M) and the reaction was measured at different temperatures (5, 30, and 65 °C).

8.4 RESULTS

Fig. 8.1 shows the transient absorption spectra measured for a solution of 10 mM HPTS and 1 M acetate in D_2O. The spectra show the transient response in the infrared region of the aromatic ring vibrations of HPTS* and PTS^{*-}, the carbonyl stretching vibration, and the deuteron continuum [29]. After electronic excitation of HPTS to its excited singlet state, there is a direct rise of the infrared absorption at 1480 and 1540 cm^{-1}, which we assign to HPTS*. At longer delay times, these absorptions decay and a new absorption at 1503 cm^{-1} grows in, which is assigned to the conjugate photo-base, PTS^{*-}. Fig. 8.1 also shows the transient spectrum between 1650 and 2000 cm^{-1}, containing the carbonyl-stretching of the acetic acid centered at 1710 cm^{-1} and the broadband infrared absorption that we attribute to the deuteron signal [29]. The rise of the carbonyl absorption (coinciding with the decay of the deuteron absorption) signals the arrival of the deuteron at the acetate base to form acetic acid. In the following, we will focus primarily on the dynamics of the HPTS* band.

The data sets consist of a matrix of pump induced, frequency (ν) and time resolved absorption difference measurements $\Delta\alpha(t,\nu)$, and their corresponding standard deviations $\epsilon(t,\nu)$. These absorption differences are assumed to arise as a result of two spectral responses, $\sigma(\nu)$, that are proportional to the time

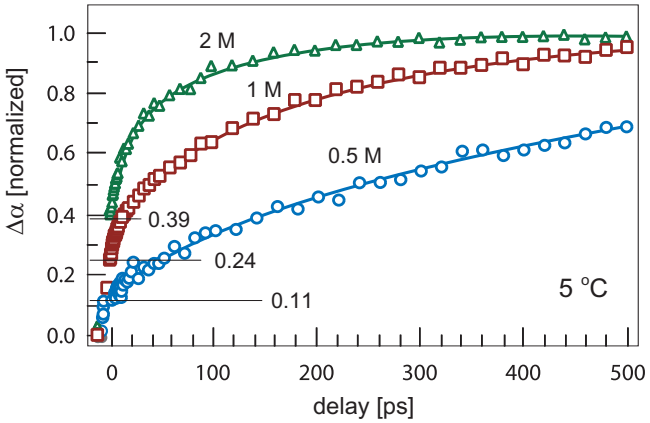

FIGURE 8.2. Time-resolved infrared signal of the carbonyl vibration of acetic acid measured at 1710 cm^{-1} for three different acetate concentrations. The data is shown with markers while the lines show the fitted model. The signals contain an initial contribution (not shown) that results from ultrafast (<150 fs) proton transfer in directly hydrogen-bonded HPTS-acetate reaction complexes. The amplitudes at 1 ps are marked in the figure.

dependent populations in either the $HPTS^*$ or PTS^{*-} state:

$$\Delta\alpha(t,\nu) = N_{\mathrm{HPTS}}(t)\,\sigma_{\mathrm{HPTS}}(\nu) + N_{\mathrm{PTS^-}}(t)\,\sigma_{\mathrm{PTS^-}}(\nu)\,. \tag{8.9}$$

Furthermore it is assumed that the total population of excited $HPTS^* + PTS^{*-}$ is conserved, i. e. $N_{\mathrm{HPTS}} + N_{\mathrm{PTS^-}} = 1$. This assumption is valid because the excited-state decay is negligible on the time scale of the measurements. The spectral responses of $HPTS^*$ and PTS^{*-} are estimated by taking the spectra for $\Delta\alpha$ at early and late pump-probe delay times, respectively. Next we using the temporal decomposition methods described in Section 4.2.4, to calculate the population occupying the $HPTS^*$ state for all times t by minimizing

$$\chi^2(\tilde{N}) = \int d\nu \left(\frac{\Delta\alpha(t,\nu) - \tilde{N}\,\sigma_{\mathrm{HPTS}}(\nu) - (1-\tilde{N})\,\sigma_{\mathrm{PTS^-}}(\nu)}{\epsilon(t,\nu)} \right)^2 . \tag{8.10}$$

The least squares fitting value for $\tilde{N}(t)$ is calculated by equating the derivative of the above expression to zero. The value of $\tilde{N}(t)$ thus obtained is proportional to the population N_{HPTS} at time t. This results in a model independent estimate for the amount of population residing in either state at each time.

On the sub-ps timescale, there is an intense coherent peak that interferes with the population dynamics. Due to this peak, N_{HPTS} determined from the above procedure is not properly normalized. We can overcome this problem by monitoring the signal of the carbonyl stretching vibration of the acetic acid product at 1710 cm^{-1} because this band provides a direct measure of completed

proton transfer events (Fig. 8.2). Rini *et al.* [125] observed the fractions of acetic acid formed within 150 fs to be 0.11, 0.24 and 0.39 at 0.5, 1 and 2 M of acetate, respectively. We find similar numbers from the analysis of the carbonyl band shown in Fig. 8.2. This figure shows an initial contribution within the time resolution of ∼200 fs with an amplitude that agrees well with the results of Rini *et al.* [125]. We therefore normalize N_{HPTS} at 1 ps (where the coherent process is mostly over) to 0.89, 0.76 and 0.61 at 0.5, 1 and 2 M of acetate, respectively.

The normalized time-resolved infrared signal from HPTS* (1480 cm^{-1}) in D_2O and three acetate concentrations at 5 °C are shown in Fig. 8.3. The signal drops significantly on the sub-ps timescale indicating an initially very fast acid-base reaction [125]. After the first picosecond the decay of the signal becomes more moderate.

The theoretical lines in Fig. 8.3 were obtained from a numerical solution of Eq. (8.7). With the SCK model (delta function sink term, Eq. (8.8)), it was not possible to get a good description of the very early time dynamics (< 1 ps), and thus in Fig. 8.3 we only give the best fits (dashed lines) with the SCK model for $t > 1$ ps (renormalizing the calculation at 1 ps as described above). In these fits we have set the 'contact radius' (distance of minimal approach), a, to 6.8 Å (the precise value has little effect on the quality of the fit), corresponding to an acid-base separation of at least one water molecule [157]. It is seen that the SCK model is inappropriate for $t < 100$ ps, which we remedy by determining a more suitable functional form for $k(r)$.

Considering next the family of functions $k(r)$ defined in Eq. (8.2), we search for an optimal value for n for which the theoretical $S(t)$ fits the experimental data over the *entire* time-scale. Given that the early dynamics are due to directly hydrogen-bonded pairs [125], this means that $k(r)$ depicts the proton transfer reaction over all distances from the hydrogen-bond distance of 2.8 Å outwards. Hence we set $a \approx 2.8$ Å in Eq. (8.2). The optimal value of n was subsequently determined from the short-time kinetics as follows.

For each concentration and each value of $n = 1$, 2 and 3, we have first fitted the entire time dependence of N_{HPTS} to $S(t)$ from Eqs. (8.5)–(8.7). These solutions were subsequently convoluted with a Gaussian instrument response function of 500 fs full-width at half maximum (FWHM) and shifted from the time-origin by 250 fs. Fig. 8.4 shows this comparison using the 2 M data from Fig. 8.3 on an expanded scale, focussing on the first few ps. Due to the presence of the coherence peak at $t < 1$ ps, the differences between the fits for different n are observed best at the highest concentration (2 M). It is seen that a fit with $n = 1$ (exponential sink) is somewhat inferior to fits with $n = 2$ or 3 (the latter two giving similar results). Therefore for the remainder of this work we have selected a Gaussian sink, $n = 2$. In addition to globally fixing a and n, the on-contact rate-constant in Eq. (8.2) was given a large and constant value, $k_0 = 10^{14}$ s^{-1}. This leaves only two parameters to be adjusted at each value of ρ and T, namely Γ, determining the width of $k(r)$, and the diffusion coefficient D. Unfortunately, there are no directly measured values of D available. Variation of D does not affect the ultrafast phase, but does affect rather strongly the

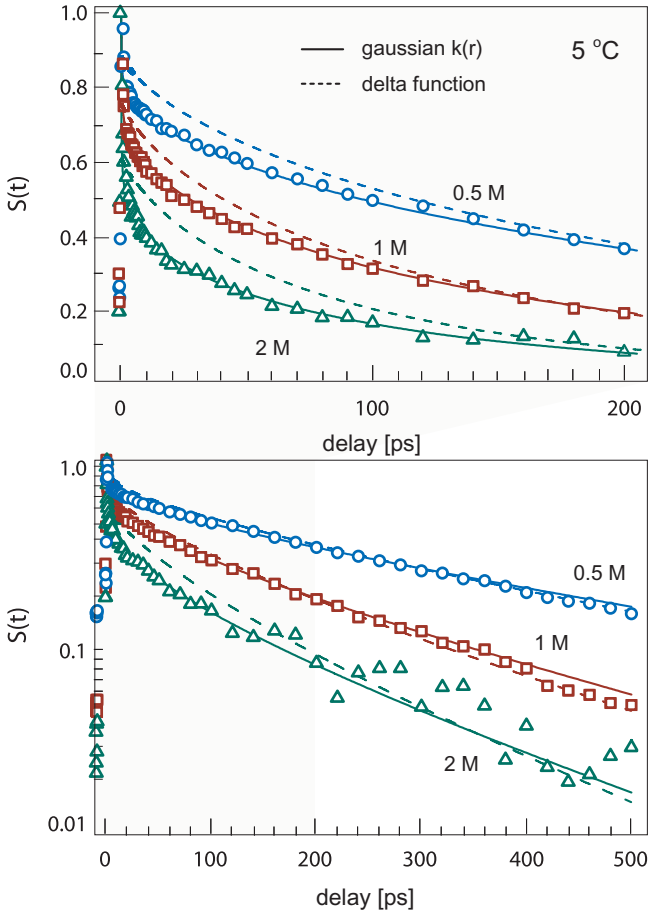

FIGURE 8.3. Time resolved infrared signals (symbols) from excited HPTS in D_2O at 5 °C and three acetate concentrations, normalized at 1 ps (to 0.89, 0.76, and 0.61 for $c = 0.5$, 1, and 2 M acetate, respectively), are depicted as symbols on two different timescales: (top) linear (up to 200 ps), and (bottom) semi-logarithmic (up to 500 ps). Lines are fits to the solution of Eqs. (8.5)–(8.7) with two different sink terms: (dashed lines) Delta-function sink, Eq. (8.8), with $a = 6.8$ Å and $k_0 = 100$, 60, and 35 ns^{-1} for $c = 0.5$, 1, and 2 M acetate, respectively. (full lines) Gaussian sink term, Eq. (8.2) with $n = 2$, and parameters in Tables I and II.

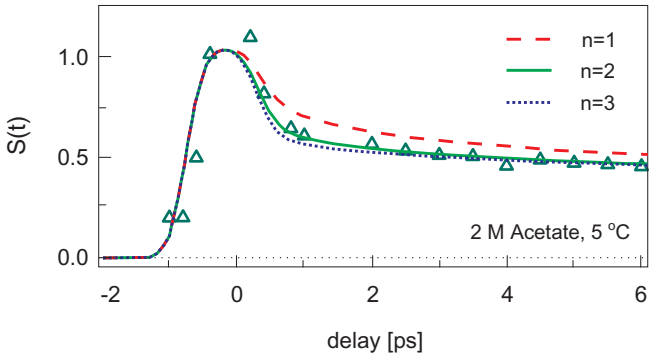

FIGURE 8.4. The 2 M data from Fig. 8.3, on a linear scale and up to 6 ps, is compared with the theoretical solution which is convoluted with an instrument response function of 500 fs (FWHM). The values of D used in the calculation are given in Table I. For $n = 2$ (full lines) the values of Γ are collected in Table II (see Eq. (8.2)). The best fits for $n = 1$ and 3 are shown by the dashed lines. The values of Γ for $n = 1$ are 0.44, 0.4, and 0.37 Å for $c = 0.5$, 1, and 2 M, respectively, while for $n = 3$ they are 5.0, 3.7, and 3.0 Å^3.

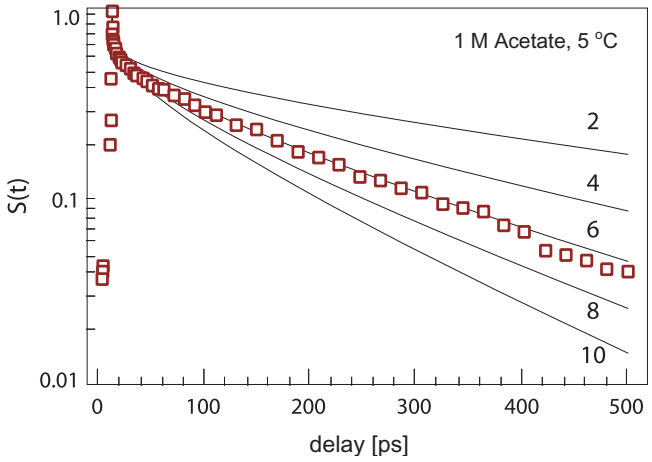

FIGURE 8.5. The effect of varying the diffusion constant on the acid-base kinetics, demonstrated for the reaction of HPTS* with 1.0 M acetate at 5° C (same data as in Fig. 8.3). The lines were calculated with $\Gamma = 1.2$ Å^2 (see Table II) and the indicated values of D (in units 10^{-6} cm^2/s).

ρ / M	5 °C	30 °C	65 °C
0.5	6.9	14.0	26.7 (26.0)
1.0	5.9	12.1 (11.5)	23.1
2.0	4.5 (3.5)	9.1 (7.0)	17.4 (17.0)

TABLE I. Estimated relative diffusion coefficients (in units 10^{-6} cm^2/s) between HPTS and acetate, $D \equiv D_{\mathrm{HPTS}} + D_{\mathrm{Ac}^-}$, in liquid D_2O containing sodium acetate salt at different concentrations (rows) and different temperatures (columns). See Appendix 8.7 for further detail. Values in parentheses are those actually used in the fits (when different from the estimated ones).

ρ / M	5 °C	30 °C	65 °C
0.5	1.5	1.2	0.7
1.0	1.2	1.0	0.9
2.0	1.1	0.9	0.8

TABLE II. Fitting parameter Γ (in Å^2) for $k(r)$ of Eq. (8.2) with $n = 2$, $k_0 = 10^{14}$ s^{-1}, $a = 2.8$ Å and D from Table I.

longer time kinetics, as demonstrated in Fig. 8.5. With increasing values of D, the HPTS-acetate collision events become more frequent leading to faster proton transfer kinetics.

In order to limit the variation of D in the fitting procedure, we have adopted the following approach. We have assumed that in water $D = 1.0 \times 10^{-5}$ cm^2/s at 25 °C and 2 M acetate, and obtained $D(T, c)$ in D_2O by utilizing experimental data for D_2O viscosities as a function of temperature [23] and concentration [52]. The underlying assumption here is the validity of the Stokes-Einstein relation between diffusion constant and viscosity. The analysis is detailed in the Appendix 8.7, with the ensuing values of D summarized in Table I. In the final fits, a few values of D are somewhat different from those in Table I. These values are shown in parentheses there.

Using predetermined values of D leaves only a *single* adjustable parameter, Γ, in fitting the kinetics at the 9 combinations of ρ and T (see Table II). Fig. 8.3 shows the fits to the 5 °C data as solid lines, whereas Fig. 8.6 shows these fits at the two higher temperatures, 30 °C and 65 °C respectively. Although the noise in the experimental data increases with increasing T, it is apparent that the model provides a good description of the experimental results at all temperatures. The values of Γ (Table II) obtained from these fits decrease with increasing T, meaning that $k(r)$ decays more rapidly with r at higher

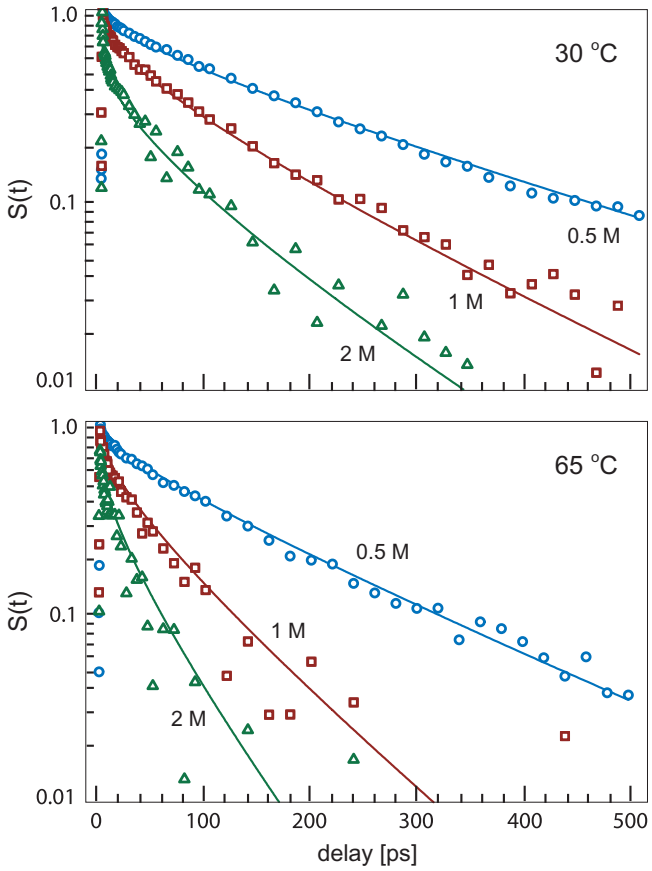

FIGURE 8.6. Near-infrared kinetics for proton transfer between HPTS* and acetate at 30 °C and 65 °C. Other details as in Fig. 8.3.

temperatures. At the lowest concentration of 0.5 M, Γ shows the strongest decrease with temperature. The dependence of $k(r)$ on T in this case is depicted in Fig. 8.7.

The reactive flux density in our model is given by $k(r)\varphi(r,t)$. The reactive flux density multiplied with r^2 depicts the radial reaction flux density at different acid-base separations. Fig. 8.8 shows this function at different times for the lowest temperature and concentration measured in this study. Because at $t = 0$ we have $\varphi(r,0) = 1$, the flux density is initially equal to $k(r)$ and thus peaks at $r = a$. At $t = 100$ fs most of the reaction still takes place close to contact, within directly bound acid–base pairs. By $t = 1$ ps we get a flux peaking around 5 Å, which corresponds to acid and base separated by one water molecule. This distribution has a tail to large distances. Because the peak diminishes strongly with time, the relative contribution of the tail increases with t, and it corre-

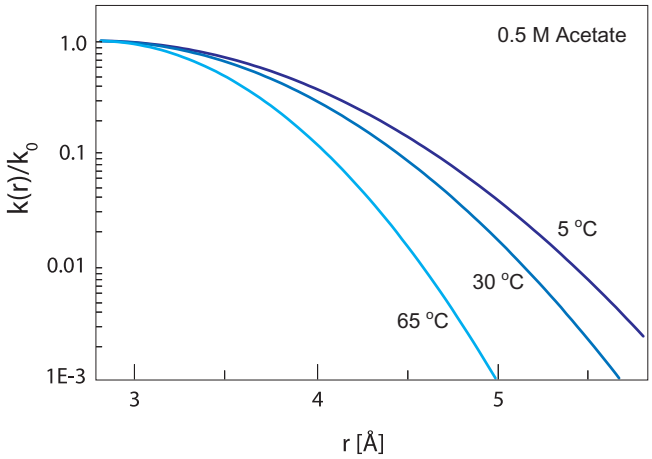

FIGURE 8.7. Temperature dependence of the distance-dependent rate constant for proton transfer between HPTS* and 0.5 M acetate, using the values of Γ from Table II.

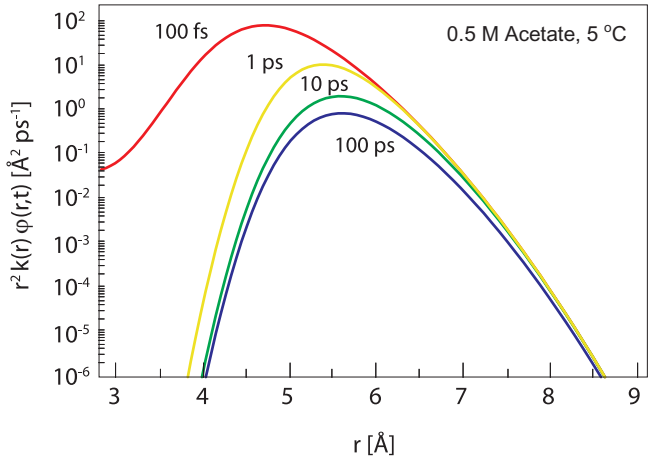

FIGURE 8.8. The distance dependence of the radial reactive flux density for proton transfer between HPTS* and 0.5 M acetate at 5 °C, with $\Gamma = 1.5$ Å^2 (Table II).

sponds to water wires containing more than one water molecule [132]. The long-r tails show the onset of diffusive motion as follows. At short times, when the population is static, $k(r)\varphi(r,t)r^2$ tends to the same large r asymptotes. A similar inhomogeneous limit was previously recognized in the short-time behavior of carbon monoxide binding to myoglobin [3]. As diffusion sets in, the outer part of the distribution moves inward to compensate for reacting pairs, as seen in the long-r tail for $t = 100$ ps.

8.5 DISCUSSION

According to the traditional view of proton transfer in solution [40,41], acid and base molecules diffuse first to a 'contact distance' at which they are separated by one water molecule ('inner-sphere' mechanism). At this particular distance the proton transfer reaction takes place. However, from the present and previous femtosecond mid-infrared experiments it follows that there exists a range of distances at which the proton can be transferred from the acid to the base [29, 97, 99, 132, 133].

At early times (<1 ps), a very rapid simultaneous decay of the HPTS* band and rise of the acetic-acid carbonyl band are observed. This phase reflects an ultrafast proton transfer reaction most likely occurring in acid-base pairs that were directly hydrogen-bonded already in the ground state [125, 126]. At longer times the observed decay becomes much slower and considerably more sensitive to temperature. The dynamics of this slower phase was originally attributed to diffusion bringing the acid-base pair into contact. Following a successful application of the SCK model to acid-base reactions in glycerol-water mixtures [25,26], Rini *et al.* [125,126] have applied this model to the HPTS/acetate system. However, the experimental data deviates from exponential behavior more than predicted by the SCK model, as illustrated in Fig. 8.3. To explain these observations, Rini *et al.* [125, 126] and later Mohammed *et al.* [97–99] introduced additional subsets of acid-base complexes with different kinetics to fit the data. The final model involved coupled kinetic equations for sequential proton hopping along water chains of different lengths, with additional rate constants for changing the chain length, totalling in some two dozen adjustable parameters (including the ultimate diffusion process) [99]. Siwick *et al.* also found evidence for proton transfer taking place in a distribution of hydrogen-bound reaction complexes that differ in the number of water molecules separating the acid and the base [132, 133]. The observed proton transfer kinetics could be modeled well by assuming that the distribution of reaction complexes is statistical (only determined by the base concentration), and that the rate of proton transfer within a complex scales down by a constant factor for every additional water molecule in the chain separating the acid and the base. This description implies that the rate constant of proton transfer is assumed to depend exponentially on the length of the water wire connecting the acid and the base.

Here we have fit the whole time dependence of the proton transfer kinetics (including the fs phase) with a single distance-dependent rate coefficient, $k(r)$,

adjusting essentially a *single* parameter Γ at each ρ and T. We found from the short-time kinetics that proton transfer is best described by a Gaussian-shaped $k(r)$ (see Fig. 8.4). Our model is mathematically similar to the Wilemski-Fixman [158] models applied to fluorescence quenching by electron transfer in solution [104,129,135]. Because a Gaussian starts to decay rapidly only beyond a certain distance r, its r-dependence is qualitatively similar to assuming static quenching within an inner spherical shell, and exponential quenching outside it [129]. Despite these formal similarities between the electron-transfer studies and the present study of proton transfer, the physical mechanisms responsible for the distance dependencies are different. For electron-transfer reactions, the distance dependence is thought to reflect the exponential decay of the electronic wave-function at large distances. Hence, for electron-transfer the coupling is through space. For proton transfer, the reaction is not through space but proceeds through more or less randomly coiled water wires, and this could lead to a Gaussian dependence of the transfer rate on the radial distance r as follows.

Suppose the water wire forms a freely joint chain (no angular restrictions). The mean end-to-end distance, $\langle (r-a)^2 \rangle^{1/2}$, of the water wire is then proportional to the square root of N, the number of water molecule monomers, by [46] $\langle (r-a)^2 \rangle^{1/2} = N^{1/2} L$, where L is the distance between the water molecules ($\approx$ 2.8 Å). From this relation it follows that the Gaussian-shaped $k(r)$ corresponds to an exponential dependence on the water wire length NL: $k(N) = k_0 \exp(-NL/\Gamma')$, with $\Gamma' = \Gamma/L$. This argument may explain a Gaussian $k(r)$ for long chains. However, it should be realized that the angles between the hydrogen bonds in the water wire are not arbitrary and the water wires will contain only a limited number of water molecules. For short wires it is thus possible that the functional form of $k(r)$ arises from a different origin such as quantum effects. This relation therefore requires further study.

A central question is how proton transfer across these 'water wires' takes place. Previous work argued for a sequential single-proton transfer mechanism, in which the proton released from the photo-acid hops along the wire until it eventually reaches the base [97–99,125,126]. This scenario supports a localized D_3O^+ cation on a water molecule separating acid and base [98], based on the observation of a narrow-band absorption around 1900 cm^{-1} (cf. Fig. 8.1). In a sequential scenario, if each hop between a pair of water molecules took 1–2 ps as in liquid water [93], crossing the chain would induce a ps delay between the rise in the acetic acid signal and the decay of the HPTS absorption, which is not observed. In addition we find here that proton transfer can be described by a *single* rate constant, $k(r)$, rather than a series of rate constants for sequential proton hops as previously assumed [99].

An alternative scenario that is consistent with our findings is a *concerted* mechanism. Concerted proton transfer means that in chains of N water-molecules connecting acid and base, $N+1$ protons move simultaneously and unidirectionally, each hopping across a single hydrogen-bond. The concerted scenario is not only supported by the absence of any delay between the photo-acid decay and the rise of acetic acid signal, but also by the measured temperature effect. In a sequential scenario, each hopping event should become

more rapid with increasing temperature, as is the case for proton mobility in liquid water. [4] Therefore, if $k(r)$ were an 'effective' function depicting the overall transfer rate, it should have increased with increasing temperature. In the present case the opposite is observed. The parameter Γ in Eq. (8.2) decreases with increasing T, see Table II, implying that $k(r)$ decreases with increasing T for $r > a$, as seen Fig. 8.7. This decrease can be explained by the enhanced disorder that disrupts the wire structure that is required for concerted proton transfer process to occur.

Concerted double- and triple-proton transfer is a common observation in intramolecular proton transfer through water-molecule bridges [69]. Intermolecularly, synchronous multi-proton motion was observed in quantal simulations of proton transfer along a water wire in carbonic anhydrase [30] and the green fluorescent protein (GFP) [152]. For GFP, the proton released from the photo-excited chromophore hops to a nearby water molecule at the same time as another proton hops from this water to Ser205 and a third proton moves from Ser205 to Glu222. Related to these observations, it was found that the proton dissociation rate coefficient for GFP *increases* as T is decreased from room-temperature to 230 K (Figure 6 in Ref. [82]). Although the time-resolution of the TCSPC system utilized there is inferior to that of the present method (and the quantal calculations), such an inverse temperature dependence may nevertheless reflect an increasing probability for concerted multi-proton transfer to occur at lower temperatures.

The conditions for concerted transfer are thus clearly different from those promoting incoherent proton transfer between water molecules in the liquid phase [4]. In liquid water, proton transfer along extended hydrogen-bonded chains of water molecules was observed (computationally) only within a narrow pore that restricts the water configuration to a single file traversing the pore. The proton mobility along such chains can be over ten times faster than that of bulk liquid water [17]. In the chain, the coordination number of the water molecules is reduced, each water molecule being engaged in only two hydrogen bonds. In particular one of the 'donor' hydrogen bonds which normally stabilizes the hydronium structure is missing. This hydrogen bond strength is estimated to be markedly larger ($\sim$20 kJ/mol) as compared to the average hydrogen bond of bulk water ($\sim$11 kJ/mol) [91]. Because a hydronium structure cannot be stabilized on any water molecule along the pathway, the concerted scenario becomes dominant.

8.6 CONCLUSIONS

We studied the mechanism of proton transfer between the photo-acid 8-hydroxypyrene 1,3,6-trisulfonate (HPTS) and the base acetate with femtosecond mid-infrared spectroscopy. In this study we varied both the base concentration (0.5, 1 and 2 M) and the temperature (5, 30, and 65 °C). We find that the data cannot be fitted with the conventional Smoluchowski-Collins-Kimball (SCK) model in which the proton transfer is assumed to occur only at a particular

acid-base separation. Instead, we find that the data at all studied concentrations and temperatures can be best described with a distance-dependent rate function $k(r)$, that shows a Gaussian dependence on r. The distance r is related to the length of the hydrogen-bonded water wires connecting the acid and the base. If the conformation of the water wires can be approximated as freely joint chains, r shows a square-root dependence on the length of the water wires, which implies that the Gaussian dependence of $k(r)$ on the radial coordinate r corresponds to an exponential dependence on the length of the water wires.

We find several indications that the proton transfer is a *concerted* process in which the proton is conducted from the photo-acid to the base via hydrogen-bonded chains of intervening water molecules. The concerted nature of the proton transfer is supported by the observation that the signal associated with the proton arriving at the base rises simultaneously with the decay of the photo-acid signal. In addition, we find that the parameter Γ and hence also $k(r)$ at $r > a$, Eq. (8.2), decrease with increasing temperature. If the proton transfer had proceeded via a sequential hopping process, the rate would have increased with temperature. The inverse temperature dependence of the concerted process can be explained from the fact that the increased disorder of the water solvent disrupts the water chain structures that are required for the concerted proton transfer to occur.

8.7 APPENDIX: DIFFUSION COEFFICIENT

We wish to estimate the relative HPTS-acetate diffusion coefficient in D_2O, containing sodium acetate salt at different concentrations and temperatures. We assume that the diffusion satisfies the Stokes-Einstein relation

$$D \propto 1/\eta\,, \tag{8.11}$$

where D is the diffusion constant and η is the viscosity. The temperature-dependence of the viscosity of H_2O/D_2O is described well by the approximation used in Ref. [23]. The resulting viscosities are summarized in Table III.

TABLE III. **Temperature dependent viscosity η**

T / °C	η_{H_2O} / mPa·s	η_{D_2O} / mPa·s	η_{D_2O}/η_{H_2O}
5	1.519	1.988	1.309
25	0.8903	1.100	1.236
30	0.7973	0.9759	1.224
65	0.4334	0.5104	1.178

The relative viscosity of H_2O/D_2O at room temperature and the estimates of diffusion coefficients D at different concentrations of sodium acetate (NaAc) salt were taken from Ref. [52] and are summarized in Table IV.

TABLE IV. **Concentration dependent relative viscosity and diffusion**

$c = [\mathrm{NaAc}]$ / M	$\eta_{\mathrm{H_2O}}(c)/\eta_{\mathrm{H_2O}}$	$\eta_{\mathrm{D_2O}}(c)/\eta_{\mathrm{H_2O}}$	$D(c)$ / 10^{-5} cm^2 s^{-1}
0.0	1.00	1.24	1.64/1.32
0.5	1.07	1.32	1.53/1.24
1.0	1.24	1.53	1.32/1.07
2.0	1.64	2.03	1.00/0.81
3.0	2.30	2.84	0.71/0.58
4.0	3.00	3.71	0.55/0.44

Using the relative viscosity data given in Tables III and IV we estimate the relative HPTS-acetate diffusion coefficients using:

$$D_{\mathrm{D_2O}}(T,c) = D_{\mathrm{H_2O}}(T_0,c_0) \times \frac{\eta_{\mathrm{H_2O}}(T_0,c_0)}{\eta_{\mathrm{H_2O}}(T_0,c)} \frac{\eta_{\mathrm{H_2O}}(T_0)}{\eta_{\mathrm{D_2O}}(T)} \tag{8.12}$$

where $c_0 = 2.0$ M, $T_0 = 25$ °C, and $D_{\mathrm{H_2O}}(T_0,c_0) = 1.00 \times 10^{-5}$ cm^2 s^{-1}. The resulting diffusion coefficients $D_{\mathrm{D_2O}}(T,c)$ are those given in Table I.

9 Proton Transfer in Ice

We have studied proton transfer in ice samples containing the photo-acid HPTS and the base sodium-formate using femtosecond pump-probe spectroscopy. Pump pulses, centered at a wavelength of 400 nm, electronically excited the photo-acid molecules which released their protons. These protons subsequently traveled from the photo-acid through the ice lattice to the base and were observed as they arrived at the base using the transient absorption of an infrared probe pulse. Both the temperature and concentration dependence of the proton transfer dynamics were modeled using a discrete set of two intrinsic transfer rates, associated with short and long range proton transfer, respectively. Proton transfer in configurations where the acid and base were separated by up to about two water molecules, was found to occur on a ∼1 ps timescale for all temperatures (240-270 K). Long range direct proton transfer through water wires of about four water molecule length was found to occur on a ∼300 ps timescale for 270 K. This latter process was observed to slow down significantly with decreasing temperature, with an activation energy of ∼80 kJ/mol.

9.1 Introduction

Hexagonal ice I_H is the most common form of ice on earth. One of the outstanding properties of ice I_H is its relatively high proton mobility. This mobility is important since it forms the basis of most of the anomalous mechanical and electrical properties of ice. That protons can be mobile in ice is in fact quite surprising, because in a perfect ice crystal the hydrogen atoms are expected to be completely immobilized. Therefore the proton mobility is believed to result from the presence and rapid migration of particular defects of the ice lattice.

Whereas liquid water consists of a wide variety of different hydrogen bond distances, strengths and angles, the structure in ice is much more rigid. The molecules in ice I_H form nearly homogeneous hydrogen bond connections with all four of their neighbors at directions close to the tetrahedral angle (109.5 °). This tetrahedral arrangement causes the open structure of ice I_H and explains its relatively low density compared to water (0.92 g/cm^3 vs 1.00 g/cm^3).

The tetrahedral arrangement of hydrogen bonds in ice allows for a total of six different orientations of the two hydrogen atoms of the water molecule. Ice

I_H has a proton-disordered arrangement as in various other ice polymorphs. In general the orientation of the molecules is determined by the so called Bernal-Fowler ice rules [15]. These rules state that each oxygen atom is connected to two nearby hydrogen atoms and that on each connection between two oxygen atoms, exactly one hydrogen resides. Deviation from these rules can lead to ionic and orientational (Bjerrum [16]) defects. If a proton moves along the hydrogen bond to a neighboring water molecule, the first rule is violated and a pair of OH^- and H_3O^+ ions are created. If a hydrogen atom rotates around the oxygen it is covalently bound to, then the second rule is violated resulting in a pair of Bjerrum L and D defects.

According to Jaccard theory [58] both types of defects contribute to the long range conduction of protons in ice. Intermolecular proton transfer, where a proton hops to the next water molecule is mediated by the migration of ionic defects while intramolecular proton transfer, where a proton moves around the oxygen while staying on the same molecule, is mediated by the migration of Bjerrum defects. In general, such a proton hopping relay cannot continue indefinitely and stops after a certain distance [79] depending on the local arrangement of the 'water wire'.

The number of defects in ice depends on various factors such as the type of ice, the temperature, and the presence of solutes. For example, going from hexagonal ice I_H to the cubic phase (I_C), the protons become more ordered. At lower temperatures, the number of defects decreases and the ice becomes more structured. The introduction of acidic molecules in the ice creates excess protons in the form of ionic H_3O^+ defects. Similarly, ionic OH^- defects are obtained by adding base molecules. Finally, molecules that do not fit into the periodic ice lattice, act both as sources of lattice defects and as obstacles to defect motion.

Measurements on the conductivity of ice started already in the 19th century when Ayrton and Perry connected two metal electrodes to a block of ice and found an anomalously high conductivity [9]. Later experiments by Eigen [39] seemed to indicate that the proton mobility in ice is much larger than in water. However this increased conductivity was later attributed to surface mobility and not to bulk conduction. Since then a variety of spectroscopic techniques have been used to explore the dynamics of protons and defects in ice crystals. Kunst and Warman [68] used a 50 ns laser pulse to create ionic defects in ice and measured proton mobility using time resolved microwave conductivity measurements. Wooldridge and Devlin [160] used the excitation of the photo-acid 2-naphtol by a mercury lamp to inject protons into deuterated ice and followed the dynamics of protons by monitoring the FTIR spectrum. From their results they estimated the enthalpy of self-ionization in ice to be about 70 kJ/mol.

In recent years the ability to generate ever shorter laser pulses have extended the regime at which we can observe proton transfer down to the sub-ps time range. The excitation of photo-acids with ps laser pulses provide the possibility to release a proton at a very specific instant in time. Huppert [118, 119] was among the first to observe excited-state geminate recombination using time-

correlated single-photon counting (TCSPC). Using this technique, this group has since performed excellent and extensive studies on a wide variety of proton transfer reactions in both liquid water and ice [81, 83, 149–151]. From their experiments they concluded that proton diffusion in ice is ten times larger than in water of the same temperature.

In the previous chapter on proton transfer between HPTS and acetate in liquid D_2O, we successfully described the data obtained from a range of temperatures (5-65 °C) and base concentrations (0.5-2.0 M) with an extended Smoluchowski [124, 143] model which included a distance-dependent reaction rate $k(r)$. From the temperature dependence, it was concluded that this rate $k(r)$ represents *concerted* proton transfer across water wires of different lengths r, connecting acid-base pairs. In such a concerted transfer event, multiple protons move simultaneously, through Grotthus [4,31] hopping, along a pre-formed chain of hydrogen-bonded water molecules. The length and stability of such chains depends strongly on the structure of the water, e. g. the average number of hydrogen bonds [17].

In this chapter we extend these measurements to the solid phase and present measurements on the carbonyl stretching mode which directly reflects the excited state proton transfer in ice I_H. Unlike geminate recombination studies, we are sensitive only to those protons that have made a *complete* transfer from acid to base. Because of the high degree of structuring of water molecules in ice and because diffusion of acid and base molecules is negligible, it can be expected that proton transfer takes place along pre-formed aqueous water wires. Such water wires are of particular importance in biology where they mediate the transfer of a proton through membrane protein channels [89].

9.2 EXPERIMENTAL

We used a pump-probe laser setup similar to the one described in Chapter 8. The time and frequency dependent absorption changes, following the photo-excitation of the photo-acids by a 400 nm pump pulse, were measured with an infrared probe pulse tuned to the frequency of the carbonyl stretch (1700 cm^{-1}). The pump pulses were focussed in the sample to a relatively large spot size. We took care that the intensity of the pump remained below the threshold where water starts to ionize due to multi-photon absorption, which would create a spectral response from dissolved electrons. To check the absence of this electron response, we also measured a sample where the photo-acid was omitted. The focus of the pump was tuned, using a telescope, well below the point where no more electron signal was detected. The sample was then replaced with one containing the photo-acid.

Even though the intensity was low enough that no measurable electrons were formed, long term exposure of the sample to UV pump pulses still caused a gradual degradation of the sample quality as witnessed by the decreasing signals and fluorescence. The *liquid samples* could be simply rotated in circles inside the pump focus to spread out the damage over a larger area of the sample. This

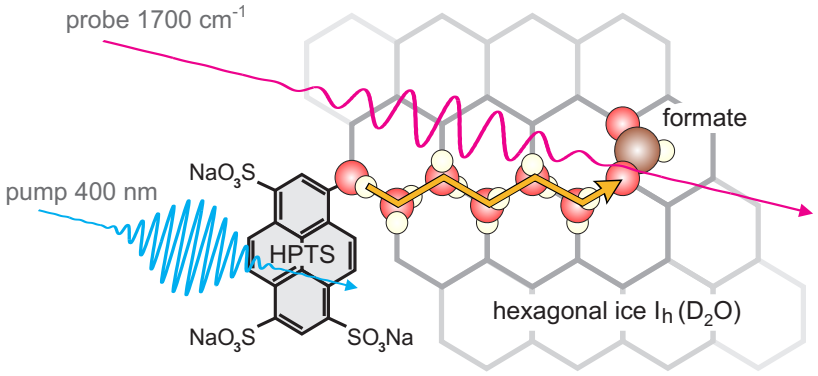

FIGURE 9.1. Schematic diagram of the experiment and sample composition. First, the HPTS photo-acid is electronically by the 400 nm pump pulse. Then, the proton transfers through the hexagonal ice by Grotthus [4,31] conduction along a water wire. Finally, the arrival of the proton at the base is detected through the carbonyl stretch, using a 1700 cm^{-1} probe pulse. The size of the HPTS molecule and the hexagonal structure of the ice are approximately to scale (C-C bond length in benzene ring 1.4 Å, O–H$\cdots$O distance in ice 2.7 Å).

allowed sufficiently long measurement times of about an hour before gradual signal loss could be observed. However, from earlier test measurements on a smaller, rotating (peltier cooled) ice sample we learned that sample degradation came much sooner for frozen samples than for liquid samples, probably because long timescale diffusion of photo-acids in and out of the pump trajectory could no longer take place. It was observed that a ring of decreased fluorescence was quickly 'burned' along the trajectory of the pump. To make things worse the signal to noise ratio of the rotating ice samples were also much poorer than in the liquid samples even though great care was taken to form homogeneous, clear ice samples with minimal scattering properties. To resolve these issues we used the home-built 'cryostat-rotator' discussed in Section 3.3.

The samples consisted of D_2O in which we dissolved 20 mM of the photo-acid HPTS (8-hydroxypyrene 1,3,6-trisulfonate, see Fig. 9.1) and 0.10, 0.25, or 0.50 M of the base sodium formate (Na^+HCOO^-). The samples were enclosed in a round cell between two c-cut sapphire windows of 31 mm diameter. The optical path length was set by a 25 μm teflon spacer. The sample cell was placed inside the vacuum housing of a closed-cycle liquid-helium cooled cryostat. The cryostat was suspended on a construction above the laser table that allowed the sample cell to be rotated while remaining in the focus of the overlapping pump and probe beams (i. e. the 'cryostat rotator', see Fig. 3.2 in Section 3.3).

We used D_2O instead of H_2O, because the absorption band of the HOH bending mode blocks our spectral observation window around 1700 cm^{-1}. Al-

though the transfer rate of deuterons is expected to be somewhat lower than that of protons, no fundamental difference in their transfer mechanisms is expected [83]. The concentration of HPTS we use here (20 mM) is high enough to allow for a sufficient pump-probe signal but low enough to prevent the formation of aggregates that would otherwise quench the excited state and hinder the proton release [6]. As the accepting base, we use sodium formate because it is the smallest of the carboxylic class molecules and will thus cause minimal disruptions to the surrounding ice lattice. The COO group has two stretching modes, symmetric and asymmetric. When the proton arrives at one of the two oxygen atoms, these two modes decouple, shifting the frequency of the carbonyl (C=O) stretch into the region around 1700 cm^{-1}. Compared to the previous chapter we here use relatively low concentrations of base molecules. From the analysis of signals for various base concentrations it was found that the statistical distribution of base molecules in the ice was maintained up to 0.5 M, but not at 1.0 M. Hence it appears that formate does not dissolve uniformly in ice around 1.0 M, but instead is being pushed towards the grain boundaries.

Upon freezing of the sample a dramatic decrease in signal and fluorescence was noticed. This is presumably caused by aggregation of HPTS molecules in the solid phase and was previously observed by the Huppert group [149]. Following their example, we added a small fraction of (deuterated) methanol (0.5%) to the sample which allows the HPTS to better dissolve into the ice lattice and to prevent the formation of aggregates. The methanol itself is expected to have negligible effects on the proton transfer at these low concentrations [81].

The choice for sapphire windows was made after several calcium fluoride windows broke in the freezing process. Whereas calcium fluoride is very vulnerable to thermal shock, sapphire is much harder and constitutes a very good heat conductor. The only disadvantage is its birefringence which may cause a rotation of the polarization. This drawback is circumvented by using c-cut windows that have the optical axis perpendicular to the cut of the window. The spacing of 25 μm was thin enough to cause minimal scattering of the probe light and the formation of a uniform ice sample, yet thick enough to allow enough absorption of the pump light.

The cryogenic setup allowed for both heating and freezing of the samples with a temperature stability of about 0.5 K. For the preparation of ice samples we first held the samples at 273 K for about 10 minutes followed by a rapid cooling to a low temperature (240 K) while monitoring the pump-probe signal. The sample was kept at 240 K for about 10 more minutes and then heated up to the desired temperature. Once the sample had reached its desired temperature, a linear spectrum was taken using an infrared spectrometer (Perkin-Elmer). From the linear spectrum we could clearly see that the sample was still frozen from the narrowed peak of the O–D stretch vibration of the D_2O solvent. During and after each measurement additional linear spectra were taken to confirm that the sample did not thaw (especially around 270 K).

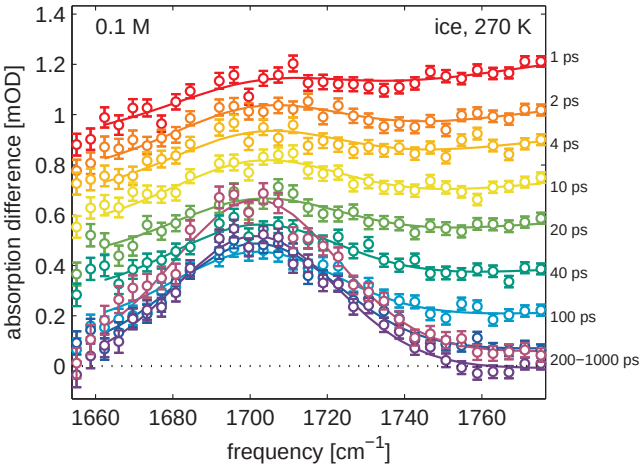

FIGURE 9.2. Transient absorption data in the region of the carbonyl stretch mode following excitation of the HPTS photo-acid. The sample contained 0.10 M sodium formate and was held at a temperature of 270 K. The points are the measured absorption difference spectra at various pump-probe delay times (indicated on the right). The data contains contributions of the ingrowing carbonyl stretch mode and a decaying featureless background. The lines show the result of the spectral fitting routine used to extract the population dynamics of the carbonyl stretch.

9.3 RESULTS

9.3.1 DECOMPOSITION

The pump-probe data sets $\Delta\alpha(t,\nu)$ consist of frequency (ν) resolved transient absorptions at various pump-probe delay times (t). A typical data set of ice at 270 K with 0.10 M formate is depicted in Fig. 9.2. Around 1700 cm^{-1} we clearly observe the ingrowing of the carbonyl (C=O) stretch as the proton reaches the formate molecule. Besides this ingrowing feature, the signal also shows a weakly sloped background band that decreases over time. The origin of this background band is likely the absorption of the (partially) dissolved proton/deuteron [60].

We extract the dynamics of the ingrowing carbonyl signal i. e. the arrival of the proton at the base, by decomposing the signal into its underlying constituent spectra. From a singular value decomposition (Section 4.2.1) on the data matrix $\Delta\alpha(t,\nu)$ we find that it is well described using a two component model. The first two singular values total 88% of the total signal while the subsequent components are $< 1\%$, indicating the noise threshold. We proceed to describe each component as the product of a time evolving population $N(t)$ and a corresponding spectral signature $\sigma(\nu)$:

$$\Delta\alpha(t,\nu) \;=\; N_{\mathrm{co}}(t)\cdot\sigma_{\mathrm{co}}(\nu) \;+\; N_{\mathrm{bg}}(t)\cdot\sigma_{\mathrm{bg}}(\nu)\,, \tag{9.1}$$

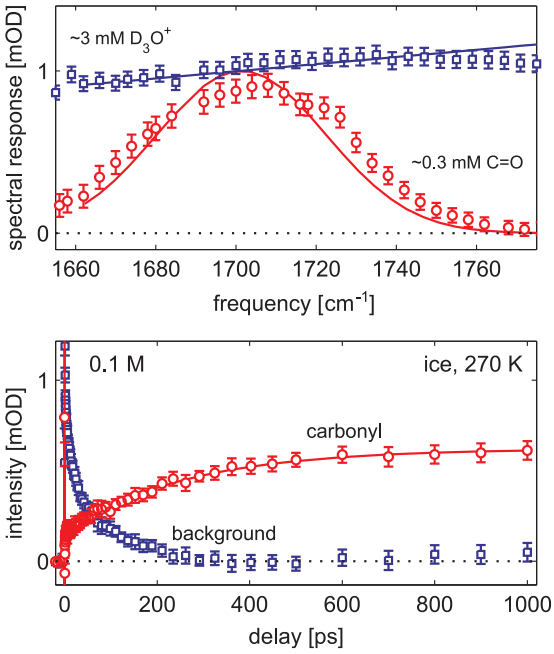

FIGURE 9.3. Decomposed spectra (left) and population dynamics (right) of 270 K ice with 0.1 M sodium acetate (Fig. 9.2). Left: for comparison the fitted carbonyl spectrum of the pump-probe data (Gaussian line) is superimposed with a linear difference spectrum of ∼0.3 mM formic acid and sodium formate (circles). The pump-probe background spectrum (line) is superimposed with a spectrum of ∼3 mM D_3O^+ (squares), obtained by taking a difference spectrum of deuterium iodide (DI) and sodium iodide (NaI). Right: The population dynamics of the ingrowing carbonyl peak can be fitted using a bi-exponential of ∼1 and ∼300 ps. The dynamics of the background show a strong peak around zero.

where the subscripts co and bg signify the carbonyl and (dissolved deuteron) background components, respectively.

To get the spectral signature of the carbonyl stretch, $\sigma_{co}(\nu)$, we take linear spectra of (frozen) D_2O solutions containing either formic acid or sodium formate. The shape of the difference spectrum is shown in the left of Fig. 9.3. As expected, the difference between the two samples is the presence of a band around 1700 cm^{-1}, belonging to the C=O stretch mode of formic acid. Formic acid is not a very strong acid (pK_a 3.7), therefore the difference spectrum does not contain much of the deuteron background band. To determine the response of a deuteron in ice we take a difference spectrum between a strong acid, deuterium iodide (pK_a -10) and sodium iodide, resulting in the other spectrum shown in Fig. 9.3.

The linear difference spectra illustrate that indeed the peak is due to C=O and the background is due to deuterons. We approximate the carbonyl stretch

with a (unity amplitude) Gaussian band of certain width and central frequency and the background as a single line with unity offset and certain tilt (see top panel of Fig. 9.3). The unity amplitudes serve to normalize the responses of different data sets. We then fit these two shapes to all delay times where for each iteration we calculate the best fitting linear combination of population amplitudes using the temporal decomposition methods described in Section 4.2.4:

$$\chi^2(\tilde{N}_{\mathrm{co}}, \tilde{N}_{\mathrm{bg}}) = \int d\nu \left(\Delta\alpha(t,\nu) \; - \; \tilde{N}_{\mathrm{co}} \cdot \sigma_{\mathrm{co}}(\nu) \; - \; \tilde{N}_{\mathrm{bg}} \cdot \sigma_{\mathrm{bg}}(\nu) \right)^2 , \quad (9.2)$$

The least squares fitting values for $\tilde{N}_{\mathrm{co}}$ and $\tilde{N}_{\mathrm{bg}}$ at each delay time are calculated by equating the derivatives of the above expression with respect to both variables to zero. The fit proceeds to vary the spectra until a global minimum is achieved. The result of this procedure is shown in Fig. 9.2. The fitted spectra σ_{co} and σ_{bg} are shown as lines in the top panel of Fig. 9.3 where it is shown that they are very similar to the linear spectra of the C=O and hydrated deuteron, respectively.

Because the fitted spectra are normalized, the values of $\tilde{N}(t)$ thus obtained are directly proportional to the population dynamics of the carbonyl stretch and background. This also means that we can compare different data sets without the need for any renormalization. It does not matter in principle what exactly constitutes the background, as long as its spectral signature does not resemble the carbonyl stretch mode (i. e. they are linearly independent).

9.3.2 TEMPERATURE DEPENDENCE

The bottom of Fig. 9.3 shows the decomposed population dynamics of both the carbonyl stretch and the background. The carbonyl intensity shows an initial, rapid (∼1 ps) ingrowth to about one third of of the end level, followed by a slower (∼300 ps) ingrowth. These two processes will be designated with the subscripts 0 and 1, respectively.

The rapid ingrowth fraction f_0 has a rate k_0 of about 1 ps^{-1}, which corresponds roughly to the proton hopping time of 1-2 ps that has been measured with NMR techniques [6, 90]. We note that f_0 is present both for the ice and supercooled water. This leads us to the assumption that f_0 is caused by directly connected acid-base pairs, since neither in water nor in ice would these configurations experience a diffusion limited reaction rate. This direct connection is formed either between a direct contacting acid-base pair [52] or a (short) wire of intermediate water molecules, aligned such that a concerted (multi proton) jump process can immediately take place between acid and base. We further note that the fraction f_0 does not increase upon freezing of the sample which would be the case if HPTS and base molecules would start to cluster in the ice formation process. The similarity in amplitude of f_0 in water and ice indicates that the quantum yield of proton release after excitation is also similar in these two systems.

The fitted line in the bottom of Fig. 9.3 shows that the slower proton transfer fraction f_1 with rate k_1 is well described using an ingrowing mono-exponential

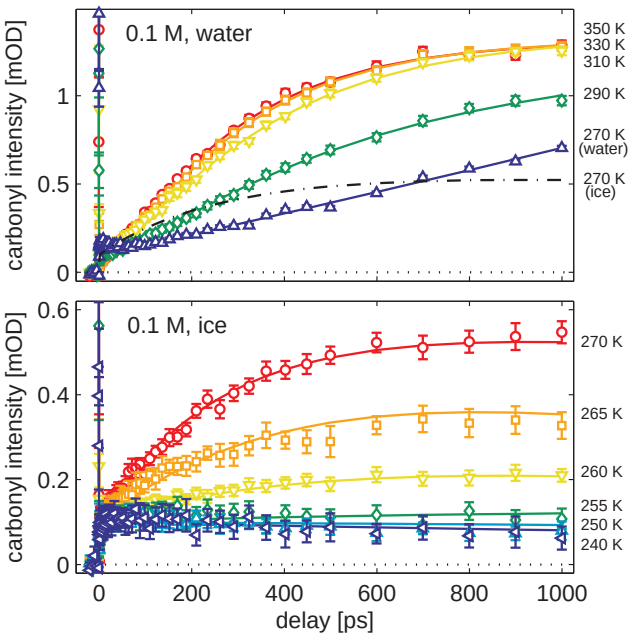

FIGURE 9.4. Ingrowth of the carbonyl stretch mode at different temperatures in liquid water (top) and ice (bottom). In the top figure the dashed line shows the ice data for 270 K to compare it more easily to the liquid water of the same temperature. For liquid water at low temperatures there is a delay between the excitation of the photo-acid and the ingrowth of the carbonyl peak. This delay is not present for ice of the same temperature. For higher temperatures the delayed ingrowth disappears and above 330 K no additional changes in proton transfer dynamics is observed. For liquid water the initial, rapid transfer (k_0) is seen to decrease for higher temperatures. For ice, no temperature dependence of this rapid fraction is observed. The long range transfer component (k_1) however is highly temperature dependent and its signal becomes dominated by the back transfer of k_0, below 255 K.

of about $1/300$ ps^{-1}. This finding is in stark contrast to the usual highly non-exponential behavior found for proton transfer in water [81, 98, 132]. Indeed, if we compare the transfer dynamics between 270 K ice and supercooled water (see top Fig. 9.4), we notice a striking difference. Whereas in water the carbonyl signal experiences a delayed ingrowth, in ice this signal grows in directly after the excitation. This delayed ingrowth was previously explained [29] as an indirect transfer channel, where the proton is first transferred from the acid to the water solvent and subsequently from the water to the base. It was also noted that this indirect transfer channel is much less noticeable for either higher base concentrations or stronger base molecules. The current observations we show that this type of indirect proton transfer does not occur as readily in ice as it does in water.

Concerning the carbonyl intensity, we note that after the initially slower start, it reaches a much higher end level in water compared to ice. Because we previously argued that the quantum yield of proton release is similar in water and ice (similar fraction f_0), this indicates that the total proton transfer reaction (in particular f_1) reaches a larger number of base molecules in water than in ice (within the HPTS excited state lifetime). This difference may at least in part be caused by the diffusion of the acid and base molecules themselves. In ice the diffusion of acid and base molecules is expected to be practically zero for these timescales. This means that, whereas in water a distant base molecule may still diffuse into the 'reaction radius' of either the acid or dissolved proton, this will not be the case for ice.

For higher temperatures of water, the indirect ingrowth channel diminishes, being almost unnoticeable above room temperature. Above 330 K no further increase in the proton transfer rate is observed. We speculate that, up to this temperature, diffusion of the proton itself is the rate limiting step for the indirect channel of proton transfer in water. This means that in this channel the proton is first released and can then find a base molecule. Conversely, as will be shown below, the indirect channel is completely absent in ice and proton transfer only occurs, provided a direct connection between acid and base is formed. We conclude that for the fraction f_0 this connection exists from the start and the proton can immediately transfer to the base, while for f_1 the formation of this direct connection is the rate limiting step in the whole transfer process. An example of such a (temperature dependent) step would be the reorientation of a 'misaligned' water molecule somewhere along the interconnecting water wire. Once this misaligned molecule has reoriented in a favorable manner, a concerted proton transfer immediately follows that brings the proton from the acid to the base molecule.

For different temperatures of ice (bottom Fig. 9.4), we see that the fraction f_0 stays about the same while f_1 is highly temperature dependent and quickly diminishes with decreasing temperature. Below 255 K the carbonyl intensity mainly shows a decreasing signal. This decrease is in fact present in all data and can be explained by the limited excited state lifetime of the HPTS. When the excited state of the HPTS (or PTS^-) decays, the molecule switches back to being a base and will try to reclaim its proton from the formic acid molecule. This process will occur almost instantaneously for the directly connected base molecules which dominate the signal at lower temperatures. For the higher temperatures the limited excited state lifetime is only observed at later delays when the proton transfer reactions (f_1) are near complete (see 265 K data in bottom Fig. 9.4).

9.3.3 CONCENTRATION SCALING

In Fig. 9.5 we see the effects of increasing the concentration of base molecules on the dynamics of the carbonyl ingrowth. First of all we clearly notice that the end levels start to increase for higher concentrations. Furthermore we note that the initial rapid fraction also increases. However these increases are not

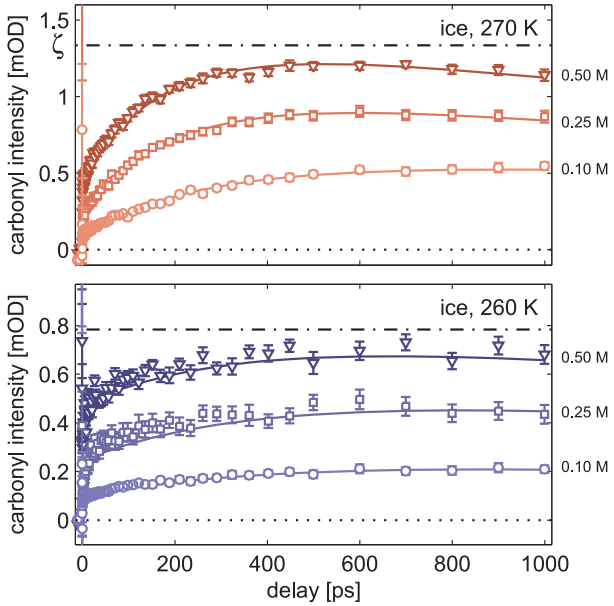

FIGURE 9.5. Concentration dependent ingrowth of the carbonyl intensity in ice for 270 K (top) and 260 K (bottom). The circles, squares, and triangles are the data for base concentrations of 0.10, 0.25, and 0.50 M, respectively. Lines are the result of a global fit described in the text. The dash-dotted line indicates the maximum intensity of the carbonyl ingrowth for high concentrations (ζ in Eq. (9.5)).

directly proportional to the increase of base concentration, meaning a doubling of the base concentration does not lead to a doubling of the end level.

As we have done in Chapter 8, we wish to describe the proton transfer in ice as a pseudo-unimolecular process. As we have shown in Section 4.5, the survival probability of the protonated photo-acid should scale as

$$S(t) = \exp\left(-\rho\, P(t)\right) , \tag{9.3}$$

where ρ is the concentration of base molecules and $P(t)$ the pair reaction probability.

In the absence of excited state decay, the measured carbonyl population $\tilde{N}_{\mathrm{co}}$ and the survival probability are related as:

$$\tilde{N}^{\,0}_{\mathrm{co}}(t) = \zeta\, (1 - S(t)) , \tag{9.4}$$

where ζ is a scaling constant that normalizes the maximum intensity of the carbonyl stretching mode. This scaling constant is the same for all base concentrations at a certain temperature because it only relates the signal of the carbonyl to the survival probability of the HPTS molecule. In Fig. 9.5 ζ, obtained from the relative scaling of the three concentrations, is indicated as the dash-dotted line above the graphs.

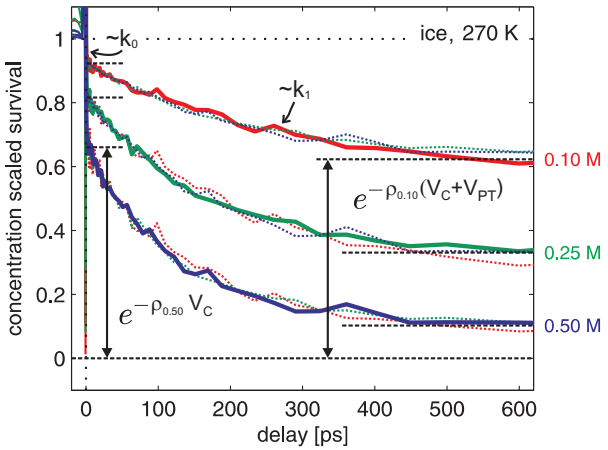

FIGURE 9.6. Concentration dependent 'survival probability' in ice at 270 K. Each concentration can be scaled using Eq. (9.6), and overlapped with the other two concentrations, showing that the distribution of base molecules obeys Poisson statistics. At longer delays (> 500 ps) a deviation occurs due to proton transfer back to the photo-acid. The contact and total reaction volumes may be deduced from the graphs using the short (< 10 ps) and long (> 500 ps) time range plateaus indicated with horizontal dashed lines (see Eqs. (9.14) and (9.15)).

Including the excited state decay of the HPTS molecule can be quite difficult and depends on the exact model for proton transfer. However in the simplest case where the excited state decay is much slower than the proton transfer rate we may decouple the two processes and simply write:

$$\tilde{N}_{\mathrm{co}}(t) = \zeta_{\mathrm{co}}(1 - S(t))e^{-k^* t}\,, \tag{9.5}$$

This equation no longer holds for lower temperatures where the proton transfer rate becomes comparably slow to the excited state decay. In that case we will have to revert to the rate equations of all processes involved. For now we will first treat the higher temperatures > 260 K.

Using Eq. (9.3) we can show that the survival probabilities of two concentrations ρ_1 and ρ_2 should scale as:

$$S_1(t) = \exp\left(-\frac{\rho_1}{\rho_2}\ln(S_2(t))\right)\,, \tag{9.6}$$

i. e. independent of the pair reaction probability, $P(t)$.

In Fig. 9.6 we show again the ice data of 270 K for three different concentrations (compare top of Fig. 9.5). However, for this figure all data were divided by $\zeta_{\mathrm{co}} = 1.3$ mOD and flipped vertically according to Eq. (9.4) in order to retrieve the survival probabilities. Superimposed on each survival trace are the two other 'concentration-scaled' survivals (dotted lines). We see that we can

quite nicely reproduce all traces: both the end levels but also the rapid ingrowth and the longer time dynamics. This shows that our conceptually simple model is very plausible.

However, as shown in Fig. 9.6, for the lowest concentration at long delay times (>500 ps) the curves start to deviate. In the top panel of Fig. 9.5, for the higher concentrations the back transfer rate starts to dominate at later delays while for the lower concentrations the carbonyl intensity is still ingrowing. The deviation is caused whenever the decay rate is not proportional to the number of base molecules (as is the case in the presence of back transfer).

9.3.4 QUANTITATIVE MODEL

Now that we have established a simple qualitative model for proton transfer in ice, we will expand this model in a more quantitative way. First of all, because we find essentially only two proton transfer rates for the 0.10 M data, it does not make sense to introduce any sort of distance dependent transfer rate as was done for water in Chapter 8. Instead we use the discrete version of Eq. (9.3), i. e. Eqs. (4.47)–(4.51) on page 58:

$$S(t) = \exp\left[-\sum_i \lambda_i \,(1 - e^{-k_i\, t})\right] \tag{9.7}$$

$$= \prod_i \sum_{n_i=0}^{\infty} \frac{e^{-\lambda_i} \lambda_i^{n_i}}{n_i!}\, e^{-n_i\, k_i\, t}\,, \tag{9.8}$$

The quantitative model uses the following assumptions and conventions:

- Each reaction rate k_i corresponds to a certain 'reaction volume' V_i, i. e. the volume containing the reacting base molecules. No explicit distance dependence of this volume with respect to the photo-acid is required. Nevertheless it is obvious that closer volumes will have faster reaction rates and further away volumes will be bigger.

- The average number of base molecules λ_i in a reaction volume V_i is proportional to the overall concentration ρ:

$$\lambda_i \propto \rho \cdot V_i\,. \tag{9.9}$$

  If the local concentration equals the overall concentration, the reaction volume may be equated to the actual volume and the proportionality turns into an equality. In that case the reaction volume is directly related to the physical size of the volume to which proton transfer takes place. However, if e. g. the local concentration is twice as high as the overall concentration due to clustering of base molecules, the physical volume will be twice as small as determined from the number of reacting base molecules.

- We convert the concentrations to a density ρ using the following:

$$1\text{ M} = 1\text{ mol/dm}^3 = 1\text{ mol} \cdot N_A/(10^{27}\text{Å}^3) = 6.0 \cdot 10^{-4}\text{Å}^{-3}\,, \tag{9.10}$$

where $N_A = 6.0 \cdot 10^{23}$ mol^{-1} is Avogadro's number. For ice, where the density of the solvent itself is lower, we scale all base densities and concentrations by the relative densities of ice and water:

$$\rho_{base\ in\ ice} = \frac{\rho_{ice}}{\rho_{water}} \times \rho_{base\ in\ water} \approx 0.92 \times \rho_{base\ in\ water} \tag{9.11}$$

- The actual number of base molecules n_i in a reactive volume is an integer value and is distributed over all possible configurations according to the Poisson statistics of the expectation value λ_i:
- The reaction rate to a volume is directly proportional to the number of base molecules residing in that volume.

Note that Eqs. (9.7) and (9.8) also contains $n_i = 0$ which will be the chance to find no base molecules within the reactive volume. If the concentration is low enough the probability will be high to find configurations where no reactions take place (rate $0 \times k$). This is essentially what causes the different end levels for lower concentrations: the chance that no proton transfer will occur.

Unlike the previous chapter we will not assume any distance dependence, because we previously observed that for the lowest concentration we could only observe two unimolecular rates. In fact the two rates k_0 and k_1 are so far apart (1 and 1/300 ps^{-1}) that we found it was nearly impossible, let alone meaningful, to fit them with a continuous distance dependence. We will thus determine $S(t)$ as being the result of only two unimolecular rates: the rapid transfer rate k_0 and the slower transfer rate k_1. Following the data of Fig. 9.4 and Fig. 9.5 we will allow k_1 to be temperature dependent but not concentration dependent.

We limit the number of reaction volumes to just two. First, the direct contact volume V_0 and second the 'long distance' proton transfer volume V_1, each with a corresponding rate k_0 and k_1:

$$S(t) = \exp\left[-\rho \cdot \sum_{i=0,1} V_i \left(1 - e^{-k_i\, t}\right)\right] \tag{9.12}$$

We note that these equations fulfill the concentration scaling properties of Eq. (9.6), that were used earlier. Furthermore, for long time delays the survival probability goes to

$$S(t \to \infty) = \exp\left[-\rho \cdot (V_0 + V_1)\right] . \tag{9.13}$$

This equation will go to zero only for high concentrations or large reaction volumes. From the end levels of Fig. 9.6 we can now deduce directly the total reaction volume $(V_0 + V_1)$ of proton transfer at 270 K ice. This reaction volume is most accurately calculated using the end level of the lowest concentration, 0.10 M:

$$V_0{+}V_1 = \frac{-\ln(S(t \to \infty))}{\rho} \approx \frac{-\ln(0.63)}{0.10 \times 0.92 \times 6.0 \cdot 10^{-4}\ \text{Å}^{-3}} = 8.4{\cdot}10^3\ \text{Å}^3 \tag{9.14}$$

The average number of base molecules in this volume at 0.10 M is $\rho \cdot (V_0 + V_1) = 0.46$. From this average we calculate that the (Poisson) chance to find more than one base molecule within the reaction volume is about 8%. This is the reason that a mono-exponential ingrowth fits so well to the data in Fig. 9.3. The higher concentrations of 0.25 and 0.50 M however have on average 1.2 and 2.3 base molecules within the reaction volume. This means that especially the highest concentration shows a distribution of rates (as expressed in Eq. (9.8)).

Using the fact that the direct contact rate k_0 is so much faster than k_1 we can assume that the initial rapid ingrowth (up to 4 ps) is predominantly caused by reactions with the direct contact volume. This allows us to estimate separately the direct contact volume. For example, for the concentration of 0.50 M in Fig. 9.6 we measure an initial drop down to about 0.68. This means that the direct contact volume equals:

$$V_0 = \frac{-\ln(0.68)}{0.50 \times 0.92 \times 6 \cdot 10^{-4}\ \text{Å}^{-3}} = 1.4 \cdot 10^3\ \text{Å}^3\,. \tag{9.15}$$

Of course this means that the volume $V_1 \approx (8.4 - 1.4) \cdot 10^3\ \text{Å}^3 = 7.0 \cdot 10^3\ \text{Å}^3$.

9.3.5 GLOBAL FIT

As noted before, the fact that the proton transfer process at low temperatures becomes comparable to the excited state lifetime, causes deviations from the model of Eq. (9.5). Basically what happens is that when the excited state decays, the proton does not immediately go back to the photo-acid. This process should be included in the complete model. Furthermore we wish to include the possibility that, due to quenching, the excited state lifetime is different depending on the position of the proton, be it at the photo-acid or at the base [54].

We therefore construct a set of rate equations based on the model described in Fig. 9.7. In this model we keep track of the position of the proton, either at the photo-acid (HPTS) or dissociated from the photo-acid (PTS^-) and at the carbonyl of the base molecule in any of the two reaction volumes V_0 or V_1. We assign the rates $n_0 \cdot k_0$ and $n_1 \cdot k_1$ to proton transfer from the photo-acid depending on the number of base molecules (n_0 and n_1) residing in the respective reaction volumes. This number is Poisson distributed over different configurations and dependent on the concentration. The super-scripted star in $HPTS^*$ and PTS_i^{*-} indicates the excited state of the photo-acid in this configuration. This excited state is allowed to decay with two different rates k_q^* and k^*, depending on the position of the proton (near the photo-acid or base, respectively). If the proton is near the photo-acid, there is a chance that it will recombine (non-adiabatically) with the HPTS and quench its excited state [6]. If the excited state of the conjugate base decays, it becomes a strong base and it will take up the proton again. This results in the back-going transfer rates k_0' and k_1' that were chosen here to have the same value as the forward going rates. Unlike the forward rates, the backward rates are not multiplied with the

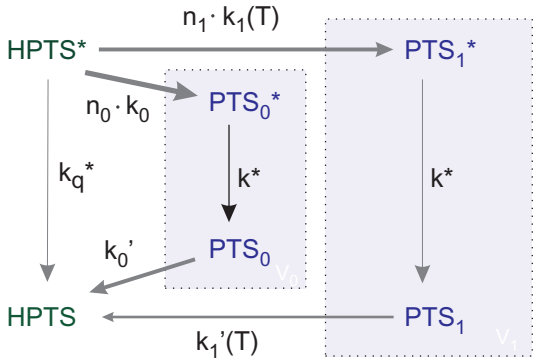

FIGURE 9.7. Schematic diagram of the model used for the global fit. Arrows indicate population transfer between different components HPTS*, HPTS, PTS$_i^{*-}$, and PTS$_i^-$. HPTS and PTS$^-$ are configurations where the proton reside at the photo-acid or base molecule, respectively. The star (*) indicates that the originating photo-acid is in the excited state. Horizontal/diagonal arrows indicate proton transfer with rates k_0 and k_1, to and from the base molecule. The two boxes indicate the reaction volumes V_0 and V_1, where the base molecules conceptually reside. The reaction rate of proton transfer to a reaction volume is multiplied with the number n_0 or n_1 of base molecules residing in that volume. Vertical downward arrows indicate the excited state decay k^* and k_q^* of the photo-acid, when the proton is at the base or by the photo-acid, respectively.

number of base molecules n_i in the reaction volume V_i, therefore the total back reaction rate is concentration independent.

The rate equations can be written in the form of a matrix as follows:

$$\frac{d}{dt}\begin{pmatrix} N_{\mathrm{HPTS}^*}(t) \\ N_{\mathrm{PTS}_0^*}(t) \\ N_{\mathrm{PTS}_1^*}(t) \\ N_{\mathrm{PTS}_0}(t) \\ N_{\mathrm{PTS}_1}(t) \\ N_{\mathrm{HPTS}}(t) \end{pmatrix} = \begin{bmatrix} -n_0\cdot k_0 - n_1\cdot k_1 - k_q^* & 0 & 0 & 0 & 0 & 0 \\ +n_0\cdot k_0 & -k^* & 0 & 0 & 0 & 0 \\ +n_1\cdot k_1 & 0 & -k^* & 0 & 0 & 0 \\ 0 & +k^* & 0 & -k_0 & 0 & 0 \\ 0 & 0 & +k^* & 0 & -k_1 & 0 \\ k_q^* & 0 & 0 & +k_0 & +k_1 & 0 \end{bmatrix} \begin{pmatrix} N_{\mathrm{HPTS}^*}(t) \\ N_{\mathrm{PTS}_0^*}(t) \\ N_{\mathrm{PTS}_1^*}(t) \\ N_{\mathrm{PTS}_0}(t) \\ N_{\mathrm{PTS}_1}(t) \\ N_{\mathrm{HPTS}}(t) \end{pmatrix} \tag{9.16}$$

with starting conditions $N_i(0) = \delta_{i,\mathrm{HPTS}^*}$, i. e. all protons are initially at the excited photo-acid molecule. The values of n_i are determined by the Poisson distribution and thus concentration dependent.

We solve this set of equations (through matrix diagonalization) as a function of the parameters k_0, $k_1(T)$, k_q^*, and k^* and we keep track of the total (time dependent) sub-populations at the base molecule for any particular configuration of base molecules n_0 and n_1:

$$\tilde{N}_{\mathrm{co}}(n_0, n_1) = N_{\mathrm{PTS}_0^*} + N_{\mathrm{PTS}_1^*} + N_{\mathrm{PTS}_0} + N_{\mathrm{PTS}_1}\,. \tag{9.17}$$

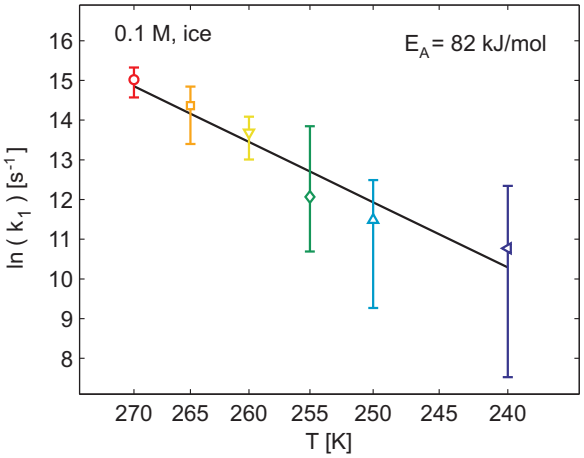

FIGURE 9.8. Arrhenius plot of proton transfer rates k_1 in ice with 0.10 M formate, resulting from the global fit. The rate shows a dramatic temperature dependence and was barely distinguishable below 250 K. The rate k_0 showed no significant temperature dependence and is given in Table I.

To get the total population contributing to the carbonyl stretch signal, we weigh each configuration by the fractional chance that it occurs as given by the Poisson distribution:

$$\tilde{N}_{\mathrm{co}} = \sum_{n_0=0}^{\infty} \sum_{n_1=0}^{\infty} \frac{\lambda_0^{n_0}\, \lambda_1^{n_1}}{n_0!\; n_1!} e^{-\lambda_0-\lambda_1} \times \tilde{N}_{\mathrm{co}}(n_0, n_1)\,, \tag{9.18}$$

where λ_i is the concentration dependent, average number of base molecules in reaction volume V_i, given by Eq. (9.9).

The time dependent population thus calculated is globally fitted to all concentrations and temperatures where only k_1 is allowed to be temperature dependent. The resulting least-squares fitting parameters are given in Table I and Fig. 9.8. Many of the parameter values were already estimated to some degree. We note that the reactive volumes V_0 and V_1 that result from the global fit are close to what had previously been estimated from Fig. 9.6 (Eqs. (9.14) and (9.15)), demonstrating that even the simple model of Eq. (9.12) yields reasonable results. What had not yet been estimated was the temperature dependent proton transfer rate through the ice $k_1(T)$. From the Arrhenius plot of Fig. 9.8 we can clearly see a dramatic slowdown with decreasing temperatures. In fact below 255 K the ingrowth of the proton transfer is so slow that the observed dependencies are completely dominated by the excited state decay of the photo-acid.

TABLE I. **Parameter values**

$1/k_0$	$(1.1\pm0.5)\cdot10^0$ ps
$1/k_1$	$(3\pm0.5)\cdot10^2$ ps (@ 270 K)
V_0	$(1.1\pm0.3)\cdot10^3$ Å^3
V_1	$(6.4\pm1.2)\cdot10^3$ Å^3
$1/k^*$	$(2.6\pm0.5)\cdot10^3$ ps
$1/k_q^*$	$(1.2\pm0.5)\cdot10^3$ ps

9.4 DISCUSSION

The arrival of the proton at the base as measured through the intensity of the carbonyl band has two distinct time scales. The initial rapid ingrowth is presumably caused by direct contact complexes. The associated time of about 1.1 ps is similar to values found by Genosar *et al.* [52] for direct transfer between HPTS and acetate in water. They described this component with a phenomenological model with a set of two time constants one of which was concentration dependent: 0.7 ps and 1 to 3 ps. From the fitted (direct reaction) volume $V_0 = (1.1 \pm 0.3) \cdot 10^3$ Å^3 we can estimate the total number of water molecules involved. The density of ice I_h is about

$$\frac{0.92 \text{ g/cm}^3}{18 \text{ g/mol}} = 51 \text{ mol/dm}^3 = 3.1 \cdot 10^{-2} \text{ Å}^{-3} = \frac{1 \times H_2O(s)}{33 \text{ Å}^3}\,. \qquad (9.19)$$

This means that V_0 contains about 30 water molecules. To get an idea of the distance over which the direct proton transfer reaction takes place, and thus the typical length of the water wires involved, we will make the following simplified assumption about the geometry involved in the experiment. If we assume a spherical distribution of water molecules around a (point source) HPTS molecule we find that the typical direct reaction takes place over a distance of about two water molecules, i. e. $(30/\frac{4}{3}\pi)^{1/3}$. Of course this distance could be different if we also take into account the volume of the HPTS molecule itself or if we take a different distribution of participating water molecules (e. g. a branching tree of hydrogen bonded water shells [132]). In any case it appears that the direct connection volume is larger than would be expected if this component would only contain directly contacting acid-base pairs. We speculate that there exist a range of stable structures with the proper arrangement of interconnecting water wires, being able to transfer their proton very quickly to the neighboring base molecule.

We use the same procedure for the reaction volume $V_1 = (6.4 \pm 1.2) \cdot 10^3$ Å^3 and find that it involves about 200 water molecules. Assuming a spherical distribution, we find that the 300 ps proton transfer process k_1 corresponds to a typical water wire length of about 4 water molecules.

For the short range transfer k_0 we found no appreciable slowdown in the proton transfer speed. This means that the (single) activated process that is

essential for the long range transfer k_1 is not present for the short range k_0. From the temperature dependence of k_1 we find an activation energy of about 80 kJ/mol for (long range) proton transfer in ice. This number is a bit higher than the numbers found by Leiderman *et al.* [83], who found a temperature dependent activation energy which was about 65 kJ/mol for 270 K ice and was observed to become smaller with decreasing temperatures. However in that study the geminate recombination without base molecules was probed, so a direct comparison is not possible.

The long range transfer rate k_1 could be a process that is rate limited by the favorable reorientation of a single misaligned water molecule in the water wire connecting acid and base. Using NMR techniques, Wittebord *et al.* [159] determined the activation energy for reorientation in ice I_H to be about 55 kJ/mol. It is conceivable that the reorientation energy in our sample was a bit higher due to the solutes present in the ice, or simply that not all reorientations lead to a favorable configuration. Configurations involving the misalignment of multiple water molecules would require a multitude of the activation energy of a single reorientation, which makes them simply too slow to observe here. Therefore we only observe the cases where there are 0 or 1 water molecules misaligned, thus explaining the observation of only two components in the kinetics. The chance to find 'misaligned' water molecules in any particular water wire increases with the length of the chain, which explains why the reaction volume V_0 is smaller than V_1.

For the reaction volume V_1 the average number of base molecules at the highest concentration (0.5 M) is almost 2 and there is even a $> 12\%$ probability to find 4 or more base molecules in the reactive volume. This means that for this fraction of acid-base pairs the data shows *parallel* reaction pathways to at least 4 base molecules (i. e. four times faster initial rate). By itself the high concentration data could perhaps be explained by using a distance dependent reaction rate. However, this would not agree with the data of 0.10 M where we found essentially only one rate k_1. This single rate is explained by the fact that there is only $< 6\%$ chance to have > 1 base molecule in V_1 at 0.10 M. The observation of a single rate k_1 strengthens the case for a discrete model over that of a continuous (distance dependent) model where there would equally exist a range of rates for all concentrations.

From the concentration scaling procedure we learn that the distribution of base molecules up to 0.5 M behaves according to Poisson statistics. Using Eq. (9.9) we can calculate the average number of base molecules in the reaction volumes for different concentrations. For the highest concentration, measured here, these numbers are $\lambda_0(0.50\text{ M}) = 0.3$ and $\lambda_1(0.50\text{ M}) = 1.9$. For volume V_0 this means that the chance to find more than one base molecule is less than 4%. If we would go to even higher concentrations this percentage would become appreciably high. If no more than one base molecule would physically fit in this contact volume, we will see deviations from the current model. In that case we are no longer in the dilute limit and need to switch to binomial statistics [132, 133].

The model used here, where we show that we can fit our data to a Poisson

distributed sum of discrete rates is mathematically not dissimilar from the 'Inhomogeneous Proton-Transfer Kinetics Model' used by the Leiderman *et al.* [81]. They use this model to interpret their TCSPC data on ice samples at short times (i. e. < 1 ns), because they found that the fit quality using the regularly used 'Geminate Recombination Model' [6] was rather poor. The inhomogeneous model essentially assumes a Gaussian distribution of rates depending on the distribution of ice around the HPTS molecule.

A big difference with other models on proton transfer in ice (or water), such as the geminate recombination model, is that we do not observe any sign of an indirect proton transfer channel, i. e. proton release to the ice lattice followed by diffusion of the proton to the base. However we note that the base concentrations used in the TSCPC experiments of Huppert *et al.* [149] are usually in the mM range, which is much lower than we can measure with our infrared pump-probe experiment. For these low concentrations and for their longer time range (up to 50 ns) the diffusion of the proton itself may become an important factor.

All proton transfer reactions in ice were modeled here as a direct transfer from acid to base without intermediate steps. In liquid water this direct transfer pathway also exists, but is accompanied by an indirect transfer mechanism, where the proton may first transfer to the water solvent and subsequently from the water to the base [29] (compare the indirect ingrowth of 270 K water compared to ice in Fig. 9.4). This intermediate step, involving a dissolved proton may be energetically unfavorable in ice [62], where all molecules are four-fold coordinated and the structure is quite rigid. Conversely, in liquid water the number of hydrogen bonds may vary to accommodate the additional charge of the proton, e. g. by the formation of a stable Eigen [41] (H_3O^+) cation.

After the initial startup time, the total amount of successful proton transfer reactions is higher in water than in ice. Presumably, in ice, proton transfer can only take place for an initially suitable configuration of the water molecules or for configurations with little (only one) defects, whereas in water these configurations may still adapt, e. g. through the diffusion of acid and base molecules or the reorientation and rearrangement of several intermediate water molecules. Also, in liquid water, the proton may first be transferred to solvent and diffuse towards the base.

The difference between proton transfer in water and ice is also noted in theoretical study by Kobayashi *et al.* [62]. They show that whereas the Grotthus [31] type proton transfer mechanism in water is governed in large part by the inter-conversion of Eigen [41] (H_3O^+) and Zundel [56] ($H_5O_2^+$) type water structures, in ice this is no longer the case. Although the density of ice I_H is lower than that of water (0.92 vs 1.0 g/cm^3) due to its relatively open structure, the intermolecular hydrogen bond distance is actually a bit smaller (2.75 vs 2.82 Å). Furthermore, in ice all water molecules are four fold coordinated, including the protonated water molecule. The fourth-coordinated water molecule pushes through a repulsive force on the protonated water molecule in ice, thus contributing further to the shortening of the O–H$\cdots$O distance to the next water molecule. This shortened distance means that the proton can move

freely in a single potential well [92].

Furthermore Kobayashi *et al.* [62] found that the O–H$\cdots$O coordinates near the proton are coupled to facilitate the sequential proton transfers in a *concerted fashion*. They found that water molecules up to the fourth solvation shells yield significant contributions to the potential energy surface. They thus conclude that especially the initial part of the proton transfer can be very fast in ice. This conclusion agrees well with our current results that show that direct proton transfer is possible over distances of about four water molecules (either immediately or after the reorientation of a misaligned water molecule).

In our model we allowed two different excited state decay rates for the bound and unbound states of the HPTS and its proton. The bound rate k_q^* is faster than the unbound rate k^*, because the proximity of the proton allows it to quench the excited state of the HPTS [6]. Such a difference in excited state lifetime was previously observed by Gopich using time-resolved fluorescence decay measurements of 5-cyano-2-naphthol in DMSO [54]. For our data, the two lifetimes control different aspects of the ingrowth of the carbonyl peak. Whereas the rate k^* may be directly observed as the rate of decay for the low temperature data (see Fig. 9.4), the bound rate k_q^* is only observed indirectly as the decreasing rate of ingrowth due to the depletion of the source of protons.

9.5 CONCLUSION

We directly observed the arrival of transferred protons in ice from a photo-acid to a base in the time range between 0.2 and 1000 ps. The signature of the transfer is the ingrowth of the carbonyl stretching mode of the base molecule. The dynamics of this mode shows two very distinct time scales of around 1 and 300 ps. Because we can fit the low concentration proton transfer data with these two timescales alone, we adopt a model with discrete transfer rates. The model can fit higher concentrations of base molecules assuming that the rate is proportional to the number of parallel transfer channels. This number depends on the statistical chance to find one or more base molecules in the reaction volume. Unlike in water we can neglect the diffusion of the protons in ice, because the existence of a 'free' proton complex in ice is energetically unfavorable.

The two transfer rates each correspond to a specific reaction volume. The size of these volumes follows directly from the relative contributions to the total proton transfer process at different concentrations. The fast rate $k_0 = 1$ ps^{-1} corresponds to a volume of about 30 water molecules. Assuming a spherical distribution, this number indicates that it involves base molecules that are connected to the photo-acid with up to two water intermediate water molecules. The second transfer rate $k_1 = 1/300$ ps^{-1} corresponds to a reaction volume of about 200 water molecules which is indicative of proton transfer across water wire lengths of about 4 molecules. This latter rate shows a strong temperature dependence with an activation energy of about 80 kJ/mol. We speculate that this activation corresponds to the reorientation of a single misaligned water

molecule in the water wire connection between acid and base.

We find a couple of striking differences between proton transfer in ice compared to water. First of all, we find that proton transfer in ice can be described with a discrete set of transfer rates as opposed to a distribution of distance dependent rates like in water. This discrete nature was explained from the more rigid structure of ice, that does not readily allow for the rearrangement and reorientation of 'water wires' or the diffusion of solutes. We observe two classes of transfer rates characterized by the number of defects (0 or 1) of the water wire that connects the acid and the base. Secondly, the proton transfer process in ice was observed to consist of a single concerted process along a water wire between acid in base. This contrasts with proton transfer in supercooled water, where a parallel reaction channel was observed in which the proton is first transferred to the water solvent. This difference was explained from the strict four-fold coordination in ice compared the more adaptable hydrogen bond structure in water. Finally, we find concerted proton jumps in ice over as many as 4 connecting water molecules. This was explained by the higher structure and the increased sphere of influence that the excess proton charge exhibits in ice compared to water.

10 Förster Transfer to Hydrated Protons

We have studied the influence of excess protons on the vibrational energy relaxation of the O–H and O–D stretching modes in water, using femtosecond pump-probe spectroscopy. Without excess protons, we observe exponential decays with time constants of 1.7 and 4.3 ps for the bulk and anion bound O–D stretch vibrations. The addition of protons introduces a new energy relaxation pathway, which leads to an increasingly non-exponential decay of the O–D stretch vibration. This new pathway is attributed to a distance dependent long range dipole-dipole interaction (i. e. Förster transfer) between the O–D stretching vibration and modes associated with dissolved protons. The high efficiency of hydrated protons as receptors of vibrational energy follows from the very large absorption cross-section and broad bandwidth of protons in water. For a proton concentration of 1 molal we find that Förster energy transfer occurs over an average distance of 4.5 Å, which corresponds to a separation of about two water molecules. Using polarization resolved information, it is furthermore shown that the addition of protons has a negligible influence on the reorientation time of bulk water (2.7±0.2 ps).

10.1 Introduction

An important property of water is its extremely high density of O–H oscillators. This high density enables a rapid resonant energy transfer of excitations of the O–H stretch vibrations between different water molecules. This transfer is based on a dipole-dipole coupling mechanism, called Förster energy transfer [48]. Previous studies on pure liquid water have shown that this process results in the transfer of energy between different water molecules on a time scale <100 fs [28, 162]. A similar type of interaction has been observed for the amide vibrations of peptides [43] and for vibrations of adsorbed molecules [102]. Characteristic for this energy transfer process is that the energy remains in the same type of molecular vibration, e. g. the O–H stretch vibrations of water molecules or the amide modes of peptides. Here we demonstrate the presence of Förster energy transfer between vibrational modes that have different character. We observe that hydrated protons form very efficient dipolar antennas for other vibrational

modes.

The coupling efficiency between hydrated protons and other molecular vibrations cannot be derived from the linear absorption or Raman spectrum because these spectra are strongly inhomogeneously broadened. Hence, this coupling can only be studied with nonlinear spectroscopic techniques. We use femtosecond mid-infrared pump-probe laser pulses to measure the rate at which hydrated protons accept the energy of a nearby vibrational excitation. The goal of this study is to find the influence of excess protons on the molecular motions and energy dynamics of water molecules. Although we are primarily interested here in bulk water behavior, we will also study the fraction of water molecules bound to the anion that inevitably accompanies the excess proton.

10.2 EXPERIMENT

PUMP-PROBE SPECTROSCOPY The vibrational energy relaxation and orientational dynamics of the O–H and O–D stretch vibrations in water are studied with polarization-resolved pump-probe spectroscopy. The pump and probe pulses are generated via a sequence of nonlinear frequency-conversion processes described in Section 3.1. Their central frequencies were in the regions around 2500 and 3400 cm^{-1}, coinciding with the O–D and O–H stretch modes, respectively. The pump and probe pulses with a FWHM of about 200 cm^{-1} had pulse energies of 5 μJ and 20 nJ, respectively.

We measured the pump-induced frequency-resolved transient absorption spectra ($\Delta\alpha$) of various samples as a function of time delay between pump and probe. The relative polarizations of pump and probe beams were varied between parallel and perpendicular to allow for the determination of both vibrational relaxation and rotational diffusion characteristics. The instrument response time was 200 fs.

As explained in Section 2.5.4, the pump promotes population from the equilibrium ground-state $\nu = 0$ to the first excited state, $\nu = 1$. This excitation is observed as a bleach and stimulated emission at frequencies matching $\nu = 0 \rightarrow 1$, and an induced absorption at frequencies matching $\nu = 1 \rightarrow 2$. The latter transition will lie at a lower frequency for anharmonic oscillators such as the O–H stretching mode of water. Together these transitions provide a spectral signature that allows for the tracking of the population of the $\nu = 1$ state. Population transfer to a different state can also be monitored, provided the excitation of this state leads to a distinct spectral signature.

SAMPLES UNDER STUDY The samples consisted of various mixtures of sodium perchlorate ($NaClO_4$) and perchloric acid ($HClO_4$) dissolved in isotopically diluted (8%) aqueous solutions of either HDO in H_2O or HDO in D_2O. These mixtures had molar ratios 4:0, 3:1, 2:2, 1:3 and 0:4 (see Fig. 10.1), meaning that the amount of perchlorate was kept constant (4 molal) while the acid concentration varied between 0 and 4 molal. This was done to exclude the influence of the anion on any comparative observations. The sample cell had an optical path length of 25 μm.

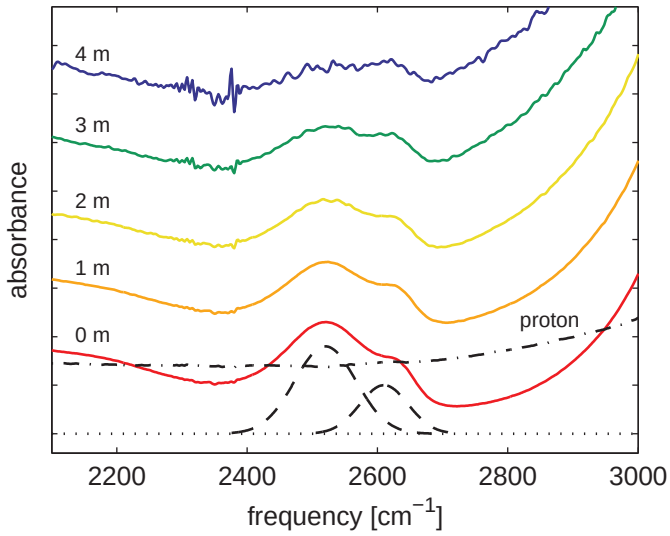

FIGURE 10.1. Linear absorption spectra of aqueous mixtures containing varying relative amounts of $NaClO_4$ and $HClO_4$. From bottom to top the concentrations of $HClO_4$:$NaClO_4$ are 0:4, 1:3, 2:2, 3:1 and 4:0. The different offsets are caused by the broadband absorption of the increasing proton concentrations. The two bands around 2520 and 2610 cm^{-1} (dashed lines) are assigned to the O–D stretch vibrations of bulk and anion bound water, respectively. The dash dotted line shows the absorption cross-section of the dissolved proton, obtained by taking the difference spectra between subsequent acid concentrations.

Fig. 10.1 shows two distinct absorptions bands. The absorption around 2520 cm^{-1} is associated with the O–D stretch of HDO, hydrogen bonded to the oxygen of another water molecule. The other band, in the region around 2610 cm^{-1} is the result of O–D stretch oscillators that are hydrogen bonded to perchlorate ions. This band is blue shifted which indicates that water forms weaker hydrogen bond to perchlorate anions than to water. This spectral separation is important because it allows us to deconvolve the behavior of bulk and anion-bound water. The sodium cation has been shown [49, 110] to have negligible effects on both the relaxation and reorientation time of water molecules.

Perchloric acid belongs to the class of so-called super acids, having a pK_a =-7. This means that the amount of dissolved protons (or deuterons) can be assumed to increase linearly with the amount of dissolved acid. Fig. 10.1 shows that the increasing proton concentration gives rise to a large broadband background signal which was isolated by taking the difference spectrum between various acid concentrations (dash-dotted line). This background can be assigned to a wide variety of hydrated proton vibrations, among which the most well known are the modes of the so-called Eigen [41] (H_3O^+) and Zundel [56] ($H_5O_2^+$) structures (see also Fig. 1.6). The broad featureless offset is considered to arise

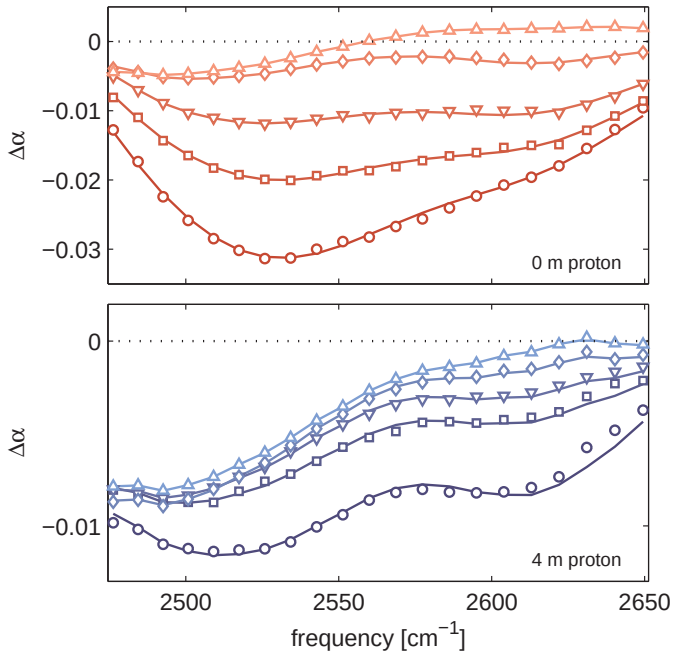

FIGURE 10.2. Transient absorption spectra showing the O–D stretching modes of 4 molal $NaClO_4$ (top) and 4 molal $HClO_4$ (bottom). Data is shown for pump-probe delays of 0.5 (circles), 1 (squares), 2 (downward triangles), 4 (diamonds) and 100 ps (upward triangles). The lines show the Gaussian fits used to calculate the population per mode.

from the strong coupling between proton transitions and collective vibrational excitations in the surrounding medium [60].

Finally, it may be noted that as the acid concentration rises, the cross-section of the O–D stretch modes seems to diminish. This is not a result of a lower concentration of deuterium, because the ratio D/H was kept at 4%, taking into account the added protons from the acid. This decrease is due to the frequency shift of O–D oscillators that are participating in the solvation of the excess proton, such as those appearing in DH_2O^+ and $DH_4O_2^+$ complexes. The frequencies of such oscillators will be strongly red shifted due to the added proton. This means that when we look at the region around 2550 cm^{-1}, we are not observing these direct-contact complexes.

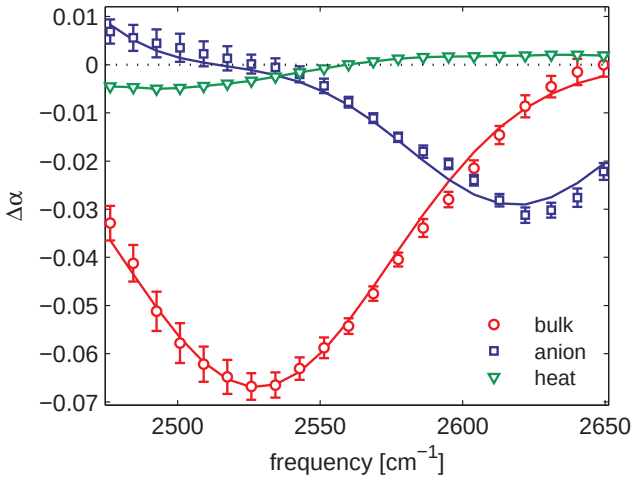

FIGURE 10.3. Decomposed spectra $\sigma_b(\nu)$, $\sigma_a(\nu)$, and $\sigma_{0^*}(\nu)$. Markers show the least-squares decomposed spectra using a kinetic fitting model on the 4 molal $NaClO_4$, HDO in H_2O sample. The bulk and anion-bound O–D stretching modes are shown with circles and squares, respectively, and the thermalized end spectrum is shown with triangles. The lines show the Gaussian fits resulting from the global analysis used to calculate the time dependent population per mode.

10.3 RESULTS AND DISCUSSION

10.3.1 TRANSIENT SPECTRA

Fig. 10.2 shows two isotropic pump-probe measurements on the O–D stretch vibrations in aqueous solutions of 4 molal sodium perchlorate (top) and 4 molal perchloric acid (bottom). Both panels show a structure of two negative bands, corresponding to the pump induced bleach of the ground state and stimulated emission from the first excited state. Not visible in this Figure is the lower frequency induced absorption resulting from transitions between the first and second excited states. This induced absorption can be observed when going to lower frequencies.

The main difference between the two data sets is the considerably faster decay of both bands in the protonated sample. Comparing the linear spectra (Fig. 10.1) of these two samples we note the broad background absorption due to these proton associated modes. An obvious speculation, at this point, is that these protons are somehow facilitating the vibrational relaxation of the O–D stretch modes. The exact mechanism for this relaxation pathway is what we will investigate.

We start our analysis by modeling the simplest case of the sample without added protons (top Fig. 10.2). From a singular value decomposition [106] on its data matrix $\Delta\alpha_{iso}(t, \nu)$ we find that these data are well described ($> 96\%$)

using a three component model where each component is the product of a time evolving population $N(t)$ and a corresponding spectral signature $\sigma(\nu)$.

$$\Delta\alpha_{iso}(t,\nu) = N_b(t)\cdot\sigma_b(\nu) + N_a(t)\cdot\sigma_a(\nu) + N_{0^*}(t)\cdot\sigma_{0^*}(\nu)\,, \tag{10.1}$$

The first component consists of O–D stretch oscillators in the first excited state that donate hydrogen bonds to other water molecules. This component gives rise to a decreased absorption around 2520 cm^{-1} and will be referred to as 'bulk' water, b. The second component consists of O–D stretch oscillators in the first excited state that are hydrogen bonded to the perchlorate anion. This blue shifted absorption band, around 2610 cm^{-1}, will be referred to as the anion-bound water a and decays with a much slower timescale. Finally there are molecules residing in a heated thermalized ground state, referred to as 0^*. The thermalization of the energy of the excitation leads to a blue shifted ground state spectrum as a result of anharmonic coupling between low frequency modes to the O–D stretch vibration. Its spectral signature can be directly observed at later time delays (100 ps) and its population increases as the other two modes decay.

We thus construct a kinetic model that assumes two separate components, bulk and anion-bound, each decaying with a different rate (k_b and k_a) towards a thermalized end-state (i. e. parallel model, Section 4.4.2). Rate equations that describe the populations in bulk ($N_b(t)$), anion-bound ($N_a(t)$) and thermalized end-state ($N_{0^*}(t)$) can be written as:

$$\frac{d}{dt}\begin{pmatrix} N_b(t) \\ N_a(t) \\ N_{0^*}(t) \end{pmatrix} = \begin{bmatrix} -k_b & 0 & 0 \\ 0 & -k_a & 0 \\ k_b & k_a & 0 \end{bmatrix} \begin{pmatrix} N_b(t) \\ N_a(t) \\ N_{0^*}(t) \end{pmatrix} \tag{10.2}$$

The solutions $N_b(t)$, $N_a(t)$ and $N_{0^*}(t)$ are a function of rate constants k_b and k_a and initial conditions $N_b(0)$, $N_a(0)$ and $N_{0^*}(0)$. These two rate constants are fitted to the data in combination with least squares calculated spectra $\sigma_b(\nu)$, $\sigma_a(\nu)$ and $\sigma_{0^*}(\nu)$. This spectral decomposition calculation is explained in Section 4.2.3.

Fig. 10.3 shows the shape of the spectra (markers) for initial conditions $N_b(0) = 0.5$, $N_a(0) = 0.5$ and $N_{0^*}(0) = 0$. These spectral signatures look as expected, when compared to the linear spectrum of Fig. 10.1. We find that the bulk decay rate k_b corresponds to a time constant around 1.7 ps, the same as was found in a previous study [123] for neat HDO in H_2O. The anion-bound decay rate k_a corresponds to a significantly slower time constant of around 4.3 ps.

We now wish to continue the analysis of the solutions containing $HClO_4$. However, because we do not know, a priori, how the added protons affect the vibrational equilibration pathways, we will instead make use of the acquired knowledge of the constituent spectra $\sigma_b(\nu)$ and $\sigma_a(\nu)$. These spectra are assumed to be similar across all acid concentrations. So instead of modeling the population dynamics and calculating the least squares fitting spectra, we will fit the spectra and calculate the least squares fitting population dynamics (temporal decomposition Section 4.2.4). Thereby we can decompose the population dynamics without prior knowledge of the relaxation model.

We use the decomposed spectra from Fig. 10.3 as a starting point to construct spectra for the bulk and anion-bound O–D vibration bands. For simplicity we will use two Gaussian bands for each spectrum. One negative band ($\Delta\alpha < 0$), corresponding to bleach and stimulated emission at $\nu = 0 \rightarrow 1$, and one positive band ($\Delta\alpha > 0$) corresponding to induced absorption at $\nu = 1 \rightarrow 2$. For each data set, we furthermore extract the thermalization spectrum that we get at late time delays. The three spectra (bulk, anion-bound, thermalization) are then used to find the least squares temporal decomposition (see Section 4.2.4) which gives us three time traces that describe the best fitting amplitudes of these spectra to the data at each time. This procedure is iterated while the first two spectra are allowed to vary, such that they best fit (least squares) the five pump-probe data sets and the linear spectra of Fig. 10.1.

The resulting Gaussian spectra for all data sets are shown as lines in Fig. 10.3. The $\nu = 0 \rightarrow 1$ parts of these spectra are shown as dashed lines in the linear spectra of Fig. 10.1. Finally, the lines shown in Fig. 10.2 shows how these spectra, multiplied by their respective time traces, fit with the data sets.

10.3.2 Energy relaxation

The time traces that come out of this procedure are proportional to the populations $N_b(t)$ and $N_a(t)$. These are subsequently normalized at $t = 0$ and shown in Fig. 10.4 for 5 different proton concentrations. We observe a clear dependence of the relaxation rate on acid concentration: with increasing acid concentration the relaxation becomes faster and non-exponential. The presence of the hydrated protons thus appears to open up an additional relaxation channel. While it may seem as if the added protons have more effect on the anion-bound water than the bulk, this is only because the anion bound water was slower to begin with and is more affected by an additional relaxation pathway. Finally, it may be noticed, especially for the anion bound water, that the decay rate for higher proton concentrations is still faster at delay times up to 5 ps. This means that the effect of the protons is still present at that time, otherwise the population traces would start to go parallel on this logarithmic scale.

To investigate the proton relaxation channel further, we perform an additional set of experiments in which we reverse the roles of hydrogen and deuterium. This time we use five aqueous solutions of HDO in D_2O at different ratios of (deuterated) perchloric acid ($DClO_4$) and sodium perchlorate ($NaClO_4$) and do the same pump-probe experiments as before, but now on the O–H stretching modes at 3400 cm^{-1}. This reciprocal system has one major difference: the O–H stretching frequency does not overlap spectrally with the deuteron (acid) background band, which lies at frequencies below the O–D stretching mode (2500 cm^{-1}). We find a decay time of 0.8 ps for the bulk O–H stretch, similar to a previously found value of 0.7 ps for neat HDO in D_2O [123]. The anion bound O–H stretch is again a bit slower with a vibrational relaxation time of 1.4 ps. Using the same procedure as before we show the time dependent population dynamics as a function of acid concentration in Fig. 10.5. Here we see a trend that is quite different from that of the O–D

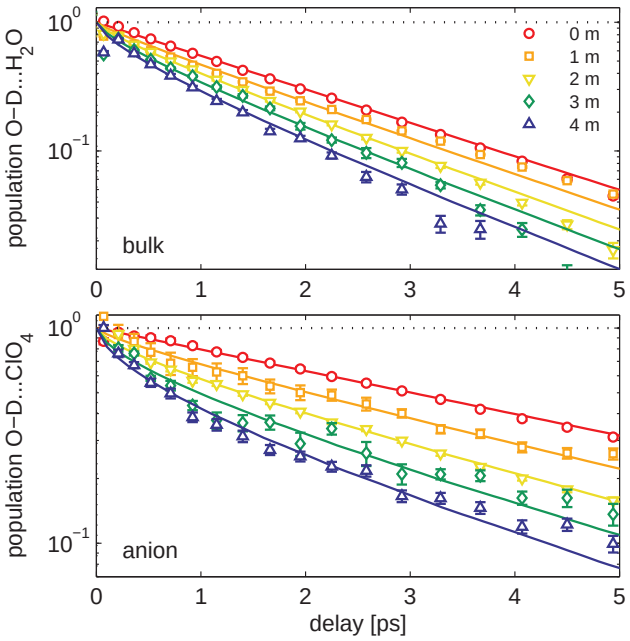

FIGURE 10.4. Population dynamics for bulk (top) and anion-bound (bottom) water (O–D vibration of HDO in H_2O). Markers show the least-squares decomposed populations for increasing proton concentrations from 0 up to 4 molal. The lines are a global fit, described in the text, which finds a bulk rate $k_b = 0.6$ ps^{-1} and anion-bound rate $k_a = 0.23$ ps^{-1}. The Förster transfer rate $k_F = 1450$ ps^{-1}Å^6 and the minimum transfer radius $a_0 = 1.5$ Å.

relaxation: the deuterons have a negligible effect on the vibrational relaxation of the O–H stretch vibrations!

From these observations it is quite clear that the additional relaxation pathway observed for the O–D stretching mode upon the addition of acid requires spectral overlap (i. e. resonance) with modes associated with the dissolved proton. Schematically the flow of energy for the O–D may be drawn as in Fig. 10.6. We add another relaxation pathway from the O–D to the hydronium mode that is dependent on acid concentration and causes a speedup of the O–D relaxation rate. This proton associated mode decays very fast and is only observed indirectly through the thermalization spectrum and faster relaxation of the O–D.

There are several ways in which the vibrational energy may be transferred. One might think that the fast relaxation is associated with O–D vibrations in DH_2O^+ complexes. However, these directly contacting protons cause a significant red shift of the O–D stretch. By pumping and probing only at bulk O–D stretching frequencies, we automatically exclude these red shifted O–D stretch modes. For modes of H_3O^+ that are further away, vibrational energy may be

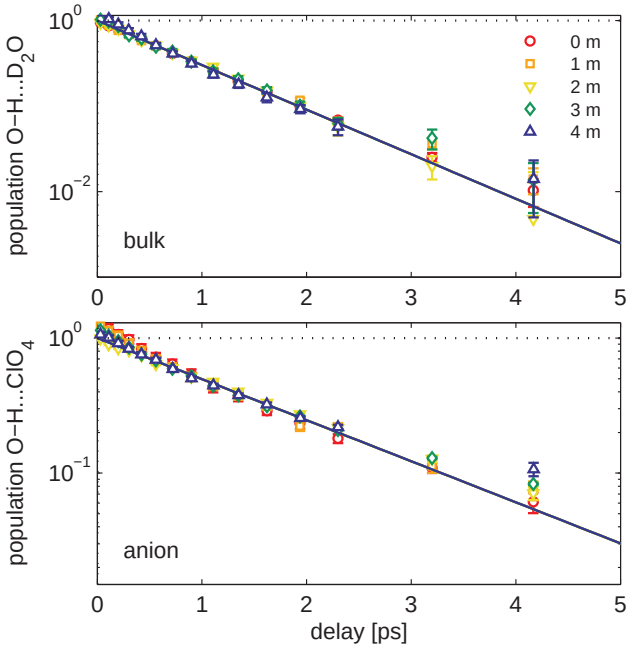

FIGURE 10.5. Same as Fig. 10.4, but now for the bulk and anion bound O–H vibrations of HDO in D_2O at 5 different acid concentrations. The lines show the result of a global fit finding a bulk rate $k_b = 1.2$ ps^{-1} and anion-bound rate $k_a = 0.7$ ps^{-1}. The Förster transfer was found to be negligible (=0), using the same minimal transfer radius $a_0 = 1.5$ Å as for HDO in H_2O.

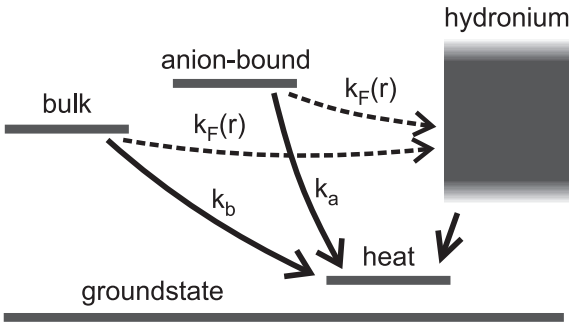

FIGURE 10.6. Schematic energy level diagram. Arrows indicate channels for vibrational energy transfer. The relaxation rates of bulk (k_b) and anion-bound (k_a) water are mentioned in the text. The dashed arrows indicate the additional equilibration channels of Förster transfer to the hydronium band with distance dependent rate k_F.

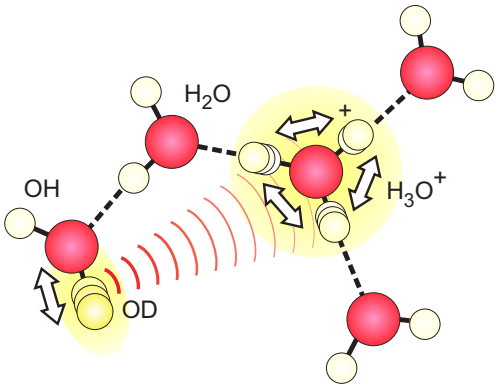

FIGURE 10.7. Schematic representation of the Förster energy transfer process between the O–D stretch vibration and a nearby proton (associated) mode. White arrows indicate the direction of the transition dipole moments and the curved lines represent the dipole field.

transferred through resonant dipole-dipole coupling, i. e. Förster energy transfer (see Fig. 10.7).

10.3.3 FÖRSTER TRANSFER

In modeling the data we describe the survival probability of O–D stretch modes which can relax their energy through a Förster transfer process to a radially uniform distribution of receiving proton (associated) modes. Once a transfer reaction has taken place, the energy is quickly dissipated by the proton mode [163] and this reaction is considered to be unidirectional. Since the Förster rate is highly dependent on distance, O–D modes that have protons in close proximity will show a higher energy transfer rate than those with protons at longer distances. Once the close configurations have reacted, the transfer rate will gradually slow down to that of the longer distance Förster transfer. This distance dependence will thus lead to a time dependent transfer rate and survival probability.

As we did in the previous chapters about proton transfer, we will use the pseudo-unimolecular approximation (Section 4.5) to describe time dependence of the survival probability. The main difference is the functional form of the distance dependent reaction rate. As we have shown in Section 4.6 (Eq. (4.69)) the rate of Förster transfer is proportional to:

$$k_F(r) = \frac{\hat{k}_F}{r^6}, \tag{10.3}$$

where $\hat{k}_F$ is the Förster rate for a single reaction pair at distance $r = 1$, averaged over all orientations. Here we have assumed that the orientational factor κ_{ab} in Eq. (4.69) is uniform enough to be averaged out.

A population of Förster transmitters (O–D stretch) is placed in the origin ($r = 0$) and we assume a radial distribution of receivers (proton modes) with initial concentration ρ for distances $> a_0$ (minimal transfer radius, i. e. excluded volume of the transmitter). Filling in the distance dependence of Eq. (10.3) into Eq. (4.65) of Section 4.5, we obtain the survival probability of the O–D stretch as a result of Förster transfer:

$$S_F(t,\rho) \quad = \quad \exp\left(-\rho \int_{a_0}^{\infty} dr\, 4\pi r^2\, [1-\exp(-\frac{\hat{k}_F}{r^6}t)]\right) . \qquad (10.4)$$

In the absence of Förster transfer (no acid, $\rho = 0$ molal), we have found that the O–D stretch for bulk and anion-bound water have standard decay rates k_b=1/(1.7 ps) and k_a=1/(4.3 ps), respectively. In terms of their respective survival probabilities S_b and S_a, we can write:

$$S_b(t) \quad = \quad \exp(-k_b\, t) , \qquad (10.5)$$

$$S_a(t) \quad = \quad \exp(-k_a\, t) . \qquad (10.6)$$

Assuming that the standard and Förster relaxation processes constitute two parallel channels as shown in Fig. 10.6, the total population dynamics are proportional to the product of these two survival probabilities Eq. (10.4) and Eqs. (10.5)–(10.6):

$$S_{b,F}(t,\rho) = \exp\left(-k_b\, t - \rho \int_{a_0}^{\infty} dr\, 4\pi r^2\, [1-\exp(-\frac{\hat{k}_F}{r^6}t)]\right) \qquad (10.7)$$

$$S_{a,F}(t,\rho) = \exp\left(-k_a\, t - \rho \int_{a_0}^{\infty} dr\, 4\pi r^2\, [1-\exp(-\frac{\hat{k}_F}{r^6}t)]\right) \qquad (10.8)$$

These two equations have the following parameters: the bulk and anion decay rates k_b and k_a, that have already been obtained from the 0 M proton data set. The concentrations ρ (0-4 molal) are also known for each sample. That only leaves the Förster rate $\hat{k}_F$ and minimum radius a_0 to be determined. For this we use a global fit on all 10 population decays (bulk and anion-bound for 5 concentrations) and show the results as solid lines through the data points in Fig. 10.4. We have assumed, for simplicity, that the Förster rate from the bulk and anion-bound populations was the same, an assumption that is justified given the broad and featureless profile of the proton background band. We find for the Förster rate between the O–D stretch and the proton associated modes $\hat{k}_F = 1450$ ps^{-1}Å^6 and a minimum transfer radius a_0 of 1.5 Å. For the O–H stretch vibration, all concentrations fit well with a Förster rate of zero, as shown in Fig. 10.5 (taking the same value for a_0).

To get a molecular picture for the obtained rate of Förster transfer we calculate the distribution of Förster transfer events as a function of the distance between the donor O–D vibration and the acceptor hydrated proton vibrations (1 molal). To obtain this distribution $C(r)$ we use Eq. (4.67) from Section 4.5.3

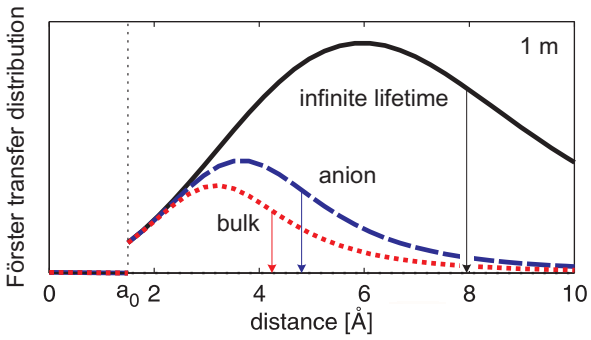

FIGURE 10.8. Distance distribution of the Förster energy transfer events to hydrated protons for a proton concentration of 1 molal. The solid line represents the distribution in case there would be no vibrational relaxation. The dashed and dotted curves represent the cases for which the donating O–D group is bonded to ClO_4^- (T_1=4.3±0.3 ps) and to H_2O (T_1=1.7±0.1 ps), respectively. The downward arrows indicate the average distances.

and fill in Eq. (10.3) for $k(r)$:

$$C(r) = \rho\, 4\pi r^2 dr\, \frac{\hat{k}_F}{r^6}\, A(0) \int_0^\infty dt\, \exp\left(-\frac{\hat{k}_F}{r^6}\, t\right)\, S(t)\,, \tag{10.9}$$

$$\propto \frac{1}{r^4} \int_0^\infty dt\, \exp\left(-\frac{\hat{k}_F}{r^6}\, t\right)\, S(t)\,. \tag{10.10}$$

The distance distribution of Förster transfer events $C(r)$, depends on the survival probability $S(t)$ through all channels, including the regular vibrational relaxation. We evaluate this function by numerical integration for three different scenarios. To evaluate the distribution for very slow vibrational relaxation ('infinite lifetime'), we use $S(t)$ from Eq. (10.4). For the bulk or anion-bound lifetimes, we use $S(t)$ given by Eqs. (10.7) or (10.8), respectively. The three resulting distance distributions of Förster events is shown in Fig. 10.8. For the limiting case where vibrational relaxation is very slow ('infinite lifetime'), the average distance over which energy transfer takes place equals about 8 Å. In the presence of the parallel vibrational relaxation process this distribution shifts to shorter distances, because for the longer distances the excitation has relaxed before energy transfer can occur. For the O–D bonded to H_2O and to ClO_4^- we find average distances of 4.2 and 4.8 Å, respectively. These distances correspond to a separation between the donating O–D group and the hydrated proton of about two water molecules. This leads to the microscopic picture shown in Fig. 10.7. These distances are slightly larger than the corresponding Förster radii, $R_f = (\hat{k}_F/k_i)^{1/6} = 3.7$ and 4.3 Å, because of the excluded volume ($a_0 > 1.5$ Å).

10.3.4 Implications

The present observations demonstrate that Förster energy transfer constitutes an effective long range coupling mechanism between vibrations, also of different character. Normally, interactions between different vibrations, result from the anharmonic coupling of vibrational modes involving the same atoms of the molecule, meaning that this coupling is very local in character. In the present case, the interaction between different vibrational modes results from their long-range dipole-dipole coupling. This coupling leads to energy transfer between vibrational modes that are separated by several water molecules. For a proton at a distance of 4 Å we find a transfer rate of 0.35 ps^{-1}, which is comparable to the relaxation rate of the O–D vibration of HDO in pure water. This result shows that the dipole-dipole interactions to hydrated protons can be of similar strength as intramolecular anharmonic couplings. Hydrated protons are particularly efficient in this non-local interaction because of the large cross-section of their vibrations. This large cross-section is due to the large polarizability of the proton in water, i. e. the strong effect of (dipolar) electric fields on the positions and charges of the oxygen and hydrogen atoms of the hydrated proton solvation structures.

Hydrated protons will couple to all infrared-active molecular vibrations with frequencies between 1000 and 3400 cm^{-1}, because of the extremely large absorption bandwidth of the hydrated proton [60] (see also Fig. 10.1. The energy taken up by the proton vibrations will be quickly dissipated [163]. The combination of rapid dissipation and their role as highly efficient dipolar antennas makes protons into highly efficient non-local energy sinks in biochemical reactions. Biological systems are highly inhomogeneous and it is thus conceivable that a local proton would reside a few water molecules away from an affected molecular vibration. Finally, it should be noted that the coupling to hydrated protons does not rely on the excitation of the vibrational modes. The excitation of the vibrations only forms a very useful tool to measure the strength and distance dependence of this coupling. The dipole-dipole coupling is also present in the vibrational ground state and leads to a mixing of the character of the vibrational modes of the hydrated proton with the infrared-active modes of nearby molecular systems. This means that in aqueous media protons cannot only affect dissolved molecules by chemical interactions, i. e. (reversible) chemical binding, but also by mixing their vibrational character into the vibrational modes of the molecule. The effects depend on the proximity of single protons, which for biological systems can be quite close.

10.3.5 Rotational diffusion

Using the additional information we get from the polarization resolved data we now study the effect of the addition of protons on the reorientation rate of water. If the data would only consist of one component, it would be straightforward to calculate the anisotropy using Eq. (4.4). However in this case the data consists of three different components: bulk, anion-bound and thermalized O–D oscillators.

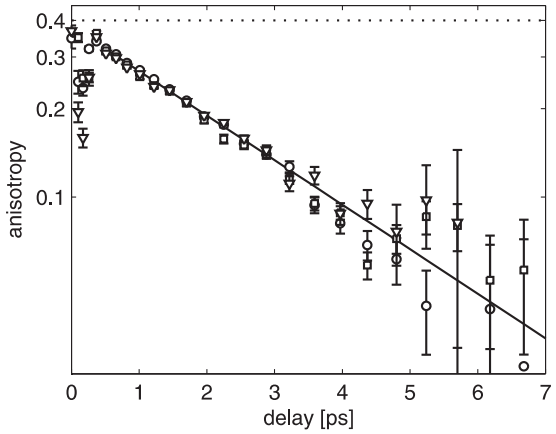

FIGURE 10.9. Anisotropy decays of bulk water molecules for proton concentrations of 0, 1 and 2 molal (circles, squares and triangles). The lines show exponential fits with time constants of 2.7±0.2 ps.

The last one is expected to be isotropic while the first two may have a very different rate of anisotropy decay. We now employ the methods explained in Section 4.2.5 to find the anisotropic decomposition for each of the components, using the spectral signatures determined previously (Fig. 10.3). Unfortunately, this was not possible for the highest acid concentrations due to limitations of the deconvolution procedure (low signal compared to thermalization).

The anisotropy decay curves of the bulk O–D oscillators with proton concentrations of 0, 1 and 2 molal are shown in Fig. 10.9. The three curves show no discernable trend with increasing proton concentration and all can be fitted well with exponentials using time constants of 2.7±0.2 ps. This rotational diffusion time is very similar to the 2.5 ps found previously [123] for neat solutions of HDO in H_2O. This means that we find only a negligible influence of the proton on these anisotropy decays.

On first sight we might be led to believe that if the reorientation mechanism of water depends on the making and breaking of hydrogen bonds [73], we *should* see an effect for water molecules, whose hydrogen bonds have clearly been strengthened (case in point, the red shifted linear spectrum, Fig. 10.1), and are perhaps also connected through more than the normal amount of hydrogen bonds. However there are two reasons why we would not see the effects here. First, previous experiments [110] have found only negligible change of the anisotropy decay under the influence of cations. Secondly, as was argued before, we are preferentially not looking at water molecules in the direct proximity to the proton, because of the selection of the bulk frequency region. Unfortunately, pump-probing the DH_2O^+ cation does not seem very feasible because, if the short lifetime of H_3O^+ is any indication, there will be only a very short time window for anisotropy measurements.

10.4 Conclusion

We investigated the energy relaxation pathways of O–D and O–H stretching modes in water with acid concentrations varying between 0 and 4 molal and perchlorate counter ions. Water molecules that form hydrogen bonds with the anion have a blue shifted spectrum compared to the bulk water. Using this spectral separation we measured the decay times for the bulk and anion-bound O–D stretch modes for the neutral sample to be 1.7 and 4.3 ps, respectively. Using the spectral signatures found in this data set we created a model independent set of population time traces for all acid concentrations. These time traces were seen to possess an additional time dependent decay rate for higher acid concentrations. This rate increase was fitted using a custom Förster transfer model, for all concentration, using a distance dependent rate of 1450 $ps^{-1}Å^6$ and a minimum transfer radius of 1.5 Å.

Using the same procedure on the reciprocal system of the O–H stretch in D_2O and varying concentrations of excess deuterons, no Förster transfer was observed. The bulk and anion-bound decay times were found to be 0.8 and 1.4 ps, respectively, independent of acid concentration. This shows that Förster transfer is not favorable for the O–H because it lacks spectral overlap with the dissolved deuteron background band. Both bulk relaxation rates correspond well to values previously found for neat water [123].

We find evidence for energy transfer between vibrational modes that are separated by several water molecules. For a proton at a distance of 4 Å the rate of Förster transfer is comparable to the relaxation rate of the O–D vibration of HDO in pure water.

The anisotropy decay was investigated for the bulk O–D stretching mode in acid concentrations up to two moles. No trends were found for concentrations up to 2 molal of acid and the reorientation rate is largely unaffected at 2.7±0.2 ps which is very similar to the reorientation time of 2.5 ps measured previously for the reorientation of neat HDO in H_2O [123].

11 Förster Transfer in Ice

We have studied Förster energy transfer between O–H vibrations in H_2O/D_2O ice I_H using femtosecond, two-color, mid-infrared pump-probe spectroscopy. We find that as a result of couplings to nearby O–H stretch modes, the vibrational relaxation time decreases from 480 fs for dilute HDO in D_2O down to 300 fs for pure H_2O ice. The anisotropy shows an initial 140 fs decay down to a concentration-dependent end level. This end level for low concentrations can be explained from the limited rotational freedom ($\sim 20\,^\circ$) of a water molecule in the ice lattice over time scales > 15 ps. The decreasing end levels for higher concentrations of H_2O result from Förster energy transfer to the next nearest (six) O–H groups. No Förster transfer beyond these neighbors is observed. Variation of the ice temperature between 200 and 270 K was found to have negligible effect on the dynamics.

11.1 Introduction

In the previous chapter we studied intermolecular Förster energy transfer transfer between different vibrational modes in liquid water. The structure of liquid water is very inhomogeneous and the frequencies of these modes are continuously modulated through variations in the hydrogen bond distance, strength and angle [8,76]. In comparison to water, the structure of ice is much more rigid and the molecules form nearly homogeneous hydrogen bond connections with all four of their neighbors at directions close to the tetrahedral angle (109.5 °). Due to its simple and ordered structure, ice provides an ideal environment in which to test different theoretical models of the water molecule, such as those concerning dipole-dipole interactions and vibrational energy transfer.

The preferential absorption of polarized light along the direction of the vibrational transition dipole moment axis can be used to track the changing direction of the excitation that results from either reorientational diffusion [38,84,123] or Förster energy transfer between modes located on differently oriented (water) molecules. Because the molecules in ice are expected to exhibit only limited reorientational diffusion, we expect that the main mechanism for a change in the direction of the excitation will be vibrational Förster energy transfer. Previous studies using polarization-resolved spectroscopy found that the rate of vibrational Förster transfer between O–H oscillators in liquid water occurs on sub

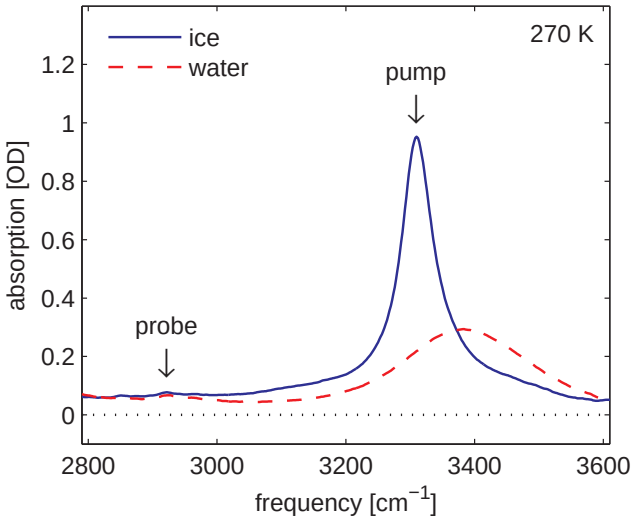

FIGURE 11.1. Linear absorption spectra of the O–H stretch vibration in ice and water ($f_H = 2\%$). The arrows indicate the pump and probe frequencies used in the experiments. The pump coincides with the $\nu = 0 \rightarrow 1$ transition (3310 cm^{-1}) and the probe with the $\nu = 1 \rightarrow 2$ induced absorption (2925 cm^{-1}).

100 fs timescales [28,162]. Here we study these dynamics for the O–H stretching mode in ice, using various mixtures of normal (H_2O) and heavy (D_2O) water. Thereby we vary the density and thus the average distance between O–H oscillators in the ice lattice.

11.2 EXPERIMENTAL SECTION

Samples consisted of mixtures of normal water (H_2O) and heavy water (D_2O) with the fraction of hydrogen,

$$f_H = \frac{[H_2O]}{[H_2O] + [D_2O]} = \frac{H}{H + D}\,, \tag{11.1}$$

varying between 0.1 and 100%. The samples were frozen using a closed-circuit liquid helium pumped cryostat (temperature stability 0.5 K). The freezing procedure consisted of a rapid (few minute) cool down to 250 K, until the sample showed a homogenous ice crystal. The sample temperature was then set to 270 K and a series of linear spectra was taken before, during and after the experiment to confirm that the sample remained frozen (see Fig. 11.1).

The experiments were performed using the polarization-resolved, two-color, mid-infrared pump-probe laser setup, described in Section 3.2. The pump and probe pulses were generated via a sequence of nonlinear frequency-conversion

processes as described in Section 3.1. The central frequency of the pump was set at 3310 cm^{-1}, resonant with the $\nu = 0 \rightarrow 1$ transition of the O–H stretch in ice (see Fig. 11.1). The probe had a central frequency of 2900 cm^{-1}, resonant with the $\nu = 1 \rightarrow 2$ transition. The pump and probe pulses had pulse energies of 5 μJ and 20 nJ, respectively. The instrument response time was about 200 fs.

As was explained in Section 2.5.4, depopulation of the ground state leads to a reduced absorption or 'bleach' at frequencies corresponding to the $\nu = 0 \rightarrow 1$ transition which is enhanced by $\nu = 1 \rightarrow 0$ stimulated emission of the excited population back to the ground state. At the same time the newly created population in the first excited state $\nu = 1$ starts to absorb light at frequencies that correspond to the $\nu = 1 \rightarrow 2$ transition. For anharmonic oscillators, such as the O–H stretch vibration, the energy spacing between the levels goes down with increasing quantum number. This means that the $\nu = 1 \rightarrow 2$ transition lies at a lower frequency than the $\nu = 0 \rightarrow 1$ transition. In the current experiment, we pump the $\nu = 0 \rightarrow 1$ transition and probe the $\nu = 1 \rightarrow 2$ induced absorption. There are several advantages to this approach:

- Although the ice crystal appeared optically clear we experienced considerable scatter light of the pump beam in the direction of the probe. Detection of this scattered light can be avoided by probing at a different frequency than the pump.

- In a previous study on the transient absorption spectrum of ice I_H [35], it was shown that the decay of the excited state occurs through a blue-shifted intermediate level. The spectrum of this intermediate level complicates the analysis of the anisotropy and can be avoided by probing the $\nu = 1 \rightarrow 2$ absorption.

- For samples containing higher concentrations of H_2O, the optical density was such that hardly any probe light was transmitted in the region of the $\nu = 0 \rightarrow 1$ absorption. This problem is not present in the region of the $\nu = 1 \rightarrow 2$ induced absorption. In addition the narrowing of the O–H absorption peak upon freezing helped helping in clearing the probe region.

- For the reorientation of the O–H group in liquid water it was shown [123] that the anisotropy in the frequency region of the $\nu = 0 \rightarrow 1$ absorption may be distorted by a slightly faster reorientation of excited molecules during their relaxation compared to unexcited molecules. This higher mobility ultimately leads to the creation of an anisotropic orientational distribution of O–H groups in the ground state. The effect is thus only present for the ground state ($\nu = 0 \rightarrow 1$) absorption spectrum and does not influence the dynamics at the not at the $\nu = 1 \rightarrow 2$ frequency.

From the isotropic signal $\Delta\alpha$ we obtain information about the vibrational relaxation rate k which depends on the density and cross-section of nearby accepting modes. In Section 4.1 and Fig. 4.1 we have shown that the anisotropic signal R reveals information about reorientational motion (or lack thereof) and

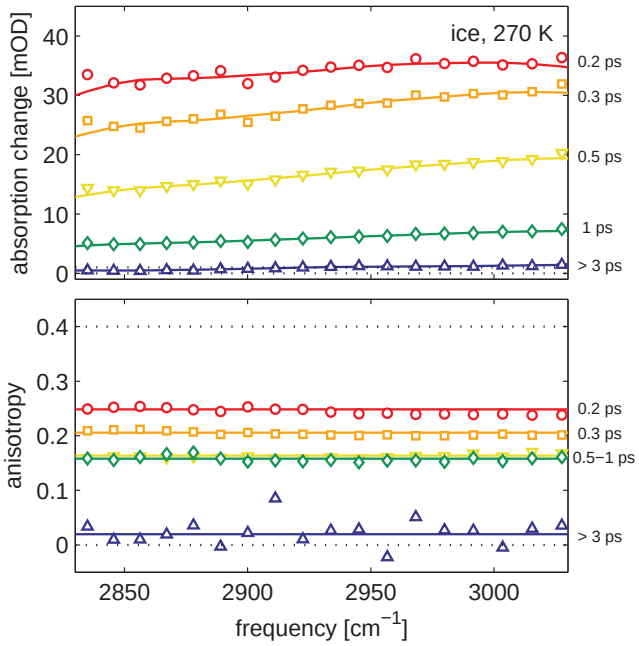

FIGURE 11.2. Transient absorption spectra of 15% H_2O ice at various delays between pump and probe. The probe region shows part of the $\nu = 1 \rightarrow 2$ induced absorption which for ice I_H is unusually broad [35] (2700-3300 cm^{-1}). The isotropic signal (top) shows a quick decay to a small end spectrum (> 3 ps). The anisotropy (bottom) shows a frequency independent rapid initial decay that halts between 0.5 and 1 ps and then resumes decaying. The initial decay is attributed to Förster energy transfer while the latter is attributed to the increasing influence of the isotropic end spectrum (see also Fig. 11.3).

vibrational Förster transfer. The anisotropy that results from reorientational motion of an excitation within a cone of half-angle θ_r is given by Eq. (4.7):

$$R_{\text{cone}} = \tfrac{2}{5}\left(\tfrac{1}{2}\cos(\theta_r)\cdot[1+\cos(\theta_r)]\right)^2 , \tag{11.2}$$

(11.3)

Conversely, the anisotropy that results from an excitation that changes direction over an angle θ_t as a result of energy transfer, is given by Eq. (4.8):

$$R_{\text{transfer}} = \tfrac{1}{5}\left(3\cos^2(\theta_t) - 1\right) , \tag{11.4}$$

(11.5)

11.3 RESULTS

11.3.1 LINEAR SPECTRUM

From the linear spectra in Fig. 11.1, we note that there is a large difference in the absorption cross-section between water and ice of the same temperature. Upon freezing, the central frequency of the O–H stretch mode shifts to the red, the absorption band becomes much narrower, and the total cross-section increases. The frequency of the O–H stretch mode is a direct measure of the strength of its donating hydrogen bond. The red shift in ice indicates that the hydrogen bond has become stronger (leading to a weaker O–H chemical bond). The width of the spectrum is a measure of the amount of inhomogeneity present in the system. The fact that the spectrum narrows, shows that ice possesses a more homogeneous distribution of hydrogen bonds than water. The spectrum thus reflects the fact that ice is more rigid and more structured than water. The increased cross-section is an indication that the O–H stretch mode has become more polarizable in ice.

11.3.2 TRANSIENT SPECTRA

Fig. 11.2 shows a typical data set of 15% H_2O with the frequency resolved (isotropic) absorption changes and anisotropy decays for various delay times between pump and probe. The isotropic spectra show part of the $\nu = 1 \rightarrow 2$ induced absorption, which extends between 2700 and 3300 cm^{-1}. We observe a rapid decay and a small (2%) thermalization end spectrum at delay times > 3 ps. This end spectrum shows a delayed ingrowth, indicative of an intermediate state between vibrational depopulation and thermalization. This intermediate state was previously shown [35] to have a blue-shifted spectrum that has no absorption cross-section in the current probe window. The total isotropic pump-probe signal, in this frequency region, can thus be described as the sum of a decaying vibrational spectrum $\sigma_1(\nu)$ and a delayed ingrowing thermalized end spectrum $\sigma_{\mathrm{H}}(\nu)$ (compare cascade model, Section 4.4.3):

$$\begin{aligned} \Delta\alpha(t,\nu) &= \sigma_1(\nu) \cdot \exp(-k_1\, t\,) \\ &+ \sigma_{\mathrm{H}}(\nu) \cdot \left(\frac{k_1}{k^* - k_1} \exp(-k^*\, t\,) - \frac{k^*}{k^* - k_1} \exp(-k_1\, t\,) + 1 \right), \end{aligned} \tag{11.6}$$

where k_1 is the vibrational relaxation rate and k^* the thermalization rate.

The anisotropy data of Fig. 11.2 show no significant frequency dependence. Within the first 500 fs the anisotropy drops to a value of about 0.18, where it stays for the next 500 fs. Finally it continues to drop down to zero where it stays for all times > 3 ps. From Eq. (4.6) we know that when the pump-probe signal consists of multiple components that have different anisotropies, the total observed anisotropy will be the average of the individual anisotropies $R_i(t)$, weighted with the isotropic intensities $\Delta\alpha_i(t,\nu)$:

$$R_{\mathrm{total}} = \frac{\sum_i \Delta\alpha_i \cdot R_i}{\sum_i \Delta\alpha_i} = \frac{\Delta\alpha_1 \cdot R_1 + \Delta\alpha_{\mathrm{H}} \cdot R_{\mathrm{H}}}{\Delta\alpha_1 + \Delta\alpha_{\mathrm{H}}}, \tag{11.7}$$

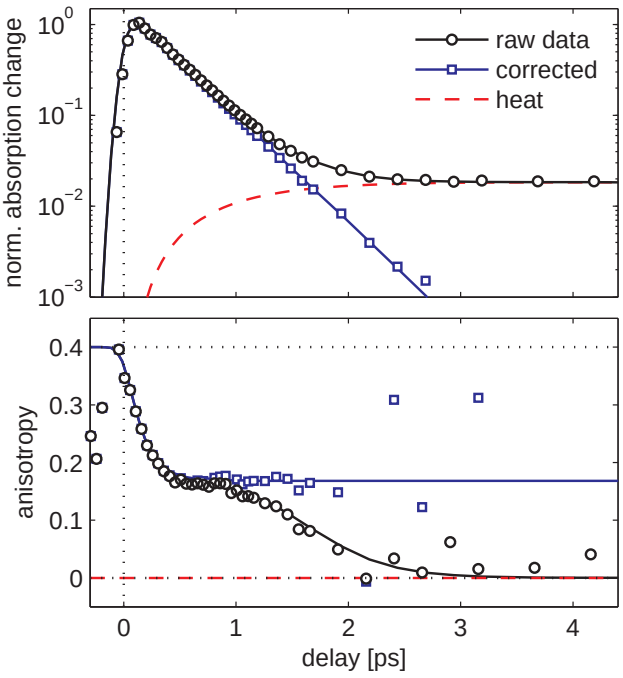

FIGURE 11.3. Frequency averaged isotropic (top) and anisotropic (bottom) signals of 15% H_2O ice. The circles indicate the raw data and the squares indicate the corrected data where an indirectly ingrowing isotropic heat (dashed line) has been subtracted (see text $\tau_1 = 350$ fs, $\tau^* = 600$ fs). The lines indicate the fitted model, which has been convoluted with an instrument response time of 200 fs.

where R_1 is the (time dependent) anisotropy of the excited state ($\nu = 1$) that we are interested in, and R_H is the anisotropy of the thermalized end level.

11.3.3 HEAT CORRECTION

To further analyze the data we take the weighted average of Fig. 11.2 over all frequencies. The resulting time traces are shown in Fig. 11.3 ('raw data'). The isotropic signal has been plotted logarithmically to show more clearly the initial exponential decay of the vibrational excitation, before the delayed ingrowth of the thermalization end level. Note that before the thermalization grows in, the anisotropy already shows a certain end level ($R = 0.18$). All fits are convoluted with the instrument response time of 200 fs:

The isotropic trace was fitted using Eq. (11.6), resulting in the rates $k_1 = 1/350\ \text{fs}^{-1}$ and $k^* = 1/600\ \text{fs}^{-1}$. From the bottom part of Fig. 11.2, we note that at later delay times (> 3 ps), where the thermalization signal is dominant, the signal becomes isotropic ($R = 0$). We therefore set R_H to zero, while leaving R_1

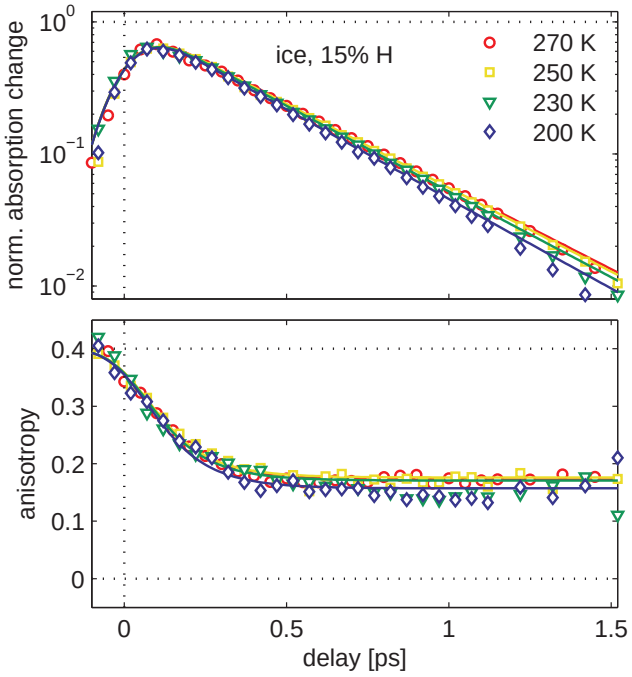

FIGURE 11.4. Isotropic and anisotropic signals of 15% H_2O ice at temperatures between 200 and 270 K. The data show a minimal dependence on temperature with decay times τ_1 between 320 and 340 fs. The anisotropy end levels range between 0.16 and 0.18.

free. We proceed by subtracting the fitted thermalization parts ('heat') from the 'raw data' using Eqs. (11.6) and (11.7). The resulting traces are shown as 'corrected' data for both the isotropic and anisotropic parts. Note that the isotropic part of the corrected data shows a mono-exponential decay as expected from Eq. (11.6). The anisotropy of the corrected data shows a continuation of the end level at $R = 0.18$. Note from Eq. (4.4) that the anisotropy can only be accurately determined as long as the vibrational excitation persists, which is why the noise goes up beyond 2 ps. Fortunately, the end level is reached before that time at about 0.8 ps, so that this level can be accurately determined.

11.3.4 TEMPERATURE DEPENDENCE

Fig. 11.4 shows heat-corrected and normalized data traces of 15% H_2O for temperatures between 200 and 270 K. We observe little temperature dependence, both in the isotropic and anisotropic data traces. The vibrational relaxation time goes down slightly with decreasing temperature (340→320 fs). The anisotropy traces show no clear temperature dependence, neither in the end lev-

els (0.16–0.18), nor in the rate of the initial decay (∼140 fs). This temperature independence implies that all conclusions drawn from the data, will be equally valid for all temperatures of hexagonal ice I_H between 200–270 K.

In a previous study on the reorientational diffusion of liquid water [146] (4% D_2O in H_2O), the anisotropy decay time decreased from 5 to 1 ps, for a temperature increase from 5 to 70 °C (278–343 K), respectively. Also, the anisotropies decayed fully down to zero. Clearly the anisotropy decay observed in Fig. 11.4 is of a different origin. Whereas the anisotropy decay in liquid (isotopically diluted) water is caused by reorientational diffusion (Eq. (11.2)), the anisotropy decay in ice is the result of vibrational Förster energy transfer (Eq. (11.4)).

We assign the initial decay process with a time constant of ∼140 fs to Förster transfer between nearby O–H oscillators and the lack of decay after 0.5 ps to the absence of reorientational motion due to the restrictions of the ice crystal. Taking into account the noise of the end level and the short interval over which the anisotropy can be measured, the orientational diffusion time τ_R of a water molecule in ice is estimated to be > 15 ps. For all current purposes this means that the reorientational motion is 'frozen'.

We note further that the presence of a nonzero end level is a clear indication that the Förster transfer radius in ice has a cutoff. Perhaps Förster transfer beyond this cutoff radius does exist, but because of the $1/R^6$ distance dependence [47], it is significantly slower.

11.3.5 CONCENTRATION DEPENDENCE

Fig. 11.5 shows normalized and heat-corrected data for concentrations of f_H between 0.1 and 100%. To better show the difference in the isotropic signals (top), all data were divided by the mono-exponential fit to the lowest concentration (0.1%). This concentration of 0.1% is expected to be low enough to prevent vibrational Förster transfer between O–H groups [117]. From the resulting decay traces it is clear that increasing f_H results in an additional *mono-exponential* relaxation channel. All isotropic data can be described with:

$$\Delta\alpha(t) = \exp\left[-\left(k_0 + \Delta k(f_H)\right)\ t\right] , \tag{11.8}$$

where $k_0 = 1/450$ fs^{-1} is the rate of decay of $f_H = 0.1\%$ and $\Delta k(f_H)$ is the concentration dependent additional decay rate. The fitted decay rates $k_0 + \Delta k(f_H)$ are summarized in Fig. 11.6. The decay rate goes up quickly for the initial concentration increases but levels off beyond 35%.

Next, we examine the anisotropic data of Fig. 11.5 (bottom). We note that all traces exhibit a similar rapid initial decay to a clear and distinct end level. These traces can be fitted well using:

$$R(t) = E(f_H) + [0.4 - E(f_H)] \cdot \exp\left(-k_F\ t\right) , \tag{11.9}$$

where $k_F = 1/140$ fs^{-1} is the rate and $E(f_H)$ is the concentration dependent end level. The resulting fitted end levels are summarized in Fig. 11.6. The end

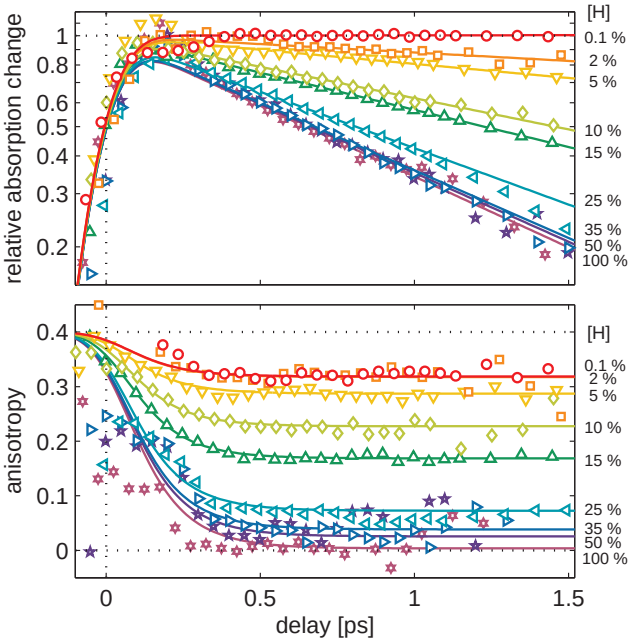

FIGURE 11.5. Heat corrected data and fits of all measured concentrations of H_2O in D_2O ice at 270 K. The isotropic data (top) has been divided by $\exp(2.2t)$ (i. e. the relaxation rate for 0.1% H_2O) to better show the effect of increasing H_2O concentrations. It may be noted that the additional relaxation channel is still mono-exponential, which means that the effect of adding H_2O is simply to increase the overall relaxation rate (from 2.2 up to 3.3 ps^{-1}). The anisotropy end levels show a clear decreasing trend indicative of Förster energy transfer between nearby O–H stretch vibrations as the H_2O concentration increases. For 100% H_2O we observe complete isotropic redistribution. The lines in the top figure indicate mono exponential fits to the data while for the bottom figure they show exponentials decaying to an end level. In both cases the fits were convoluted with the instrument response time (200 fs). Data points for delay times < 200 fs are affected by coherent artifacts.

levels drop significantly when the concentration is increased from 5% to about 35%.

11.3.6 ICE STRUCTURE

Comparing the top and bottom panels of Fig. 11.6, we observe a strong similarity between the increase of the isotropic decay rate and the drop in the end levels of the anisotropy. This observation indicates that a similar cause may be at the root of both phenomena.

The decrease of the end levels of the anisotropy is directly related to the increased chance for vibrational Förster transfer between neighboring O–H groups.

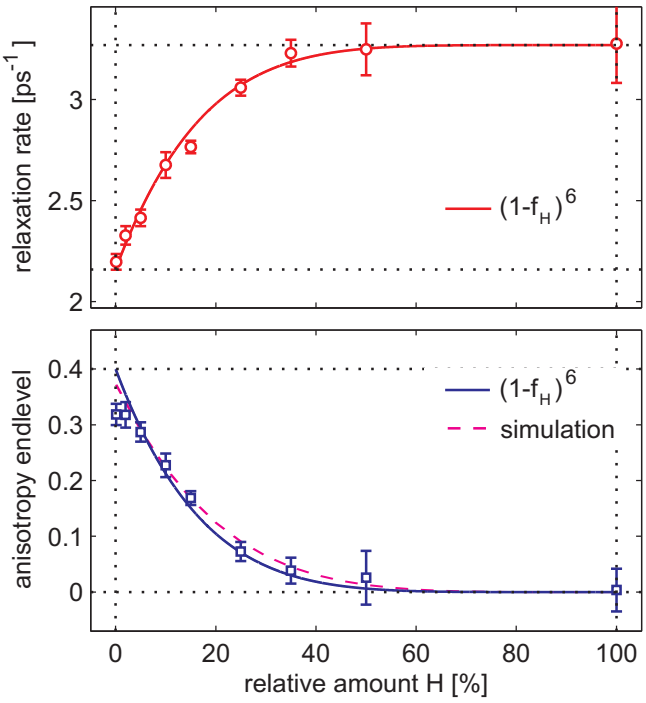

FIGURE 11.6. Decay rates and anisotropy end levels for all concentrations of H_2O in D_2O ice at 270 K. The lines show that both data closely follow the trend $(1 - f_H)^6$, where f_H is the fraction of H_2O in the sample. This indicates that both the rate increase and the anisotropy end level are dependent on the proximity of at least one hydrogen in the (nearest) six neighbors.

To get an idea about the effects of vibrational energy transfer on the anisotropy, we examine more closely the structure of ice I_H in Fig. 11.7. This figure shows part of a hexagonal ice crystal, where the oxygen atoms are arranged according to the $P6_3/mmc$ space group [16, 103], and are surrounded tetrahedrally by hydrogen atoms according to the Bernal-Fowler ice rules [15]. We set the covalent O–H distance to 1.0 Å and the hydrogen bond O$\cdots$H distance to 1.8 Å in accordance with neutron and x-ray diffraction studies on ice [57].

For the analysis we will assume that the direction of the transition dipole moment lies along the O–H bond of the water molecule, which is true if we neglect the motions of the much heavier oxygen atom. Furthermore, we use a harmonic approximation of the position of the oscillating dipole, which means we assume that the charge oscillation is centered around the position of the hydrogen atom.

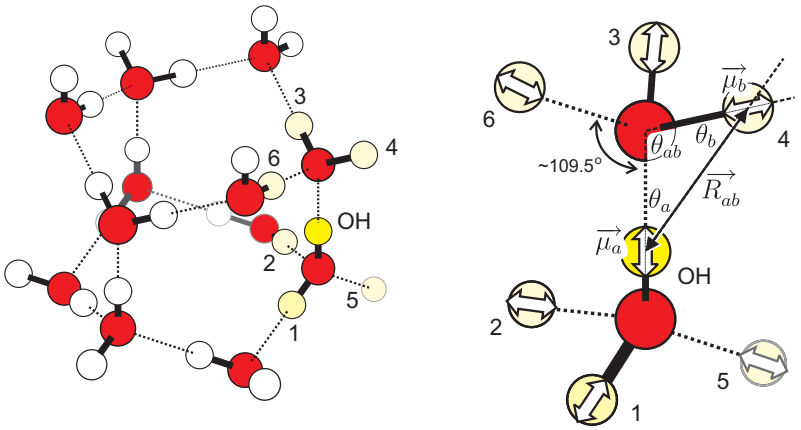

FIGURE 11.7. Three dimensional structure of hexagonal ice (c-axis vertical) showing the excited O–H stretch vibration and the nearest six hydrogen atoms. The solid lines indicate covalent bonds while the dashed lines indicate hydrogen bonds. The white arrows indicate the direction and position of the transition dipole moments of the O–H or O–D stretch vibrations.

11.3.7 FÖRSTER RATE

The rate of Förster energy transfer k_F between two dipole oscillators a and b is given by Eq. (4.69):

$$k_{F,ab} \propto \frac{|\vec{\mu}_a|^2 |\vec{\mu}_b|^2 \kappa_{ab}^2}{|\vec{R}_{ab}|^6} \int d\nu \; \sigma_a(\nu)\, \sigma_b(\nu)\,, \tag{11.10}$$

where $\vec{\mu}_a$ and $\vec{\mu}_a$ are the transition dipole moments of the transmitting and receiving dipole modes, $\vec{R}_{ab}$ is the distance vector between the dipoles, σ_a and σ_b are the normalized vibrational line shapes of the two modes, and κ_{ab} is a geometrical factor expressing the relative orientations of the dipole moments (see Fig. 11.7):

$$\kappa_{ab} = \hat{\mu}_a \cdot \hat{\mu}_b - 3(\hat{\mu}_a \cdot \hat{R}_{ab})(\hat{\mu}_a \cdot \hat{R}_{ab}) \approx \cos\theta_{ab} + 3\cos\theta_a \cos\theta_b\,, \tag{11.11}$$

where the hats denote normalized unit vectors. The latter equality only holds if all vectors lie in a plane along a triangle as drawn in Fig. 11.7, i. e. the transition dipoles point along the O–H$\cdots$O bonds.

The overlap integral of the vibrational line shapes of the O–H and O–D stretch modes is virtually zero due to their frequency mismatch. This means that an O–H vibration in a predominant D_2O ice lattice, will only be dipole coupled to other O–H groups in the lattice. We take the dipole strengths of different oscillators to be uniform in the ice crystal as is corroborated by the homogeneous spectrum in Fig. 11.1. The difference in coupling strength between O–H groups is thus only caused by their relative distance R_{ab} and orientational factor κ_{ab}.

TABLE I. **Förster parameters**

atom	κ_{ab}	R_{ab}	κ_{ab}^2/R_{ab}^6
1	1.6	1.6	1.5×10^{-1}
2-5	1.6	2.3	1.7×10^{-2}
6	1.6	2.9	4.3×10^{-3}
2^{nd} shell	0.9	3.6	3.7×10^{-4}

The regular structure and angles of the ice crystal lead to well-defined geometrical factors κ_{ab}. For example, we see from Fig. 11.7 that the neighboring O–H groups are all oriented with angles close to $\theta_a \approx \theta_b \approx (180 - 109.5)/2 \approx 35\,^\circ$. This leads to a similar orientational factor for these neighbors (all $\kappa_{ab} \approx 1.6 \pm 0.1$). The main factor to consider in the estimation of the Förster coupling strength is thus the distance R_{ab} between O–H oscillators (i. e. the distance between hydrogen atoms).

For atom 1, which is the hydrogen that is part of the same water molecule, this distance is the smallest: $R_{OH,1} \approx 1.6$ Å. The next four closest hydrogen atoms are those on the neighboring water molecules (atoms 2-5), all with a distance of ∼2.3 Å, followed by atom 6 which donates a hydrogen bond to the same oxygen as the excited O–H ($R_{OH,6} \approx 2.9$ Å). We note that for any configuration according to the Bernal-Fowler ice rules [15], there will always exist these six closest neighbors in the hexagonal ice lattice. Beyond these six, the next nearest neighbor, is at a distance of ∼3.6 Å and possesses a lower geometrical factor $\kappa_{ab} \approx 0.9$.

11.3.8 LIMITED TRANSFER RANGE

The distance and geometrical information is summarized in Table I, together with the resulting influence on the Förster transfer rate according to Eq. (11.10). We note that this rate quickly diminishes by about an order of magnitude for each next neighbor. We now speculate that this strong distance dependence, together with the highly ordered structure of ice is the reason for the clearly different time-regimes of the rapid initial drop in end-level and the subsequent much slower decay.

11.3.9 MODEL

Let us assume that the presence of a sufficiently nearby O–H to the original excitation will lead to a decay of the anisotropy. Or inversely, if no nearby O–H exists, the anisotropy will not decay. The measured anisotropy end-level will be the average over all possible configuration of hydrogen and deuterium. As a simple approach we consider the chance p that the nearest N atoms, to which Förster transfer can take place, are all deuterium. This chance is dependent on

the fraction of hydrogen f_H as:

$$p(f_H) = (1 - f_H)^N \,. \tag{11.12}$$

This will also be the fraction of excited O–H oscillators that cannot Förster transfer their vibrational energy to any nearby neighbor and will keep their original orientation. As we have seen in Eq. (11.7), the total anisotropy end level is the average over all configurations. If we assume, for simplicity, that if no transfer can take place the anisotropy remains $R = 0.4$, while any transfer leads to an anisotropy $R = 0$, the end level E will be given simply by:

$$E(f_H) = 0.4 \cdot (1 - f_H)^N \,. \tag{11.13}$$

We fit this simple model to the data in Fig. 11.6, and find that the data can be best described using a value of N between 5 and 6. This number indicates that the O–H vibration is Förster coupled to at most six of its nearest neighbors, and negligible beyond. Basically, the steepness of the end level decrease has to agree with the number of contributing neighbors. If only the nearest neighbor (of the same water molecule) were involved, a linear dependence ($N = 1$) would have been found. Conversely, if more than six neighbors were involved, the end level would have dropped more rapidly.

We note finally that although the vibrational relaxation is well described by the current model (top panel Fig. 11.6), the description of the anisotropy end level deviates somewhat for the lowest concentrations $f_H < 2\%$ (bottom panel Fig. 11.6). We observe that even for the lowest concentration $f_H = 0.1\%$, the anisotropy end level does not remain at 0.4. The most likely explanation for this observation is, that the direction of the transition dipole moments in the ice crystal is not completely fixed, even though no (complete) reorientation of the water molecules takes place. This phenomenon has been previously observed in the initial rapid anisotropy decay of liquid water and was interpreted as a 'librational cone' [45]. This effect is of less importance if the vibrational energy can jump to another O–H group, since it only tends to lower the overall anisotropy. From Eq. (11.2) we may deduce that the observed end level of $R = 0.33$ would correspond to a librational cone angle of about $\sim 20\,^\circ$.

11.3.10 FÖRSTER RADIUS

The distance dependent Förster rate $k_F(R)$ can be calculated using Eq. (11.14):

$$k_F(R) = \frac{1}{\tau_1} \left(\frac{R_0}{R} \right)^6 \,, \tag{11.14}$$

where R is the distance between donor and acceptor, τ_1 is the donor lifetime, and R_0 is the Förster radius defined as the distance where $k_F(R_0) = 1/\tau_1$. Using Eq. (11.14) we first calculate the Förster radius of the O–H vibration in ice. We fill in $\tau_1 = 0.45$ ps, the vibrational lifetime of $f_H = 0.1\%$, and $k_F(R) = 1/140$ fs^{-1} for a transfer to the nearest neighbors (atoms 2-5) at a distance $R = 2.3$ Å (see Table I). This results in a radius $R_{0,\mathrm{OH(s)}} = 2.8$ Å.

This radius is bigger than those previously found for the O–H in liquid D_2O [162] ($R_{0,\mathrm{OH}(\ell)} = 2.1$ Å) and the O–D in liquid H_2O [117] ($R_{0,\mathrm{OD}(\ell)} = 2.3$ Å). To compare the rates of Förster transfer between liquid water and ice we use Eq. (11.14) to derive:

$$\hat{k}_F \equiv k_F(R) \times R^{\,6} = \frac{R_0^6}{\tau_1}\,, \tag{11.15}$$

where $\hat{k}_F$ is the normalized Förster rate for $R = 1$. Filling in the lifetime and Förster radius of the O–H vibration in ice results in $\hat{k}_{F,\mathrm{OH(s)}} = 1.1 \times 10^3$ ps^{-1} Å$^{\,6}$. For the O–H vibration in liquid water we use $\tau_1 = 0.7$ ps [123] and calculate $\hat{k}_{F,\mathrm{OH(l)}} = 1.2 \times 10^2$ ps^{-1} Å$^{\,6}$. So we find that the Förster rate in ice is almost ten times higher than in liquid water. We note that these two rates were derived using quite different methods. The rate in liquid water was derived from a fit to a continuum model [162], while the currently found rate in ice was estimated from the discrete set of rates to the closest neighbors.

A previous study [117], comparing the Förster rates of the O–H and O–D stretch vibrations in liquid water, found that the differences in transfer rates ($\hat{k}_{F,\mathrm{OH(l)}} \approx 2.3\,\hat{k}_{F,\mathrm{OD(l)}}$) could be explained from the differences in the linear absorption spectra, i. e. the differences in transition dipole strength. We have already seen in Fig. 11.1 that the absorption cross-section of ice is much higher than that of liquid water, thus explaining at least part of the increased Förster rate. Another part could be explained by looking at the difference in the shape of the absorption spectra. We note in Fig. 11.1 that the absorption line shape of liquid water (i. e. Gaussian) indicates a significant amount of inhomogeneous broadening, whereas the absorption line shape of ice looks much more like a Lorentzian (indicative of homogeneous broadening). Because the O–H stretch modes in ice are more homogeneous than in liquid water, the average absorption and emission spectra in ice will also be very similar and thus better overlapped. As can be seen from the overlap integral in Eq. (11.10), an enhanced frequency overlap between donor and acceptor leads to an enhanced Förster rate.

From Table I we note that the expected rate of Förster transfer to the second shell (beyond atom 6) is 12 times slower than to atom 6 and that it is 46 times slower than to atoms 2–5. This large gap in coupling strength could explain why we do not notice the influence of hydrogen atoms beyond those of the closest six neighbors. If we assume the rate of Förster transfer to O–H groups 2–5 to be 1/140 fs^{-1}, the rate to groups beyond O–H group 6 (2^{nd} shell) would be on a time scale > 6.4 ps. This explains why we see a plateau in the anisotropy decay: after the initial rapid transfer to the nearest neighbors has taken place, the rate to the next neighbors is too slow to observe in a picosecond time window.

A major difference between liquid water and ice is the amount of inhomogeneity (see also Fig. 11.1). Whereas in liquid water there exist a wide variety of different hydrogen bond angles, distances and strengths, the water molecules in ice are much more rigidly positioned. That is why we do not observe a continuous distance dependence for Förster transfer in ice. Of course, for water such a continuum description will also break down for transfer distances comparable

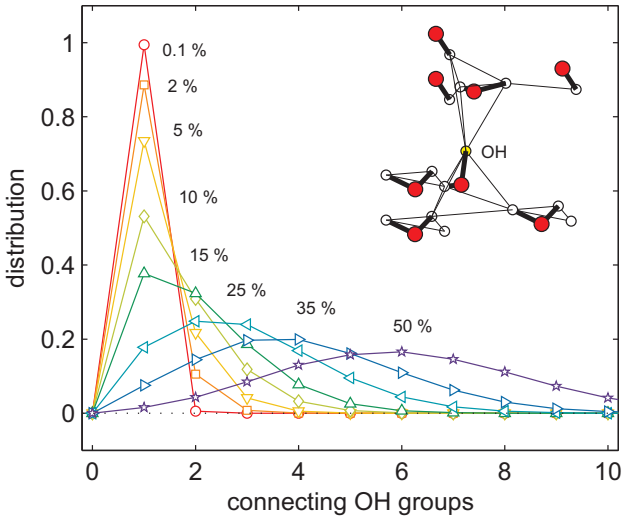

FIGURE 11.8. Distribution of the number of (consecutively) neighboring O–H groups (H–H distance < 3 Å) in H_2O/D_2O hexagonal ice as a function of H_2O concentration. The top-right inset shows an example cluster where thin lines connect each hydrogen atom to its closest neighbors.

to the molecular size, but because the anisotropy decay in water is convoluted by the molecular reorientation, such effects are less noticeable than in ice.

11.3.11 CLUSTER SIMULATION

Several assumptions were made in the simplified model of Eq. (11.13). To check the justification of these assumptions we perform a set of simulations that more accurately reflect the physical layout (i. e. orientations and positions) of the O–H stretch oscillators in the hexagonal ice lattice.

For the simulation we use a series of randomly generated hexagonal ice crystals, similar to the one shown in Fig. 11.7, but more extended. Starting from a central hydrogen atom, we use configurations of up to 20 nearest neighbors and loop over all possible 2^{20} configurations of hydrogen and deuterium atoms. Within each configuration we determine the cluster of (consecutively) neighboring O–H groups, where a connection is defined as $R_{H-H} < 3$ Å (six nearest, see Table I). Fig. 11.8 shows an example cluster and the distribution of close O–H groups for different concentrations that were used. From this figure we note that for concentrations up to 15%, the dominant configuration consists of a set of two neighboring O–H groups and that the number of neighboring O–H groups remains finite for concentrations up to 50%.

We allow the vibrational excitation to randomly hop to any O–H group within the interconnecting cluster and record the relative angles of the transition

dipole moments, with respect to the original excitation (assuming they lie along the O–H bond). Using Eq. (11.4) we proceed to calculate the corresponding anisotropies of the individual O–H groups. These individual anisotropies are averaged to yield the anisotropy of the cluster. These cluster anisotropies are weighted with the (binomial) chance of that particular cluster occurring, finally yielding the total anisotropy (end level). The result of this simulation is shown as the dashed line in Fig. 11.6. It shows good agreement with both the data and the simple model of Eq. (11.13).

11.3.12 VIBRATIONAL RELAXATION RATE

We now turn our attention to the concentration dependent vibrational relaxation rate, recorded in Fig. 11.6. As we noted before, the trend of the increasing relaxation rate is very similar to that of the anisotropy end level, which means they are likely caused by the same phenomenon. Indeed we see in Fig. 11.6 that we may fit the vibrational relaxation time quite nicely using:

$$\Delta k(f_H) = \Delta k_{\max} \cdot \left[1 - (1 - f_H)^N\right] , \tag{11.16}$$

where $\Delta k_{\max} = 1.1$ ps^{-1} is the maximum rate increase observed for a concentration of $f_H = 100\%$.

We find an excellent fit with $N = 6$. This value of N can be explained from the proximity of at least one hydrogen atom in one of the six nearest neighbors. We note that the Förster transfer of a vibrational excitation does not necessarily lead to the decay of that excitation, but only to a displacement (and different direction). The local density of accepting modes may be different after this displacement, but not necessarily higher. So this displacement need not lead to an enhanced relaxation of the O–H stretch mode. We therefore need to look for the effect of a nearby hydrogen atom on any of the possible accepting modes of the O–H stretch.

To understand the nature of this additional channel it is useful to first determine the principal relaxation channel for the O–H stretch mode in ice. In a previous study [35] on 2.5% H_2O in D_2O ice I_h, it was observed (in agreement with our current findings) that the relaxation proceeds through an intermediate level, before manifesting as a thermalized end spectrum. Also, the relaxation time that was found in that study (420 fs) is in excellent agreement with the current results (cf. $f_H = 2.5\%$ in Fig. 11.6). It was noted [35], that the anisotropy of the intermediate level did not deviate from that of the $\nu = 0 \rightarrow 1$ transition. This leads to the conclusion that the intermediate level consists of a mode that is located nearby the original excitation. Finally, the intermediate level has an associated spectrum that is wider and blue-shifted compared to the $\nu = 0 \rightarrow 1$ transition. This blue-shift can be caused both as a result of a weakened hydrogen bond or as the result of an anharmonic coupling between the O–H stretch mode and the H–O–D bending mode [84].

For the observed rate increase, we note that replacing a deuterium atom in HDO with a hydrogen atom, will affect its bending mode and improve the coupling strength to the O–H stretch mode. However, the additional relaxation

increases with a trend that suggests it is facilitated by the presence of hydrogen in one of *six* nearby neighbors. If it were only influenced by the hydrogen present in the same molecule, we would have found a linear concentration dependence. These observations indicate that *also* intermolecular coupling must play a role in the current observations. We speculate that the *additional* relaxation channel consists of the coupling between the O–H stretch mode and a combination of two H–O–D bending modes on two neighboring water molecules. A similar relaxation path, where the energy of the O–H stretch was redistributed over the H–O–H bending modes of two water molecules was previously observed for the vibrational relaxation of pure liquid water [84].

11.4 Conclusion

We have measured the relaxation time and anisotropy decay of the O–H stretch vibration in ice I_H for a range of temperatures and ratios H_2O/D_2O. We used a model with an intermediate level to correct for the effects of the (isotropic) thermalization dynamics on the relaxation and anisotropy. For increasing concentrations of H_2O we find that the vibrational relaxation time decreases from 480 fs (0.1%) down to 300 fs (100%), and that the anisotropy end level decreases from ∼0.33 (0.1%) to 0 (100%). The initial decrease in the anisotropy level from 0.4 to 0.33 is interpreted as the result of the librational motion of the water molecules over a cone of $\sim 20\,^\circ$. The subsequent ∼140 fs decay of anisotropy is attributed to vibrational Förster energy transfer to nearby O–H stretch modes.

We observe the relaxation rate to become slightly faster (∼5%) when the temperature is decreased from 270 to 200 K. The concentration dependence of the anisotropy end level and the relaxation rate can be modeled (phenomenologically) assuming a $(1 - f_H)^6$ dependence on the fraction of hydrogen atoms f_H. The exponent is interpreted as the influence of the six nearest neighboring hydrogen atoms. The strong cut-off between these six neighbors and those further away is caused by a combination of the strong $1/R^6$ distance dependence of the dipole-dipole (Förster) coupling and the discrete character of the distances between atoms in the ice crystal.

This phenomenological model was checked using a set of (cluster) simulations that contained a more complete description of the exact structure and distances in hexagonal ice. For ice there exists a discrete set of distances where the dipolar coupling of the neighbors in the second shell is about two orders of magnitude less than those of the nearest neighbors in the first shell. This picture contrasts with the continuum description of Förster transfer in liquid water, used in previous work. The strong correlation of the concentration dependence of the relaxation rate with the Förster energy transfer indicates that the hopping between O–H oscillators helps in finding a vibrational relaxation pathway for the O–H stretch excitation.

Bibliography

1. Vienna standard mean ocean water.
2. N. Agmon. From energy profiles to structure-reactivity correlations. *Intern. J. Chem. Kinet.*, 13(4):333–365, 1981.
3. N. Agmon. Reactive line-shape narrowing in low-temperature inhomogeneous geminate recombination of CO to myoglobin. *Biochem.*, 27(9):3507–3511, May 1988.
4. N. Agmon. The Grotthuss mechanism. *Chem. Phys. Lett*, 244:456, 1995.
5. N. Agmon. Structure of concentrated HCl solutions. *J. Phys. Chem. A*, 102(1):192–199, Jan. 1998.
6. N. Agmon. Elementary steps in excited-state proton transfer. *J. Phys. Chem. A*, 109(1):13–35, 2005.
7. J. B. Asbury, T. Steinel, C. Stromberg, S. A. Corcelli, C. P. Lawrence, J. L. Skinner, and M. D. Fayer. Water dynamics: Vibrational echo correlation spectroscopy and comparison to molecular dynamics simulations. *J. Phys. Chem. A*, 108(7):1107–1119, Feb. 2004.
8. B. Auer, R. Kumar, J. R. Schmidt, and J. L. Skinner. Hydrogen bonding and Raman, IR, and 2D-IR spectroscopy of dilute HOD in liquid D_2O. *PNAS*, 104(36):14215–14220, Sept. 2007.
9. W. E. Ayrton and J. Perry. Ice as an electrolyte. *Proc. Phys. Soc. London*, 2(1):171–182, 1877.
10. H. J. Bakker. Structural dynamics of aqueous salt solutions. *Chem. Rev.*, 108(4):1456–1473, 2008.
11. H. J. Bakker, J. J. Gillijamse, and A. J. Lock. Energy transfer in single hydrogen-bonded water molecules. *Chem. Phys. Chem.*, 6:1146–1156, 2005.
12. H. J. Bakker, S. Woutersen, and H.-K. Nienhuys. Reorientational motion and hydrogen-bond stretching dynamics in liquid water. *Chem. Phys.*, 258(2-3):233–245, Aug. 2000.
13. L. D. Barron, L. Hecht, and G. Wilson. The lubricant of life: A proposal that solvent water promotes extremely fast conformational fluctuations in mobile heteropolypeptide structure. *Biochem.*, 36(43):13143–13147, Oct. 1997.

14. P. A. Bergstroem, J. Lindgren, and O. Kristiansson. An IR study of the hydration of perchlorate, nitrate, iodide, bromide, chloride and sulfate anions in aqueous solution. *J. Phys. Chem.*, 95(22):8575–8580, Oct. 1991.

15. J. D. Bernal and R. H. Fowler. A theory of water and ionic solution, with particular reference to hydrogen and hydroxyl ions. *J. Chem. Phys*, 1(8):515–548, 1933.

16. N. Bjerrum. Structure and properties of ice. *Kong. Danske Vid. Selsk. mat.-fys. Medd.*, 27:56, 1951.

17. M. L. Brewer, U. W. Schmitt, and G. A. Voth. The formation and dynamics of proton wires in channel environments. *Biophys. J.*, 80(4):16911702, Apr. 2001.

18. B. S. Brunschwig, S. Ehrenson, and N. Sutin. The distance dependence of electron transfer reactions: rate maxima and rapid rates at large reactant separations. *J. Am. Chem. Soc.*, 106(22):6858–6859, Oct. 1984.

19. A. I. Burshtein. Unified theory of photochemical charge separation. *Adv. Chem. Phys.*, 114:419–587, 2000.

20. A. I. Burshtein and V. S. Malinovsky. Free-induction decay in the framework of sudden-modulation theory. *J. Opt. Soc. Am. B*, 8(5):1098–1113, May 1991.

21. H. S. Carslaw and J. C. Jaeger. *Conduction of Heat in Solids*. Oxford University Press: Oxford, 2 edition, 1959.

22. M. Chaplin. Water structure and science. www.lsbu.ac.uk/water, 2009.

23. C. H. Cho, J. Urquidi, S. Singh, and G. W. Robinson. Thermal offset viscosities of liquid H_2O, D_2O, and T_2O. *J. Phys. Chem. B*, 103(11):1991–1994, Mar. 1999.

24. S. Chowdhuri and A. Chandra. Dynamics of halide ion-water hydrogen bonds in aqueous solutions: Dependence on ion size and temperature. *J. Phys. Chem. B*, 110(19):9674–9680, May 2006.

25. B. Cohen, D. Huppert, and N. Agmon. Non-exponential smoluchowski dynamics in fast acid-base reaction. *J. Am. Chem. Soc.*, 122(40):9838–9839, Oct. 2000.

26. B. Cohen, D. Huppert, and N. Agmon. Diffusion-limited acid-base nonexponential dynamics. *J. Phys. Chem. A*, 105(30):7165–7173, Aug. 2001.

27. F. C. Collins and G. E. Kimball. Diffusion-controlled reaction rates. *J. Colloid Sci.*, 4:425–437, 1949.

28. M. L. Cowan, B. D. Bruner, N. Huse, J. R. Dwyer, B. Chugh, E. T. J. Nibbering, T. Elsaesser, and R. J. D. Miller. Ultrafast memory loss and energy redistribution in the hydrogen bond network of liquid H_2O. *Nature*, 434:199, 2005.

29. M. J. Cox and H. J. Bakker. Parallel proton transfer pathways in aqueous acid-base reactions. *J. Chem. Phys*, 128(17):174501, 2008.

30. Q. Cui and M. Karplus. Is a proton wire concerted or stepwise? a model study of proton transfer in carbonic anhydrase. *J. Phys. Chem. B*, 107(4):1071–1078, Jan. 2003.

31. C. J. T. de Grotthus. Sur la décomposition de l'eau et des corps qu'elle tient en dissolution à l'aide de l'électricité galvanique. *Ann. Chim.*, 58:54–74, 1806.

32. J. C. Deak, Y. Pang, T. D. Sechler, Z. Wang, and D. D. Dlott. Vibrational energy transfer across a reverse micelle surfactant layer. *Science*, 306:473 – 476, 2004.

33. P. G. Debenedetti. Supercooled and glassy water. *J. Phys. Cond. Matt.*, 15(45):R1669–R1726, 2003.

34. H. Decornez and S. Hammes-Schiffer. Effects of model protein environments on the dynamics of proton wires. *Israel J. Chem.*, 39:397–407, 1999.

35. A. M. Dokter and H. J. Bakker. Transient absorption of vibrationally excited ice ih. *J. Chem. Phys*, 128(2):024502, 2008.

36. O. K. Dudko and A. Szabo. Time-dependent rate coefficients for diffusion-influenced reactions with centrosymmetric potentials. *J. Phys. Chem. B*, 109(12):5891–5894, Mar. 2005.

37. J. C. Duplan, L. Mahi, and J. L. Brunet. Nmr determination of the equilibrium constant for the liquid H_2O-D_2O mixture. *Chem. Phys. Lett*, 413(4-6):400 – 403, 2005.

38. J. D. Eaves, J. J. Loparo, C. J. Fecko, S. T. Roberts, A. Tokmakoff, and P. L. Geissler. Hydrogen bonds in liquid water are broken only fleetingly. *PNAS*, 102:13019–13022, 2005.

39. M. Eigen. Proton transfer, acid-base catalysis, and enzymatic hydrolysis. part I: Elementary processes. *Angew. Chem. Intl. Ed.*, 3(1):1–19, 1964.

40. M. Eigen, W. Kruse, G. Maass, and L. D. Maeyer. Rate constants of protolytic reactions in aqueous solution. *Prog. React. Kinet*, 2:287–318, 1964.

41. M. Eigen and L. D. Maeyer. Self-dissociation and protonic charge transport in water and ice. *Proc. Royal. Soc. London A- Math. Phys. Sci.*, 247:505–533, 1958.

42. D. Eisenberg and W. Kauzmann. *The Structure and Properties of Water*. Oxford University Press, New York, 1969.

43. C. Fang, A. Senes, L. Cristian, W. F. DeGrado, and R. M. Hochstrasser. Amide vibrations are delocalized across the hydrophobic interface of a transmembrane helix dimer. *PNAS*, 103:16740, 2006.

44. C. J. Fecko, J. D. Eaves, J. J. Loparo, A. Tokmakoff, and P. L. Geissler. Ultrafast hydrogen-bond dynamics in the infrared spectroscopy of water. *Science*, 301:1698–1701, 2003.

45. C. J. Fecko, J. J. Loparo, S. T. Roberts, and A. Tokmakoff. Local hydrogen bonding dynamics and collective reorganization in water: Ultrafast infrared spectroscopy of hod/D_2O. *J. Chem. Phys*, 122:054506, 2005.

46. P. J. Flory. *Statistical Mechanics of Chain Molecules*. Interscience: New York, 1969.

47. T. Förster. Experimentelle und theoretische untersuchung des zwischenmolekularen ubergangs von elektronenanregungsenergie. *Z.Naturforschg.*, 4:821–827, 1940.

48. T. Förster. Zwischenmolekulare energiewanderung und fluoreszenz. *Ann. Physik*, 2:55–75, 1948.

49. F. Franks, editor. *Water: A Comprehensive Treatise*, volume 3. Plenum, London, 1973.

50. G. M. Gale, G. Gallot, F. Hache, N. Lascoux, S. Bratos, and J.-C. Leicknam. Femtosecond dynamics of hydrogen bonds in liquid water: A real time study. *Phys. Rev. Lett.*, 82:1068–1071, 1999.

51. G. Gallot, S. Bratos, S. Pommeret, N. Lascoux, J. C. Leicknam, M. Kozinski, W. Amir, and G. M. Gale. Coupling between molecular rotations and OH$\cdots$O motions in liquid water: Theory and experiment. *J. Chem. Phys*, 117(24):11301–11309, 2002.

52. L. Genosar, B. Cohen, and D. Huppert. Ultrafast direct photoacid-base reaction. *J. Phys. Chem. A*, 104(29):6689–6698, July 2000.

53. J. J. Gilijamse, A. J. Lock, and H. J. Bakker. Dynamics of confined water molecules. *PNAS*, 102:3202–3207, 2004.

54. I. V. Gopich, K. M. Solntsev, and N. Agmon. Excited-state reversible geminate reaction. i. two different lifetimes. *J. Chem. Phys*, 110(4):2164–2174, 1999.

55. E. Guardia, D. Laria, and J. Marti. Hydrogen bond structure and dynamics in aqueous electrolytes at ambient and supercritical conditions. *J. Phys. Chem. B*, 110(12):6332–6338, Mar. 2006.

56. D. Hadzi and S. Bratos. *The Hydrogen Bond*, volume 2. Elsevier, 1976.

57. E. Isaacs, A. Shukla, P. Platzman, D. Hamann, B. Barbiellini, and C. Tulk. Covalency of the hydrogen bond in ice: A direct x-ray measurement. *Phys. Rev. Lett.*, 82(3):600–603, Jan. 1999.

58. C. Jaccard. Theoretical and experimental studies of the electrical properties of ice. *Helv. Phys. Acta*, 32:89, 1959.

59. S. R. Keiding, D. Madsen, J. Larsen, S. K. Jensen, and J. Thogersen. When molecules meet : a femtosecond study of the protonation of a base. *Chem. Phys. Lett*, 390:94, 2004.

60. J. Kim, U. W. Schmitt, J. A. Gruetzmacher, G. A. Voth, and N. E. Scherer. The vibrational spectrum of the hydrated proton: Comparison of experiment, simulation, and normal mode analysis. *J. Chem. Phys*, 116(2):737–746, 2002.

61. J. T. Kindt and C. A. Schmuttenmaer. Far-infrared dielectric properties of polar liquids probed by femtosecond terahertz pulse spectroscopy. *J. Phys. Chem.*, 100(24):10373–10379, Jan. 1996.

62. C. Kobayashi, S. Saito, and I. Ohmine. Mechanism of fast proton transfer in ice: Potential energy surface and reaction coordinate analyses. *J. Chem. Phys*, 113(20):9090–9100, 2000.

63. M. F. Kropman and H. J. Bakker. Dynamics of water molecules in aqueous solvation shells. *Science*, 291:2118, 2001.

64. M. F. Kropman and H. J. Bakker. Femtosecond mid-infrared spectroscopy of aqueous solvation shells. *J. Chem. Phys*, 115(19):8942–8948, 2001.

65. M. F. Kropman and H. J. Bakker. Effect of ions on the vibrational relaxation of liquid water. *J. Am. Chem. Soc.*, 126(29):9135–9141, July 2004.

66. M. F. Kropman, H.-K. Nienhuys, and H. J. Bakker. Real-time measurement of the orientational dynamics of aqueous solvation shells in bulk liquid water. *Phys. Rev. Lett.*, 88:077601, 2002.

67. R. Kubo, M. Toda, and N. Hashitsume. *Statistical Physics II*. Solid-state Sciences. Springer, 2 edition, 1995.

68. M. Kunst and J. M. Warman. Nanosecond time-resolved conductivity studies of pulse-ionized ice. 2. the mobility and trapping of protons. *J. Phys. Chem.*, 87(21):4093–4095, 1983.

69. A. Kyrychenko and J. Waluk. Excited-state proton transfer through water bridges and structure of hydrogen-bonded complexes in 1H-pyrrolo[3,2-h]quinoline: Adiabatic time-dependent density functional theory study. *J. Phys. Chem. A*, 110(43):11958–11967, Nov. 2006.

70. A. D. Laage and J. T. Hynes. Do more strongly hydrogen-bonded water molecules reorient more slowly? *Chem. Phys. Lett*, 433:80–85, 2006.

71. D. Laage and J. T. Hynes. A molecular jump mechanism of water reorientation. *Science*, 311:832–835, 2006.

72. D. Laage and J. T. Hynes. Reorientational dynamics of water molecules in anionic hydration shells. *PNAS*, 104:11167, 2007.

73. D. Laage and J. T. Hynes. On the molecular mechanism of water reorientation. *J. Phys. Chem. B*, 112:14230, 2008.

74. R. Laenen, C. Rauscher, and A. Lauberau. Dynamics of local substructures in water observed by ultrafast infrared hole burning. *Phys. Rev. Lett.*, 80:2622–2625, 1998.

75. J. R. Lakowicz. *Principles of Fluorescence Spectroscopy*. Springer, 1999.

76. C. P. Lawrence and J. L. Skinner. Vibrational spectroscopy of HOD in liquid D_2O. III. spectral diffusion, and hydrogen-bonding and rotational dynamics. *J. Chem. Phys*, 118(1):264–272, 2003.

77. C. P. Lawrence and J. L. Skinner. Vibrational spectroscopy of HOD in liquid D_2O. VII. temperature and frequency dependence of the OH stretch lifetime. *J. Chem. Phys*, 119:3840–3848, 2003.

78. W. R. Laws and L. Brand. Analysis of two-state excited-state reactions. the fluorescence decay of 2-naphthol. *J. Phys. Chem.*, 83(7):795–802, Apr. 1979.

79. C.-W. Lee, P.-R. Lee, Y.-K. Kim, and H. Kang. Mechanistic study of proton transfer and h/d exchange in ice films at low temperatures (100–140 k). *J. Chem. Phys*, 127(8):084701, 2007.

80. P. Leiderman, L. Genosar, and D. Huppert. Excited-state proton transfer: Indication of three steps in the dissociation and recombination process. *J. Phys. Chem. A*, 109(27):5965–5977, July 2005.

81. P. Leiderman, R. Gepshtein, A. Uritski, L. Genosar, and D. Huppert. Temperature dependence of excited-state proton transfer in water electrolyte solutions and water. *J. Phys. Chem. A*, 110(29):9039–9050, 2006.

82. P. Leiderman, D. Huppert, and N. Agmon. Transition in the temperature-dependence of gfp fluorescence: From proton wires to proton exit. *Biophys. J.*, 90(3):1009–1018, Feb. 2006.

83. P. Leiderman, A. Uritski, and D. Huppert. Temperature dependence of excited state proton transfer in ice. *J. Phys. Chem. A*, 111(23):4998–5007, 2007.

84. J. Lindner, P. Vohringer, M. S. Pshenichnikov, D. Cringus, D. A. Wiersma, and M. Mostovoy. Vibrational relaxation of pure liquid water. *Chem. Phys. Lett*, 421:329–333, 2006.

85. G. Lipari and A. Szabo. Effect of librational motion on fluorescence depolarization and nuclear magnetic resonance relaxation in biomolecules and membranes. *Biophys. J.*, 30:489–506, 1980.

86. E. R. Lippincott and R. Schroeder. One-dimensional model of the hydrogen bond. *J. Chem. Phys*, 23(6):1099–1106, 1955.

87. A. J. Lock and H. J. Bakker. Temperature dependence of vibrational relaxation in liquid H_2O. *J. Chem. Phys*, 117(4):1708–1713, 2002.

88. J. J. Loparo, S. T. Roberts, and A. Tokmakoff. Multidimensional infrared spectroscopy of water. ii. hydrogen bond switching dynamics. *J. Chem. Phys*, 125(19):194522, 2006.

89. H. Luecke, H.-T. Richter, and J. K. Lanyi. Proton transfer pathways in bacteriorhodopsin at 2.3 Ångstrom resolution. *Science*, 280(5371):1934–1937, June 1998.

90. Z. Luz and S. Meiboom. The activation energies of proton transfer reactions in water. *J. Am. Chem. Soc.*, 86(22):4768–4769, Nov. 1964.

91. O. Markovitch and N. Agmon. Structure and energetics of the hydronium hydration shells. *J. Phys. Chem. A*, 111(12):2253–2256, Mar. 2007.

92. D. Marx. Proton transfer 200 years after von Grotthuss: Insights from ab initio simulations. *Chem. Phys. Chem.*, 7:1848–1870, 2006.

93. S. Meiboom. Nuclear magnetic resonance study of the proton transfer in water. *J. Chem. Phys*, 34(2):375–388, 1961.

94. E. Meyer. Internal water molecules and h-bonding in biological macromolecules: A review of structural features with functional implications. *Protein Science*, 1:1543–1562, 1992.

95. W. Mikenda. Stretching frequency versus bond distance correlation of hydrogen bonds in solid hydrates. *J. Mol. Struct.*, 147:1–15, 1986.

96. R. E. Miller. The vibrational spectroscopy and dynamics of weakly bound neutral complexes. *Science*, 240:447, 1988.

97. O. Mohammed, D. Pines, E. Nibbering, and E. Pines. Base-induced solvent switches in acid-base reactions. *Angew. Chem. Intl. Ed.*, 46(9):1458–1461, 2007.

98. O. F. Mohammed, D. Pines, J. Dreyer, E. Pines, and E. T. J. Nibbering. Sequential proton transfer through water bridges in acid-base reactions. *Science*, 310(5745):83–86, Oct. 2005.

99. O. F. Mohammed, D. Pines, E. Pines, and E. T. Nibbering. Aqueous bimolecular proton transfer in acid-base neutralization. *Chem. Phys.*, 341(1-3):240–257, Nov. 2007.

100. D. E. Moilanen, E. E. Fenn, Y. Lin, J. L. Skinner, B. Bagchi, and M. D. Fayer. Water inertial reorientation: Hydrogen bond strength and the angular potential. *PNAS*, 105:5295, 2008.

101. D. E. Moilanen, D. Wong, D. E. Rosenfeld, E. E. Fenn, and M. D. Fayer. Ion-water hydrogen-bond switching observed with 2d ir vibrational echo chemical exchange spectroscopy. *PNAS*, 106(2):375–380, Jan. 2009.

102. M. Morin, P. Jakob, N. J. Levinos, Y. J. Chabal, and A. L. Harris. Vibrational energy transfer on hydrogen-terminated vicinal si(111) surfaces: Interadsorbate energy flow. *J. Chem. Phys*, 96(8):6203–6212, 1992.

103. I. Morrison, J. Li, S. Jenkins, S. Xantheas, and M. Payne. Ab-initio total energy studies of the static and dynamical properties of ice ihn. *J. Phys. Chem. B*, 101(32):6146–6150, Aug. 1997.

104. S. Murata, S. Y. Matsuzaki, and M. Tachiya. Transient effect in fluorescence quenching by electron transfer. 2. determination of the rate parameters involved in the marcus equation. *J. Phys. Chem.*, 99(15):5354–5358, Apr. 1995.

105. B. J. Murray, D. A. Knopf, and A. K. Bertram. The formation of cubic ice under conditions relevant to earth's atmosphere. *Nature*, 434(7030):202–205, Mar. 2005.

106. J. C. Nash. *Compact Numerical Methods for Computers: Linear Algebra and Function Minimisation, 2nd ed.* Bristol, England, 1990.

107. H.-K. Nienhuys. *Femtosecond mid-infrared spectroscopy of water.* PhD thesis, FOM institute AMOLF, 2002.

108. H.-K. Nienhuys, R. A. Van Santen, and H. J. Bakker. Orientational relaxation of liquid water molecules as an activated process. *J. Chem. Phys*, 112:8487–8494, 2000.

109. B. Numerov. Note on the numerical integration of $\mathrm{d}^2x/\mathrm{d}t^2 = f(x,t)$. *Astr. Nach.*, 230(19):359–364, 1927.

110. A. W. Omta, A. M. Kropman, S. Woutersen, and H. J. Bakker. Negligible effect of ions on the hydrogen-bond structure in liquid water. *Science*, 301:347, 2003.

111. A. W. Omta, M. F. Kropman, S. Woutersen, and H. J. Bakker. Influence of ions on the hydrogen-bond structure in liquid water. *J. Chem. Phys*, 119(23):12457–12461, 2003.

112. S. K. Pal, J. Peon, B. Baghi, and A. H. Zewail. Biological water: Femtosecond dynamics of macromolecular hydration. *J. Phys. Chem. B*, 106:12376–12395, 2002.

113. S. K. Pal and A. H. Zewail. Dynamics of water in biological recognition. *Chem. Rev.*, 104:2099, 2004.

114. S. Park and M. D. Fayer. Hydrogen bond dynamics in aqueous nabr solutions. *PNAS*, 104(43):16731–16738, Oct. 2007.

115. S. Park, D. E. Moilanen, and M. D. Fayer. Water dynamics - the effects of ions and nanoconfinement. *J. Phys. Chem. B*, 112(17):5279–5290, May 2008.

116. J. B. Pedersen and P. Sibani. The long time behavior of the rate of recombination. *The Journal of Chemical Physics*, 75(11):5368–5372, 1981.

117. L. Piatkowski, K. B. Eisenthal, and H. J. Bakker. Ultrafast intermolecular energy transfer in heavy water. *Phys. Chem. Chem. Phys.*, 11:9033–9038, 2009.

118. E. Pines and D. Huppert. Geminate recombination proton-transfer reactions. *Chem. Phys. Lett*, 126(1):88 – 91, 1986.

119. E. Pines, D. Huppert, and N. Agmon. Geminate recombination in excited-state proton-transfer reactions: Numerical solution of the debye–smoluchowski equation with backreaction and comparison with experimental results. *J. Chem. Phys*, 88(9):5620–5630, 1988.

120. E. Pines, B.-Z. Magnes, M. J. Lang, and G. R. Fleming. Direct measurement of intrinsic proton transfer rates in diffusion-controlled reactions. *Chem. Phys. Lett*, 281(4-6):413–420, Dec. 1997.

121. R. Rey, K. B. Moller, and J. T. Hynes. Hydrogen bond dynamics in water and ultrafast infrared spectroscopy. *J. Phys. Chem. A*, 106(50):11993–11996, Dec. 2002.

122. Y. L. A. Rezus and H. J. Bakker. On the orientational relaxation of HDO in liquid water. *J. Chem. Phys*, 123:114502, 2005.

123. Y. L. A. Rezus and H. J. Bakker. Orientational dynamics of isotopically diluted H_2O and D_2O. *J. Chem. Phys*, 125(14):144512, 2006.

124. S. A. Rice. *Diffusion Limited Reactions*, volume 25 of *Comprehensive Chemical Kinetics*. Elsevier, Amsterdam, 1985.

125. M. Rini, B.-Z. Magnes, E. Pines, and E. T. J. Nibbering. Real-time observation of bimodal proton transfer in acid-base pairs in water. *Science*, 301(5631):349–352, July 2003.

126. M. Rini, D. Pines, B.-Z. Magnes, E. Pines, and E. T. J. Nibbering. Bimodal proton transfer in acid-base reactions in water. *J. Chem. Phys*, 121(19):9593–9610, 2004.

127. C. Rønne, P. O. Astrand, and S. R. Keiding. THz spectroscopy of liquid H_2O and D_2O. *Phys. Rev. Lett.*, 82(14):2888–2891, 1999.

128. D. J. Segelstein. The complex refractive index of water. Master's thesis, University of Missouri, Kansas City, 1981. Referenced by Scott Prahl on the 'optical absorption of water' website.

129. C. F. Shannon and D. D. Eads. Diffusion-controlled electron transfer reactions: Subpicosecond fluorescence measurements of coumarin 1 quenched by aniline and n,n-dimethylaniline. *J. Chem. Phys*, 103(13):5208–5223, 1995.

130. I. Shiklomanov. *Water in Crisis: A Guide to the World's Fresh Water Resources*. Oxford University Press, New York, 1993.

131. M. Sikorski, E. Krystkowiak, and R. Steer. The kinetics of fast fluorescence quenching processes. *Journal of Photochemistry and Photobiology A: Chemistry*, 117(1):1–16, Aug. 1998.

132. B. J. Siwick and H. J. Bakker. On the role of water in intermolecular proton-transfer reactions. *J. Am. Chem. Soc.*, 129(44):13412–13420, 2007.

133. B. J. Siwick, M. J. Cox, and H. J. Bakker. Long-range proton transfer in aqueous acid-base reactions. *J. Phys. Chem. B*, 112(2):378–389, 2008.

134. D. W. G. Smith and J. G. Powles. Proton spin-lattice relaxation in liquid water and liquid ammonia. *Mol. Phys.*, 10(5):451–463, 1966.

135. L. Song, R. C. Dorfman, S. F. Swallen, and M. D. Fayer. Influence of dlffuslon on photoinduced electron transfer. *J. Phys. Chem.*, 95:3454–3457, 1991.

136. A. K. Soper and C. J. Benmore. Quantum differences between heavy and light water. *Phys. Rev. Lett.*, 101(6):065502, 2008.

137. T. Steinel, J. B. Asbury, S. Corcelli, C. Lawrence, J. Skinner, and M. Fayer. Water dynamics: dependence on local structure probed with vibrational echo correlation spectroscopy. *Chem. Phys. Lett*, 386(4-6):295 – 300, 2004.

138. T. Steinel, J. B. Asbury, J. Zheng, and M. D. Fayer. Watching hydrogen bonds break: A transient absorption study of water. *J. Phys. Chem. A*, 108:10957 –10964, 2004.

139. J. Stenger, D. Madsen, P. Hamm, E. T. J. Nibbering, and T. Elsaesser. Ultrafast vibrational dephasing of liquid water. *Phys. Rev. Lett.*, 87:027401, 2001.

140. J. Stenger, D. Madsen, P. Hamm, E. T. J. Nibbering, and T. Elsaesser. A photon echo peak shift study of liquid water. *J. Phys. Chem. A*, 106:2341–2350, 2002.

141. L. Stryer and R. P. Haugland. Energy transfer: a spectroscopic ruler. *PNAS*, 58(2):719–726, Aug. 1967.

142. A. Szabo. Theory of diffusion-influenced fluorescence quenching. *J. Phys. Chem.*, 93(19):6929–6939, Sept. 1989.

143. A. Szabo, R. Zwanzig, and N. Agmon. Diffusion-controlled reactions with mobile traps. *Phys. Rev. Lett.*, 61(21):2496–2499, 1988.

144. M. Tachiya. *Rad. Phys. Chem.*, 21:167–175, 83.

145. T. Takamuku, D. Matsuo, M. Tabata, T. Yamaguchi, and N. Nishi. Structure of aqueous mixtures of n,n-dimethylacetamide studied by infrared spectroscopy, x-ray diffraction, and mass spectrometry. *J. Phys. Chem. B*, 107:6070–6078, 2003.

146. K. Tielrooij, C. Petersen, Y. Rezus, and H. Bakker. Reorientation of HDO in liquid H_2O at different temperatures: Comparison of first and second order correlation functions. *Chem. Phys. Lett*, 471(1-3):71 – 74, 2009.

147. R. L. A. Timmer and H. J. Bakker. Water as a molecular hinge in amidelike structures. *J. Chem. Phys*, 126(15):154507, 2007.

148. N. M. Trieff and B. R. Sundheim. The effect of solvent on the acid-base kinetics of the excited state of beta-naphthol. *J. Phys. Chem.*, 69(6):2044–2059, June 1965.

149. A. Uritski, P. Leiderman, and D. Huppert. Proton reaction with a mild base in ice studied by proton. *J. Phys. Chem. C*, 111(25):8856–8865, 2007.

150. A. Uritski, I. Presiado, Y. Erez, R. Gepshtein, and D. Huppert. Temperature dependence of proton diffusion in ih ice. *J. Phys. Chem. C*, 113(23):10285–10296, 2009.

151. A. Uritski, I. Presiado, and D. Huppert. Indication of a very large proton diffusion in ice ih. *J. Phys. Chem. C*, 112(31):11991–12002, 2008.

152. O. Vendrell, R. Gelabert, M. Moreno, and J. M. Lluch. Operation of the proton wire in green fluorescent protein. a quantum dynamics simulation. *J. Phys. Chem. B*, 112(17):5500–5511, May 2008.

153. M. von Smoluchowski. Versuch einer mathematischen theorie der koagulationskinetik kolloider loesungen. *Z. Physik. Chem.*, 92:129–168, 1917.

154. G. E. Walrafen. Raman spectral studies of the effects of electrolytes on water. *J. Chem. Phys*, 36(4):1035–1042, 1962.

155. A. Weller. Allgemeine basenkatalyse bei der elektrolytischen dissoziation angeregter naphthole. *Z. Elektrochem.*, 58:849–853, 1954.

156. A. Weller. *Z. Phys. Chem. NF*, 17:224–245, 1958.

157. A. Weller. Fast reactions of excited molecules. *Prog. React. Kinet.*, 1:187–214, 1961.

158. G. Wilemski and M. Fixman. General theory of diffusion-controlled reactions. *J. Chem. Phys*, 58(9):4009–4019, 1973.

159. R. J. Wittebort, M. G. Usha, D. J. Ruben, D. E. Wemmer, and A. Pines. Observation of molecular reorientation in ice by proton and deuterium magnetic resonance. *J. Am. Chem. Soc.*, 110(17):5668–5671, Aug. 1988.

160. P. J. Wooldridge and J. P. Devlin. Proton trapping and defect energetics in ice from FT-IR monitoring of photoinduced isotopic exchange of isolated D_2O. *J. Chem. Phys*, 88(5):3086–3091, 1988.

161. S. Woutersen and H. J. Bakker. Hydrogen bond in liquid water as a brownian oscillator. *Phys. Rev. Lett.*, 83(10):2077–2080, Sept. 1999.

162. S. Woutersen and H. J. Bakker. Resonant intermolecular transfer of vibrational energy in liquid water. *Nature*, 402:507–509, 1999.

163. S. Woutersen and H. J. Bakker. Ultrafast vibrational and structural dynamics of the proton in liquid water. *Phys. Rev. Lett.*, 96:138305, 2006.

164. S. Woutersen, U. Emmerichs, and H. J. Bakker. Femtosecond mid-IR pump-probe spectroscopy of liquid water: Evidence for a two-component structure. *Science*, 278:658–660, 1997.

165. S. Woutersen, U. Emmerichs, and H. J. Bakker. A femtosecond midinfrared pump-probe study of hydrogen-bonding in ethanol. *J. Chem. Phys*, 107(5):1483–1490, 1997.

166. S. Woutersen, U. Emmerichs, H.-K. Nienhuys, and H. J. Bakker. Anomalous temperature dependence of vibrational lifetimes in water and ice. *Phys. Rev. Lett.*, 81:1106–1109, 1998.

167. A. Wulf and R. Ludwig. Structure and dynamics of water confined in dimethyl sulfoxide. *Chem. Phys. Chem.*, 7:266–272, 2006.

168. S. Yeremenko, M. S. Pshenichnikov, and D. A. Wiersma. Hydrogen-bond dynamics in water explored by heterodyne-detected photon echo. *Chem. Phys. Lett*, 369(1-2):107–113, Feb. 2003.

169. H. Zhou and A. Szabo. Theory and simulation of the time-dependent rate coefficients of diffusion-influenced reactions. *Biophys. J.*, 71(5):2440–2457, Nov. 1996.

Summary

Pump-probe This thesis describes experiments on the microscopic behavior of water molecules in various environments including liquid water and ice. The reported studies are roughly divided into three main categories: molecular reorientation, charge transfer, and energy transfer. Because these processes typically occur on an extremely fast (picosecond) timescale we need a special technique to resolve their time-dynamics. The method of choice here is femtosecond pump-probe spectroscopy. This technique involves the interaction of two ultrashort (∼100 fs) laser pulses with vibrational and electronic transitions in the sample under study. The first pulse (pump) interacts with the sample to create a non-equilibrium situation which subsequently evolves in time. This evolution is recorded by a probe pulse which is delayed with respect to the pump. This procedure is repeated for various delays between pump and probe to yield a molecular movie of the events following pump excitation.

The most basic pump-probe experiment involves the isotropic redistribution of (vibrational) energy following the local vibrational excitation of an oscillator in the sample. The flow of energy can be observed by analyzing the spectral signatures of the components that are involved. These signatures not only reveal the states of the excited molecules (water), but also their interaction with the environment. A more intricate approach of pump-probe spectroscopy involves the use of the different polarizations of the laser pulses. A linearly polarized pump beam preferentially excites oscillators in the sample whose transition dipole moments are aligned with that of the pump polarization. The resulting anisotropy can be monitored to reveal the reorientation of the molecules that were originally excited or the resonant transfer of the vibrational energy to nearby (randomly oriented) oscillators.

Reorientation In Chapter 5 we describe experiments on the molecular reorientation mechanism of liquid water. We study this mechanism with a polarization-resolved pump-probe experiment on the O–D stretch mode in HDO/D_2O water. We find that the spectral dynamics of the observed anisotropy decay strongly depend on the frequency of the pump excitation. When the pump frequency is tuned to the blue side of the O–D stretch band, a rapid decay of the anisotropy is observed on the red side. This finding is explained with a model which includes a molecular 'jumping model' for the reorientation of liquid water. As the name indicates this model implies that the reorientation of water molecules occurs through a sudden jump between hydrogen bond acceptors rather than by a gradual (diffusive) change in orientation. The occurrence of such a jump is found to be more likely for water molecules on the blue side of the spectrum where hydrogen bonds are weak. The combina-

tion of the collective slow hydrogen-bond dynamics of liquid water with a time constant of ∼700 fs and this jumping mechanism lead to the average molecular reorientation time of liquid water of ∼2.5 ps.

In Chapter 6 we continue our experiments on the reorientation of water. This time we study the dynamics of isolated water molecules in a solution of N,N-dimethylacetamide (DMA). DMA is a model system that strongly resembles the amide groups which constitute the backbone of protein molecules. We find that single water molecules form double hydrogen-bond connections to the DMA molecules resulting in the formation of DMA-water-DMA complexes. Using the anisotropy decay of three different directions of the complexes we find that the system exhibits bimodal rotational dynamics with two distinct timescales: a slow (7±1 ps) reorientation of the entire DMA-water-DMA complex and a fast (0.5±0.2 ps) 'hinging' motion of the water molecule around the axis defined by the two connecting hydrogen bonds. Additionally, we observe an exchange of vibrational energy between the two normal modes of H_2O at a timescale of 0.8±0.1 ps, and find that the excitation decays through the symmetric stretch normal mode with a time constant of 0.8±0.2 ps.

In Chapter 7 we conclude our study of the reorientational dynamics of water an investigation of water molecules in the hydration shell of bromide anions. By comparing the vibrational lifetimes of O–H groups attached to the bromide ion for low and high salt concentrations we deduce that water molecules rotate out of the solvation shell with a time constant of ∼7 ps. We study also the frequency fluctuations of the O–H stretch vibrations of HDO molecules near bromide anions using spectral hole-burning spectroscopy. These frequency fluctuations are correlated to the hydrogen bond fluctuations of the $\text{O–H}\cdots\text{Br}^-$ hydrogen bonds of the hydration shell of the bromide anion and are found to occur on a timescale of 4.3±0.3 ps. This time scale is found to be independent of the concentration (5–15 mol/kg) and the nature of the cation (Na, Li).

CHARGE TRANSFER In the following two chapters we study the molecular mechanisms of proton (charge) transfer in water and ice. In our pump-probe experiments we can trigger and observe the flow of proton charges through the samples. To this purpose we use special molecules called photo-acids that can be electronically excited by an ultraviolet pump pulse resulting in the release of a proton into the solvent environment at a well defined instance in time. This release and the subsequent travel of the proton charge through the solvent is monitored by observing the time-resolved spectral signatures of the release, travel, and arrival of the proton at different types of base molecules.

In Chapter 8 we use the photo-acid HPTS to study proton transfer dynamics in liquid water at different temperatures and base concentrations (acetate). The experimental data comprise the spectral signatures of the protonated and unprotonated photo-acid molecule and are described quantitatively using an extended Smoluchowski (diffusion) model. This extension includes a reactivity that shows a Gaussian dependence on the separation between acid and base molecules. This distance dependence contrasts with the classic view that acid and base molecules diffuse around in the water until they find each other at a

specific reaction distance. We find that the distance dependent reactivity likely represents the rate of concerted (multi-)proton hopping across 'water wires' of different length connecting acid-base pairs in solution. The concerted nature of the proton transfer is supported by the fact that the rate shows a steeper dependence on the distance at higher temperatures. This steepness results from the enhanced disorder at higher temperatures which disrupts the wire structure that is required for concerted proton transfer. In a sequential proton transfer scenario the opposite dependence would be expected, as each hopping event is expected to become more rapid with increasing temperature.

In Chapter 9 we continue our experiments on proton transfer, but this time in ice of temperatures down to -30 °C. Just as in the previous chapter we use HPTS photo-acid molecules and different concentrations of base molecules (formate). We probe the rise of the carbonyl mode as a fingerprint for the arrival of the proton at the base molecule. We find that the dynamics at all concentrations can be described using a discrete set of only two rates for proton transfer and a Poisson distribution of base molecules. Proton transfer in configurations where the acid and base were separated by up to about two water molecules, was found to occur on a ∼1 ps timescale for all temperatures (240-270 K). Long range direct proton transfer through water wires of about four water molecule length was found to occur on a ∼300 ps timescale for 270 K. This latter process was observed to slow down significantly with decreasing temperature, with an activation energy of ∼80 kJ/mol. A continuous model of rates, such as used for liquid water, cannot account for the observations for low concentrations because the data displays no intermediate rate between 1 and 300 ps. The main difference found between proton transfer in liquid water and ice is a much stronger temperature dependence and the fact that in ice we observe no parallel process in which the proton is taken up by the solvent (ice lattice) before transfer to the base.

Energy Transfer In this thesis we describe two mechanisms for the transfer of vibrational energy between different modes. In one mechanism, energy is transferred between molecular modes that are anharmonically coupled by a common set of coordinates. Examples of this transfer include the vibrational relaxation of the O–H stretch mode in water to the H–O–H bending mode or the O–H$\cdots$O hydrogen bond mode. The other mechanism relies on a resonant dipole-dipole coupling between two modes and is called Förster energy transfer. In the previous chapters on molecular reorientation we have mostly used isotopically dilute water samples to minimize the amount of Förster transfer that would otherwise scramble the direction of the vibrational transition. In these final chapters however, it is precisely this Förster transfer mechanism that we are interested in.

In Chapter 10 we study Förster energy transfer between the O–H and O–D stretch modes in liquid water on one hand and solvated proton modes on the other hand. These proton modes have an unusually high absorption cross-section in water which allows them to act as high efficiency acceptors for Förster energy transfer. We study this energy transfer by measuring the vibrational

relaxation times of the O–D and O–H stretch mode in samples with varying concentrations of excess protons (0–4 mol/kg). We find that the addition of protons introduces a non-exponential energy relaxation pathway for the O–D stretch mode, but not for the O–H stretch mode. This observation confirms that the relaxation pathway relies on the resonant (Förster) energy transfer between the O–D stretch and proton modes, which is not possible for the O–H. The relaxation is modeled for all proton concentrations using a distance-dependent ($1/R^6$) transfer rate. For a proton concentration of 1 mol/kg we find that Förster energy transfer occurs over an average distance of about two water molecules. Using polarization resolved information, it is furthermore shown that the addition of protons has a negligible influence on the reorientation time of bulk water (2.7±0.2 ps).

In Chapter 11 we conclude with a study of Förster energy transfer in ice. We use different mixtures of H_2O and D_2O to control the distance between O–H stretch modes in the ice lattice and thus the rate of Förster energy transfer between them. We find that the vibrational relaxation time of the O–H stretch decreases from 480 fs for dilute HDO in D_2O down to 300 fs for pure H_2O ice. The anisotropy shows an initial 140 fs decay down to a concentration-dependent end level. For low concentrations the end level can be explained from the limited rotational freedom ($\sim 20^\circ$) of a water molecule in the ice lattice over time scales >15 ps. The decrease of the end level for higher concentrations of H_2O result from Förster energy transfer to the next nearest (six) O–H groups. No Förster transfer beyond these neighbors is observed for timescales <5 ps. Variation of the ice temperature between 200 and 270 K was found to have negligible effect on the energy transfer dynamics.

Samenvatting

Gewoon Water Water is zo verweven met ons dagelijks leven dat wij het vaak nauwelijk opmerken en beschouwen als een 'gewone' vloeistof. Maar is water eigenlijk wel zo gewoon? Op school leren we dat een water molecuul wordt aangeduid met de chemische formule H_2O, oftewel één zuurstofatoom verbonden met twee waterstofatomen. Als we water vergelijken met andere 'kleine' moleculen zoals bijvoorbeeld CO_2, dan valt op dat water bij kamertemperatuur een vloeistof is terwijl veel andere kleine moleculen zich dan in de gasfase bevinden. Deze observatie illustreert een belangrijke eigenschap van water, namelijk de mogelijkheid om waterstofbruggen te vormen. Deze waterstofbruggen kunnen gevormd worden doordat de ladingsverdeling binnen een watermolecuul niet helemaal symmetrisch verdeeld is tussen de waterstofatomen en het zuurstofatoom. De positieve lading van een waterstofatoom op het ene watermolecuul wordt aangetrokken door de negatieve lading op het zuurstofatoom van een ander watermolecuul waardoor een (waterstofbrug)verbinding ontstaat.

Water kan met deze waterstofbruggen verbindingen aangaan met vier andere watermoleculen en zo een uitgebreid driedimensionaal netwerk vormen. Een waterstofbrug is tien tot honderd maal sterker dan een gewone intermoleculaire (Van der Waals) binding. De waterstofbrug is dus sterk genoeg om ervoor te zorgen dat water kan condenseren bij kamertemperatuur. Hij is echter niet zo sterk dat het watermolecuul totaal geïmobiliseerd is. Sterker nog, vergeleken bij de tijdschalen die wij in ons dagelijks leven gewend zijn is het watermolecuul onvoorvoorstelbaar wendbaar. Zo blijkt in dit proefschrift bijvoorbeeld dat veel processen in water zoals reoriëntatie, energie- en ladingstransport, plaats vinden op tijdschalen van soms minder dan een picoseconde (10^{-12} seconde). Ter vergelijking: één picoseconde verhoudt zich tot één seconde als één seconde tot meer dan dertigduizend jaar!

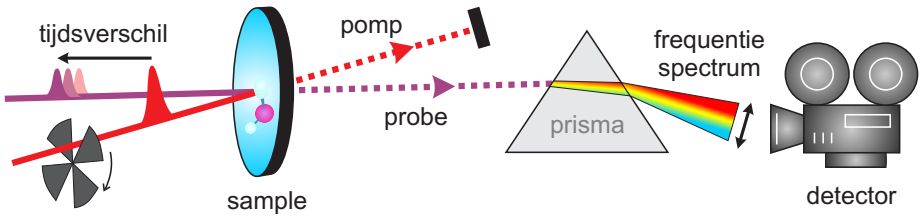

Figuur 1. Schematische weergave van een pomp-probe experiment.

MOLECULAIR FILMPJE Om de tijdsdynamica van zulke ultrasnelle processen te kunnen waarnemen gebruiken we een speciale techniek, genaamd pomp-probe spectroscopie (Figuur 1). Deze techniek bestaat uit een opeenvolging van twee ultrakorte laserpulsen, pomp en probe, elk met een pulsduur van ongeveer één-tiende picoseconde. Het tijdsverschil tussen de twee pulsen kan worden ingesteld door één van beide bundels langs een klein omweggetje te sturen (delaystage).

Zowel de pomp als de probe pulsen bestaan uit een verzameling frequenties (trillingen) die we afzonderlijk kunnen detecteren door bijvoorbeeld een prisma in de bundel te plaatsen. In pomp-probe spectroscopie kijken we naar het effect van de pomp pulsen op de absorptie van de probe pulsen. Om alleen gevoelig te zijn voor pomp-geïnduceerde veranderingen in het sample (het stofje dat we bestuderen) hebben we een soort ventilator in de pomp bundel geplaatst die elke tweede pomp puls blokkeert. Hierdoor kunnen we telkens de absorptie van de probe pulsen vergelijken mét en zonder pomp.

Als de frequenties van het licht in de pomp pulsen overeen komen met de frequenties van de moleculen in het sample zal dit leiden tot het in trilling brengen van de moleculen. Deze trillingen kunnen wij vervolgens detecteren met de probe pulsen door te kijken naar de frequenties van het licht die door het sample worden geabsorbeerd. Deze absorptiefrequenties van het sample zijn direct gerelateerd aan de specifieke toestand waarin de moleculen zich bevinden. Dankzij de korte tijdsduur van de pulsen zijn de momenten van aanslaan en bekijken zeer goed gedefinieerd. Door nu het relatieve tijdsverschil tussen de pomp en probe te variëren en telkens een absorptiespectrum op te nemen van de probe, maken wij als het ware een filmpje van de moleculaire dynamica die plaatsvindt in het sample.

Uit deze moleculaire filmpjes kunnen wij informatie halen over bijvoorbeeld de snelheid waarmee trillingsenergie wordt doorgegeven tussen de moleculen. Deze overdracht van energie is een belangrijke indicator voor de mate van moleculaire interactie tussen de aangeslagen moleculen en hun omgeving. Als de interactie zwak is zal deze energie overdracht langzamer gaan dan wanneer de interactie sterk is. Bijvoorbeeld, een geïsoleerd watermolecuul in de gasfase zal zijn energie veel langer vasthouden dan een watermolecuul in de vloeistoffase.

VINGERAFDRUK Een molecuul bestaat over het algemeen uit meerdere atomen. Groepen van atomen trillen elk met een frequentie die karakteristiek is voor die groep. Deze frequentie wordt bepaald door de massa van de atomen en krachten waarmee zij tot elkaar worden aangetrokken. Dit is te vergelijken met een klassiek massa-veer systeem waarbij een zwaardere massa (atoom) langzamer trilt dan lichtere. Elk molecuul heeft een specifieke combinatie van atomen en dus ook een specifieke set van (absorptie)frequenties: een spectrale vingerafdruk.

Deze vingerafdruk gebruiken wij niet alleen om te bepalen welke moleculen er in een sample zitten, maar ook in welke toestand deze moleculen zich bevinden. Veranderingen binnen een molecuul of tussen moleculen leiden namelijk tot veranderingen in de karakteristieke frequenties van dat molecuul. Bijvoor-

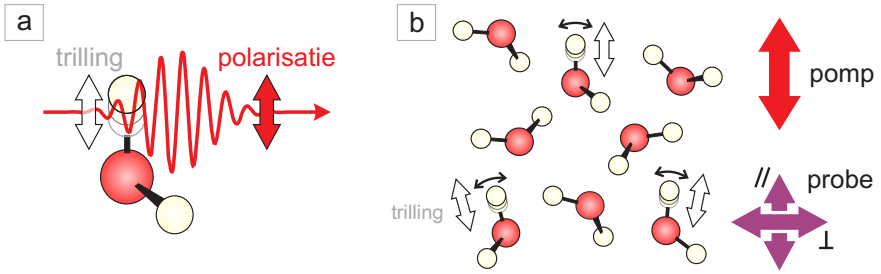

FIGUUR 2. (**a**) Gepolariseerd licht brengt een molecuul in trilling langs de richting van het elektrisch veld. (**b**) De trillingsrichting van draaiende moleculen kan gemeten worden door probe polarisaties te vergelijken die parallel (//) en loodrecht (⊥) op die van de pomp staan.

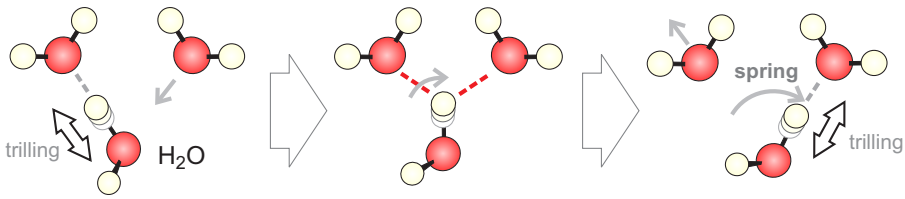

FIGUUR 3. Van links naar rechts: sprongsgewijze draaiing van een water molecuul.

beeld, het spectrum van watermoleculen in de vloeistoffase is veel breder dan het spectrum van watermoleculen in ijs. Deze breedte is gerelateerd aan de hoeveelheid wanorde in het sample waaruit dus volgt dat ijs gestructureerder is dan water. Door de veranderingen in het spectrum goed te bestuderen kunnen wij informatie afleiden over veranderingen binnen moleculen. Ook kunnen wij precies volgen hoe de energie van de pomp zich over verschillende moleculen verspreidt.

DRAAIEND WATER Behalve energieoverdracht kunnen we met onze experimenten ook kijken naar het *ronddraaien* van moleculen. Om deze draaiing te bepalen maken wij gebruik van het feit dat het oscillerend electrisch veld waaruit licht bestaat bij voorkeur wordt geabsorbeerd door moleculen waarvoor de trilling dezelfde richting (polarisatie) heeft als die van het elektrisch veld. (Figuur 2a). De pomppulsen in ons experiment zullen dus voornamelijk trillingen aanslaan in een richting parallel aan hun polarisatie. Omdat de moleculen draaien zal deze voorkeursrichting (anisotropie) veranderen als functie van tijd. Door gebruik te maken van twee probe-polarisaties (Figuur 2b) kunnen wij deze

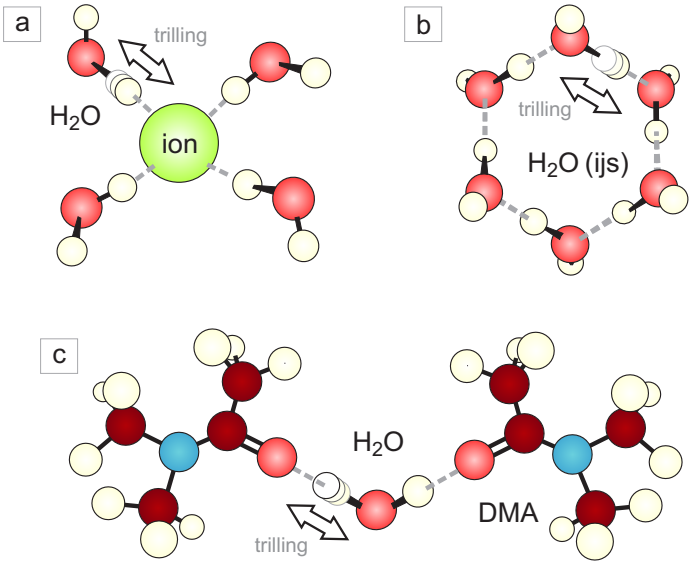

FIGUUR 4. Trillingen van water moleculen in verschillende systemen. (**a**) Water in een solvatatieschil rondom een negatief geladen zoution. (**b**) Watermoleculen in een hexagonale structuur in ijs. (**c**) Een geïsoleerd watermolecuul werkt als een scharnier tussen twee DMA moleculen.

draaiing van de oorspronkelijk aangeslagen trillingen volgen en zo een filmpje maken van de moleculaire draaiing.

Uit deze filmpjes hebben wij informatie afgeleid over de manier waarop een watermolecuul zich ronddraait. Het blijkt dat watermoleculen niet gewoon willekeurig rondtollen, maar dat de draaiing gepaard gaat met een 'sprongetje' waarbij het watermolecuul alleen zijn waterstofbrug verbreekt als het direct daarna een nieuwe brug kan vormen met een nieuw watermolecuul (Figuur 3). Uit andere experimenten aan water in de buurt van zouten blijkt dat watermoleculen een soort schilletje kunnen vormen rondom de geladen deeltjes (ionen) waaruit deze zouten bestaan (Figuur 4a). Uit onze moleculaire filmpjes blijkt dat de watermoleculen die zich in zo'n schilletje bevinden zich veel langzamer draaien dan gewoon water.

Onze experimenten aan water en biologische modelsystemen tonen aan hoe het watermolecuul kan fungeren als een soort lijm in de verbindingen die gemaakt worden binnen een eiwit. Deze functie wordt mogelijk gemaakt doordat het watermolecuul met zijn waterstofbruggen een 'scharnierverbinding' kan vormen tussen specifieke groepen binnen het eiwit molecuul (Figuur 4c). Op deze manier zijn de moleculaire eigenschappen van watermoleculen dus bepalend voor de vorm en functie van eiwitten en andere bio-moleculen.

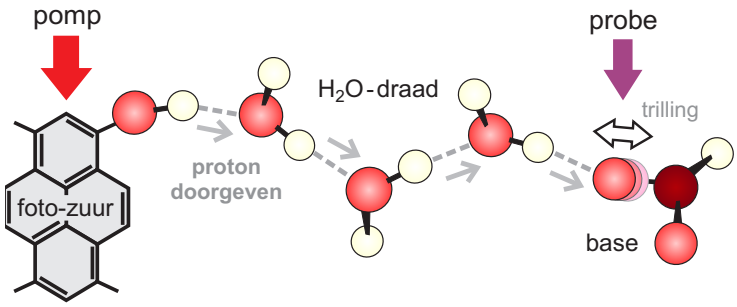

FIGUUR 5. Een fotozuur-molecuul (HPTS) geeft een proton door aan een base via een draad van watermoleculen. De opname van het proton door het base molecuul (HCOO) brengt een verandering teweeg in de trillingsfrequentie van de C–O groep.

ZURE KNIKKERS Een belangrijke biologische eigenschap van water is de oplosbaarheid en geleiding van geladen deeltjes, zoals zouten, en in het bijzonder protonen. Een proton is in feite niets anders dan een waterstofkern, H^+, en is dus één van de twee bouwstoffen waaruit H_2O water bestaat. Het is dan ook niet verwonderlijk dat er een bijzondere relatie bestaat tussen protonen en water. Wanneer er een overschot aan protonen in water is opgelost spreken we van een zuur. Onze smaaksensatie is bijzonder gevoelig voor deze extra protonen, bijvoorbeeld een zure appel (pH 2) heeft slechts één extra proton per vijfduizend watermoleculen!

In onze experimenten hebben we ondermeer gekeken naar de manier waarop protonen zich door het water kunnen bewegen. Dit kunnen wij doen met behulp van twee speciale moleculen: een fotozuur en een base. Een fotozuur bevat een extra proton dat stevig wordt vastgehouden totdat we het molecuul beschijnen met ultraviolet licht. Op dat moment wordt het proton losgelaten in het omringende water. Eenmaal in het water kan het proton zich razendsnel verplaatsen langs een zogenaamde 'waterdraad' totdat het wordt opgezogen door een basemolecuul.

Een waterdraad is een keten van aaneengesloten watermoleculen die allemaal zijn verbonden met een waterstofbrug (Figuur 5). Deze waterdraad is te vergelijken met een buis vol met knikkers waarbij de protonen de knikkers zijn. Op het moment dat we aan de ene kant een knikker in de buis drukken komt er op hetzelfde moment aan de andere kant een knikker uit. Ieder watermolecuul in de draad neemt aan de ene kant een proton op en geeft tegelijk aan de andere kant een proton af. Het is dus feitelijk niet hetzelfde proton dat wordt doorgegeven maar alleen de lading die op het proton zit.

IJSDRAAD Water is, zoals eerder gezegd, een bijzonder dynamische vloeistof: de moleculen draaien zich razendsnel rond en breken en vormen zo voortdurend nieuwe waterstofbruggen. Deze dynamica heeft tot gevolg dat er steeds weer nieuwe waterdraden worden gevormd terwijl de oude worden afgebroken. Het blijkt uit onze metingen dat juist deze vorming van waterdraden de beperkende factor in de proton overdracht is. Hoe verder een proton moet reizen, des te verder moet de waterdraad reiken om de overdracht mogelijk te maken.

Om meer inzicht te krijgen in de rol van deze waterdraad-dynamica hebben we ook gekeken naar proton overdracht in ijskristallen. Binnen een ijskristal staan de watermoleculen allemaal netjes in rijen naast elkaar en vormen ze een speciale 'honingraat' structuur (Figuur 4b). Het blijkt uit onze metingen dat watermoleculen in deze starre structuur zich maar weinig kunnen bewegen. Ze kunnen slechts een beetje trillen op de plaats terwijl ze van alle kanten stevig worden vastgehouden door hun buren. Toch kan er zo af en toe nog een watermolecuul verspringen en een nieuwe waterstofbrug vormen met een andere buur.

Deze starre structuur heeft gevolgen voor de manier waarop protonen zich door het ijs kunnen bewegen ten opzichte van water. Aan de ene kant zien we dat het gebrek aan dynamica zorgt dat waterdraden in ijs veel langer kunnen bestaan dan in water. Aan de andere kant zien we dat wanneer er geen geschikte draad voor handen is, dat het dan ook veel langer duurt om zo'n draad te vormen. In feite moet het proton wachten totdat een tussenliggend watermolecuul verspringt en zo de draad verbindt. In principe kan proton transport in ijskristallen dus sneller zijn dan in water, mits de juiste structuur voor waterdraden aanwezig is.

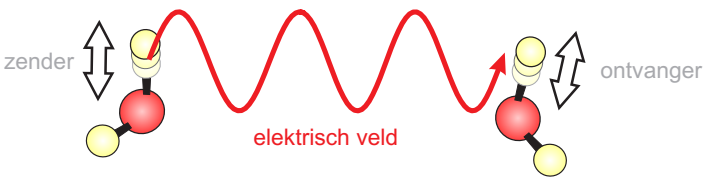

FIGUUR 6. Watermolecuul geeft trillingsenergie door via het elektrisch veld.

WATER ANTENNES Tenslotte hebben we nog gekeken naar een bijzondere manier van energieoverdracht tussen trillende water moleculen. De bewegende lading in een watermolecuul lijkt erg op de bewegende lading in een antenne. Net als in het geval van de antenne kan het watermolecuul elektrische velden verzenden en ontvangen. Op deze manier kan een trilling via het elektrisch veld worden overgedragen tussen moleculen ook zonder dat ze met elkaar in verbinding zijn (Figuur 6). Het blijkt dat deze manier van energieoverdracht een dominante rol speelt voor de verspreiding van trillingsenergie in water en

ijs. Onze experimenten laten onder andere zien hoe een trillend watermolecuul in ijs binnen een fractie van een picoseconde zijn energie doorgeeft aan zijn buren. Vanaf deze buren wordt de energie weer verder doorgegeven totdat het uiteindelijk wordt omgezet in warmte.

Protonen blijken bij deze manier van energieoverdracht ook nog een bijzondere rol te spelen. De lading van het proton versterkt namelijk de trillende lading in de omringende watermoleculen waardoor hun zendcapaciteit aanmerkelijk wordt vergroot. Deze versterkte waterantennes zijn bijzonder efficiënt in het opnemen en afvoeren van energie van moleculen uit hun omgeving. Dit mechanisme kan dus belangrijk zijn voor de energiehuishouding van biologische systemen waar protonen een prominente rol vervullen.

Dankwoord

Graag wil ik alle mensen bedanken die hebben bijgedragen aan de totstandkoming van dit proefschrift en de vele leuke jaren die ik op AMOLF en daarbuiten heb beleefd. Allereerst ben ik natuurlijk veel dank verschuldigd aan mijn promotor Huib die mij gedurende mijn verblijf altijd heeft bijgestaan met begeleiding en advies. Ik kon altijd bij hem terecht voor de meest uiteenlopende zaken, van experimenten in het lab tot detailleerde aspecten uit de niet-lineaire spectroscopie. Met zijn scherpe fysische intuïtie was hij veelal onmisbaar in de interpretatie en implicaties van de experimentele resultaten. Zijn feedback en input hebben een essentiële bijdrage geleverd bij het tot stand komen van zowel de artikelen als dit proefschrift.

Als tweede wil ik graag Yves bedanken, die gedurende vele jaren mijn kamergenoot was. Vooral in het begin heb ik veel van hem geleerd over zo ongeveer alle aspecten die belangrijk waren tijdens mijn promotie. Ik hecht veel belang aan onze discussies over fysica, chemie en de wiskundige aspecten van modellering. Met zijn gevoel voor humor hebben we samen vele grappen uitgehaald met veelal nietsvermoedende collega's (en bazen).

Łukasz, Woekie, Cousin Koekasz: hij is bekend onder vele namen en altijd een bijzondere kamergenoot en 'comrade' geweest, op mijn werk en daarbuiten. Ik heb Łukasz door de jaren heen zien groeien tot een vaardig experimentator en uitstekende wetenschapper. Ook Christian Petersen bedank ik voor de goede discussies en leuke sfeer op ons kantoor. Jocelyn en Klaas bedank ik voor de goede wetenschappelijke samenwerkingen die we hadden maar natuurlijk ook voor de vriendschap daarbuiten.

Adriaan en Joop wil ik graag bedanken omdat ze mij in mijn eerste half jaar hebben begeleid in het lab en de experimentele kneepjes van het vak hebben bijgebracht. Verder zouden mijn experimenten onmogelijk zijn geweest zonder de technische ondersteuning van Hinco, die vaak actief heeft meegedacht over het ontwerp van nieuwe opstellingen en apparaten. Ook Henk en Iliya bedank ik voor hun ondersteuning. Han-Kwang heeft mij vaak geholpen met allerhande zaken in het lab maar ook daarbuiten. Ook bedank ik hem voor de layout van dit proefschrift. Voor de goede sfeer op het werk en daarbuiten bedank ik nog de overige mensen van de groep Ultrafast Spectroscopy en de groepen van Mischa en Sander. In het bijzonder zijn dat: Bratley, Ellen, Christian, Sietse, Janneke, Nuria, Maria, Maaike, Avi, Ronald, Ruben, James, Joep, Pavol, Matthijs en Sergiy. In de privé sfeer bedank ik verder nog Bastiaan voor onze goede vriendschap.

Ten slotte wil ik dicht bij huis eindigen en mijn zussen Nicoline en Léonie, mijn ouders en mijn lieve vriendin Alena bedanken voor hun steun en betrokkenheid door de jaren heen.